NBSIR 76-839

SEMI-ANNUAL REPORT ON MATERIALS RESEARCH IN SUPPORT OF SUPERCONDUCTING MACHINERY

R. P. Reed, J. G. Hust, M. B. Kasen, H. M. Ledbetter,
D. T. Read, R. E. Schramm, L. L. Sparks, and R. L. Tobler

Cryogenics Division
Institute for Basic Standards
National Bureau of Standards
Boulder, Colorado 80302

April 1976

Prepared for :
Advanced Research Projects Agency
1400 Wilson Boulevard
Arlington, Virginia 22209

NBSIR 76-839

SEMI-ANNUAL REPORT ON MATERIALS RESEARCH IN SUPPORT OF SUPERCONDUCTING MACHINERY

R. P. Reed, J. G. Hust, M. B. Kasen, H. M. Ledbetter,
D. T. Read, R. E. Schramm, L. L. Sparks, and R. L. Tobler

Cryogenics Division
Institute for Basic Standards
National Bureau of Standards
Boulder, Colorado 80302

April 1976

Prepared for :

Advanced Research Projects Agency
1400 Wilson Boulevard
Arlington, Virginia 22209

U.S. DEPARTMENT OF COMMERCE, Elliot L. Richardson, Secretary
James A. Baker, III, Under Secretary
Dr. Betsy Ancker-Johnson, Assistant Secretary for Science and Technology

NATIONAL BUREAU OF STANDARDS, Ernest Ambler, Acting Director

SEMI-ANNUAL REPORT ON MATERIALS RESEARCH

IN SUPPORT OF SUPERCONDUCTING MACHINERY

Sponsored by
Advanced Research Projects Agency
ARPA Order No. 2569
Program Code 4D10
August 10, 1975 - October 1, 1976

Program Director
Dr. E. C. van Reuth
Materials Sciences
Advanced Research Projects Agency
1400 Wilson Boulevard
Arlington, Virginia 22209

Program Manager
Dr. R. P. Reed
Cryogenics Division
Institute for Basic Standards
National Bureau of Standards
Boulder, Colorado 80302

The views and conclusions contained in this document are those of the authors and should not be interpreted as necessarily representing the official policies, either expressed or implied, of the Advanced Research Projects Agency or of the U.S. Government.

Abstract

Results are reported of a six-month study, ending March 1976, on candidate materials for superconducting machinery. The results cover five areas--advanced composites, elastic properties, fatigue resistance and fracture toughness, magnetothermal conductivity, and thermal conductivity. Material properties were studied over the temperature range 4 to 300 K. Materials studied include: aluminum alloys 1100, 2014, 2219; a nickel-chromium-iron alloy; iron-47.5 nickel; and the composite materials boron/aluminum, boron/epoxy, S-glass/epoxy; graphite/epoxy. Some notable results of the study are: first reports of compressive mechanical testing on composite materials at 4 K; regular temperature behavior of the elastic constants of aluminum 2014 and 2219 and of iron-47.5 nickel, which is magnetic; none of the mechanical properties of the nickel-chromium-iron alloy tested were affected deleteriously by cryogenic temperatures; in aluminum alloy 2219, J_{Ic} and K_{Ic} are not equivalent because of sub-critical crack extension; both electrical and thermal conductivities of aluminum alloy 1100 are reduced by magnetic fields.

This work was supported by the Advanced Research Projects Agency of the U.S. Department of Defense.

Keywords: Aluminum alloys; composites; elastic properties; engineering materials; fatigue; fracture; iron alloys; cryogenic temperatures; mechanical properties; nickel alloys; superconducting machinery; thermal conductivity.

Report Contents

Page

ADVANCED COMPOSITES
R. E. Schramm and M. B. Kasen 1

Reprint: Mechanical and Thermal Properties of Filamentary-Reinforced Structural Composites at Cryogenic Temperatures. 2: Advanced Composites; M. B. Kasen; Cryogenics 15 (1975) 701-22 19

ELASTIC PROPERTIES OF ENGINEERING MATERIALS AT CRYOGENIC TEMPERATURES
H. M. Ledbetter and D. T. Read 41

Low-Temperature Elastic Constants of Precipitation-Hardened Aluminum Alloys 2014 and 2219
D. T. Read and H. M. Ledbetter 43

Low-Temperature Elastic Properties of an Iron-47.5 Nickel Alloy
H. M. Ledbetter and D. T. Read 58

Reprint: Low-Temperature Elastic Properties of a Nickel-Chromium-Iron Alloy; W. F. Weston and H. M. Ledbetter; Mater. Sci. Eng 20 (1975) 287-90 66

Reprint: Low-Temperature Elastic Properties of Four Wrought and Annealed Aluminum Alloys; E. R. Naimon, H. M. Ledbetter and W. F. Weston; J. Mater. Sci. 10 (1975) 1309-16 70

Reprint: Low-Temperature Elastic Constants of a Superconducting Coil Composite; W. F. Weston; J. Appl. Phys. 46 (1975) 4458-65 78

FRACTURE MECHANICS PARAMETERS OF ENGINEERING MATERIALS AT CRYOGENIC TEMPERATURES
R. L. Tobler, D. T. Read, and R. P. Reed 87

Low-Temperature Effects on the Fracture Behavior of Inconel 718
R. L. Tobler 89

Effects of Specimen Thickness on Fracture Toughness of Some Aluminum Alloys
D. T. Read and R. P. Reed 110

MAGNETOTHERMAL CONDUCTIVITY
L. L. Sparks 139

THERMAL CONDUCTIVITY
J. G. Hust 149

Disclaimer

Tradenames of equipment and materials are used in this report for clarity and to conform with standard usage in the scientific and engineering literature. Selection of materials for discussion and examination with regard to application in superconducting machinery is based on properties reported in the literature, and must be regarded as preliminary and tentative. In no case does such selection imply recommendation or endorsement by the National Bureau of Standards, nor does it imply that the material or equipment is necessarily the best available for the purpose.

SEMI-ANNUAL REPORT ON MATERIALS RESEARCH IN SUPPORT OF SUPERCONDUCTING MACHINERY

ADVANCED COMPOSITES

R. E. Schramm and M. B. Kasen

Cryogenics Division
Institute for Basic Standards
National Bureau of Standards
Boulder, Colorado 80302

April 1976

Summary: Advanced Composites

Phase II of the experimental program has been completed. This report contains 295 K, 76 K and 4 K uniaxial compressive laminate mechanical property data on the following commercial composites: 5.6 mil boron/6061 aluminum, 5.6 mil boron/5505 epoxy*, S-901 glass/NASA Resin 2 epoxy, and type AS graphite/NASA Resin 2 epoxy. A reprint of a review of the literature on the mechanical and thermal properties of advanced composites at cryogenic temperatures is also included.

Contents: Advanced Composites

		Page
1.0	Review	3
2.0	Phase II (Continued): Static Mechanical Properties of Uniaxial Composites at Cryogenic Temperatures	3
2.1	Introduction	3
2.2	Experimental Procedures	4
2.3	Results and Discussion	5
2.3.1	Compressive Modulus	5
2.3.2	Compressive Strength	5
2.4	Conclusions	6
3.0	Future Work	7
4.0	References	7
5.0	List of Figures	7
6.0	List of Tables	8
Appendix I:	Calculation of Compressive Moduli	18
Appendix II:	M. B. Kasen, "Mechanical and thermal properties of filamentary-reinforced structural composites at cryogenic temperatures. II: Advanced composites," Cryogenics 15 (12), pp. 701-722 (1975)	19

* The use of trade names or designations in this paper is essential to proper understanding of the work presented. Their use in no way implies approval, endorsement, or recommendation by NBS.

1.0 Review

Work on this project was initiated by preparing state-of-the-art reviews on the mechanical and thermal properties of structural composites at cryogenic temperatures. A general review has been published(1). More comprehensive reviews of glass-reinforced composites and of advanced-fiber (high-modulus) composites have been published(2,3). A reprint of Ref. 3 is included in the present report. Reprints of Refs. 1 and 2 have appeared in a previous Semi-Annual Report(4).

The reviews suggested that boron-aluminum, boron-epoxy, graphite-epoxy, glass-epoxy and Kevlar 49-epoxy composites warranted further study to characterize key static mechanical properties at cryogenic temperatures. Key properties are those required for a prediction of strength or stiffness limits in complex crossply layups using macromechanical composite theory. The properties are obtained from uniaxial composite laminates, and consist of strengths and elastic moduli in tension and compression in the longitudinal and transverse directions plus in-plane elastic shear moduli.

Phase I of the experimental work was the development of apparatus and procedures for obtaining these data at cryogenic temperatures. Results have been reported previously(5,6). Phase II encompassed the static characterization work. The tensile and in-plane shear portion of this Phase was reported previously(4). The static compressive mechanical properties of these composites are presented and discussed in the present report.

In Phase III of this work, the performance of boron-epoxy and boron-aluminum composites in tensile-tensile fatigue will be examined at cryogenic temperatures. This work is presently under way and will be reported subsequently.

2.0 Phase II (Continued): Static Mechanical Properties of Uniaxial Composites at Cryogenic Temperatures

2.1 Introduction

This report presents compressive static mechanical property data for the composites listed in Table 1, all of which had previously been characterized in tension and in-plane shear. The boron-reinforced composites were fabricated from state-of-the-art commercial preimpregnated tape materials, not optimized for cryogenic use. The cryogenic properties reported for these materials in the present work are believed representative of the properties of boron-reinforced aluminum or epoxy composites as a class, independent of the specific manufacturer.

NASA Resin 2 is a non-proprietary formulation, developed for cryogenic filament-wound pressure vessles(7). It consists of Epon 828/DSA/Empol 1040/BDMA in proportions of 100/115.9/20/1 by weight.

The Kevlar 49/NASA Resin 2 composite, previously included in the tensile evaluation, was not included in the compressive test program. The very low transverse strength of the material obtained for this program suggested that the composite was not representative of good production quality.

Key compressive static mechanical properties include uniaxial longitudinal and transverse ultimate strengths, elastic moduli, and ultimate failure strains. Where possible, the stresses at the proportional limit and the 0.2% offset yield strengths were also determined.

The present data have been obtained from rod or bar type specimens

designed to fail in approximately 45° shear. This is believed to best approximate compressive failure in bulk composite structures in the absence of significant column bending or end brooming. The reader should be aware that compressive properties obtained by the sandwich beam method may differ somewhat from those reported in the present work.

2.2 Experimental Procedures

The compression fixture shown in Figure 1 converts pull rod separation into compression by means of interlocking yokes. Specimen (A) with its end caps is inserted into compression blocks (B). Alignment is maintained by sleeve (C), which slips around the blocks. The compression blocks are anodized to minimize friction. Additionally, MoS_2 lubricant sprayed on the fixture during assembly serves as both a release agent for the end caps and as a lubricant between the compression blocks and alignment tube. Extraneous frictional forces are typically 5-10 N (1-2 lb).

The split compression blocks are joined by stainless steel bolts, facilitating removal of the end caps after testing. Fixture dimensions and construction materials are detailed in Figure 2.

The compression fixture was designed to interchange with the tensile fixture in the cryostat previously described(5). Helium consumption was typically 5-6 liters per specimen test.

The desired 45° shear failure mode was reliably obtained after several iterations of specimen design. The two final configurations are shown in Figure 3. Specimens of square cross section, embedded in 6061-T6 aluminum end caps, proved satisfactory for most materials and orientations (Figure 3(a)). However, the very high compressive strengths developed by the boron-reinforced materials when tested along the fiber direction required round specimens and stainless steel end caps (Figure 3 (b)). Both specimen types were diamond ground to finished dimensions of Figure 3.

A longitudinally-slit tube, having an i.d. matching the o.d. of the end caps, was used to align and support the specimens during room temperature curing of the epoxy used to bond the specimens into the end caps. Several conventional types of epoxy proved satisfactory for this application.

All polymer-matrix composites were environmentally conditioned for a minimum of 40 hours at 23 ± 1° C in 50 ± 10% relative humidity prior to testing. The boron/6061 aluminum was tested in the as-fabricated condition (F temper) without additional conditioning.

A universal testing machine was used for all tests. The crosshead speed was 0.10-0.13 cm min^{-1} (0.04-0.05 in min^{-1}), providing a strain rate of 0.06-0.08 min^{-1}.

Specimens of square cross-section were instrumented with a single longitudinal strain gage. On transverse specimens, the gage was always on the side parallel to the fiber reinforcement. The initial tangent modulus was obtained from load-displacement traces recorded at high sensitivity on an x-y plotter; maximum stress was limited to less than 25% of the ultimate strength. Specimens were subsequently compressed to failure while recording load and strain at lower sensitivity. The strain gage typically failed prior to specimen fracture. However, simultaneous load-time traces on a strip-chart recorder permitted calculation of overall failure strain.

Strain gages were not used with specimens of round cross section. However, the compressive moduli of these specimens were calculated from the load-time trace of the strip chart recorder using the procedure described in Appendix I.

2.3 Results and Discussion

Individual specimen data appear in Tables 2-5. Table 6 presents average values, omitting data from invalid fractures when calculating ultimate strain and strength. The inaccuracy of the data is estimated at ± 3% for ultimate strength, ± 10% for modulus and ultimate strain, and ± 20% for proportional limits and yield strengths.

The maxima of the compressive ultimate strengths and elongations are presented in Table 7. It is probable that the values in this Table are a better reflection of the true ultimate properties of the bulk composites than are the average values of Table 6. Particularly when testing in the uniaxial longitudinal direction, values obtained from relatively small cross section rod specimens are probably lower due to premature failure in other than pure compression.

The desired shear mode of compressive failure is evident in the fractures of the various materials illustrated in Figure 4.

2.3.1 Compressive Modulus

The compressive moduli of the boron-epoxy, glass-epoxy and graphite-epoxy materials are very close to their tensile moduli in both the longitudinal and transverse directions. In contrast, the longitudinal compressive moduli of the boron-aluminum composite was computed to be 30-80% higher than the tensile value, while the transverse compressive moduli was computed to be 10-30% less than the corresponding tensile value.

The authors do not believe that the compressive moduli calculated for the boron-aluminum composite represent valid material properties. An average longitudinal compressive modulus of 359 GN/m^2 (52.1 X 10^6 psi) is hardly realistic for a composite reinforced with 50 v/o of boron which itself has a modulus of about 379 GN/m^2 (55 X 10^6 psi). Furthermore, preliminary studies of the elastic constants of the same boron-aluminum composite using dynamic resonance techniques indicate that the average of the tensile and compressive moduli is about 234 GN/m^2 (34 X 10^6 psi), with a small temperature sensitivity on cooling to cryogenic temperatures(8). It therefore appears that the method used to obtain compressive moduli in the present work is invalid for boron-aluminum composites. We do not know the reason for this discrepancy. However, until the problem is resolved, the authors suggest that tensile moduli values be used to approximate compressive moduli when working with boron-aluminum composites.

The longitudinal compressive moduli of the boron-epoxy and glass-epoxy composites increased about 20% on cooling to 4 K, while that of the graphite-epoxy composite remained relatively unchanged. A much larger temperature dependence of modulus was observed in the transverse direction, with increases of 67%, 108% and 178% being observed for the graphite-epoxy, boron-epoxy, and glass-epoxy, respectively. Similar temperature dependences had been previously observed for the tensile moduli of these materials.

2.3.2 Compressive Strength

Present data suggest that boron-reinforced composites are capable of providing longitudinal compressive strengths approaching 3.4 GN/m^2 (50 X 10^4 psi) at 4 K in the absence of column bending. This is twice the tensile strength at that temperature. Conversely, the 4 K longitudinal compressive strengths of the glass and graphite-epoxy composites were 30-50% lower than their 4 K longitudinal tensile strengths. The superior ability of the boron fibers to sustain compressive loads is clear.

The transverse compressive strength of all four composite types are substantially higher than their transverse tensile strengths. This is

particularly noticeable in the graphite-epoxy composite.

The compressive strength of the boron-reinforced composites in the longitudinal direction appears to be relatively independent of temperature, although present data are incomplete. However, the longitudinal compressive strengths of the glass-epoxy material is very temperature dependent, increasing by 180% on cooling. A 25% increase in strength was observed for the graphite-epoxy on cooling. In the transverse direction, the compressive ultimate strength of the boron-aluminum, boron-epoxy, and glass-epoxy increased by 100-170% on cooling. However, cooling to cryogenic temperatures decreased the transverse compressive strength of the graphite-epoxy composite by about 30%.

2.4 Conclusions

Commercial, state-of-the-art boron-6061 aluminum and boron-epoxy composites have excellent static compressive properties at cryogenic temperatures. The compressive strength is particularly outstanding, approaching 3.4 GN/m^2 (50 X 10^4 psi) in the uniaxial longitudinal direction at 4 K. Transverse compressive strengths of 620 MN/m^2 (90 X 10^3 psi) for boron-aluminum and 427 MN/m^2 (62 X 10^3 psi) for boron-epoxy at 4 K are substantially higher than in other composite systems. The compressive strength properties of the boron-reinforced materials are superior to the already high tensile strength properties at all cryogenic temperatures. With a modulus of 206-240 GN/m^2 (30-35 X 10^6 psi), the boron-reinforced composites appear to be excellent cryogenic structural materials.

At 4 K, NASA Resin 2 epoxy reinforced with S-901 glass fibers has about half the compression strength of the boron materials in both the longitudinal and transverse directions. The longitudinal compressive strength of this composite is 30-60% lower than the corresponding tensile strength, while the transverse compression strength is 100-200% greater than in tension. Compressive moduli increase with cooling, attaining about 62 GN/m^2 (9 X 10^6 psi) longitudinally and about 31 GN/m^2 (4.5 X 10^6 psi) in the transverse direction at 4 K.

NASA Resin 2 reinforced with Type AS graphite fiber had the lowest compressive strength of the composites tested. Uniaxial longitudinal strengths at 4 K were about 25% of that of the boron materials, while transverse strengths averaged about 130 MN/m^2 (19 X 10^3 psi). The longitudinal compression modulus of about 117 GN/m^2 (17 X 10^6 psi) was about the same as the tensile modulus.

The comparatively poor performance of the graphite-epoxy composite in the present work should not be construed as indicating a general inferiority of this type of composite for cryogenic applications. The data suggest that an incompatibility may exist between the fiber and matrix in the AS/NASA Resin 2 composite selected for this study.

Present data indicate that the compressive and tensile moduli of the boron-epoxy, graphite-epoxy and glass-epoxy composites are substantially the same from 295 K to 4 K. In view of the experimental difficulty, there appears to be little justification for a separate determination of compressive moduli if tensile moduli are available.

We conclude from this study that the compressive moduli of uniaxial boron-6061 aluminum composites cannot be reliably measured by the procedures used in this study, even though such procedures were satisfactory for the epoxy-matrix composites.

3.0 Future Work

Phase III of this program will examine the extent to which cryogenic temperatures affect the wear-out rate of boron-aluminum and boron-epoxy composites under tension-tension fatigue. Criteria will be changes in specimen modulus and damping. This study is presently under way using composites of [0/± 45/0]s orientation and stacking.

4.0 References

1. Kasen, M. B., "Properties of Filamentary-Reinforced Composites at Cryogenic Temperatures," Composite Reliability, ASTM STP 580, American Society for Testing and Materials, 1975, pp. 586-611.

2. Kasen, M. B., "Mechanical and Thermal Properties of Filamentary-Reinforced Structural Composites at Cryogenic Temperatures. I: Glass-Reinforced Composites," Cryogenics, 15 (6), 1975, pp. 327-349.

3. Kasen, M. B., "Mechanical and Thermal Properties of Filamentary-Reinforced Structural Composites at Cryogenic Temperatures. II: Advanced Composites," Cryogenics, 15 (12), 1975, pp. 701-722.

4. Schramm, R. E. and Kasen, M. B., "Advanced Composites," in Semi-Annual Technical Reports on Materials Research in Support of Superconducting Machinery - IV; R. P. Reed, A. F. Clark, E. C. van Reuth (Eds.); Nat. Bur. Stds., Boulder, CO; October 1975; ADA019230.

5. Kasen, M. B., "Advanced Composites," in Semi-Annual Technical Reports on Materials Research in Support of Superconducting Machinery; R. P. Reed, A. F. Clark, E. C. van Reuth (Eds.); Nat. Bur. Stds., Boulder, CO; March 1974; AD780596.

6. Kasen, M. B. and Schramm, R. E., "Advanced Composites," in Semi-Annual Technical Reports on Materials Research in Support of Superconducting Machinery - II; R. P. Reed, A. F. Clark, E. C. van Reuth (Eds.); Nat. Bur. Stds., Boulder, CO; October 1974; ADA004586.

7. Soffer, L. M. and Molho, R., "Cryogenic Resins for Glass Filament-wound Composites," NASA CR-72114 (Final), 1967, N67-25076.

8. Read, D. T. and Ledbetter, H. M., NBS-Boulder, personal communication (March 1976).

5.0 List of Figures

1. Fixture for compression testing of composites at cryogenic temperatures.
   (a) Specimen with end caps
   (b) Anodized aluminum compression blocks
   (c) Aluminum alignment sleeve

2. Drawing of fixture for compression testing of composites at cryogenic temperatures.

3. Specimen configurations used in determining static compressive properties of composites at cryogenic temperatures.
   (a) Square specimen for glass-epoxy, graphite-epoxy and transverse boron-aluminum and boron-epoxy
   (b) Round specimen for longitudinal boron-aluminum and boron-epoxy

4. Typical composite compressive fractures.
   (a) Glass-epoxy, longitudinal, 295 K
   (b) Glass-epoxy, transverse, 295 K
   (c) Glass-epoxy, longitudinal, 4 K
   (d) Boron-aluminum, longitudinal, 4 K
   (e) Boron-epoxy, longitudinal, 4 K
   (f) Boron-epoxy, transverse, 4 K
   (g) Graphite-epoxy, longitudinal, 295 K
   (h) Graphite-epoxy, longitudinal, 4 K

6.0 List of Tables

1. Composites Tested in Compression

2. Compression Properties of 5.6-mil Boron-6061 Aluminum Composite (Individual Specimens)

3. Compression Properties of 5.6-mil Boron-5505 Epoxy Composite (Individual Specimens)

4. Compression Properties of S Glass-NASA Resin 2 Composite (Individual Specimens)

5. Compression Properties of Type AS Graphite-NASA Resin 2 Composite (Individual Specimens)

6. Compressive Properties of Composites (Averages of Specimens Tested)

7. Compressive Properties of Composites (Maxima of Ultimate Strength Values)

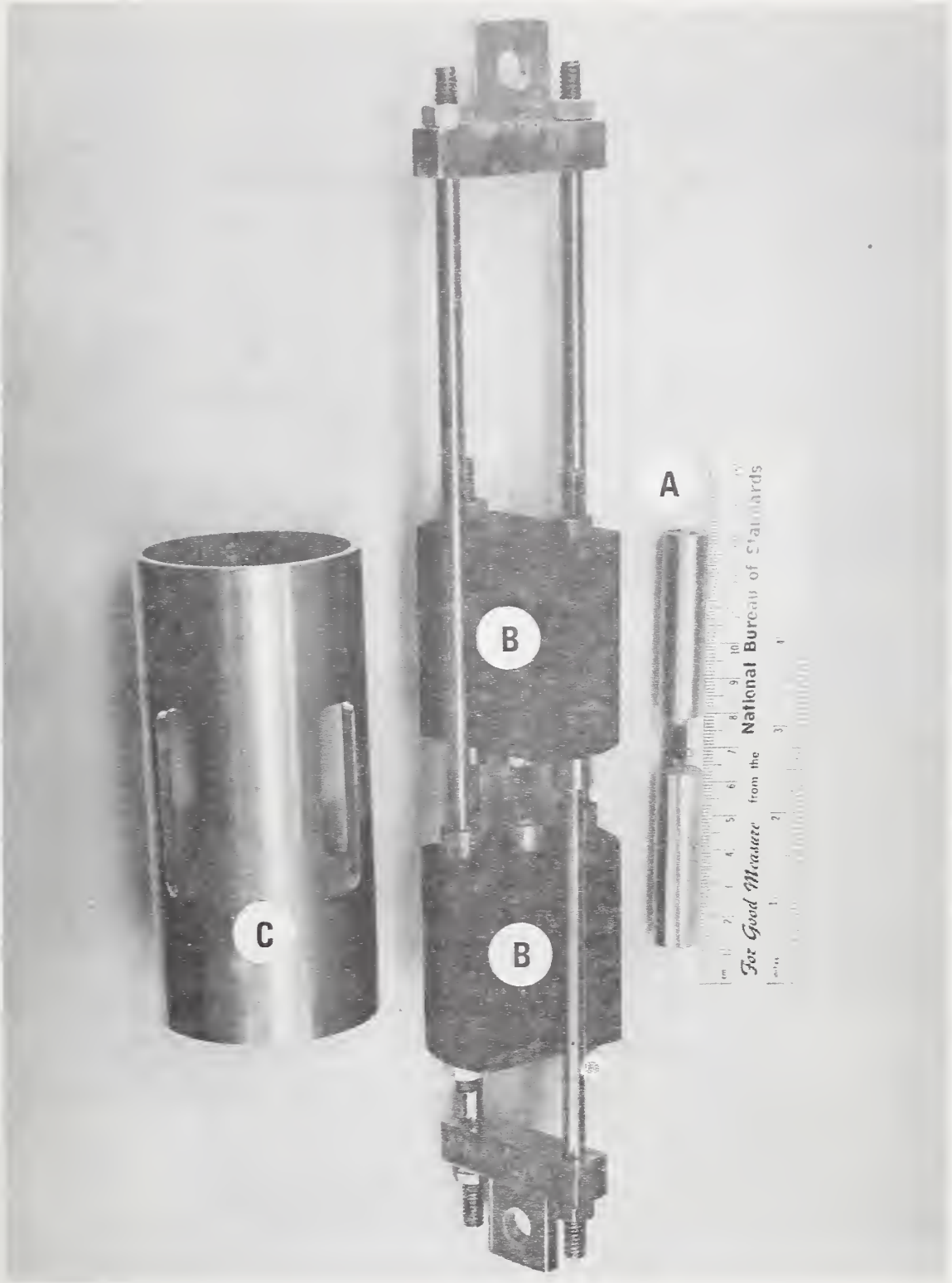

Fig. 1. Fixture for compression testing of composites at cryogenic temperatures.
(a) Specimen with end caps
(b) Anodized aluminum compression blocks
(c) Aluminum alignment sleeve

emperature

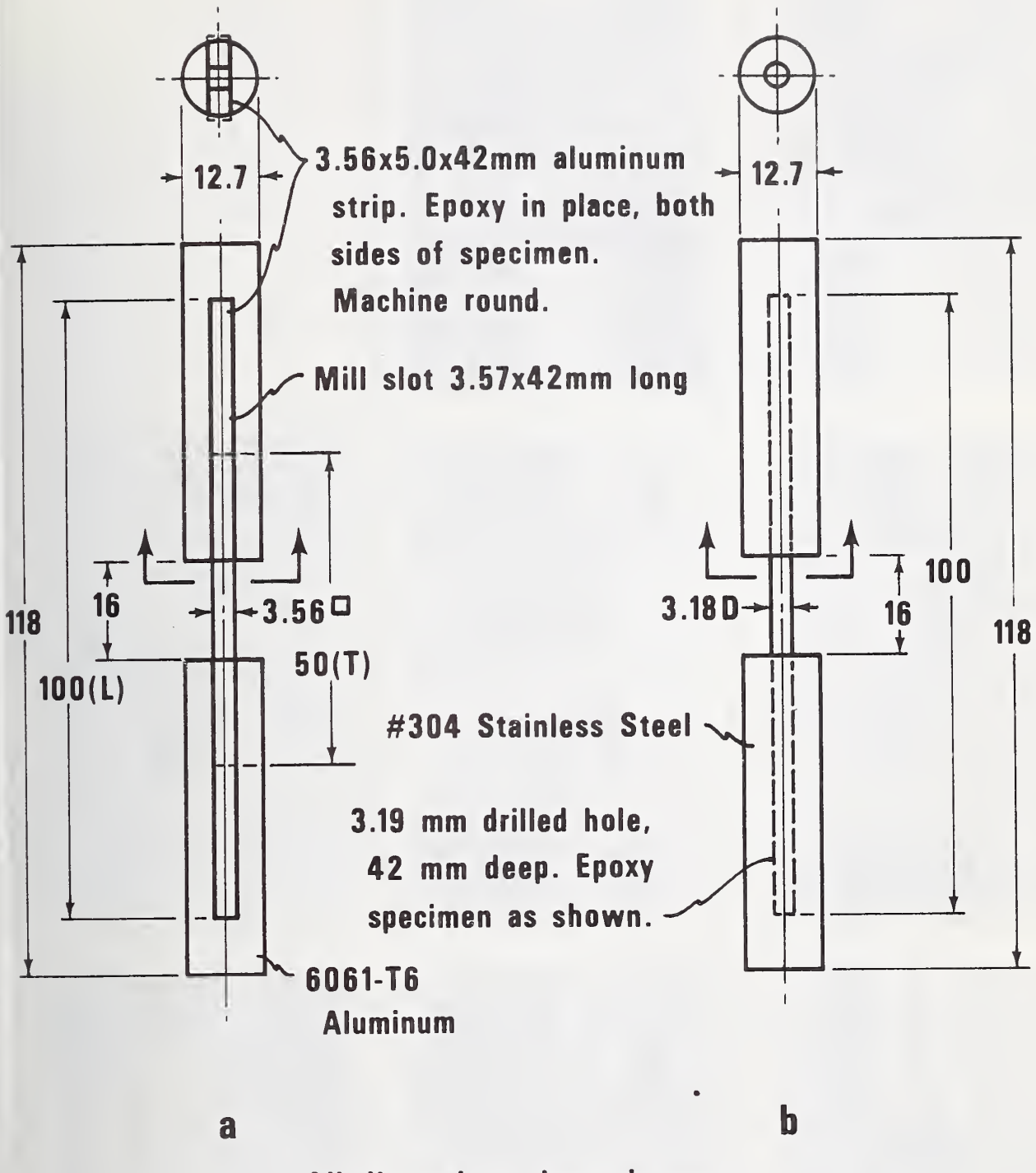

Fig. 3. Specimen configurations used in determining static compressive properties of composites at cryogenic temperatures.
(a) Square specimens for glass-epoxy, graphite-epoxy and transverse boron-aluminum and boron-epoxy.
(b) Round specimen for longitudinal boron-aluminum and boron-epoxy.

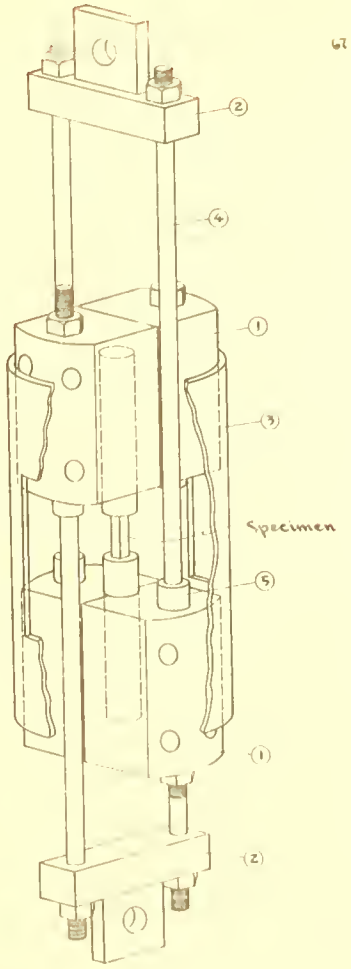

ASSEMBLY

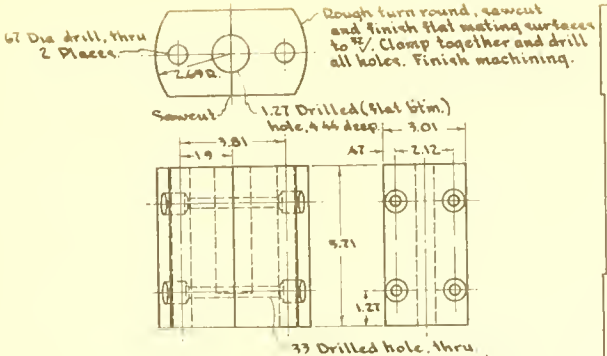

MATERIAL: 6061-T6 ALUMINUM
(2) Two Required
Anodized after completion

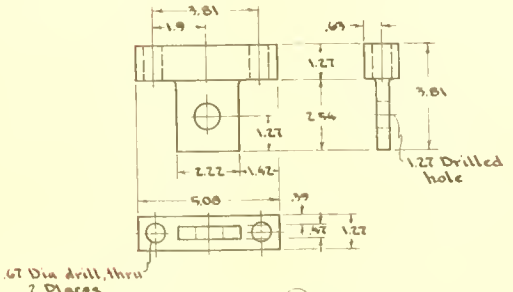

2

MATERIAL: AISI 304 STAINLESS STEEL
(2) Two Required

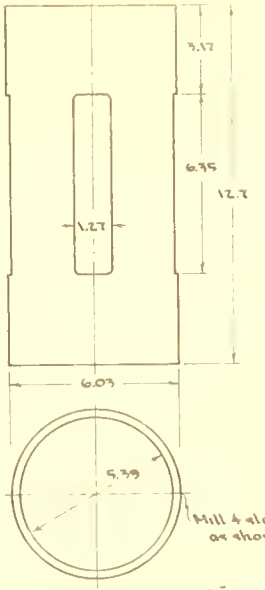

3

MATERIAL: 6061-T6 ALUMINUM
(1) One Required

¼-20 UNC 2.
both ends.

4

MATERIAL: ⅝ DIA
Ti-6Al-4V
(2) Req'd as shown
(2) Req'd. 27.3 long.

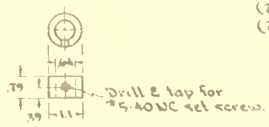

5

MATERIAL: AISI 304 STAINLESS STEEL
(4) Four Required

All dimensions shown in cm.

(a) Glass-epoxy, longitudinal, 295K

(b) Glass-epoxy, transverse, 295K

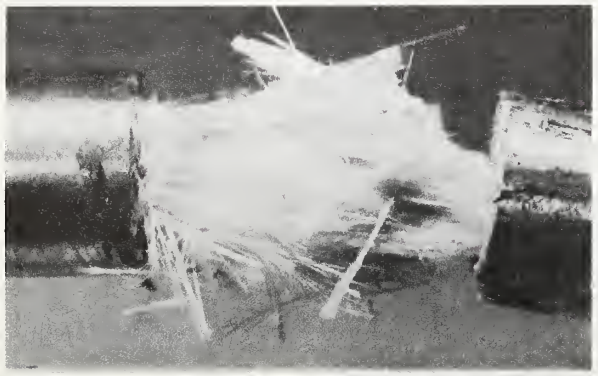

(c) Glass-epoxy, longitudinal, 4K

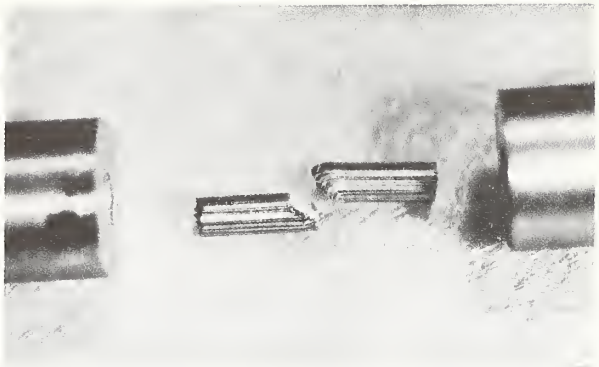

(d) Boron-alum., longitudinal, 4K

(e) Boron-epoxy, longitudinal, 4K

(f) Boron-epoxy, transverse, 4K

(g) Graphite-epoxy, longitudinal, 295K

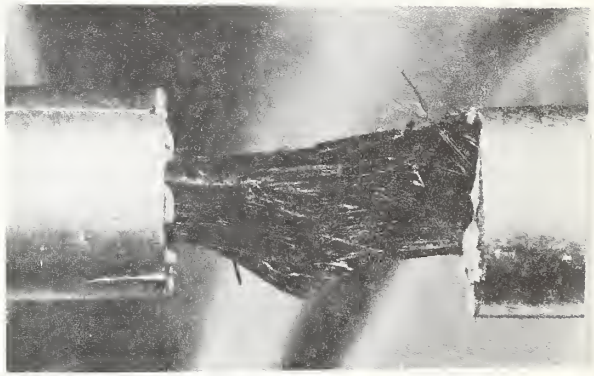

(h) Graphite-epoxy, longitudinal, 4K

Fig. 4. Typical composite compressive fractures.

Table 1. Composites Tested in Compression

Composite Type	Plate Thickness (cm)	Plate Thickness (in)	Nominal Ply Thickness (cm)	Nominal Ply Thickness (in)	Average Fiber Volume Percent*
5.6 mil Boron-6061 Aluminum (condition F)	0.373	0.147	0.0175	0.0069	47
5.6 mil Boron-5505 Epoxy	0.345	0.137	0.0170	0.0067	52
S-901 Glass-NASA Resin 2 Epoxy	0.462	0.182	0.0206	0.0081	66
Type AS Graphite-NASA Resin 2 Epoxy	0.366	0.144	0.0193	0.0076	64

* Plate-to-plate variation was ± 2%.

Table 2. Compressive Properties of 5.6 mil Boron-6061 Aluminum Composite[a] (Individual Specimens)

Temperature (K)	Young's Modulus, E[c] (10^9 N/m^2)	Young's Modulus, E[c] (10^6 psi)	Proportional Limit, σ^{pl} (10^8 N/m^2)	Proportional Limit, σ^{pl} (10^3 psi)	0.2% Yield Strength, σ^{cy} (10^8 N/m^2)	0.2% Yield Strength, σ^{cy} (10^3 psi)	Ultimate Strength, σ^{cu} (10^8 N/m^2)	Ultimate Strength, σ^{cu} (10^3 psi)	Ultimate Strain, ε^{cu} (%)
				Longitudinal (0°)					
295	221	32.0					19.2	278	1.8
295	293	42.5					15.2	224	0.7
76	311	45.1					21.7	314	1.0
76[b]	407[c] *	59.0[c] *					28.7	416	0.5[c]
4[b]	335[c]	48.6[c]					28.5	413	0.6[c]
4[b]	337[c]	48.8[c]					26.0	377	0.5[c]
4[b]	302[c]	43.8[c]					32.6	473	0.7[c]
				Transverse (90°)					
295[d]	150	21.2	0.588	8.53	1.43	20.8	2.60	37.7	0.4[c]
295	186	27.0	0.545	7.97	1.43	20.7	2.54	36.8	0.4[c]
295	107	15.5	0.594	8.61	1.03	15.0	2.59	37.5	0.5[c]
76	101	14.7	0.833	12.1	1.95	28.4	4.56	66.2	0.6[c]
76	89 *	12.9 *	0.818	11.9	2.06	30.0	4.45	64.6	0.8[c]
76	101	14.6	0.967	14.0	1.99	28.9	4.50	65.3	0.9[c]
4	123	17.8	1.13	16.4	2.82	40.9	6.56	95.1	0.7[c]
4	90	13.0	1.11	16.0	2.44	35.3	6.29	91.2	1.2[c]
4	90	13.1	1.01	14.6	2.39	34.7	5.83	84.5	1.0[c]

[a] Square specimens except as marked.
[b] Round specimen.
[c] Estimated from strip-chart recording.
[d] This is the only boron-aluminum specimen that was load cycled.

Underlined values represent invalid fractures.

* See text discussion on validity of these values.

Temperature (K)	Elastic Modulus, E^c (10^9 N/m^2)	(10^6 psi)	Proportional Limit, σ^{pl} (10^8 N/m^2)	(10^3 psi)	0.2% Yield Strength, σ^{cy} (10^8 N/m^2)	(10^3 psi)	Ultimate Strength, σ^{cu} (10^8 N/m^2)	(10^3 psi)	Ultimate Strain, ε^{cu} (%)
				Longitudinal (0°)					
295[a]	186	27.0					11.8	171	0.7
295[a]	190	27.6					12.9	186	0.8
295[b]	260	37.7					14.1	204	0.6
76[a]	225	32.6					22.8	331	1.1
76[a]	234	33.9					18.2	263	0.8
4[a]	239	34.7					13.0	188	0.6
4[c]	257[d]	37.3[d]					25.9	375	0.4[d]
4[c]	233[d]	33.7[d]					19.2	278	0.3[d]
4[c]	291[d]	42.2[d]					36.6	531	0.6[d]
				Transverse (0°)					
295[a]	20.9	3.03	0.395	5.7	1.78	25.8	2.27	32.3	1.6
295[a]	13.3	2.02	0.975	14.1	--	--	1.41	20.5	1.6
295[b]	20.0	2.90	0.715	10.4	1.79	25.9	2.10	30.5	1.2
295[b]	22.4	3.24	0.790	11.4	1.80	26.1	1.96	28.4	1.4
76[a]	38.7	5.62	2.31	33.6			4.23	61.4	1.2
76[a]	39.0	5.64	1.98	28.6			3.84	55.6	0.5
76[a]	37.7	5.46	1.66	24.1			1.80	26.1	0.5
76[b]	39.5	5.74	2.72	39.5			4.56	66.2	1.5
76[b]	41.4	5.99	3.38	49.0			4.36	63.1	1.1
4[b]	42.8	6.20					4.24	61.4	1.1
4[b]	37.8	5.49					1.67	24.2	0.4
4[b]	41.3	5.98					4.52	65.5	1.1
4[b]	39.4	5.71					4.08	59.2	0.9

[a] Rectangular specimen.
[b] Square specimen.
[c] Round specimen.
[d] Estimated from strip-chart recording.

Underlined values represent invalid fractures.

Table 4. Compressive Properties of S Glass-NASA Resin 2 Composite (Individual Specimens)

Temperature (K)	Elastic Modulus, E^c (10^9 N/m^2)	(10^6 psi)	Proportional Limit, σ^{pl} (10^8 N/m^2)	(10^3 psi)	0.2% Yield Strength, σ^{cy} (10^8 N/m^2)	(10^3 psi)	Ultimate Strength, σ^{cu} (10^8 N/m^2)	(10^3 psi)	Ultimate Strain, ε^{cu} (%)
				Longitudinal (0°)					
295	40.4	5.87	1.36	19.8			4.72	68.5	1.2
295	59.2	8.44	0.93	13.5			5.62	81.6	1.3
295	53.2	7.71	3.14	45.6			4.75	68.8	0.9
76	69.7	10.1	1.78	25.8	7.32	106	16.5	239	3.0
76	64.2	9.3	3.24	47.0	9.87	143	13.4	195	2.5
76	72.5	10.5	3.07	44.4	--	--	10.3	150	1.5
76	48.6	7.0	4.47	64.8	7.03	102	14.0	203	2.5[a]
4	53.8	7.81	2.44	35.3	9.08	132	14.1	204	1.5
4	63.0	9.13	3.81	55.2	7.56	110	15.4	224	2.6[a]
4	64.7	9.38	3.11	45.1	--	--	13.1	190	1.8[a]
				Transverse (90°)					
295	11.7	1.70	0.550	7.97	0.733	10.6	0.962	13.9	3.4
295	12.3	1.78	0.380	5.51	0.753	10.9	0.935	13.6	2.6
295	9.8	1.42	0.422	6.12	0.703	10.2	1.052	15.3	3.4
76	19.8	2.87	0.92	13.4			2.35	34.0	0.7
76	26.0	3.77	1.31	19.0			2.84	41.2	1.1
76	22.7	3.29	1.19	17.2			3.11	45.1	0.9
4	27.2	3.95					2.76	40.0	1.1
4	39.4	5.71					2.99	43.4	0.8
4	27.3	3.96					2.13	30.9	0.7

[a] Estimated from strip chart recording.

All square specimens

Table 5. Compressive Properties of Type AS Graphite-NASA Resin 2 Composite (Individual Specimens)

Temperature (K)	Elastic Modulus, E^c (10^9 N/m^2)	(10^6 psi)	Proportional Limit, σ^{pl} (10^8 N/m^2)	(10^3 psi)	0.2% Yield Strength, σ^{cy} (10^8 N/m^2)	(10^3 psi)	Ultimate Strength, σ^{cu} (10^8 N/m^2)	(10^3 psi)	Ultimate Strain, ε^{cu} (%)
				Longitudinal (0°)					
295	137	19.8	2.25	32.6			5.61	81.2	0.5
295	125	18.1	2.66	38.6			4.96	71.9	0.4
295	125	18.2	3.55	51.5			5.38	78.0	0.4
76	115	16.7	4.54	65.9			7.95	115	0.8
76	97	14.1	--	--			4.75	69	0.5
76	110	16.0	3.95	57.3			6.72	97	0.7
76	141	20.4	5.04	73.1			12.29	178	1.0
4	109[a]	15.8[a]	--	--			8.83	128	0.7[a]
4	124	18.0	3.70	53.7			5.87	85	0.6
4	125	18.2	3.77	54.7			5.99	87	0.8
				Transverse (90°)					
295	9.09[a]	1.32[a]	0.90[a]	13.0[a]			1.04	15.1	0.8[a]
295	9.99[a]	1.45[a]	0.58[a]	8.4[a]			0.91	13.2	0.8[a]
295	9.91[a]	1.44[a]	--	--			0.71	10.3	0.6[a]
76	16.6	2.41	1.16	16.8			1.51	21.9	1.1
76	13.1	1.89	0.80	11.5			1.25	18.1	1.0
76	16.1	2.34	0.90	13.1			1.33	19.3	0.9
4	18.8	2.72	0.660	9.58			1.00	14.4	0.5
4	14.4	2.09	0.723	10.48			1.50	21.8	1.0
4	15.3	2.22	0.647	9.39			1.43	20.7	0.9

[a] Estimated from strip-chart recording.

All square specimens

Table 6. Compressive Properties of Composites (Averages of Specimens Tested[a])

Temperature (K)	Elastic Modulus, E^c (10^9 N/m^2)	(10^6 psi)	CV(%)	Proportional Limit, σ^{pl} (10^8 N/m^2)	(10^3 psi)	CV(%)	0.2% Yield Strength, σ^{cu} (10^8 N/m^2)	(10^3 psi)	CV(%)	Ultimate Strength, σ^{cu} (10^8 N/m^2)	(10^3 psi)	CV(%)	Ultimate Strain, ϵ^{cu} (%)	CV(%)	Number of Specimens Tested	Valid Fractures
					5.6 mil 8oron-6061 Aluminum											
					Longitudinal (0°)											
295	257 (51)	37.2 (7.4)	20.0												2	0
76	359 (68)*	52.1 (9.8)*	18.9							28.7	416		0.5		2	1
4	325 (20)	47.1 (2.8)	6.0							29.0 (3.3)	421 (48)	11.5	0.6(0.1)	16.7	3	3
					Transverse (90°)											
295	148 (40)	21.2 (5.8)	27.1	0.576(0.027)	8.4 (0.3)	4.6	1.30 (0.23)	18.8(3.3)	17.8	2.58 (0.03)	37.3(0.5)	1.3	0.4(0.1)	13.4	3	3
76	97 (7)*	14.1 (1.0)*	7.2	0.876(0.087)	12.7 (1.2)	9.9	2.00 (0.06)	29.1(0.8)	2.8	4.50 (0.06)	66.4(0.8)	1.2	0.8(0.2)	19.6	3	3
4	101 (19)	14.6 (2.7)	18.8	1.08 (0.06)	15.7 (1.0)	6.1	2.55 (0.24)	37.0(3.4)	9.4	6.23 (0.37)	90.3(5.4)	5.9	1.0(0.3)	25.9	3	3
					5.6 mil Boron-5505 Epoxy											
					Longitudinal (0°)											
295	212 (42)	30.8 (6.0)	19.6												3	0
76	229 (6)	33.2 (0.9)	2.8												2	0
4	255 (26)	37.0 (3.8)	10.3							27.2 (8.8)	394 (130)	32.4	0.4(0.2)	35.3	4	3
					Transverse (90°)											
295	19.1(4.0)	2.80(0.54)	20.9	0.719(0.242)	10.4 (3.5)	33.7	1.79 (0.01)	25.9(0.2)	0.6	2.11 (0.16)	30.6(2.3)	7.5	1.5(0.2)	13.2	4	4
76	39.3(1.4)	5.69(0.20)	3.6	2.41 (0.67)	35.0 (9.7)	27.8				4.25 (0.30)	61.6(4.5)	7.2	1.1(0.5)	43.3	5	5
4	40.3(2.2)	5.84(0.31)	5.4							4.28 (0.22)	62.0(3.2)	5.2	1.0(0.1)	11.1	4	3
					S Glass-NASA Resin 2											
					Longitudinal (0°)											
295	50.9(9.6)	7.34(1.32)	18.9	1.81 (1.17)	26.3 (17.0)	64.7				5.03 (0.51)	73.0(7.5)	10.2	1.1(0.2)	18.4	3	3
76	63.8(10.7)	9.23(1.56)	17.0	3.14 (1.10)	45.5 (16.0)	35.1	8.07 (1.56)	117 (23)	19.3	13.6 (2.5)	197 (36)	18.8	2.4(0.6)	26.5	4	4
4	60.5(5.9)	8.77(0.84)	9.7	3.12 (0.69)	45.2 (10.0)	22.0	8.32 (1.07)	121 (16)	13.2	14.2 (1.2)	206 (17)	8.3	2.0(0.6)	28.9	3	3
					Transverse (90°)											
295	11.3(1.3)	1.63(0.19)	11.6	0.451(0.089)	6.53(1.28)	19.6	0.730(0.025)	10.6(0.4)	3.5	0.983(0.061)	14.3(0.91)	6.4	3.1(0.5)	14.7	3	3
76	22.8(3.1)	3.31(0.45)	13.6	1.14 (0.20)	16.5 (2.9)	17.5				2.77 (0.39)	40.1(5.63)	14.0	0.9(0.2)	22.2	3	3
4	31.3(7.0)	4.54(1.01)	22.4							2.63 (0.45)	38.1(6.5)	17.0	0.9(0.2)	24.0	3	3
					Type AS Graphite-NASA Resin 2											
					Longitudinal (0°)											
295	129 (7)	18.7 (1.0)	5.4	2.82 (0.66)	40.9 (9.7)	23.6				5.49 (0.16)	79.6(2.3)	2.9	0.4(0.1)	13.3	3	3
76	116 (18)	16.8 (2.6)	15.9	4.51 (0.55)	65.4 (7.9)	12.1				7.93 (3.19)	115 (46)	40.3	0.8(0.2)	27.8	4	4
4	120 (8)	17.4 (1.3)	7.3	3.73 (0.05)	54.2 (0.7)	1.3				6.90 (1.68)	100 (24)	24.3	0.7(0.1)	14.3	3	3
					Transverse (90°)											
295	9.7(0.5)	1.40(0.07)	5.2	0.74 (0.23)	10.7 (3.3)	30.6				0.89 (0.17)	12.9(2.4)	18.8	0.7(0.1)	15.8	3	3
76	15.3(1.9)	2.21(0.28)	12.8	0.95 (0.19)	13.8 (2.7)	19.7				1.36 (0.13)	19.8(1.9)	9.8	1.0(0.1)	10.0	3	3
4	16.2(2.3)	2.34(0.33)	14.3	0.677(0.041)	9.82(0.58)	6.0				1.31 (0.27)	19.0(4.0)	21.0	0.8(0.3)	33.1	3	3

[a] Standard deviations are in parentheses. CV is the coefficient of variation. Data from specimens showing an * invalid fracture are not included in the calculations of ultimate strength or elongation. See text discussion on validity of these values.

Table 7. Compressive Properties of Composites (Maxima of Ultimate Strength Values)

Temperature (K)	Ultimate Strength, σ^{cu} $(10^8$ N/m$^2)$	$(10^3$ psi)	Ultimate Compression, ε^{cu} (%)	Number of Specimens
	5.6 mil Boron-6061 Aluminum			
	Longitudinal (0^o)			
295	--	--	--	
76	28.7	416	0.5	1
4	32.6	473	0.7	3
	Transverse (90^o)			
295	2.60	37.7	0.5	3
76	4.56	66.2	0.9	3
4	6.56	95.1	1.2	3
	5.6 mil Boron-5505 Epoxy			
	Longitudinal (0^o)			
295	--	--	--	
76	--	--	--	
4	36.6	531	0.6	3
	Transverse (90^o)			
295	2.27	32.3	1.6	4
76	4.56	66.2	1.5	5
4	4.52	65.5	1.1	3
	S Glass-NASA Resin 2			
	Longitudinal (0^o)			
295	5.62	81.6	1.3	3
76	16.5	239	3.0	4
4	15.4	224	2.6	3
	Transverse (90^o)			
295	1.05	15.3	3.4	3
76	3.11	45.1	1.1	3
4	2.99	43.4	1.1	3
	Type AS Graphite-NASA Resin 2			
	Longitudinal (0^o)			
295	5.61	81.2	0.5	3
76	12.3	178	1.0	4
4	8.83	128	0.8	3
	Transverse (90^o)			
295	1.04	15.1	0.8	3
76	1.51	21.9	1.1	3
4	1.50	21.8	1.0	3

Appendix I: Calculation of Compressive Moduli

The elastic (Young's) modulus, E, is determined from a stress-strain curve by the relationship:

$$E = \frac{L}{A\varepsilon} \tag{1}$$

where L = load, A = specimen cross-sectional area and ε = specimen strain. If the only available record of the test is a strip chart trace of load as a function of time, the time axis must be calibrated in units of strain.

For an infinitely rigid test machine, the strain would be given by the product of time and crosshead speed divided by the specimen gage length. In reality, a fraction of the crosshead motion causes strain in various components of the load train other than the specimen. This extraneous strain may be accounted for if one knows the functional relationship between incremental specimen strain, $\Delta\varepsilon$, and incremental strip-chart time, Δt:

$$\Delta\varepsilon = f(\Delta t) \tag{2}$$

The factor f is a function of both the spring constant of the loading system and of specimen stiffness, E·A. It is uniquely defined for a given specimen and load train, and may be determined by comparing a strip-chart trace with a load-strain trace recorded concomitantly from a strain-gaged specimen. Specimens of differing stiffness yield differing f factors, reflecting differences in the distribution of overall strain between the specimen and the load train. However, if f factors are calculated from a large number of specimens which vary in modulus and cross-sectional area (but are of identical gage length), a plot of f versus the E·A product provides a calibration curve for the test system.

Combining Eqs. (1) and (2) yields:

$$E = \frac{\Delta L}{A \cdot f(\Delta t)} \tag{3}$$

Since ΔL, Δt and A are known, an iterative process is used to find the correct value of the factor f. An estimate is made of the modulus, the E·A product is calculated, and the corresponding f value is determined from the calibration chart. This value is substituted in Eq. (3). A few iterations suffice to narrow estimated and calculated moduli to within $\pm$ 10%, which appears to be a reasonable limit of accuracy for this method.

The same f value may be used to estimate the fracture strain from the time scale of a load-time trace.

It is also possible to estimate the ultimate strain from the total test time using Eq. (2). In those cases where a strain gage was applied but failed before specimen fracture, a comparison of the initial linear portion of the load time curve with the modulus from the load-strain curve yields an f value from Eq. (3) without recourse to the calibration curve or any iterations.

Reinforced Structural Composites at Cryogenic Temperatures-2: Advanced Composites," Cryogenics 15(12), pp. 701-722 (1975).

The low-temperature mechanical and thermal properties of advanced-fibre reinforced structural composites are reviewed. The magnitude and range of particular properties are discussed with respect to composite type and temperature. A property–material cross reference is given with a 128-entry bibliography. This is Part 2 of a two-part series. Part 1 considered glass-reinforced composites.

Mechanical and thermal properties of filamentary-reinforced structural composites at cryogenic temperatures

2: Advanced composites

M. B. Kasen

Nomenclature

σ^{tu}	tensile ultimate strength
E_1^t	initial tensile modulus
E_2^t	secondary tensile modulus
ϵ^{tu}	tensile ultimate strain
σ^{fu}	flexural ultimate strength
E_1^f	initial flexural modulus
E_2^f	secondary flexural modulus
σ^{cu}	compressive ultimate strength
E^c	compressive modulus
ϵ^{cu}	compressive ultimate strain
σ^{si}	interlaminar shear strength
η^t	fatigue strength
σ^{by}	bearing yield strength
σ^{bu}	bearing ultimate strength
σ^I	impact strength
λ	thermal conductivity
$\Delta L/L$	thermal contraction (expansion)
C_p	specific heat at constant pressure
ρ	density

This review has four main objectives: (a) to give the designer some idea of the general magnitude of property values which can reasonably be expected from a given category and class of advanced-fibre composites within the cryogenic range; (b) to provide insight into the ranking of specific composite classes with regard to a specific property; and (c) to allow him to assess whether the property of interest is likely to increase, remain unaffected, or decrease with lowering of temperature. Readers with more specific interests are referred to the Bibliography and Bibliography–Property Cross Reference for retrieval of specific documents. The Bibliography in this report is similar to that in Part 1 and includes references to both the glass and advanced-fibre reinforced composite literature. The scope of the literature survey has already been described in Part 1 (CRYOGENICS Vol 15, No 6 (June 1975) pp 327–49)

The author is in the Cryogenics Division, NBS Institute for Basic Standards, Boulder, Colorado 80302, USA. Received 16 June 1975.

We define a composite *category* by the general reinforcement type, for example, glass-fibre or advanced-fibre (graphite, boron, etc). We subdivide the category into composite *classes* by the general matrix type, for example, glass-polyester or graphite-epoxy. We subdivide the class by referring to a composite *type* when a specific reinforcement/matrix combination is specified, for example, HT-S/X-904 epoxy.

The term 'advanced-fibre' is used to distinguish fibres having high modulus (20–70 x 10^6 lb in^{-2}, 138–483 GPa) in contrast to the relatively low modulus of glass fibre (10 x 10^6 lb in^{-2}, 69 GPa). Fibres of boron, graphite or proprietary organic type dominate the advanced-fibre field.

Several differences will be noted between the presentation of the data in this work and in Part 1. First, because of the wide variation in properties among the advanced fibres (and, therefore, among the composites in which they are used), separate data are presented on each specific reinforcement type.

Secondly, as no data were available on woven-cloth advanced-fibre composites at cryogenic temperatures, present data are restricted to uniaxial longitudinal and uniaxial transverse layups. Thirdly, the overwhelming majority of the relevant data for advanced-fibre polymeric systems are reported for epoxy matrices, in contrast to the variety of polymeric matrices for which data were available in glass-reinforced systems. Finally, data are presented for advanced-fibre reinforcement of a metal matrix (aluminium).

A more subtle difference in the present work is the separation of static mechanical properties into primary and secondary categories. The former category distinguishes those properties useful in design calculations, while the latter discusses properties more qualitative in nature, which are primarily useful in quality control or for comparative performance screening of composites.

In other respects, the data presentation follows that used in Part 1, that is, literature property values are presented in graphical form as a function of temperatures at 295 K, 200 K, 77 K, 20 K, and 4 K. The absence of a data point for a given temperature indicates failure to find significant data. References are given for each plotted curve.

Curves presenting data averaged from several sources may have a considerable scatter band associated with them. We discuss the range of values associated with such curves and emphasize those specific types for which the best values were reported.

The complexity of the subject and the necessity of a cut-off data for data acquisition makes it unavoidable that some data worthy of inclusion have been inadvertently overlooked. The author would appreciate having such omissions brought to his attention. The author also wishes to emphasize that the data presented in this review reflect the published results of the cited authors. These data have not been experimentally verified by NBS, and the conclusions and evaluations presented herein do not imply approval, endorsement, or recommendation of any commercial product by NBS.

There exists no universally accepted method of determining many of the reported properties. It is not easy to obtain valid uniaxial longitudinal tensile fracture because of the difficulty of transferring the tensile load from the specimen grips into the fibres of the specimen without introducing excessive localized stress concentrations. Problems also arise in uniaxial longitudinal compression testing where an unsupported specimen may fail by the 'brooming' of its ends or by column buckling. However, such premature failures result in property values lower than the true values and tend to bias the data accordingly.

The discussion of properties of the composites included in this review does not take into consideration the effect of variations in fibre resin ratio among specific types of composites and test specimens. Boron-reinforced composites normally contain an 0.45–0.50 fibre resin ratio volume, while composites reinforced with graphite or organic fibre conventionally have an 0.50–0.65 ratio. Composite properties are strongly influenced by this ratio. Controlled variations in many of the properties are obtainable in practice by specific variation of the fibre content of the composites. The property data discussed in this paper reflect values and trends reported for composites containing of the order of 50% fibre volume. However, the reader must refer to the literature for specific composite data.

Finally, the reader should be aware that composite technology is developing so rapidly that some of the data presented in this review may not reflect the current state of the art. Recent introduction of new reinforcing fibres, improvements in composite fabrication techniques and refinement of test methods have resulted in overall improvement in both the level and the consistency of composite mechanical properties.

For the reader unfamiliar with the development of advanced composite technology, it will be useful to establish a perspective on the field. The two primary reinforcement systems are boron filaments produced by vapour deposition of boron on a very fine tungsten wire substrate and graphite fibre produced by graphitization (pyrolysis) of an organic precursor fibre. Additionally, a proprietary aromatic polyamide organic fibre commercially called Kevlar 49 (PRD 49) is currently receiving attention. The boron filaments were initially produced at 4 mil (1 mil = 25.4 μm) diameter; however, 5.6 mil diameter filaments are now widely used. Boron fibre coated with a thin layer of silicon carbide, produced under the trade name of Borsic, is reported to have improved interfacial bonding to certain matrix types. The graphite fibre is much more complex, as it is not only possible to produce such fibres from different precursor materials (the two most common being rayon and polyacrylonitrile (PAN)), but it is also possible to vary the production process to produce fibres differing greatly in modulus and strength. As the properties obtainable with graphite reinforcement may approach those with boron reinforcement at a somewhat lower cost, development of graphite fibres has proceeded at a very rapid rate. Today the user is confronted with an abundance of fibre choices, many of which are not well characterized and many of which will disappear to be replaced by newer types. At the present time, the potential user of these materials would be wise to restrict his interest to those types whose behaviour is reasonably well known, barring compelling reasons for doing otherwise.

Graphite fibres may be produced with elastic moduli varying from 25–75 x 10^6 lb in^{-2} (170–500 GPa), with strengths varying inversely to moduli. In the present report, these fibres are classified according to low, medium or high modulus, the differentiation being < 40, 40–60 and > 60 x 10^6 lb in^{-2}, respectively (< 275, 275–415, and > 415 GPa).

As composites are frequently used where weight is critical or where high specific strengths are required, typical composite densities have been summarized in Table 1.

Primary static mechanical properties

The key static mechanical properties required for preliminary design calculations with composites are: uniaxial longitudinal and transverse tensile and compressive ultimate strengths; uniaxial in-plane shear ultimate strength; and ultimate strains in the uniaxial longitudinal and transverse directions. Key elastic properties are uniaxial tensile and compressive moduli in the longitudinal and transverse direction, uniaxial in-plane shear moduli and Poisson's ratios in the longitudinal and transverse uniaxial direction (see reference 124, Vol 1, Design). The literature data available on these key properties for composites within the cryogenic range are far from complete, and in some cases, non-existent. Nevertheless, available data provide a feel for the magnitude and temperature dependence of many key properties and serve to define areas in which further data are required.

For most mechanical properties, the data for the graphite-reinforced composites have been separated from that of the other advanced composites, that is, those reinforced with boron or PRD 49 (Kevlar 49). This reflects the larger amount of available data on the graphite-reinforced materials

Table 1. Typical composite densities

Composite system	Fibre/resin ratio	Density, lb in^{-3} (g cm^{-3})
s-glass-epoxy	0.60–0.67	0.068–0.074 (1.87–2.04)
Kevlar 49-epoxy	0.60–0.65	0.047–0.050 (1.3–1.38)
Boron-epoxy	0.55	0.070–0.074 (1.93–2.04)
Graphite-epoxy	0.55–0.60	0.050–0.055 (1.38–1.52)
Boron-aluminum (4 mil)	0.50	0.10 (2.62)

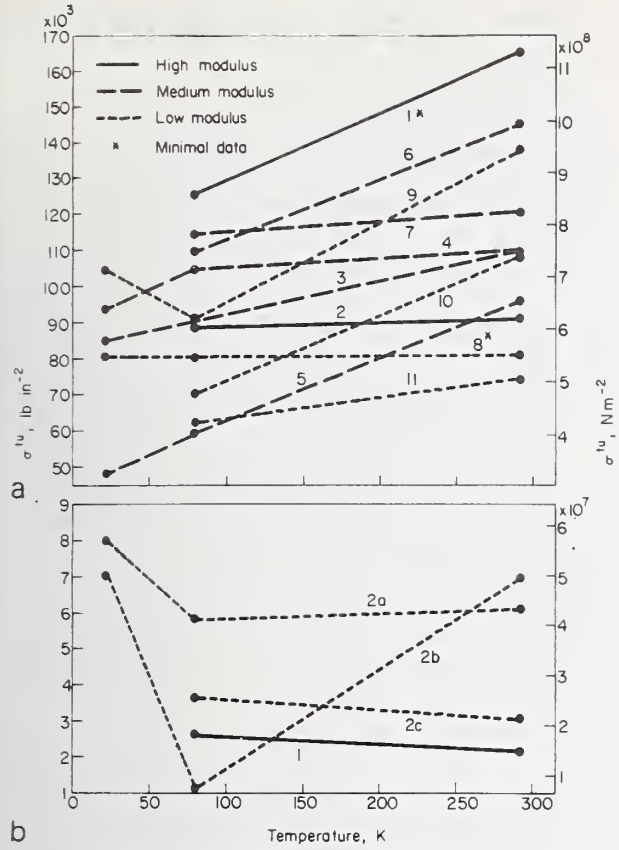

Fig.1 Ultimate tensile strength, σ^{tu}, of graphite-epoxy composites
a – Uniaxial longitudinal: 1 – Thornel 75 [51]; 2 – GY-70 [13]; 3 – Thornel 50 [8,10]; 4 – HMG – 50 [10]; 5 – MH-S [10]; 6 – Modmor I [8]; 7 – Samco 320 [8]; 8 – Thornel 25 [47]; 9 – HT-S [9,10,13,13.2,58]; 10 – Modmor II [8]; 11 – HMG-25 [8]
b – Uniaxial transverse: 1 – Thornel 75/ERLB 4617 [51]; 2a – HT-S/NASA Resin 2 [10]; 2b – HT-S/4617 (modified) [10]; 2c – HT-S/X-904 [13]

and the large variety of graphite fibres for which data have been published.

Composite tensile strength

Fig.1 summarizes the available data on the temperature dependence of the ultimate tensile strength of graphite-reinforced epoxy composites from room temperature into the cryogenic temperature range for the uniaxial longitudinal and uniaxial transverse orientations. A surprisingly large amount of cryogenic data were found in the literature for graphite-reinforced materials – 58 separate reports of test data, each report being the average of several tests on a given composite. Undoubtedly, this large effort reflects the desire to exploit the relatively low cost of graphite fibres.

The available data summarized on Fig.1 indicate that graphite-reinforced epoxy composites may suffer significant strength losses upon cooling to 77 K, and as was observed with the glass-reinforced materials in Part 1, the strength behaviour below 77 K appears to become erratic.

Fig.1a indicates that the uniaxial tensile strength obtainable in graphite-reinforced composites is about 30% of that obtainable with glass-fibre reinforcement in the cryogenic range. The ultimate tensile strength of composites tested in the uniaxial longitudinal mode should be fibre controlled; hence, the tensile strengths should inversely follow the modulus of the fibre. This trend is not reflected in the data of Fig.1a – indeed the averaged data indicate the converse; higher strengths are associated with higher modulus fibres and lower strengths with lower modulus fibres. However, a more detailed examination of the data averaged into these curves shows that the expected correlation does exist if one considers only the highest strength values reported for each modulus range. Thus, the highest overall ultimate strength at 77 K was 147 x 10^3 lb in^{-2} (1.01 GPa) reported for the low modulus HT-S graphite fibre in X-904 resin.[13] The next highest was 130 x 10^3 lb in^{-2} (0.90 GPa) reported for HMG-50 in a flexibilized epoxy matrix [10] for Modmor I and for Samco 360 in modified ERL 1156,[8] all medium modulus fibres, while 126 x 10^3 lb in^{-2} (0.87 GPa) was the maximum reported for the high-modulus Thornel 75 fibre in ERLB 4617.[51] This suggests that the higher strengths normally associated with the lower modulus fibres may have been lost in the averaging process due to variations in composite quality or perhaps due to difficulties in obtaining valid tensile fractures. Additional evidence that the test method is capable of affecting the results is found in the work of Larsen and Simon [10] who report almost diametrically opposite temperature dependence of the ultimate tensile strength for NASA Resin 2 and ERLB 4617 epoxy reinforced with HT-S fibre when each was tested, first as flat tensile coupons and subsequently as NOL (Naval Ordnance Laboratory) ring specimens. NASA 2 resin is a bisphenol A epoxy system modified for low temperature flexibility by means of a long-chain anhydride and a high molecular weight tricarboxy acid. This resin, consisting of Epon 828/DSA/Empol 1040/BDMA in proportions 100/115.9/20/1 pbw, was developed by Soffer and Molho [5] under NASA Sponsorship.

The uniaxial longitudinal tensile strength data for other types of advanced composites are presented in Fig.2a. The data for PRD 49-epoxy, boron-epoxy, boron (Borsic)-aluminium, stainless steel–aluminium, and the hybrid Borsic-steel-aluminium and Borsic-titanium-aluminium composites all have higher absolute values of tensile strength and retain their strength to lower temperatures than do the graphite-reinforced composites. Data for Borsic and boron-fibre composites have been combined except where differences in reported values justified separating the data. The hybrid Borsic-steel-aluminium (6061) composite contained 4.2 mil Borsic fibres in the tensile direction and stainless wires in the transverse direction. The hybrid Borsic-titanium-aluminium (6061) composite contained 4.2 mil Borsic fibres in the tensile direction with β-3Ti foil interleaved between the boron lamellae.[13] While the latter two composites are not strictly uniaxial, they have been included to illustrate the interesting possibilities of hybrids.

The magnitude and temperature dependence of the ultimate tensile strength of the graphite HT-S/polyimide (Skybond 703) material were comparable to that of the graphite-epoxies. A very sharp rise in strength on cooling was reported for the HT-S/epoxy-phenolic (HT-424 Primer).

The stainless steel reinforced composite contained NS-355 stainless wires in a 2024 aluminium alloy matrix. This type of composite is available commercially on special order; however, it has not received wide acceptance in view of the wider availability of boron-reinforced aluminium, which has similar strength properties.

Boron-aluminium composites are available commercially with

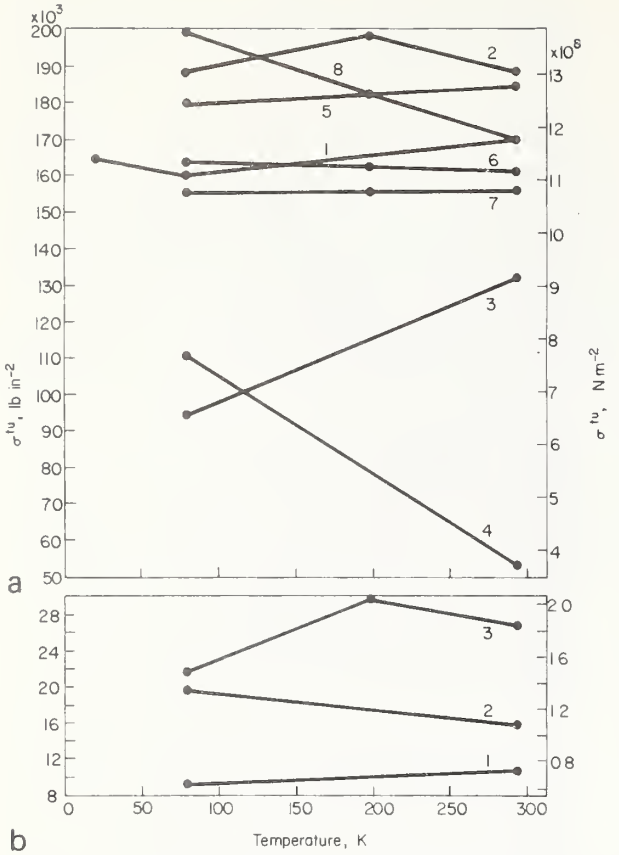

Fig.2 Ultimate tensile strength, σ^{tu}, of miscellaneous advanced composites
a — Uniaxial longitudinal: 1 — PRD 49—1/epoxy [59,60]; 2 — boron-epoxy [13,22,47,53,58,81]; 3 — HT-S/polymide [13]; 4 — HT-S/epoxy-phenolic [58]; 5 — boron-aluminium (6061) [13]; 6 — Borsic-steel-aluminium (6061) [13]; 7 — Borsic-titanium-aluminium (6061) [13]; 8 — stainless steel-aluminium (2024) [7,74]
b — Uniaxial transverse: 1 — boron-epoxy [13,81]; 2 — boron-aluminium (6061) [13]; 3 — Borsic-titanium-aluminium [13]

either 4 or 5.6 mil boron or Borsic reinforcement, while 8 mil boron fibers are currently being studied. Available literature values of uniaxial tensile strength at 77 K ranged from 163—202 x 10^3 lb in^{-2} (1.12—1.39 GPa), with highest values reported for 5.6 mil Borsic/6061.[13] Data were not available for any other aluminium alloy matrix. Boron-epoxy composites containing either 4 mil or 5.6 mil fibre are commercially available in the form of prepreg tape, that is, with the plastic matrix partially cured to facilitate component fabrication and to improve composite quality. The literature values for boron-epoxy composites tested in the longitudinal direction at 77 K varied from 167—226 x 10^3 lb in^{-2} (1.15—1.56 GPa), the highest value being reported for the commercial SP-272 product.[13]

PRD 49 (Kevlar 49) is a relatively new type of organic fibre. Present data indicate that this fibre in an epoxy matrix is capable of developing tensile strengths at cryogenic temperatures comparable to that developed with the graphite fibres. Hoggatt [59] reports NOL ring ultimate strengths of 146 x 10^3 lb in^{-2} (1.0 GPa) for PRD 49—1 in a NASA Resin 2 matrix and 183 x 10^3 lb in^{-2} (1.26 GPa) in an ERLB 4617 matrix at 20 K. There is some evidence of a slight decrease in strength on cooling to 77 K; however, available data indicate that the ultimate tensile strength of this material is relatively independent of temperature within the cryogenic range.

The hybrids Borsic-steel-aluminium and Borsic-titanium-aluminium complete the group of advanced composites that has reasonably high strength in uniaxial tension. The somewhat lower strength of these hybrids, compared to the conventional boron-aluminium composite, reflects the reduced density of boron fibres in the loading direction.

Metal-matrix composites are clearly superior to polymer-matrix composites in transverse mechanical properties. As seen in Fig.2(b), the ultimate uniaxial transverse tensile strength of boron/6061 aluminium is about 50% higher than that of boron-epoxy. Addition of titanium foil to the boron-aluminium further increases the transverse strength at 295 K and 200 K; however, the effect appears to diminish rapidly as the material is cooled to 77 K. While the transverse strength of the conventional boron-epoxy composite is much lower than that of the metal-matrix materials, values are still in excess of those developed with the graphite fibre reinforcement.

The boron/6061 aluminium data reviewed here reflects the as-fabricated (F) condition. Solution-treating and aging the composite increase the transverse ultimate strength by about 30%, with a slight decrease in transverse ductility.[13]

The literature reported a 77 K transverse ultimate strength of 14.2 x 10^3 lb in^{-2} (97 MPa) for 4.2 mil Borsic/6061 aluminium and a somewhat higher value of 24.9 x 10^3 lb in^{-2} (172 MPa) for 5.6 mil boron reinforcement.[13] It is also probable that this strength difference is real; however, available data [13,126] also indicate that the observed difference may be due to residual stresses inherent in the small diameter fibre rather than to the presence or absence of a silicon carbide coating. The reader is referred to the section on ultimate tensile strain for further discussion of this subject.

Composite tensile modulus

The primary reason for development of advanced composites is the high modulus obtainable with the newer types of fibre reinforcement. In contrast to a maximum of about 10 x 10^6 lb in^{-2} (69 GPa) for glass-reinforced composites in the fibre direction, Figs 3a and 4a show that moduli ranging from 30—40 x 10^6 lb in^{-2} (207—276 GPa) are obtainable with several of the advanced fibre composites. Thus, while glass-reinforced composites may at their best equal the modulus of aluminium, the modulus of composites using advanced fibres may at their best equal and often exceed that of steel.

Looking first at the graphite-epoxy composites, Fig.3a shows that the uniaxial longitudinal modulus of the composite does, on the average, reflect the modulus of the fibre when tested in the uniaxial longitudinal mode. The available data indicate that the modulus of the Thornel 75 composite (the only representative of the high modulus fibers) declines to about that of the medium modulus fibres at 77 K. With this exception, the average data indicate that the moduli in the fibre direction slightly increase on cooling to 77 K. No correlation is observed between fibre modulus and transverse composite moduli in Fig.3b; indeed, none is expected, as the latter is controlled by the properties of the matrix and by the fibre-matrix interfacial bond strength.

A comparison of Figs 3a and 4a shows that the uniaxial longitudinal modulus of graphite-epoxy composites may exceed that of any other type of advanced composite when certain graph-

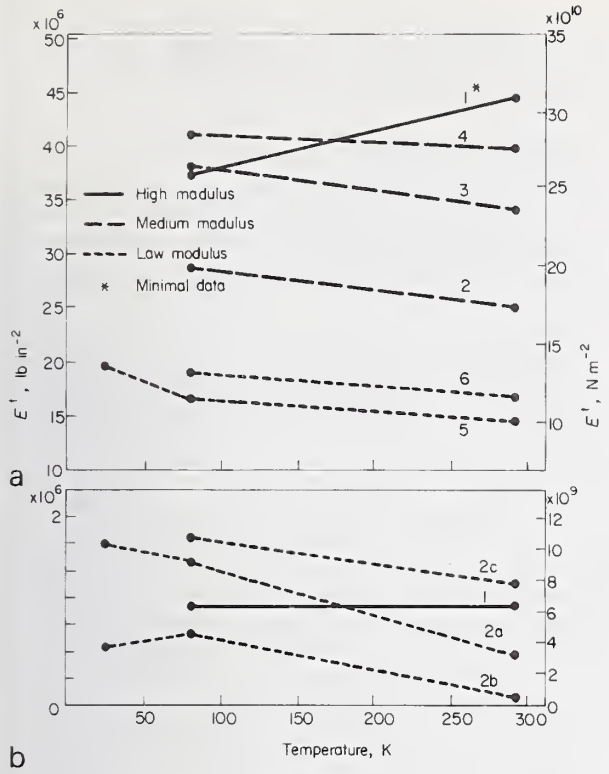

Fig.3 Initial tensile modulus, E_1^t, of graphite-epoxy composites
a – Uniaxial longitudinal: 1 – Thornel 75 [51]; 2 – Thornel 50 [8]; 3 – Modmor I [8]; 4 – Sancom 320 [8]; 5 – HT-S [8,10,13]; 6 – HMG-25 [8]
b – Uniaxial transverse: 1 – Thornel 75/ERLB 4617 [51]; 2a – HT-S/NASA Resin 2 [10]; 2b – HT-S/4617 (Modified); 2c – HT-S/X-904 [13]

ite fibres are used. However, a comparison of Figs 3b and 4b shows that the uniaxial transverse tensile moduli of graphite-epoxy composites are much lower than that developed by the other advanced composites over the entire cryogenic temperature range.

A closer look at the literature data from which Fig.3a was prepared revealed that among the medium modulus fibres, the modulus at 77 K was 39–43 x 10^6 lb in^{-2} 269–297 GPa) for Samco 360; the highest value being reported with a modified ERL 2256 resin.[8] The Modmor I fibre produced almost as high moduli, ranging from 32–42 x 10^6 lb in^{-2} (221–290 GPa), with the highest values reported for a NASA Resin 2 composite.[8] (Note that these same fibres developed high uniaxial tensile strengths). A distinctly lower range of 26–33 x 10^6 lb in^{-2} (179–228 GPa) was reported for Thornel 50; the highest values were for a modified ERL 2256 composite.[8] among the low modulus fibres, HT-S (the most tested fibre) produced 15–20 x 10^6 lb in^{-2} (103–138 GPa), the highest value being reported with X-904 resin,[13] while 17–22 x 10^6 lb in^{-2} (117–152 GPa) was the reported range for HMG-25, the highest values being obtained in a NASA Resin 2 matrix.[8]

As the transverse modulus properties are matrix dominated, Fig.3b shows significant differences for the same HT-S fibre in different epoxies. The illustrated data are for the same composites as appear in Fig.1b. Here the lower moduli of the HT-S/NASA Resin 2 and the HT-S/4617 (modified) are due to the additions of flexibilizers and elastomers to the epoxy resin, while the highest modulus was developed with the conventional X-904 matrix. In general, the transverse modulus increases with decreasing temperature. A lower composite modulus value was reported for the high-modulus Thornel 75 fibre in ERLB 4617 resin than for the HT-S/X-904 combination.

Leaving the graphite-reinforced composites and turning to those reinforced with other advanced fibres, we observe on Fig.4a that the uniaxial longitudinal moduli reported for the boron-epoxy, the boron-aluminium and the hybrid Borsic-titanium-aluminium and Borsic-steel-aluminium composites all cluster around 30–35 x 10^6 lb in^{-2} (207–242 GPa) with little temperature dependence. The PRD 49/epoxy modulus is reported to be significantly lower, at 16–18 x 10^6 lb in^{-2} (110–124 GPa), but undergoing a significant rise between 77 K and 20 K. In general, these uniaxial longitudinal moduli values compare favourable with those of the graphite-epoxies.

The uniaxial transverse moduli are another matter. As seen in Fig.4b, the transverse moduli of the aluminium-matrix materials are far higher than those of the graphite-epoxies and are, in fact, almost twice as high as that of unreinforced 6061 aluminium. The transverse moduli of the boron-epoxy is much lower than that for the same fibre in an aluminium matrix, but is still almost twice that of the graphite-epoxy materials. These data reflect the contribution made by fibre-matrix interface to the transverse modulus.

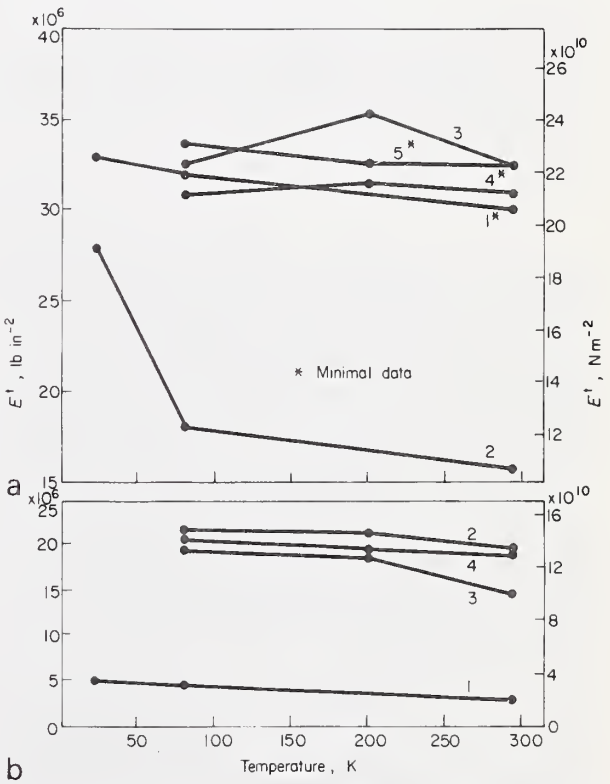

Fig.4 Initial tensile modulus, E_1^t, of miscellaneous advanced composites
a – Uniaxial longitudinal: 1 – boron-epoxy [81]; 2 – PRD 49–1/epoxy [59,60]; 3 – boron-aluminium (6061) [13]; 4 – Borsic-titanium-aluminium (6061) [13]; 5 – Borsic-steel-aluminium (6061) [13]
b – Uniaxial transverse: 1 – boron-epoxy (SP-272, Narmco 5505) [81] 2 – boron-aluminium (6061) [13]; 3 – Borsic-titanium-aluminium (6061) [13]; 4 – Borsic-steel-aluminium (6061) [13]

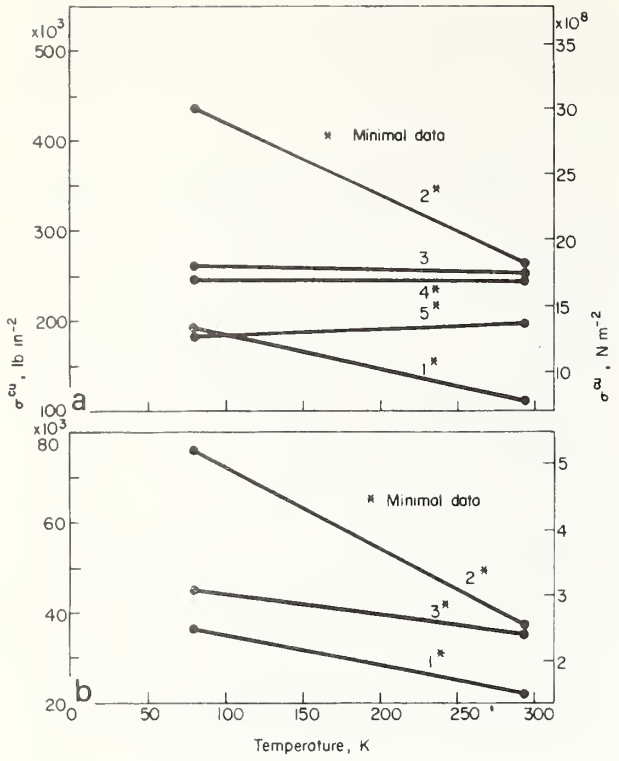

Fig.5 Ultimate compressive strength, σ^{cu}, of advanced composites
a — Uniaxial longitudinal: 1 — HT-S/X-904 [13]; 2 — boron-epoxy [81] (SP-272, Narmco 5505); 3 — boron-aluminium [13] (6061); 4 — Borsic-titanium-aluminium (6061) [13]; 5 — Borsic-steel-aluminium (6061) [13]
b — Uniaxial longitudinal: 1 — HT-S/X-904 [13]; 2 — boron-epoxy [81] (Narmco 5505, SP-272) [81]; 3 — boron-aluminium [13]

Looking in more detail at the uniaxial longitudinal data, we find that the boron (Borsic)-aluminium data ranged from 30.4–36.2 x 10^6 lb in^{-2} (210–250 GPa) with little temperature dependence. These data combine values obtained from fibres of 4 mil and 5.6 mil diameter in the two production variants, as no significant difference was reported for these materials. The boron-epoxy data represent average results reported by Nadler et al [81] on SP-272 and Narmco 5505 (data range was not available). The hybrids, Borsic-titanium-aluminium, and Borsic-steel-aluminium, were the same composites discussed in reference to the tensile data of Fig.2a. The slightly lower uniaxial tensile modulus of the hybrids compared to that of the conventional boron-aluminium reflects the lower density of fibres in the stress direction in the hybrids.

The PRD 49 data reflect input from both an ERLB 4617 and a NASA Resin 2 matrix.[59,60] The ERLB 4617 composite produced a slightly increased tensile modulus at all temperatures, its value being 18.5 x 10^6 lb in^{-2} (128 GPa) at 77 K compared to 17.5 x 10^6 lb in^{-2} (121 GPa) for the NASA Resin 2. A large rise in modulus between 77 K and 20 K was reported for both matrices.

Considering the transverse data of Fig.4b in more detail, we observe that the three aluminium-matrix composites have similar moduli, about 20 x 10^6 lb in^{-2} (138 GPa). The boron-aluminium data was again the average of data obtained from 4.2 mil Borsic and 5.6 mil boron, similar values being reported for each variant. The boron-epoxy data of Fig.4b again reflect the average values obtained from the commercial SP-272 and Narmco 5505 materials.[81]

Composite compressive strength and modulus

Data on the compressive properties of advanced composites at cryogenic temperatures were also relatively sparse. Those which were available appear in Figs 5 and 6, combining the graphite-epoxy data with those of the other composite types.

These data show that the advanced composites have significantly higher compressive strengths and moduli than those of the glass-reinforced composites. Comparison of Fig.5 with Figs 1 and 2 also shows that the compressive strengths are 100–200% higher than the tensile strengths for the same composites.

The highest uniaxial longitudinal compressive strength, more than 200% above that obtainable with glass reinforcement, was reported for the commercial boron-epoxy types SP-272 and Narmco 5505.[81] The compressive strength of this composite class was observed to increase on cooling to 77 K. Boron-aluminium reportedly has a comparatively lower uniaxial compressive strength. The latter data reflect input from both 4.2 mil Borsic and 5.6 mil boron-fibre composites.[13] A slightly higher strength was reported for the 5.6 mil composite, but not sufficiently to justify a separate plot. Again, the Borsic-titanium-aluminium and Borsic-steel-aluminium hybrids developed strengths some-

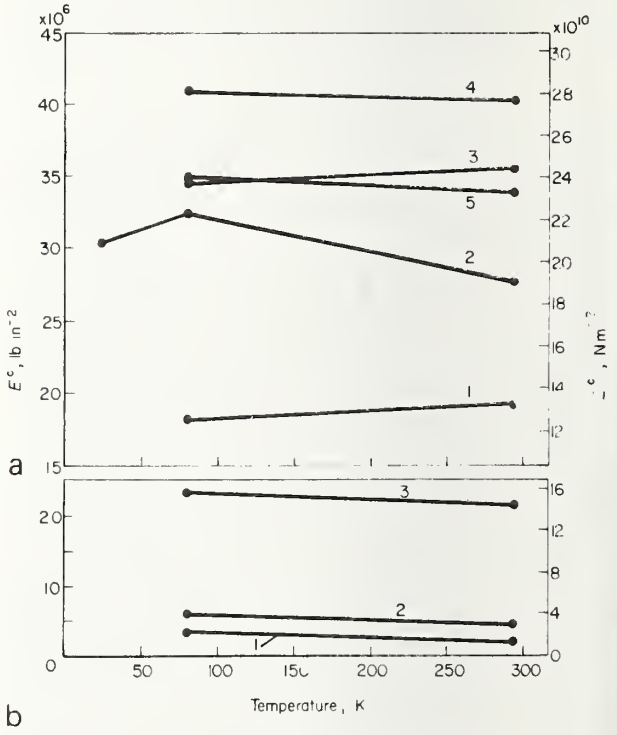

Fig.6 Compressive modulus, E^c of advanced composites
a — Uniaxial longitudinal: 1 — HT-S/X-904 [13]; 2 — boron-epoxy (Narmco 5505 SP-272) [81]; 3 — boron-aluminium (6061) [13]; 4 — Borsic-titanium-aluminium (6061) [13]; 5 — Borsic-steel-aluminium (6061) [13]
b — Uniaxial transverse: 1 — HT-S/X 904 [13]; 2 — boron epoxy (Narmco 5505, SP-272) [81]; 3 — boron-aluminium (6061) [13]

what below that of the conventional boron-aluminium, reflecting the decreased density of boron fibres in the stress direction. Lowest uniaxial longitudinal compressive strengths were reported for the HT-S/X-904 graphite-epoxy composite; however, this composite developed a compressive strength about twice that developed in tension and about 40% higher than that available with glass reinforcement. The compressive strength of the graphite-epoxy composite was reported to increase with cooling, in contrast to the tensile behaviour.

The available data on the transverse compressive strengths of boron-epoxy, boron-aluminium, and graphite-epoxy composites are compared on Fig.5b. These composites appear in the same relative order of strength as in the longitudinal test mode. The commercial SP-272 and Narmco 5505 boron-epoxy products display substantial increases in compressive strength on cooling. Lesser increases are observed in the boron/aluminium and in the HT-S/X-904 graphite-epoxy composite.

The compressive modulus of a given composite is expected to be the same as the tensile modulus. This is found to be generally true for the HT-S/X-904 graphite-reinforced material, for the boron-epoxy, for the Borsic-aluminium composites, and for the Borsic-steel-aluminium hybrid, as may be seen by comparing the compressive moduli of Fig.6a with the tensile moduli of the same composites on Fig 3 and 4. The Borsic-titanium-aluminium data are at variance with this principle, as the reported compressive modulus is about 30% higher than in tension. The boron-aluminium and the boron-aluminium hybrids again show the highest longitudinal moduli, with the boron-epoxy only slightly lower. The modulus of the HT-S/X-904 graphite-reinforced composite is again much lower than that of the boron-reinforced materials. There does not appear to be a significant temperature sensitivity of this parameter. Also, as in the tensile case, the boron-aluminium is found to have a higher transverse compressive modulus than either the boron-epoxy or the graphite-epoxy composite.

Composite failure strain

Available data on the temperature dependence of ultimate tensile strain for advanced composites are minimal: all of that which has been published reflects the work of Hertz et al.[13] Nevertheless, these data suffice to illustrate that: (a) the strain at tensile fracture is very low for the advanced composites, being of the order of $1-9 \times 10^{-3}$ in the longitudinal uniaxial direction; and (b) the strain at tensile fracture is relatively independent of temperature within the cryogenic range. These data are summarized on Fig.7. These strains are about an order of magnitude lower than those obtained with glass-reinforced composites, reflecting the negligible fracture strain of the advanced fibres.

Fig.7 includes data on one graphite-reinforced composite (HT-S/X-904), on two conventional boron-aluminium composites (4.2 mil Borsic and 5.6 mil boron, both in 6061 aluminium) and on the two Borsic-aluminium hybrids discussed previously with reference to the other properties. Both longitudinal and transverse ultimate fracture strains appear on Fig.7.

Fig.7 indicates that the transverse fracture strain of the HT-S/X-904 graphite-epoxy composite will be about 2×10^{-3}, or about 25% of the longitudinal strain. By comparison, the transverse fracture strain for the commercial HT-S/3002

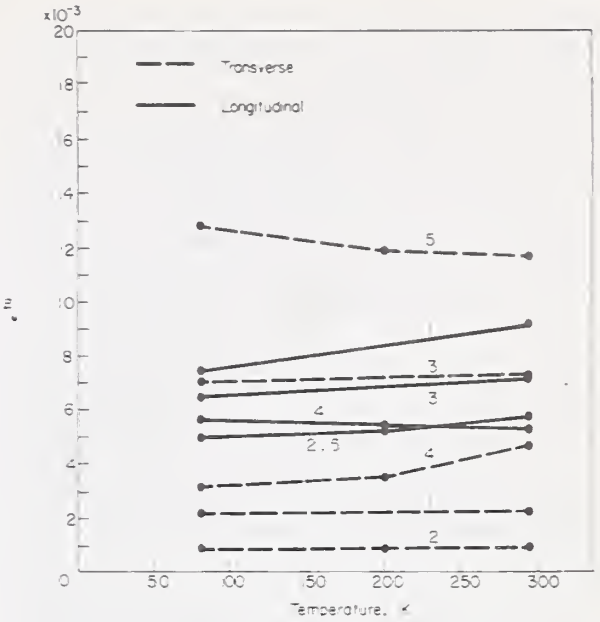

Fig.7 Ultimate tensile strain, ϵ^{tu}, of advanced composites (uniaxial tensile)
1 — HT-S/X-904 [13]; 2 — 4.2 mil Borsic-aluminium (6061) [13]; 3 — 5.6 mil boron-aluminium (6061) [13]; 4 — 4.2 mil Borsic-titanium-aluminium (6061) [13]; 5 — 4.2 mil Borsic-steel-aluminium (6061) [13]

graphite-epoxy composite is reported [12] to be 7.8×10^{-3}, only slightly less than its longitudinal fracture strain of 8.6×10^{-3}. The interfacial-bond strength between the fibre and matrix in the HT-S/3002 composite was undoubtedly superior to that existing in the HT-S/X-904 composite.

Fig.7 shows that a 5.6 mil boron/6061 aluminium composite is expected to fail at about the same strain in both the longitudinal and transverse directions. The 4.2 mil Borsic/6061 composite is expected to fail at a much lower strain when tested in the transverse direction. Hertz et al [13] found that the 4.2 mil Borsic fibre was failing by longitudinal fibre splitting during transverse testing, while such splitting did not occur in the larger diameter fibre. The authors concluded that the problem was related to the use of plasma-sprayed tape. Higher transverse strains were observed in the same type of composite when diffusion-bonded tape was used to make the test specimens. They concluded that diffusion-bonded boron-aluminium tape was superior for oriented-ply applications. Kreider and Prewo [125] has proposed an alternative explanation for longitudinal splitting of the small diameter boron fibres, citing results of diametral-compression tests of individual fibres, which indicate that such splitting reflects strength anisotropy in the small fibres due to residual stresses retained from the original fibre manufacturing process and from pre-existing flaws in the fibres. Such anisotropy was not observed in the larger fibres. Fibre splitting was not directly related to the presence or absence of a silicon carbide coating on the fibres. (Manufacturers of boron-aluminium tape report that current fabrication technology has overcome the problem of fibre splitting)

The Borsic-titanium-aluminium hybrid reportedly developed higher strain values in both directions than did the conventional 4.2 mil Borsic-aluminium, but lower values than that of the composite reinforced with 5.6 mil boron. The borsic-

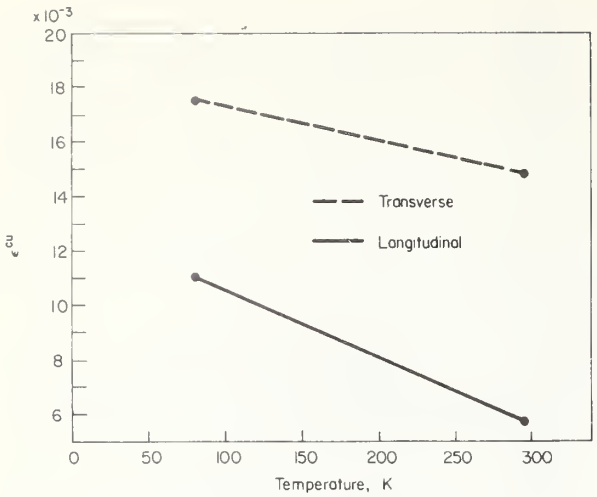

Fig.8 Ultimate compressive strain, ϵ^{cu}, of graphite-epoxy composites: unaxial compression HT-S/X 904 [13]

steel-aluminium hybrid shows clearly the increase in transverse strain capability due to the presence of stainless wires oriented in this direction. The longitudinal strain of this hybrid did not appear to be significantly affected by the transverse reinforcement.

The only data available on the temperature dependence of compressive strain within the cryogenic temperature range was for the HT-S/X-904 graphite-epoxy composite, again reflecting the work of Hertz et al.[13] These data, Fig.8, indicate an increasing compressive strain capability for this composite type as the temperature is lowered, with a substantially higher strain capability in the transverse direction. As in the tensile case, these strain values are substantially lower than those reported for an HT/S/3002 graphite-reinforced composite.[124]

Composite in-plane shear strength and modulus

The key shear properties are the in-plane ultimate strength and modulus, sometimes referred to as the intralaminar or longitudinal shear properties. The requirements for obtaining valid shear property data are the same as for metals, that is, values must reflect pure shear resolved onto a 45° shear plane with respect to the tensile axis without significant compressive or tensile forces normal to the shear plane. Three shears may be defined in a bulk, uniaxial composite laminate. Most important are the two longitudinal shears represented by shear between parallel fibres in the plane of the fibres. For example, taking the x axis parallel to the fibres, longitudinal shear strengths may be defined as σ_{yx}^{su} or σ_{zx}^{su}; however, in thin laminates, only one such in-plane shear is of consequence. A third shear, which is transverse or cross-fibre, is not an important composite design parameter.

It is important to distinguish between in-plane or intralaminar shear defined as above and *interlaminar* shear, which refers to shear between adjacent layers in a layered composite. The latter, sometimes called horizontal shear, is *not* a basic material property and is used primarily as an adjunct to quality control or in material screening tests. Because the test is simple and inexpensive, a large amount of interlaminar shear data have been reported.

In-plane shear is a difficult property to measure accurately because of the necessity of avoiding extraneous compressive or tensile stresses on the shear plane. The torque tube (torsion) method works well but is expensive. Consequently, somewhat simpler methods such as the 'rail shear' or the '± 45° laminate' test have been devised. The interested reader can find discussions of the relative merits of these latter methods in ASTM STP Vols 460, 497, and 546.

Few data are available on the in-plane shear properties of composites at cryogenic temperatures. Hertz et al [13] report a decrease in the shear strength of HT-S/X-904 graphite-epoxy from 8 592 lb in^{-2} (60 MPa) at 295 K to 7 378 lb in^{-2} (51 MPa) at 77 k, using the torsion tube test method. A concomitant shear modulus increase from 7.27 x 10^5 lb in^{-2} (10.5 GPa) was reported. Obviously, much additional in-plane shear data are required before trends in the cryogenic temperature dependence of shear properties can be defined. Room temperature values of shear strengths and moduli are reportedly about 18 x 10^3 lb in^{-2} (124 MPa) and 9.5 x 10^6 lb in^{-2} (65 GPa), respectively, for boron-aluminium, while values for boron-epoxy are about 15 x 10^3 lb in^{-2} (124 MPa) and 7 x 10^5 lb in^{-2} (0.48 GPa), respectively.[124] Reported room temperature values for the shear strength of graphite-epoxy composites vary from 9–13 x 10^3 lb in^{-2} (62 MPa) with a modulus of about 6.5 x 10^5 lb in^{-2} (0.45 GPa), the variation in strength reflecting variation in properties of the graphite fibre used in the composite. As most of the other mechanical properties of boron-aluminium and boron-epoxy composites either remain unaffected or increase upon cooling to cryogenic temperatures, these room temperature values likely represent conservative values for such materials at the lower temperatures. However, confirmation must await further testing at the cryogenic temperatures.

Secondary static mechanical properties

The properties discussed in this section are classified as secondary only in that they are not generally useful in a predictive design analysis using macromechanics composite theory. However, such secondary properties are important in other ways. Because composites are largely fabricated *in situ*, a large number of options are available among fibre (or combinations of fibres) and matrix materials. Options are also available in fabrication procedure. It is necessary to efficiently evaluate various combinations in a meaningful comparative manner in order to optimize the final selection. Furthermore, having made a selection, it is necessary to have viable techniques for measuring the consistency of composite quality over a production run. For such objectives, the flexure test and the interlaminar shear test (usually also performed in flexure) are relatively inexpensive and informative. Additionally, there are properties that are classed as secondary only in that the results are specific to a given geometry as, for example, bearing yield strength.

Composite flexural strength and modulus

The flexure test requires that a bar or plate specimen be supported near its ends while deflected by a moving ram at its cenre, providing symmetrical three-point loading. Dimensions of the fixture and specimen are proportioned to develop maximum stress in the outer (tension) fibres as flexure progresses. Fibres run lengthwise along the specimen, that is, between the supports, in uniaxial longitudinal flexure and across the specimen in uniaxial transverse flexure.

Fewer data were available on the temperature dependence of

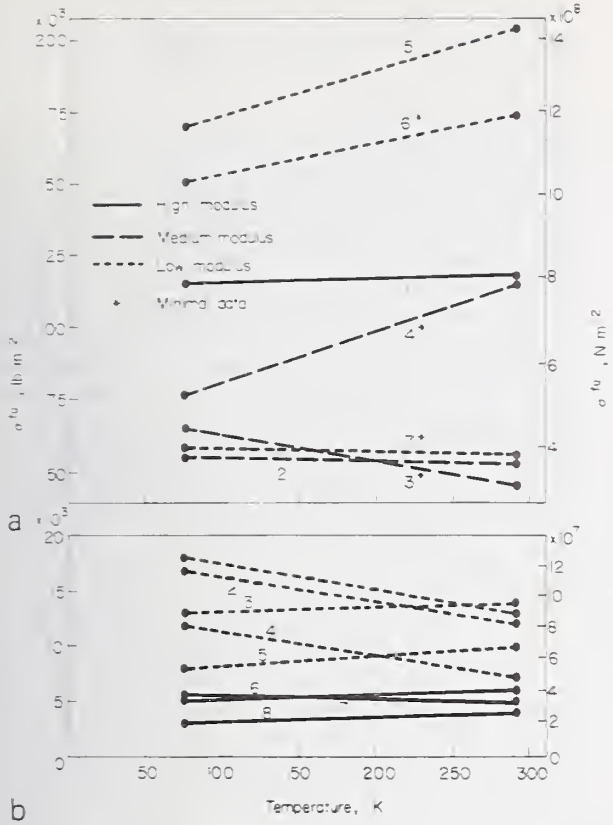

Fig.9 Ultimate flexural strength, σ^{fu}, of graphite-epoxy composites
a — Uniaxial longitudinal: 1 — GY-70 [11,13]; 2 — Thornel 50 [8]; 3 — Courtaulds HM [8]; 4 — Fibralloy 300 [13]; 5 — HT-S [11,12,13,58]; 6 — Modmor II [13]; 7 — HMG-25 [8];
b — Uniaxial transverse: 1 — Modmor II/1004 [13]; 2 — HT-S/1004 [13]; 3 — HT-S/BSP-2401 [13]; 4 — HT-S/X-904 [11,13]; 5 — HT-S/3002 [11,13]; 6 — GY-70/1004 [13]; 7 — GY-70/E-350A [13]; 8 — GY-70/X-904 [11,13]

the flexural strength and elastic modulus than for tensile properties; furthermore, most of those available were reported for graphite-epoxy composites. Fig.9 summarizes the flexural strength data for the latter, while Fig.10 summarizes the available data for other types of reinforcements or matrices. The minimal available data on flexural modulus properties appear in Fig.11.

Comparison of Fig.9 with Fig.1 shows that the graphite-epoxy flexural strength data span a much greater range of values than does the tensile strength data in both the longitudinal and transverse directions. The expected higher strength of the lower modulus fibres is more in evidence for the flexural test than it was for the tensile test mode.

By far the largest amount of data was available for HT-S/epoxy composites. Furthermore, such composites had the highest longitudinal flexural strength of all the graphite-reinforced materials for which data were available. Strengths were reported over a 113–234 x 10^3 lb in^{-2} (0.78–1.61 GPa) range at 77 K. This is significantly lower than the 325–470 x 10^3 lb in^{-2} (2.24–3.24 GPa) range reported for uniaxial glass-epoxies in Part 1. These data included test series designed to investigate cure cycles, aging effects, and environmental effects.[12,13,58] Most of the work was done with E-350, X-915, or X-904 matrices, for which the average flexural strengths at 77 K were reported to be very similar, varying only from 167–178 x 10^3 lb in^{-2} (1.15–1.23 GPa).[13]

The available data on the HT-S fibre composites remind us that processing variables are important; in particular, those variables that affect the void content. Detailed examination of the available data showed that in 84 of the 89 reported test series, the flexural strength of composites made with HT-S fibre declined markedly on cooling to 77 K. The five series for which strength increases were noted were reported by Scheck [12] to have occurred concomitantly with a change to a vacuum-bagging method of fabrication. This suggests that at least a part of the observed drop in flexural strength on cooling might have been due to the presence of voids in the composites.

Continuing this with the other fibres, we observe on Fig.9a that the order of decreasing strength is Modmor II, GY-70, and Fibralloy 300, arriving finally at a group comprising the lowest reported strengths and consisting of Courtaulds HM, HMG-25, and Thornel 50 fibres. The flexure strength of this latter group is only about a third that of the HT-S fibre composites. Among these other fibres, most data were available for the high-modulus GY-70, for which the spread of values at 77 K was 85–133 x 10^3 lb in^{-2} (586–917 MPa); the highest being reported in X-904 epoxy resin.[13]

The clear separation between the transverse flexural strengths of the low modulus HT-S composites and the high modulus GY-70 composites in Fig.9b suggests that there are

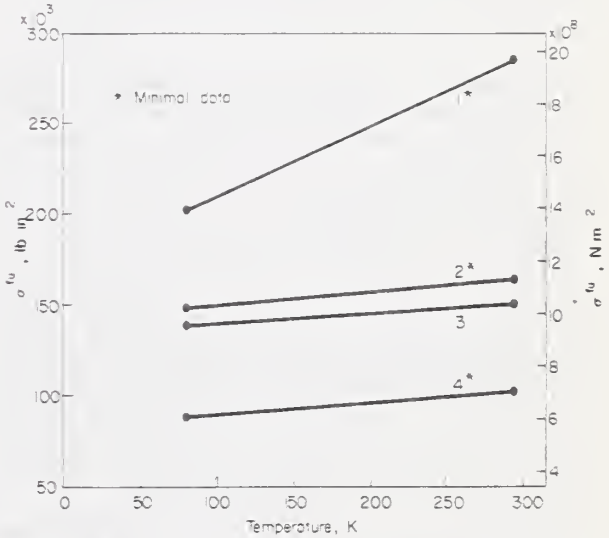

Fig.10 Ultimate flexural strength, σ^{fu}, of miscellaneous advanced composites
1 — boron-epoxy (SP-272) [57]; 2 — HT-S/polymide [11,58]; 3 — HT-S/epoxy-phenoloc [58]; 4 — GY-70/polyimide [11]

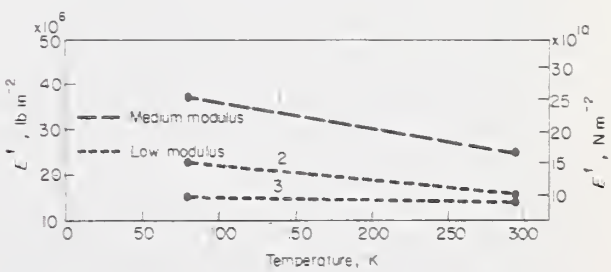

Fig.11 Initial flexural modulus, E_1^f, of advanced composites: uniaxial longitudinal
1 — Thornel 50; 2 — HMC-25; 3 — Modmor II (all reference 8)

Table 2. Comparison of ranking of specific uniaxial graphite-epoxy composites by longitudinal flexure strength and by longitudinal tensile strength (77 K)

Composite	σ^{fu}, 10^3 lb in^{-2}	Rank	σ^{tu}, 10^3 lb in^{-2}	Rank
A	178	1	147	1
B	172	2	87	6
C	167	3	103	2
D	146	4	45	8
E	117	5	92	4
F	58	6	91	5
G	55	7	71	7
H	54	8	93	3

differences in the fibre-matrix bond strength between these two fibre types, the high modulus fibre having the poorer bonding. Note that X-904 and 1004 epoxies were used with both fibre types.

Before leaving the data of Fig.9, it is of interest to consider whether or not the literature data support the contention that the relatively inexpensive flexure test may be used to obtain comparative ranking of composite strength in lieu of the more expensive tensile test. A visual comparison of the data on Fig.9a with that of Fig.1a is hardly convincing. However, such a comparison is nebulous because these graphs present data from different composite types. To clarify this question, the literature data were examined more closely and a comparison of ranking of strength in longitudinal tension versus longitudinal flexure was made at 77 K for eight specific composite types (same fibre and matrix) for which data were available. The data are summarized in Table 2. Results suggest that the flexure test results are not a very good measure of the relative tensile strengths of graphite/epoxy composites at 77 K. Insufficient data existed for similar comparisons with other mechanical properties.

Flexure data on other types of advanced composites were somewhat meagre. Fig.10 does indicate that the uniaxial longitudinal flexural strength of boron-epoxy in the form of the commercial SP-272 product is much higher than that of the graphite-epoxies, although still lower than that developed with glass reinforcement. A quite rapidly declining strength is observed on cooling to 77 K. The latter effect was not observed in the comparable tensile data (see Fig.2a). Data were available for two polyimide composites, one with the high modulus GY-70 fibre and one with the low modulus HT-S fibre. Of these, the HT-S composite developed the higher strength. A small decrease in flexure strength is evidenced in these composites at 77 K, but the magnitude of the decrease is less than that reported for the uniaxial tensile strength. Finally, the HT-S/epoxy-phenolic (HT-424 Primer) appears to possess acceptable flexure strength with little temperature dependence, in contrast to the comparatively low strength and significant temperature dependence reported for the same composite in longitudinal tension (see Fig.2a).

Very little data were available on the flexural modulus. Data for the longitudinal mode appearing on Fig.11 reflect the modulus of the reinforcing fibres and appear to agree reasonably well with the moduli of the same composites in tension. The Thornel 50 data are an average of data from two matrix types, a modified ERL 2256 epoxy and NASA Resin 2.[8] A slightly higher modulus was reported for the latter at both 295 K and 77 K.

Composite interlaminar shear strength

Interlaminar shear strength is the resistance to failure between layers in a layered laminate along the plane of their interface. Interlaminar shear is sometimes measured by the guillotine method, in which shear is forced by the imposition of opposing but offset cuts across the width of a flat tensile specimen. Alternatively, the short-beam method may be used. Here, the specimen resembles a flat flexural specimen but is proportioned to fail by shear on the central layers of the composite. The guillotine method is reputed to produce less scatter. However, the values obtained are usually higher than those obtained with the short-beam method. The latter method is the most widely used. A modification of the short-beam test is used with filament-wound NOL ring specimens. Here, a short section of the

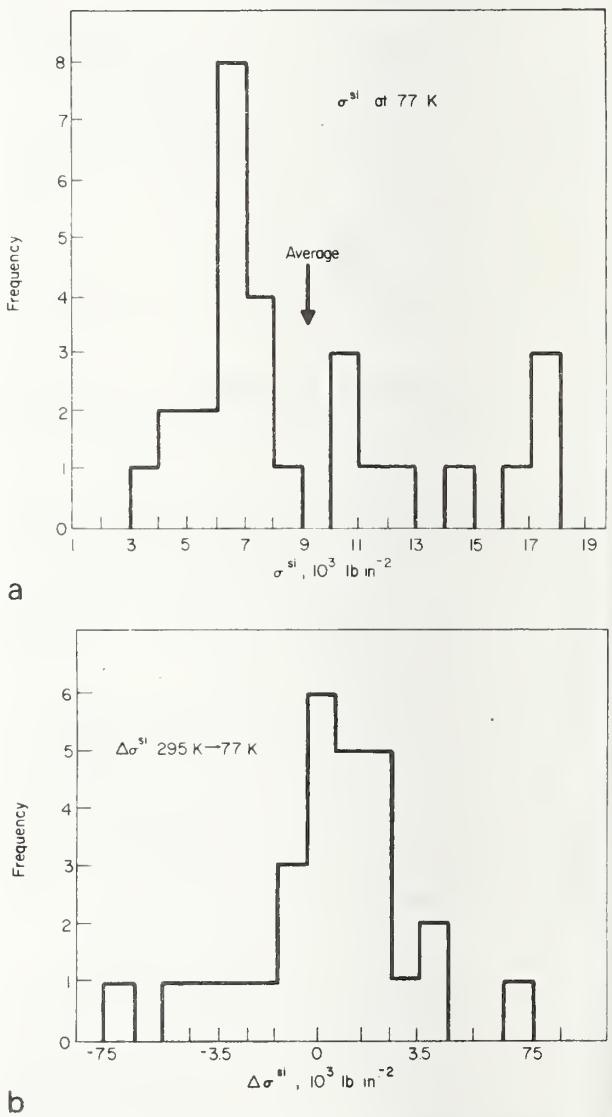

Fig.12 Histograms illustrating the reported range; of longitudinal interlaminar shear strength, σ^{si}
a — as reported for HT-S/X-904 graphite -epoxy at 77 K and
b — the reported changes in interlaminar shear strength in the same composite upon cooling from 295 K to 77 K

ring (concave downward) is substituted for the flat specimen. Results of the NOL segment and the flat short-beam tests are not equivalent.

A wide range of interlaminar shear strength values may be obtained with a single composite type. Fig.12a is a frequency histogram illustrating the range of longitudinal interlaminar shear strength reported in the literature for the graphite-reinforced composite HT-S/X-904 at 77 K. The substantial amount of data available for this composite reflects a comprehensive study of the effect of processing variables by Maximovich and Scheck.[12] These data suggest that the maximum interlaminar shear strength obtainable with this type composite is on the order of 17–18 x 10^3 lb in^{-2} (117–124 MPa).

The data of Maximovich and Scheck may be analysed further to determine what this relatively large body of data can tell statistically about the temperature dependence of interlaminar shear strength. From the frequency histogram of Fig.12b, we observe that the reported change in this parameter upon cooling from 295 K to 77 K approximates a normal distribution around zero change, suggesting that interlaminar shear strength is relatively independent of temperature for this composite over this temperature range. However, a more detailed look at the data shows that those composites at the high end of the strength range increased their interlaminar shear strength by about 4 000 lb in^{-2} (27 MPa) between 295 K and 77 K, suggesting that the temperature dependence is affected by composite quality.

Cryogenic interlaminar shear strength data have been published for other graphite-epoxy composites and for boron-epoxy, PRD 49-epoxy, and for boron-aluminium.[8,10,13,47,58] However, available data are insufficient for statistical examination. One finds that the reported 77 K interlaminar shear strengths for graphite-epoxy composites made with ten fibre types other than HT-S range from about 4–18 x 10^3 lb in^{-2} (27–124 MPa), that is, covering about the same range covered by the HT-S data of Fig.12a.

Somewhat surprisingly, available data on boron-epoxy [13,58] and boron-aluminium [13] composites suggest that the maximum interlaminar shear strengths of these composites are almost the same as for the best of the graphite-epoxy composites, that is, about 18 x 10^3 lb in^{-2} (124 MPa) at 77 K with about a 4000 lb in^{-2} (27 MPa) increase between 295 K and 77 K.

The only data on the interlaminar shear strength of PRD 49-epoxy composites are those of Hoggatt [59,60] who reported NOL-ring segment values of approximately 400 lb in^{-2} (27 MPa) in both ERLB 4617 and NASA Resin 2 matrices. Values obtained with the latter of these were found to be consistently higher by 40–70%. Very little temperature dependence was observed. It is perhaps noteworthy that the highest shear strengths reported for the graphite-epoxy composites, 21 x 10^6 lb in^{-2} (145 MPa), was also obtained with NASA Resin 2 epoxy.[10]

Composite bearing strength

The only data found in the literature on the temperature dependence of bearing properties of advanced composites in the cryogenic range were published by Hertz et al [13] for boron and Borsic-reinforced 6061 aluminium, including the steel and titanium-reinforced hybrids. These data, appearing on Fig.13, are for bearing strength in the unaxial longitudinal direction, that is, the stress required for bearing pull-out, rather than the more conventional bearing yield strength. The data on Fig.13 refer to material hole-to-free surface dimensions two and four times the diameter of a No 10 steel pin (~ 4.8 mm). An increase in bearing strength with decreasing temperature is observed for both conventional boron and Borsic-reinforced materials, the effect being more pronounced in the 4D tests. The Borsic-steel-aluminium hybrid performed much like the conventional materials, while the Borsic-titanium-aluminium hybrid performed somewhat erratically, although the highest strengths were developed with this latter composite.

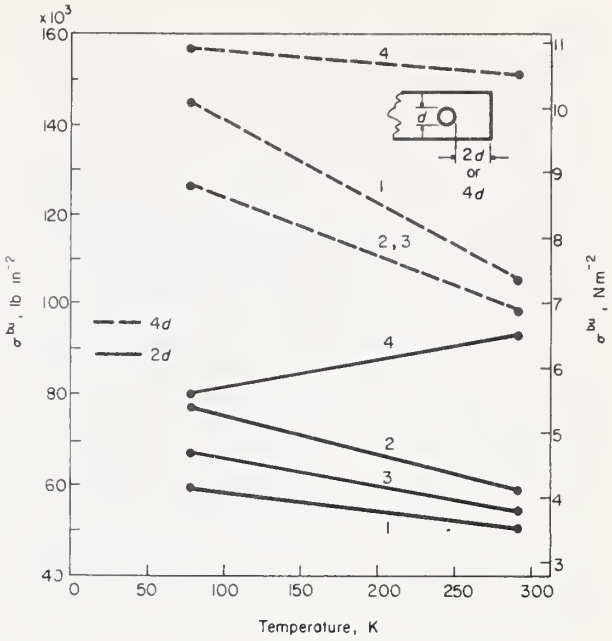

Fig.13 Ultimate bearing strength, σ^{bu}, of boron-aluminium composites, uniaxial longitudinal direction
1 – 4.2 mil Borsic-aluminium (6061); 2 – 5.6 mil Boron-aluminium (6061); 3 – 4.2 mil Borsic-steel-aluminium (6061); 4 – 4.2 mil Borsic-titanium-aluminium (6061) (all reference 13)

Dynamic mechanical properties

Composite fatigue

The only available data on the temperature dependence of the fatigue properties of advanced composites were generated during cyclic pressure testing of filament-wound pressure vessels. As the composites in these vessels were cross plied and subjected to biaxial stressing, the data are of value only in a comparative sense.

Hansom [45] has studied the cyclic fatigue perfermance of pressure vessels overwrapped with Thornel 50 graphite fibre using an ERL 2256/ZZL 0820 epoxy resin. The fatigue life at 77 K was found to be similar to that at 295 K, with 90% of the relevant single-cycle strength being retained after 10 000 cycles. This compares to a retention of only about 45% of the single-cycle strength for glass-fibre reinforced vessels. Hanson concluded that, on the basis of specific strength, graphite-fibre reinforced vessels would have fatigue performance superior to that of glass-fibre reinforced vessels after only 80 cycles.

Alfring et al [20] have reported cryogenic cyclic fatigue data on pressure vessels filament-wound with 4 mil boron in a Polaris-resin matrix. Polaris resin consists of Epon 828/Epon 1031/NMA/BDMA in proportions 50/50/90/0.55 pbw. Commercial designations are E-787 and 58–68R. The results were again reported to be independent of temperature (down to 20 K). However, the fatigue life of the boron-reinforced vessels was found to be relatively low, with residual strengths falling to 40–50% of single-cycle values after 10 000 cycles. This is about the same as for glass reinforcement.

These results suggest that graphite may be superior to boron as a reinforcement fibre for composite structures subject to fatigue at cryogenic temperatures. However, these data must be considered very tentative in view of the aforementioned tendency for the 4 mil boron fibre to split longitudinally when subjected to transverse stresses such as are present in biaxially-loaded pressure vessels. The fatigue performance at cryogenic temperatures of composites reinforced with 5.6 mil boron fibre should be substantially better than with the 4 mil fibre, if fibre splitting is a factor in the smaller diameter fibre.

Composite impact strength

Few data were available on the impact strength of advanced composites at cryogenic temperatures. The Advanced Composites Design Guide [124] includes some unpublished data on the Charpy V-notch impact values of commercial 5505–4 boron-epoxy material tested transverse to the uniaxial longitudinal direction. These data indicate a slight increase in impact strength from 22.8 ft lb in^{-1} (121.7 N m m^{-1}) at 295 K to 27.0 ft lb in^{-1} (144 N m m^{-1}) at 20 K Concomitantly, a slight decrease from 46.3 to 39.5 ft lb in^{-1} (247 to 211 N m m^{-1}) was reported for unnotched specimens over this temperature range. The notched/unnotched ratios of about 0.49 at 295 K and about 0.68 at 20 K indicate some notch sensitivity. Sumner and Davis [7] have reported a 12 ft lb in^{-1} (64 Nmm^{-1}) Charpy V-notch strength at 295 K for 25 v/o stainless steel wire reinforced 2024 aluminium, this value increasing to 18 ft lb in^{-1} (96 N m m^{-1}) at 77 K. Cryogenic impact strength data were not available for the other types of advanced composites. However, room temperature data indicate that the graphite-reinforced composites have substantially lower impact strengths than boron-reinforced types. There is no *a priori* reason to expect this relationship to change at cryogenic temperatures. Such impact strengths are substantially lower than those discussed in Part 1 for glass-reinforcement, where notched values transverse to the uniaxial longitudinal direction were seen to range from 67–162 ft lb in^{-1} (357–865 N m m^{-1}) at 77 K.[4] The critical factor has been identified as the stress-strain behaviour of the fibre reinforcement, higher impact values being associated with higher failure strains of the fibre whenever tests are made in the longitudinal (cross-fibre fracture) mode.[125,127]

Impact strengths of uniaxial composites tested in the transverse direction (anvil impact parallel to the fibres) are essentially matrix controlled. Since composite structures are usually of crossply construction and subjected to complex stresses, an improvement in the impact strength of the matrix offers the possibility of an overall improvement of composite toughness. Larsen [9] has reported efforts to improve

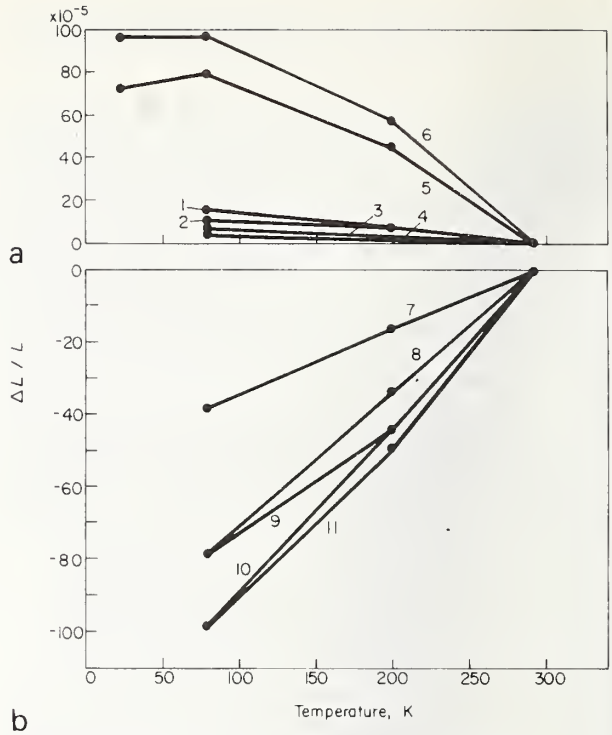

Fig.14 Longitudinal thermal expansion, $\Delta L/L$, of uniaxial advanced composites
1 – Thornel 75/ERLB 4617 [51]; 2 – GY-70/X-904 [13]; 3 – Fibrafloy 300/X-904 [13]; 4 – HT-S/X-904 [13]; 5 – PRD49–1/ERLA 4617 [59,60]; 6 – PRD49-I/NASA Resin 2 [59,60]; 7 – boron/epoxy SP-272; 8 – 5.6 mil boron/alumininium 6061; 9 – 4.2 mil Borsic-titanium-aluminium 6061; 10 – 4.2 mil Borsic-steel-aluminium (6061); 11 – 4.2 mil Borsic/aluminium (6061) (all reference 13)

the impact properties of crossplied HT-S/epoxy materials at cryogenic temperatures by addition of elastomeric components to the matrix. Results of this work were reported in terms of energy density, that is, the area under the force-deflection curve, using a cleavage-type specimen. This work showed that some improvement was indeed possible with CBTN-modified ERLB 4617 epoxy. However, the benefit gained was negated by a significant lowering of the room temperature impact properties and by unpredictable performance at cryogenic temperatures. Larsen concluded that improved overall cryogenic properties would be obtained by use of the NASA Resin 2 epoxy formulation with graphite-reinforced composites.

It appears at this time that substantial improvement of impact strength of the advanced composites will require development of hybrids, possibly combining glass with the advanced fibres.

Thermal properties

Composite thermal expansion and contraction

Unlike the glass-reinforced composites, some advanced-fibre composites expand in the fibre direction when cooled to cryogenic temperatures. Available data for the temperature dependence of dimensional changes in the uniaxial longitudinal direction are summarized in Fig.14, while comparable data for the uniaxial transverse direction appear in Fig.15.

The graphite-reinforced composites display a very small longitudinal expansion on cooling, slightly larger expansions being reported for the high modulus Thornel 75 and GY-70 fibre composites than for composites made with the medium-modulus Fibralloy 300 and the low-modulus HT-S fibres. The PRD 49 (Kevlar 49) composites undergo a comparatively large longitudinal expansion on cooling, reportedly reaching a maximum of about $8-10 \times 10^{-4}$ at about 77 K.[59,60] Slightly larger expansion was reported with a NASA Resin 2 matrix than with ERLA 4617. The other advanced composites undergo linear contraction on cooling. The least longitudinal contraction was reported for the commercial SP-272 boron-epoxy product, while boron-aluminium undergoes the largest contraction. The matrix contraction properties appear to be dominating in the latter composites, as relatively little difference is seen among the four variants, including the hybrids. The 5.6 mil composite displays a slightly lower contraction than does the 4 mil product. The longitudinal thermal contractions of these boron-aluminium composites are about 25% of that of an unreinforced 6061 aluminium alloy.

Dimensional changes in the transverse direction are strongly influenced by the matrix: all advanced composites showing contraction in this direction on cooling. These contractions are large compared to changes observed in the fibre direction, as witnessed by the necessity to change the ordinate scale on Fig.15. The data indicate that boron-epoxy composites have the least transverse contraction of the group, yet even this relatively low value is three times larger than its longitudinal change. The graphite-reinforced composites appear to undergo about twice the transverse thermal contraction of the boron-reinforced composites, reflecting the lesser constraint provided in this direction by the small graphite fibres. A slightly higher transverse contraction is reported for the high-modulus GY-70/X-904 composite than for the low modulus HT-S/X-904 material. However, such a small difference could easily be accounted for by variations in fibre volume fraction. The conventional boron/6061 aluminium composites have the next largest transverse contraction. By comparison with the contraction of unreinforced 6061 alloy (dashed curve), it is seen that the transverse contraction of the boron-aluminium composite is almost completely matrix dominated. No significant difference in thermal contraction were reported for 4.2 mil Borsic and 5.6 mil boron fibre composites.

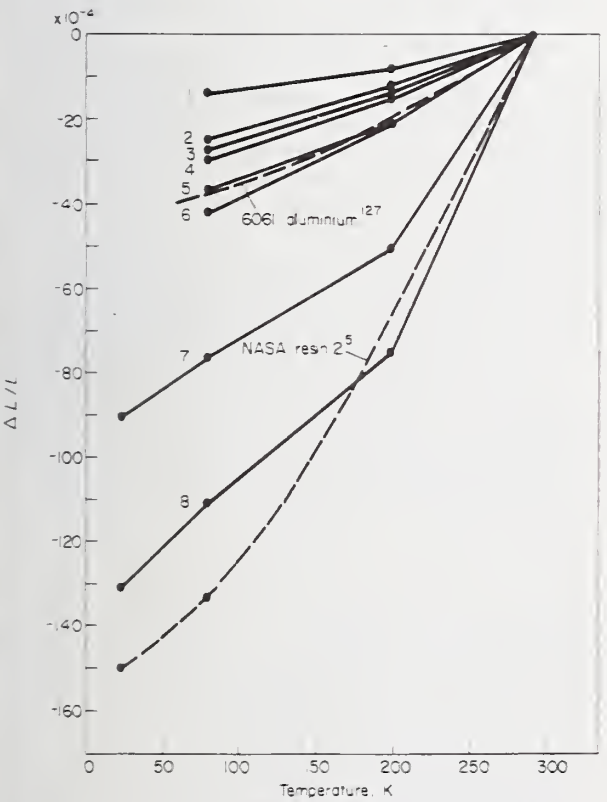

Fig.15 Transverse thermal expansion, $\Delta L/L$, of uniaxial advanced composites
1 — boron/epoxy (SP-272) [13]; 2 — Fibralloy 300/ERLA 4617; HT-S/X-904 [13]; 3 — 4.2 mil Borsic-titanium/aluminium 6061 [13]; 4 — GY-70/X-904 [13]; 5 — boron/aluminium 6061 [13]; 6 — 4.2 mil Borsic-steel/aluminium (6061) [13]; 7 — PRD 49-I/ERLA 4617 [59,60]

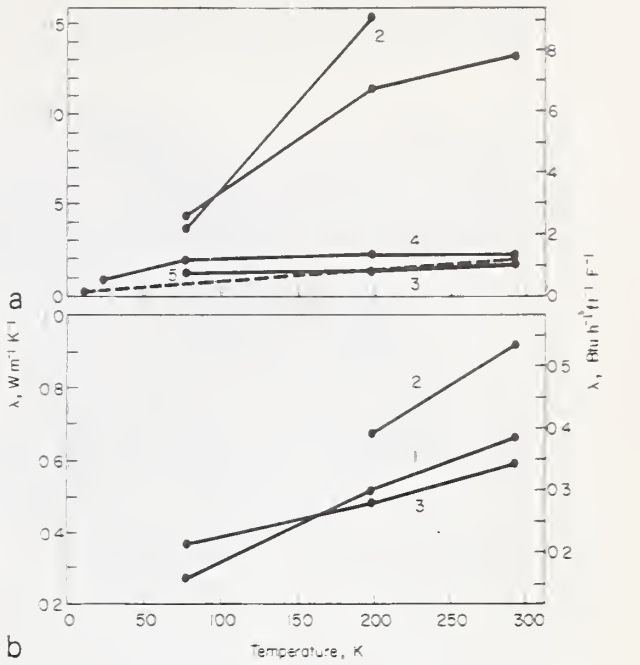

Fig. 16 Thermal conductivities, λ, of advanced composites
a — Uniaxial longitudial; 1 — HTS/X-904 [13]; 2 — Thornel 50-Polaris [38]; 3 — B-epoxy, SP-272 [13]; 4 — B-epoxy, 4.0 Boron-Polaris [18]; 5 — PRD 49-epoxy [61]
b — Unixial transverse; 1 — HT-5/X-904 [13]; 2 — Thornel 50 — Polaris[38]; 3 — B-epoxy, SP-272 [13]

The PRD 49-epoxy composites undergo the largest transverse thermal contraction. Comparing the temperature dependence of PRD 49—I/NASA Resin 2 (curve 8) with that reported by Soffer and Molho [5] for NASA Resin 2 alone (dashed curve), indicates that the matrix is also dominating the transverse dimensional changes in this composite. The PRD 49 fibres do not offer appreciable restraint to transverse contraction of the matrix because, as seen in Fig.14, this fibre expands significantly in the longitudinal direction during cooling. Of necessity, this is accompanied by significant transverse fibre contraction. Cooling to cryogenic temperatures would be expected to produce sizable interfacial shear forces between the PRD 49 fibre and matrix, with lesser forces normal to the fibres.

Composite thermal conductivity

Few data were available on the temperature dependence of uniaxial longitudinal and uniaxial transverse thermal conductivity of advanced composites. Those which were available are plotted in Fig.16. When considering these data, the

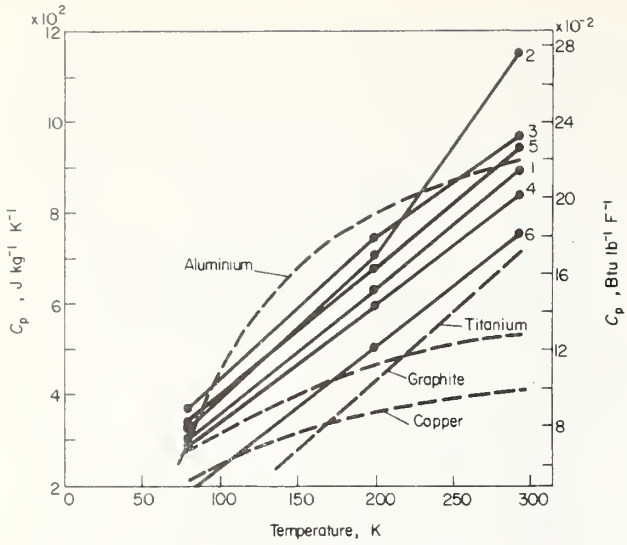

Fig.17 Specific heat, C_p, of advanced composites
1 — HT-S/X 904, GY-70/X 904 [13]; 2 — B-epoxy (SP-292) [13]; 3 — boron/6061 aluminium [13]; 4 — Borsic-titanium/aluminium [13]; 5 — Borsic-steel/aluminium [13]; 6 — graphite/phenolic [15]

reader should be aware of the difficulties and potential sources of error in determining thermal conductivity within the cryogenic range. The comments made in Part 1 of this paper on this subject apply equally well here. Furthermore, the volume fraction of fibre will influence the conductivities, particularly in graphite-reinforced composites. For these reasons, the data on Fig.16 should be considered as only indicating trends.

The graphite-reinforced composites have relatively high thermal conductivities in the fibre direction, reflecting relatively high conductivity of the graphite fibres compared to epoxy. Longitudinal conductivity in these materials is highly temperature dependent. The boron-reinforced composites have much lower conductivities than do the graphite-reinforced composites in the fibre direction and show a comparatively small temperature dependence of thermal conductivity. Data were not available for boron-reinforced aluminium; however, the thermal conductivity of such materials will certainly be much higher than that of a polymeric-matrix composite. The conductivity should be approximately, half that of unreinforced aluminium in a typical 50 volume % boron-aluminium composite. Transverse thermal conductivities are matrix dominated and very low for both the graphite and boron-reinforced epoxy materials.

The only available data for PRD 49 indicate a longitudinal thermal conductivity approximately the same as that for boron-epoxy within the cryogenic range.

These data suffice to show that the thermal conductivities of the epoxy-matrix advanced composites, particularly boron-reinforced, are low enough to make them attractive for cryogenic structural components.

Composite specific heat

Fig.17 shows the specific heat of the advanced composites to be similar to those of the glass-reinforced composites discussed in Part 1 of this paper. Again, an almost linear temperature dependence of C_p is observed from 295 K to 77 K. As a group, the specific heats of the composites are slightly lower than that of aluminium for much of the region between 295 K and 77 K, but substantially higher than that for copper and most other metals. The temperature dependence of C_p for aluminium, copper and titanium are included on Fig.17 for comparative purposes.

The highest specific heat at cryogenic temperatures was reported for boron-aluminium, the aluminium matrix undoubtedly contributing significantly to this relatively high value. The depicted curve is the average of data reported by Hertz et al [13] for 4.2 mil Borsic/6061 and 5.6 mil boron/6061. Slightly higher values were reported at 295 K and 200 K for the larger filament size, falling to slightly lower at 77 K. The data indicate that the Borsic-aluminium hybrids had slightly lower specific heats, probably reflecting the contributions from the steel and titanium reinforcements. The specific heat of the boron-epoxy composite lies between that of the boron-aluminium and the graphite-epoxy. The specific heat of the latter has undoubtedly been lowered by the graphite which, as shown by the dashed curve on Fig.17, has itself a relatively low specific heat.

The data indicate that boron-epoxy has a comparatively high specific heat at room temperature. This is not unreasonable, as boron has a room temperature specific heat of about 12.9 x 10^2 J kg^{-1} K^{-1}. No cryogenic specific heat data were available for boron or epoxy; however, the composite data suggest a rapidly decreasing value of C_p for boron as temperature decreases, while indicating that the specific heat of epoxy probably lies between the curves for boron-epoxy and graphite-epoxy.

Comments on advanced composites

The purpose of this review is to give the reader an understanding of the present state of knowledge as to the magnitude and temperature dependence of the properties of advanced fibre composites at cryogenic temperatures. It is apparent that present knowledge is incomplete in many respects; nevertheless, the available data justify considerable optimism as to the future applicability of these materials as structural components operating at cryogenic temperatures.

Available data indicate that commercial state-of-the-art boron-reinforced epoxy and aluminium perform well at cryogenic temperatures. The high tensile and compressive strengths and elastic moduli of these materials remain constant or improve as the temperature is lowered. Equally impressive is the relatively small scatter in the data, suggesting a high degree of reliability for components made from boron-reinforced composites. The data suggest that the commercial products may be used effectively at cryogenic temperatures without optimization of the composite matrix.

Although actual data are not available, boron-aluminium composites are certain to have a much higher thermal conductivity than any polymer-matrix composite (approximately half that of the unreinforced alloy). This is a distinct disadvantage in many cryogenic applications. On the other hand, the transverse strength and modulus of boron-aluminium is much higher than that of polymer-matrix composites. The latter is a distinct advantage of metal-matrix composites, simplifying composite design and increasing component reliability.

Available data on the cryogenic performance of the graphite-reinforced epoxy class of composites are less convincing.

These materials can be produced with moduli higher than those obtainable with boron-reinforced materials. Graphite-epoxies have the highest thermal stability of any composite class, which is an advantage for many cryogenic applications. However, the ultimate tensile strengths of the graphite-epoxies are substantially lower than for composites with boron reinforcement, and the strength tends to decrease upon cooling to cryogenic temperatures. Mechanical property test results are frequently unpredictable and contradictory. It is not at present known how much of the erratic behaviour is due to problems in testing and how much is an inherent characteristic of the material. Certainly, the overall performance of graphite-fibre overwrapped pressure vessels reported by Larsen and Simon [10] was much better than would have been predicted from their basic test data. We therefore conclude that graphite-reinforced composites have potential for structural use at cryogenic temperatures, in particular, for applications requiring dimensional stability. However, further development and testing are required.

PRD 49 (Kevlar 49)-reinforced epoxies also appear promising for cryogenic applications, due to the relatively low cost of the fibre and the improved modulus compared to glass. However, present data on this material are minimal, and further investigation must be undertaken before this material can be applied with confidence in a cryogenic environment. PRD 49 is unusual in that it undergoes a signficant expansion in the fibre direction during cooling to cryogenic temperatures. Large residual stresses between the fibre and the epoxy matrix might be expected to adversely affect the mechanical properties of composites made with this material. Nevertheless, the work of Hoggatt [59,60] has shown that, with proper design, PRD 49-epoxy composites can be used to good advantage in some cryogenic applications. As no compressive strength data were available at cryogenic temperatures, the potential user should investigate this parameter in applications where compressive loading is a factor.

In contrast to the boron-reinforced materials, the available data suggest that both graphite and PRD 49-reinforced composites may benefit from matrix optimization when used at cryogenic temperatures. Larsen and Simon [10] have recommended NASA Resin 2 for both uniaxial and crossply graphite-reinforced composites. The work of Hoggatt suggests that this type of matrix is also satisfactory for PRD 49 reinforcement.[59,60] When considering the use of NASA Resin 2, the reader should be aware that this resin has been optimized for cryogenic use by the addition of flexibilizers, which significantly reduce the strength at elevated temperatures. In particular, care must be taken to properly support components made with this resin whenever elevated temperature baking of a component is required.

The foregoing is not intended to imply that the NASA Resin 2 formulation is clearly the best resin for all cryogenic applications. Composite manufacturers may well recommend other types of epoxies for cryogenic applications. The present report is not intended to be prejudicial to such recommendations. However, the purchaser is advised to request documentation that the recommended resin has shown itself to be suitable for the intended cryogenic application. In particular, the suitability of various resins for crossply composites subjected to fatigue loading under cryogenic conditions has not been adequately investigated.

Summary of primary property trends in uniaxial advanced composites upon cooling to cryogenic temperatures

Tensile strength

Boron-epoxy and boron-aluminium show little temperature dependence of strength. The same appears to be true for PRD 49 (Kevlar 49)-epoxy, although data are minimal. The graphite-epoxies tend toward decreased strength on cooling, 77 K values being of the order of 20×10^3 lb in^{-2} (138 MPa) lower than at room temperature.

Tensile modulus

Boron-epoxy, boron-aluminium, and graphite-epoxy composites appear to retain their room-temperature moduli when cooled to 77 K. Minimal available data indicate that PRD 49 (Kevlar 49)-epoxy composites undergo a substantial modulus increase on cooling below 77 K.

Compressive strength

Compressive strengths of the advanced composites tend to either increase (boron-epoxy, graphite-epoxy) or to remain essentially unchanged (boron-aluminium) during cooling to 77 K. Compressive strength data were not available for PRD 49 (Kevlar 49)-epoxy composites.

Compressive modulus

Compressive moduli generally remain unchanged upon cooling to cryogenic temperatures, except for a small moduli increase reported for boron-epoxy. Data were not available for PRD 49 (Kevlar 49)-epoxy.

Ultimate tensile strain

Available data indicate a small (5–15%) decrease in longitudinal strain at failure on cooling boron-aluminium and graphite-epoxy to 77 K; the latter being the more temperature sensitive. Transverse failure strain appears almost independent of temperature in these composites. Data were not available for PRD 49 (Kevlar 49) or boron-epoxy.

In-plane shear strength and modulus

Insufficient data are available to indicate trends in these properties. One reference cited about a 14% drop in shear strength, concomitant with about a 50% shear modulus increase, for a graphite-epoxy composite upon cooling to 77 K; however, variations in fibre type and matrix composition will undoubtedly affect the temperature sensitivity of these properties. No data were available for other advanced composites.

Thermal expansion and contraction

Graphite-epoxy is the most dimensionally stable of the advanced composites, undergoing a very slight expansion longitudinally (fibre direction) and moderate transverse contraction on cooling. Boron-epoxy is the next most stable, showing moderate contraction in both directions on cooling. Boron-aluminium contracts about twice as much as boron-epoxy longitudinally; however, the contraction is only about 20% of that of the unreinforced metal. Transverse contraction of boron-aluminium is al-

most the same as that of the unreinforced metal. PRD 49 (Kevlar 49)-epoxy composites are the least dimensionally stable, expanding substantially in the longitudinal direction and contracting substantially in the transverse direction.

Thermal conductivity

Boron-epoxy and PRD 49 (Kevlar 49)-epoxy have substantially lower longitudinal thermal conductivity than graphite-epoxy composites. Differences in conductivity decrease as temperature decreases. Conductivity in the transverse direction is approximately the same for graphite and boron-epoxy, being much lower in this direction. Data were not available for PRD 49 (Kevlar 49)-epoxy and for boron-aluminium.

Specific heat

The specific heat of the advanced composites appear to be almost linear from 295 K to 77 K. As a group, the values are slightly lower than that of aluminium, but substantially above that of titanium or copper. The specific heat of boron-aluminium is slightly higher than that of boron-epoxy or graphite-epoxy. No data were available for PRD 49 (Kevlar 49)-epoxy.

The author thanks Dr R. P. Reed for consultation and review of the completed manuscript. Many thanks are also due to the NBS-NOAA library staff of the Boulder Laboratories for their assistance in retrieving the documents on which this work depended. This research was supported by the Advanced Research Projects Agency.

The use in this paper of trade names of specific products is essential to the proper understanding of the work presented. Their use in no way implies approval, endorsement or recommendation by NBS. Generic names have been substituted whenever it was possible to do so without sacrificing clarity. Manufacturers of the trade named materials are listed in the Appendix.

Appendix

The following materials are referred to in this report:

Fibres

Graphite

HT-S, HM-S	Courtaulds Ltd
HMG-25, HMG-50	Hitco Corp
Modmor I, II	Morganite Ltd
Thornel 25, 50	Union Carbide Corp
Samco 320	Samco Corp
Fibralloy 300	Monsanto Corp
GY-70	Celanese Corp

Boron

Borsic	Hamilton Standard Corp

Others

PRD 49 (Kevlar 49)	E. I. DuPont de Nemours, Inc

Resins

Epoxies

X-904, X-915	Fiberite Corp
ERL 2256, ERLB 4617	Union Carbide Plastics Co
Epon 828, 1031, 58-68R	Shell Chemical Corp, Plastics & Resin Div
E-350, E-787	US Polymeric Corp
Ciba 8183/137, 3002	Hercules Corp

Others

Skybond 703 (polyimide)	Monsanto Corp
HT-424 (epoxy-phenolic)	American Cyanimid

Flexibilizers, Hardeners

ZZL 0820	Union Carbide Plastics Co
Empol 1040	Emery Industries, Inc

DSA – dodecenyl succinic anhydride
BDMA – benzyldimethylamine
NMA – nadic methyl anhydride

Boron Composite Products

SP-272	Minnesota Mining & Manufacturing Co
5505	AVCO Corporation

Bibliography

Mechanical properties

Contract AF-33 (616)–8289

Contractor: Directorate of Materials and Processes, Aeronautical Systems Division, Air Force Systems Command, Weight-Patterson Air Force Base, Ohio

Research Facility: Narmco Research and Development, San Diego, California

1 **Brink, N. O.** 'Determination of the performance of plastic laminates under cryogenic temperatures' ASD TDR 62–794 (1962) (AD 288 944)

1.1 **Brink, N. O.** 'Mechanical behaviour of reinforced plastics at cryogenic temperatures', Technical Papers, 20th Annual Technical Conference, Society of Plastics Engineers, Vol 10, Section XV-2 (1964) 1–19

1.2 **Brink, N. O.** 'Mechanical behaviour of reinforced plastics at cryogenic temperatures, *Society of Plastics Engineers Journal* **20** (1964) 1123

1.3 **Brink, N. O.** 'Mechanical behaviour of reinforced plastics at cryogenic temperatures', Narmco Research and Development Report, Code No 105–4 (1964)

2 **Chamberlain, D. W., Lloyd, B. R., Tennant, R. L.** 'Determination of the performance of plastic laminates at cryogenic temperatures', ASD-TDR-62-794, Part II (1964) (N64–24212)

2.1 **Chamberlain, D. W.** 'Tensile fatigue testing at temperatures down to 20 K', *Advances in Cryogenic Engineering* 9 (1964) 131

2.2 **Chamberlain, D. W.** 'Mechanical properties testing of plastic laminate materials down to 20 K', *Advances in Cryogenic Engineering* **10** (1965) 117

Contract NAS 8–11070

Contractor: National Aeronautics and Space Administration, George C. Marshall Space Flight Center, Huntsville, Alabama

Research Facility: Goodyear Aerospace Corporation, Akron, Ohio

3 **Toth, L. W., Boller, T. J., Butcher, I. R., Kariotis, A. H., Yoder, F. D.** 'Programme for the evaluation of structural reinforced plastic materials at cryogenic temperatures', NASA CR-80061 (Final) (1966) (N67–12051)

3.1 **Toth, L. W.** 'Properties testing of reinforced plastic laminates through the 20 degree K range', Technical Papers, 20th Annual Technical Conference, Society of the Plastics Industry, Section 7-C (1965) 1

3.2 Toth, L. W., Kariotis, A.H. 'An assessment of test specimens and test techniques useful to the evaluation of structural reinforced plastic materials at cryogenic temperatures', *Advances in Cryogenic Engineering* 10 (1965) 126

3.3 Toth, L. W. 'Properties of glass-reinforced epoxy through the 20 K range', *Modern Plastics* 42 (1965) 123

3.4 Toth, L. W., Burkley, R. A. 'Mechanical response at cryogenic temperatures of selected reinforced plastic composite systems', Goodyear Aerospace Report GER-13169, Paper No 16, Seventieth Annual Meeting of the American Society for Testing and Materials (1967)

3.5 Toth, L. W., Boller, T. J., Kariotis, A. H., Yoder, F. D. 'Programme for the evaluation of structural reinforced plastic materials at cryogenic temperatures', NASA CR-64005 (1963–64) (N65–29724)

Contract NAS 3–6297

Contractor: National Aeronautics and Space Administration, Lewis Research Center, Cleveland, Ohio

Research Facility: Aerojet General Corporation, Azuza, California

4 Lewis, A., Bush, G. E. 'Improved cryogenic resin-glass filament mound composites', NASA CR-72163 (Final) (1967) (N67–31856)

4.1 Lewis, A., Bush, G. E., Creedon, J. 'Improved cryogenic resin glass filament-wound composites', NASA Interim Report CR-54867 (1966) (N66–28040)

Contract NAS 6–6287

Contractor: National Aeronautics and Space Administration, Research Center, Cleveland, Ohio

Research Facility: Aerojet General Corporation, Azuza, California

5 Soffer, L. M., Molho, R., 'Cryogenic resins for glass filament-wound composites', NASA CR-72114 (Final) (1967) (N67–25076)

5.1 Soffer, L. M., Molho, R., 'Mechanical properties of epoxy resins and glass epoxy composites at cryogenic temperatures', Cryogeni Properties of Polymers (J. L. Koenig (ed)] (Marcel Dekker, New York, 1968) 87 (Identical to NASA CR-84451, 1967, (N66-27217)

Contract FO4701-69-C-0059

Contractor: Space and Missiles Systems Organization, Air Force Systems Command, Los Angeles Air Force Station, Los Angeles, California

Research Facility: The Aerospace Corporation, El Segundo, California

6 Pepper, R. T., Rossi, R. E., Upp, U. W., Riley, W. E. 'Development of an aluminium-graphite composite'. SAMSO-TR-70-301 (1970) (AD 718 409)

6.1 Pepper, R. T., Upp, J. W., Rossi, R. C., Kendall, E. G. 'Aluminium graphite composites' SAMSO-TR-70-174 (1970) (AD 706 883). (Identical to *Metal lurgical Trans* 2 (1971) 117

6.2 Rossi, R. C., Pepper, R. T., Upp, J. W., Riley, W. C. 'Development of aluminium-graphite composites' *Ceramic Bull* 50 (1971) 484

Contract NAS 8–11508

Contractor: National Aeronautics and Space Administration, George C. Marshall Space Flight Center, Huntsville, Alabama

Research Facility: Harvey Engineering Laboratories, Torrance, California

7 Summer, E. V., Davis, L. W. 'Development of ultrahigh strength, low density aluminium sheet and plate composites', NASA CR-85863 (Final) (1966) (N6731181)

7.1 Davis, L. W. 'Composites at low temperature', Paper No. 15, Seventieth Annual Meeting of the American Society for Testing Materials (1967)

Contract NASA DPR C 10360-B

Contractor: National Aeronautics and Space Administration, Lewis Research Center, Cleveland, Ohio

Research Facility: Naval Ordnance Laboratory, Silver Springs, Maryland

8 Simon, R. A., Alfring, R. 'Properties of graphite fiber composites at cryogenic temperatures', NASA CR-72652 (NOLTR 69–183) (1970) Tasks I and II (AD 746 885)

9 Larsen, J. V. 'Properties of graphite fiber composites at cryogenic temperatures – effect of elastomeric additions to resin systems', NASA CR-72804 (NOLTR 70–195) (1971) Task III (AD 882 972)

10 Larsen, J. V., Simon, R. A. 'Carbon fiber composites for cryogenic filament-wound vessels', NASA CR-120899 (NOLTR 71–201) (1972) Tasks IV, V, and VI (N73–11553)

10.2 Larsen, J. W. 'Fracture energy of CBIN/epoxy-carbon fiber composites', Technical Papers, 26th Annual Technical, Conference, Society of the Plastics Industry, Section 10-D (1971)

Contract NAS 8–26198

Contractor: George C. Marshall Space Flight Center, Huntsville, Alabama

Research Facility: General Dynamics Convair, San Diego, California

11 Scheck, W. G. 'Development of design data for graphite reinforced epoxy and polyimide composites', NASA TN-D2970, Report No GDC-DBG-70-005, Final National Aeronautics and Space Administration. Marshall Space Flight Center, Alabama (1974)

12 Scheck, W. G. 'Development of design data for graphite reinforced epoxy and polyimide composites', Report No GDC-DBG70-005, General Dynamics Quarterly Report No 1 (1970) [see also Maximovich, M. and Scheck, W. G. Quarterly Report No 2, (1970)]

12.1 Stuckey, J. M., Scheck, W. G. 'Development of graphite/polyimide composites', National-Technical Conference, Society of Aerospace Material and Process Engineers, Vol 3 (1971) 717

Contract F33615–70–1442

Contractor: Air Force Materials Laboratory, Wright-Patterson Air Force Base, Ohio

Research Facility: General Dynamics/Convair, San Diego, California

13 Hertz, J., Christian, J. L., Varlas, M. 'Advanced composite applications for spacecraft and missiles, Phase 1 Final Report, Volume II: Material Development', AFML-TR 71–186, Vol 2 (1972) (AD 893 715L)

13.1 Forest, J. D., Fujimoto, A. F., Foelsch, G. F. 'Advanced composite applications for spacecraft and missiles. Phase 1 Final Report, Volume 1: Structural Development', AFML-TR-71-186, Vol 1, (1972)

13.2 Forest, J. D., Varlas, M. 'Advanced composite applications for spacecraft and missiles, Final Report, AFML-TR-72-278 (1973)

13.3 Christian, J. L., Campbell, M. D. 'Mechanical and physical properties of several advanced metal-matrix composite materials', *Advances in Cryogenic Engineering* 18 (1973) 175

2. Thermophysical properties

Contract AF-33 (657)-9160

Contractor: Air Force Materials Laboratory, Wright-Patterson Air Force Base, Ohio

Research Facility: General Dynamics/Astronautics, San Diego, California

The following reports are in a series entitled 'Thermophysical properties of plastic materials and composites to liquid hydrogen temperature (−423°F)'

14 **Haskins, J. F., Campbell, M. C., Hertz, J., Percy, J. L.** ML-TDR-64-33. Part 1 (1964) (AD 601 337)

15 **Campbell, M. D., Hertz, J., O'Barr, H. L., Haskins, J. F.** ML-TDR-64-33, Part 2 (1965) (X65−18921)

16 **Campbell, M. D., O'Barr, G. L., Haskins, J. F., Hertz, J.** ML-TDR-64-33, Part 3 (1965) (AD 468 155)

16.1 **Hertz, J., Haskins, J. F.** 'Thermal conductivity of reinfroced plastics at cryogenic temperatures', *Advances in Cryogenic Engineering* **10** (1965) 163

16.2 **Campbell, M. D.** 'Thermal expansion characteristics of some plastic materials and composites from room temperature to −253°C' *Advances in Cryogenic Engineering* **10** (1965) 154

16.3 **Campbell, M. D., Haskins, J. F., O'Barr, G. L., Hertz, J.** 'Thermophysical properties of reinforced plastics at cryogenic temperatures' *Journal of Spacecraft* **3** (1966) 596

(See also reference 13)

Contract F33615−73−C1388 (Work currently in progress)

Contractor: Air Force Materials Laboratory, Wright-Patterson Air Force Base, Ohio

Research Facility: General Dynamics/Convair, San Diego, California

17 **Forest, J. D., Schaeffer, W. H.** 'Advanced composite missile and space design data', General Dynamics Report GDCA-CHB72-001-1, Progress Report No 1 (1972)

18 **Forest J. D.** 'Advanced composite missile and space design data', General Dynamics Report GDCA-CHB72-001-2, Progress Report No 2 (1973)

3. General bibliography

19 **Aleck, B.** 'Fibreglass-overwrapped 2219−T87 aluminium alloy low-pressure cryogenic tankage', Society of Aerospace Material and Process Engineers National Technical Conference, Space Shuttle Materials, Vol 3 (1971) 131

20 **Alfring, R. J., Morris, E. E., Landes, R. E.** 'Cycle-testing of boron filament-wound tanks', NASA CR-72899, National Aeronautics and Space Administration, Lewis Research Center A (1971) (N71−38023)

21 **Barber, J. R.** 'Design and fabrication of shadow shield systems for thermal protection of cryogenic propellants', NASA CR-72595, National Aeronautics and Space Administration, Lewis Research Center, Cleveland, Ohio (1969) (N70−25098)

22 **Baucom, R. M.** 'Tensile behaviour of boron filament-reinforced epoxy rings and belts', NASA TN D-5053, Langley Research Center, Hampton, Virginia (1969) (N69−19918)

23 **Benton, W., Carr, R., Cohen, A., Gustafson, G., Lankton, C. Zeldin, B.** 'Propellant storability in space', RPL-TDR-64−75 (Final), Air Force Systems Command, Edwards Air Force Base, California, (1964) (AD 603 215)

24 **Brechna, H.** 'Superconducting magnets for high energy physics applications', Proc ICEC1 (Heywood Temple Industrial Publishers Ltd, London, 1968) 119 (CFSC1 N67−36009)

25 **Bullard, B. R.** 'Cryogenic tank support evaluation', NASA CR-72546, NASA Lewis Research Center, Cleveland, Ohio (1969) (N70−13085)

26 **Campbell, M. D.** 'Development of thermal expansion capabilities and the investigation of expansion characteristics of space vehicle materials', General Dynamics/Astronautics Report ERR-AN-251 (1962)

27 **Campbell, M. D.** 'Development of the thermal expansion capabilities and the investigation of the thermal expansion characteristics of space vehicle materials (II)', General Dynamics/Astronautics Report ERR-AN-450 (1963)

28 **Caren, R. P., Coston, R. M., Holmes, A. M. C., Dubus, F.** 'Low-temperature tensile, thermal contraction, and gaseous hydrogen permeability data on hydrogen-vapor barrier materials', *Advances in Cryogenic Engineering* **10** (1965) 171

29 **Chiao, T. T., Moore, R. L.** 'Tensile properties of PRD-49 fiber in epoxy matrix', *J Comp Mat* 6 (1972) 547

30 **Cooper, G. A., Sillwood, J. M.** 'Multiple fracture in a steel reinforced epoxy resin composite', *J Mat Sci* 7 (1972) 325

31 **Darwish, F., Tetelman, A. S.** 'Mechanical behaviour of SiO_2-epoxy composite', Conference Proceedings No 63, Advisory Group for Aerospace Research and Development, Symposium on Composite Materials, Paper No 9, Paris, April 1970 (Hartford House, London)

32 **Davis, J. G., Zender, G. W.** 'Mechanical behaviour of carbon fiber reinforced-epoxy composites', 12th National Symposium Society of Aerospace Material and Process Engineers, Vol 12 (1967) section AC-10

33 **Dervy, A. J.** 'Reinforced plastics of high strength/weight ratio for space applications', Technical Papers, 17th Annual Technical Conference, Society of the Plastics Industry section 7-D, 1 (1962)

34 **Fontana, M. G., Bishop, S. M., Spretnak, J. W.** 'Investigation of mechanical properties and physical metallurgy of aircraft alloys at very low temperatures, Part 5 − Mechanical properties of metals and a plastic laminate at low temperatures', AF Technical Report 5662, Part 5, Materials Laboratory, Wright-Patterson Air Force Base, Ohio, (1953) (AD 27726)

35 **Freeman, S. M.** 'Properties of vapour barriers, adhesives and foams at cryogenic and elevated temperatures', Lockheed Aircraft Corporation Report ER-5687 (1962)

36 **Freeman, W. T., Campbell, M. D.** 'Thermal expansion characteristics of graphite reinforced composite materials', Composite Materials: Testing and Design (Second Conference), ASTM STP 497, American Society for Testing and Materials (1972) 121

37 **Funk, C. W., Dixon, C. E.** 'Cryogenic radiation damage in structural polymers', *Trans of the American Nuclear Society* 9 (1966) 406

38 **Gille, J. P.** 'Development of advanced materials for integrated tank insulation system for the long term storage of cryogens in space', NASA CR-102570 (Final), National Aeronautics and Space Administration, Huntsville, Alabama (1969) (N70−23348)

39 **Gleich, D.** 'Development of a filament-overwrapped cryoformed metal pressure vessel', NASA CR-72753, National Aeronautics and Space Administration, Lewis Research Center, Cleveland, Ohio (1971) (N71−22401)

40 **Gray, P. D., Cornelius, G. K., O'Donnell, J. D., Howard, W. W.** 'Rockets in space environment, Volume 1: The experimental programme', RID-TDR-63-1050, Aerojet General Corporation (1963) (N63−20999)

41 **Greer, F.** 'Flexural properties of Conolon 506 at room temperature −320°F and −423°F', Convair/Astronautics Report 55E 522 J (1971) (AD 677 565)

42 **Hale, D. V.** 'Study of thermal conductivity requirements: MSFC 20−inch and 105−inch cryogenic tank analyses', NASA CR-61288, National Aeronautics and Space Administration, Marshall Space Flight Center, Alabama (1969) (N69−35811)

43 **Hall, J.** 'Cryogenic tensile tests − epoxy fiberglass', Douglas Aircraft Company Report MP 1348 (1961)

44 **Hanson, M. P.** 'Effects of temperature and creep characteristics of PRD-49 fiber epoxy composites', NASA TN D-7120, National Aeronautics and Space Administration, Lewis Research Center, Cleveland, Ohio (1972) (N73−12607)

45 **Hanson, M. P.** 'Tensile and cyclic fatigue properties of graphite filament-wound pressure vessels at ambient and cryogenic temperatures', NASA TN D-5354, National Aeronautics and Space Administration, Lewis Research Center, Cleveland, Ohio (1969) (N69−31300) (identical to *SAMPE* **15**, 249)

46 **Hanson, M. P., Richards, H. T., Hickel, R. O.** 'Preliminary investigation of filament-wound glass-reinforced plastics and liners for cryogenic pressure vessels', NASA TN D-2741, National Aeronautics and Space Administration, Lewis Research Center, Cleveland, Ohio (1965)

47 **Hanson, M. P.** 'Glass-, boron-, and graphite-filament-wound resin composites and liners for cryogenic pressure vessels', NASA TN D-4412, National Aeronautics and Space Administration, Lewis Research Center, Cleveland, Ohio (1968) (identical to NASA TM X-52350, 1967)

48 Hanson, M. P. 'Static and dynamic fatigue behaviour of glass filament-wound pressure vessels at ambient and cryogenic temperatures'. NASA TN D-5807, National Aeronautics and Space Administration, Lewis Research Center, Cleveland, Ohio (1970) (CFSTI-CSCL-20 K)

49 Haskins, J. F., Hertz, J. 'Thermal conductivity testing of coast F-224-6 phenolic-fiberglass laminate', General Dynamics/Convair Report No AR-592-2-482 (1963)

50 Haskins, J. F., Hurlich, A. 'Measured values for the coefficients of linear expansion of Plycel 420 and Conolon 506 at low temperatures', Convair/Astronautics Report MRG-154 (1960)

51 Haylett, J. W., Rottmayer, E., Butcher, I. 'Advanced composite material study for millimeter wavelength antennas', Technical Report AFML-TR-71-205, Vol 1, Air Force Materials Laboratory, Wright-Patterson Air Force Base, Ohio (1971) (AD 893 368)

52 Haylett, C. E. 'Advanced composite material study for millimeter wavelength antennas, Volume II, Environmental Tests', AFML-TR-71-205-Vol 2, Air Force Materials Laboratory, Wright-Patterson Air Force Base, Ohio (1971) (AD 893 358 L)

53 Herring, H. W., Baucom, R. M., Pride, R. A. 'Research on boron filaments and boron reinforced composites', 10th National Symposium, Society of Aerospace Material and Process Engineers, Vol 10 (1966) B-21 to B-34

54 Hertz, J. 'Tensile testing of Conolon 506 at room and subzero temperatures', Convair/Astronautics Report MRG-120

55 Hertz, J. 'Tensile testing of Adlock 851, Adlock PG-LA and Adlock EG-11A-81A from −423°F to 78°F', Convair/Astronautics Report MRG 237 (1961)

56 Hertz, J. 'Investigation of potential low temperature insulations' General Dynamics/Astronautics Report GS/A-ERR-AN-668 (1964)

57 Hertz, J. 'The effect of cryogenic temperatures on the mechanical properties of reinforced plastic laminates', General Dynamics Report AR-592-1-415 (1963) (AD 405 170)

58 Hertz, J. 'Investigation into the high-temperature strength degradation of fiber-reinforced resin composite during ambient aging', General Dynamics/Convair Report No GDCA-DBG73-005 (Final Contract NAS 8-27435) (1973)

59 Hoggatt, J. T. 'Development of cryogenic PRD-49-1 filament-wound tanks', NASA CR-120835, National Aeronautics and Space Administration, Lewis Research Center, Cleveland, Ohio (1971) (N72-24941)

60 Hoggatt, J. T. 'High performance filament wound composites for pressure vessel applications', Society of Aerospace Material and Process Engineers National Technical Conference, Space Shuttle Materials, Vol 3 (1971) 157

61 Hust, J. G. 'Low temperature thermal conductivity of two fibre-epoxy composites' *Cryogenics* 15 (1975) 126

62 Johnston, H. L., Brooks, H. E. 'Impact strength of various metals at temperatures down to 20° absolute', Ohio State University Cryogenic Laboratory Report TR 264−17 (1952)

63 Keller, C. W. 'Fiberglass supports for cryogenic tanks', NASA CR-120937 (Final), National Aeronautics and Space Administration, Lewis Research Center, Cleveland, Ohio (1972) (N72-33564)

64 Kerlin, E. E., Smith, E. T. 'Measured effects of the various combinations of nuclear radiation, vacuum and cryotemperatures on engineering Materials: Biennial report', NASA CR-77772, National Aeronautics and Space Administration, George C. Marshall Space Flight Center, Huntsville, Alabama (1966) (N66-35963)

65 Kerlin, E. E., Smith, E. T. 'Measured effects of the various combinations of nuclear radiation, vacuum and cryotemperatures on engineering materials: Annual report', NASA CR-58830, National Aeronautics and Space Administration, George C. Marshall Space Flight Center, Huntsville, Alabama (1964) (N64-33043)

66 Keys, R. D., Kiefer, T. F., Schwartzberg, F. R. 'Cryogenic properties of high-strength glass-reinforced plastics'. *Advances in Cryogenic Engineering* 11 (1966) 470

67 Krause, D. R. 'Development of lightweight material composites to insulate cryogenic tanks for 30-day storage in outer space', NASA CR-123797, National Aeronautics and Space Administration, George C. Marshall Space Flight Center, Huntsville, Alabama (1972) (N72-30495)

68 Krause, D. R., Fredrickson, G. O., Klevatt, P. L. 'Effects of cyclincal environments on high-performance multi-layer insulation materials', Society of Aerospace Material and Process Engineers National Technical Conference, Space Shuttle Materials, Vol 3 (1971) 639

69 Lantz, R. B. 'Materials for filament wound cryogenic pressure vessels', 6th National Symposium, Society of Aerospace Materials and Process Engineers, Vol 2, Engineering Paper No 1750

70 Lavengood, R. E., Anderson, R. M. 'Matrix properties controlling torsional fatigue life of fiber reinforced composites', Technical Papers, 24th Annual Technical Conference, Society of the Plastics Industry, section 11-E (1969)

71 Levin, V. A., Naumenkov, P. G., Shchitov, M. V. 'Some properties of plastics at low temperatures', *Plasticheskia Massy* 11 (1966) 64

72 Luikov, A. V., Vasiliev, L. L., Shashkov, A. G. A method for the simultaneous determination of all thermal properties of poor heat conductors over the temperature range 80 to 500 K'. Proceedings Third American Society of Mechanical Engineers Symposium, Purdue University (1965) 314

73 Lyon, D. N., Parrish, W. R. 'Low temperature thermal conductivities of two high compressive strength materials', *Cryogenics* 7 (1967) 21

74 Maher, L. E. 'Some problems arising from the use of hydrogen-fuelled propulsion systems'. *J Royal Aeronautical Society* 68 (1964) 765

75 McKannon, E. C., Gause, R. L. 'Effects of nuclear radiation and cryogenic temperatures on non-metallic engineering materials', *J of Spacecraft* 2 (1965) 558

76 Morris, E. E. 'Glass-fiber-reinforced metallic tanks for cryogenic service', 12th National Symposium, Society of Aerospace Materials and Process Engineers, Vol 12 (1967) section AS-4 (also NASA CR-72224)

77 Morris, E. E. 'The performance of glass-filament-wound pressure vessels with metal liners at cryogenic temperatures' *J of Mat* 4 (1969) 970

78 Morris, E. E., Alfring, R. J. 'Cryogenic boron-filament-wound pressure vessels', Composite Materials: Testing and Design, ASTM STP 460, American Society for Testing and Materials (1969) 430

79 Morris, E. E., Landes, R. E. 'Cryogenic glass-filament-wound tank evaluation', NASA CR-72948 (Final), National Aeronautics and Space Administration, NASA Lewis Research Center, Cleveland, Ohio (1971) (N72-14696)

80 Mowers, R. E., Leib, J. H., Sherman, S. 'Programme of testing nonmetallic materials at cryogenic temperatures', Rocketdyne Corporation Report R-3498, Rocket Propulsion Laboratories, Edwards, California (1962) (AD 294 772)

81 Nadler, M. A., Yoshino, S. Y., Darms, F. J. 'Boron/epoxy support strut for non-integral cryogenic tankage', North American Rockwell Space Division Report SD 68−99501 (1969) (see also 15th National Symposium SAMPE April 1969 and North American Rockwell Report SD 995 2, 1968)

82 Nelson, L. F. 'Compressive strength of Conolon 506 at +75°F and − 320°F', Convair/Astronautics Report No 27E 1336 (1962)

83 Nelson, L. R. 'Mechanical properties of Adlock 851 at room temperature, 1000°, −320° and −423°F', Convair/Astronautics Report No 55E 812 (1961)

84 Nelson, P. T., Archer, J. S. 'Graphite reinforced plastic EHF antenna', TRW Systems Group, Redondo Beach, California Report No 99900−7128−RO−11 (1969)

85 Patten, P. M. 'Internal insulation liner alteration', Douglas Aircraft Company Report No SM 45975 (1964)

86 Perkins-Elmer Optical Group, Norwalk, Connecticut, Work-In-Progress on Contract No F33615−72−C−2033, Air Force Systems Command, Wright-Patterson Air Force Base, Ohio

87 Pink, E., Campbell, J. D. 'The effect of strain rate and temperature on the deformation behaviour of reinforced and unreinforced epoxy resin', Oxford University Department of Engineering Report No 1040/72, Oxford, England (1972) (N73−10568)

88 Pirgon, O., Wostenholm, G. H., Yates, B. 'Thermal expansion at elevated temperatures, IV. Carbon-fibre composites' *J Physics D: Appl Phys* 6 (1973) 309

89 Pride, R. A., Stein, B. A., Schmidt, F. W. 'Mechanical properties of polyimide-resin/glass-fiber laminates for various time, temperature and pressure exposures', Technical Papers, 23rd Annual Reinforced Plastics Technical and Management Conference, Washington, DC (1968) section 17−c, 1

90 **Ratcliffe, E. H.** 'Thermal conductivities of plastics with glass, asbestos and cellulasic fiber reinforcements', *Appl Mat Res* 5 (1966) 200
91 **Roseland, L. M.** 'Materials for cryogenic usage', Technical Papers, 21st Annual Technical Conference, Society of the Plastics Industry (1966) section 4–C, 1
92 **Roseland, L. M.** 'Investigation of structural properties at cryogenic temperatures of filament-wound pressure vessels containing both organic and glass filaments', Douglas Aircraft Corporation Report No SM-48409 (1966)
93 **Ross, J. E.** 'Fiberglass laminate – ultimate tensile and flexural strength tests at room temperature, −100°F and 320°F', Convair Astronautics Report No 7E 1687 (1959) (AD 830 230)
94 **Sanders, R. H., Weleff, W.** 'Final report on GTR-17 effects of radiation on organic materials irradiated in liquid hydrogen', Aerojet-General Corporation Report No RN-S-0317 (1967)
95 **Sanger, M. J., Molho, R., Howard, W. W.** 'Exploratory evaluation of filament-wound composites for tankage of rocket oxidizers and fuels', AFML-TR-65-381, Air Force Materials Laboratory, Weright-Patterson Air Force Base, Ohio (1966) (AD 477 455)
96 **Sanger, M. J., Reinhart, T. J.** 'Development of filament-wound tankage for rocket oxidizers and fuels', Technical Papers, 12th National Symposium, Society of Aerospace Material and Process Engineers (1967) section AS-7
97 **Sewell, J. J., Kuno, J. K.** 'Aerospace use of plastic hardware and thermal insulation', Technical Papers, 17th Annual Technical Conference, Society of the Plastics Industry (1962) section 7-A
98 **Shriver, C. B.** 'Design and fabrication of an internally insulated filament wound liquid hydrogen propellant tank', NASA CR-127, National Aeronautics and Space Administration, Washington DC (1964) (N65–10775)
99 **Soltysiak, D. J., Toth, J. M.** 'Static fatigue of fiber glass pressure vessels from ambient to cryogenic temperatures', Technical Papers, 22nd Annual Technical Conference, Society of the Plastics Industry (1967) section 14-E
100 **Speare, J. C.** 'Preliminary sizing of filament-wound RNS tanks', Report No TOR-0066 (5759–07)–13, Space and Missile Systems Organization, Air Force Systems Command, Los Angeles Air Force Station, Los Angeles, California (1970) (AD 872 626)
101 **Steinhauer, R. A.** 'Linear thermal expansion of 828CL 181 cloth laminate', Douglas Aircraft Company Report No MP 11 979 (1961)
102 **Stinnett, W. D.** 'Cryogenic tensile properties of selected materials', NASA CR-71751, AEC-NASA Space Nuclear Propulsion Office, Report No 2712 (1964) (N66–22816)
103 **Suezawa, Y., Hojo, H., Nakamura, K.** 'Impact characteristics of fiberglass reinforced plastics at low temperatures', *Kagaku Kogaku (Chemical Engineering, Japan)* 33 (1969) 1051
104 **Toth, J. M.** 'Barrier films for filament-wound fiberglass cryogenic vessels', *Advances in Cryogenic Engineering* 1 (1964) 537
105 **Toth, J. M., Soltysiak, D. J.** 'Investigation of smooth-bonded metal liners for glass fiber filament-wound pressure vessels', NASA CR-72165 (Final), National Aeronautics and Space Administration, Lewis Research Center, Cleveland, Ohio (1967) (N67–25070)
106 **Toth, J. M., Sherman, W. C., Soltysiak, D. J.** 'Investigation of smooth-bonded metal liners for glass fiber filament-wound pressure vessels', Douglas Missile and Space Systems Division Report No SM-49384, Quarterly Report No 3, Contract No NAS 3 6193, NASA Lewis Research Center, Cleveland, Ohio (1966)
107 **Toth, J. M., Sherman, W. C., Soltysiak, D. J.** 'Investigation of structural properties of fiber-glass filament-wound pressure vessels at cryogenic temperatures', NASA CR-54393, National Aeronautics and Space Administration, Lewis Research Center, Cleveland, Ohio (1965) (N65-35392)
108 **Toth, J. M., Barber, J. R.** 'Structural properties of glass-fiber filament-wound cryogenic pressure vessels', *Advances in Cryogenic Engineering* 10 (1965) 134
109 **Voloshenko-Klimovitskii, Yu. Ya., Belyaev, Yu, A., L'vof, B. S., Schpakovskaya, E. I.** 'Strength of cold-hardening GRPs based on PN-1 resin under impact tension at normal (20°C) and low (−196°C) temperatures', *Plasticheski Massy* 6 (1964) 39
110 **Voloshenki-Klimovitskii, Yu. Ya., Belyaev, Yu. A., Korenkov, Yu. A.** 'Impact tensile tests on glass-fibre reinforced plastics at normal and low temperatures', *Plasticheski Massy* No 5 (1963) 51
111 **Watson, J. F., Christian, J. L., Hertz, J.** 'Selection of materials for cryogenic applications in missiles and aerospace vehicles', Convair/Astronautics Report No MRG 132–1 (1960)
112 **Weleff, W.** 'Effect of nuclear radiation and liquid hydrogen on mechanical properties of three phenolic materials', *Advances in Cryogenic Engineering* 11 (1966) 486
113 **Weleff, W.** 'Final report, GTR-16 radiation effects test on structural materials at −423°F', Aerojet-General Corporation Report No RN-S-0290 (1966)

4. Handbooks and reviews

114 **Coston, R. M.** 'Handbook of thermal design data for multilayer insulation systems', LMSC-A847882, Vol 2 (Final), George C. Marshall Space Flight Center, Huntsville, Alabama (1967) (N67–34910)
115 **Hertz, J.** 'The effect of cryogenic temperatures on the mechanical properties of reinforced plastic laminates', *Society of Plastics Engineers J* 21 (1965) 181
116 **Hertz, J., Knowles, D.** 'Survey of thermal properties of selected materials', General Dynamics/Convair Report AAL-65-008 (AR-504-1-553) (1965) (N65–31775)
117 **Jurevic, W. G., Rittenhouse, J. B.** 'Structural applications handbook', AFML TR-67-332, Air Force Materials Laboratory, Wright-Patterson Air Force Base, Ohio (1968) (AD 804 585)
118 **Landrock, A. H.** 'Properties of plastics and related materials at cryogenic temperatures', Plastec Report No 20, Plastics Technical Evaluation Center, Picatinny Arsenal, Dover, New Jersey (1965) (AD 469 126)
119 **Maximovich, M., Scheck, W. G.** 'Data summary and reference file for graphite and boron reinforced composite materials', General Dynamics/Convair Report No GDCA-DBG71-006 (1971) (Contract NAS 8-26198, George C. Marshall Space Flight Center, Huntsville, Alabama)
120 **Nored, D. L., Hennings, G., Sinclair, D. H., Smith, G. T., Smolak, G. R., Stofan, A. J.** 'Storage and handling of cryogenic fluids', NASA Special Publication SP-5053, Proceedings of Conference on Selected Technology for the Petroleum Industry, Lewis Research Center, Cleveland, Ohio (1965) (N66-33674)
121 'Plastics for aerospace vehicles, Part 1. Reinforced plastics', MIL-HDBK-17A, Department of Defense, Washington, DC (1971)
122 **Rittenhouse, J. B., Singletary, J. B.** 'Space materials handbook', 3rd edn, NASA Special Publication SP-3051, National Aeronautics and Space Administration, Washington, DC (1969) (Limited publication as AFML-TR-68-205)
123 **Schwartzberg, F. R., Hertzog, R. G., Osgood, S. H. et al.** 'Cryogenic materials data handbook (revised), Volume 2', AFML-TOR-64-280-Vol II (Revised), Air Force Materials Laboratory, Wright-Patterson Air Force Base, Ohio (1970) (AD 713 620)

5. Miscellaneous references

124 'Advanced composites design guide', 3rd edn, Vol 4: Materials, Air Force Materials Laboratory, Wright-Patterson Air Force Base, Ohio (1973)
125 **Kreider, K. G., Prewo, K. M.** 'The transverse strength of boron fibers', Composite Materials, Testing and Design, ASTM STP 497 (1972) 539
126 **Arp, V., Wilson, J. H., Windich, L., Sikora, P.** 'Thermal expansion of some engineering materials from 20 to 293 K', *Cryogenics* 2 (1962) 230
127 **Novak, R. C., DeCrescente, M. D.** 'Impact behaviour of unidirectional resin matrix composites tested in the fiber direction', Composite Materials, Testing-and-Design, ASTM STP 497 (1972) 311
128 **Kastelic, J. R., Hiltner, A., Baer, E.** 'Crazing, yielding and fracture in polycarbonate and polyethelene terepthalate at low temperatures', *J of Macro Molecular Science-Physics* B7 (4) (1973) 679

Bibliography — property cross reference

Property	Glass-Epoxy	Glass-Polyester	Glass-Phenolic	Glass-Teflon	Glass-Silicone	Glass-Polyurethane	Glass-Phenyl Silane	Glass-PBI**
σ^{tu}	1–1.3, 2–2.2, 3–3.5, 4, 5, 5.1, 22, 24, 28, 33, 35, 40, 43, 46, 47, 52, 54, 55, 57, 66, 71, 87	1–1.3, 2–2.2, 3–3.2, 3–4, 3.5, 34, 40, 55, 57, 63, 64, 66, 75, 109	1–1,3, 2–2.2, 40, 54, 55, 57, 64–66, 71, 75, 83, 93, 97, 111, 112	2–2.2, 37, 67 68, 80, 94, 102, 113	1–1.3, 2–2.2, 24, 40, 57, 64, 66, 68, 97	2–2.2, 85	2–2.2, 57, 66,	2–2.2
E_1^t	1–1.3, 2–2.2, 3–3.5, 4.5, 5.1, 24, 28, 35, 55, 56, 57, 66, 87	1–1.3, 2–2.2, 3, 34, 55, 57,	1–1.3, 2–2.2, 54, 55, 57 97, 111	2–2.2, 80	1–1.3, 2–2.2, 24, 57	2–2.2	2–2.2, 57, 66	2–2.2, 24
E_2^t	1–1.3, 2, 3–3.5, 28, 55, 56, 57	1–1.3, 2, 55, 57	1–1.3, 55, 57		1–1.3, 2, 57	2	2, 57	2
ϵ^t	3–3.5, 4, 5, 5.1, 35, 64 85	3–3.5, 64	64, 65, 112	80, 89, 102	64	85		
σ^{fu}	1–1.3, 2–2.2, 3–3.5, 4, 40, 57, 66, 71	1–1.3, 2–2.2 3–3.3, 3.5, 40, 57, 66	1–1.3, 2–2.2, 40, 41, 57, 71, 83, 93, 97	2–2.2, 80	1–1.3, 2–2.2, 40, 57, 97	2–2.2	2–2.2	2–2.2
E_1^f	1–1.3, 2, 3–3.2, 3.4, 3.5, 57	1–1.3, 2, 2.2, 57	1–1.3, 2–2.2, 57, 83, 93, 97	2–2.2, 80	1–1.3, 2–2.2 57	2–2.2	2–2.2	2–2.2
E_2^f	1–1.3, 2	1–1.3, 2	1–1.3, 2	1–1.3, 2		1–1.3, 2	2	2
σ^{cu}	1–1.3, 2, 2.2, 3–3.2, 3.4, 3.5, 24, 57, 66	1–1.3, 2, 2.2, 3–3.5, 34, 57	1–1.3, 2–2.2, 57, 82, 97	2–2.2, 80	1–1.3, 2–2.2, 24, 57	2–2.2	2–2.2, 57	2–2.2, 24
E^c	1, 1.2, 1.3, 2, 2.2, 57	1–1.3, 2, 2.2, 57, 66	1–1.3, 2–2.2, 57, 82, 97	2–2.2, 80	1–1.3, 2–2.2, 57	2–2.2	2–2.2	2–2.2
σ^{si}	3–3.2, 3.4, 3.5, 4, 4.1, 5, 5.1, 22, 47, 71	3–3.5	71					
η^t	1, 1.3, 2, 2.1, 2.2, 66, 70, 99	1–1.3, 2–2.2, 34, 70	1–1.3, 2–2.2		1–1.3, 2	2	2	2
σ^{by}	2–2.2, 3–3.2, 3.4, 3.5				2	2	2	2
σ^{l*}	4, 71, 103	62, 109	71, 97	80				
λ	3, 4.1, 14, 16–16.3, 21, 23–25, 38, 42, 56, 61, 63, 90, 114	3, 14, 16–16.3, 90	14, 16–16.3, 49	14, 16–16.3	14, 16–16.3,		14, 16–16.3	16, 24
$\Delta L/L$	3, 5, 14, 16, 16.2, 16.3, 28, 69, 85, 91, 100, 101, 104, 114	3, 14, 16–16.3	14, 16–16.3, 26, 27, 50, 111	14, 16–16.3, 80	14, 16–16.3, 67	5, 85, 91	14, 16–16.3	16, 16.2
c_p	15, 16, 16.2, 16.3, 24, 114	15, 16–16.3	15, 16–16.3, 64	15, 16–16.3	15, 16–16.3, 24		15, 16–16.3	16–16.3, 24

* includes fracture toughness
** polybenzimidezole

Bibliography—property cross reference (contd)

Property	Graphite-Epoxy	Boron-Epoxy	Boron-Aluminum	PRD-49 Epoxy
σ^{tu}	8, 9, 10, 10.2, 13, 13.2, 32, 47, 51, 58	13, 20, 22 47, 53, 58, 81	13, 13.3	29, 44, 59, 60
E_1^t	8, 9, 10, 10.1, 13, 51	13, 81	13, 13.3	44, 59, 60
ϵ^t	13	20	13	
σ^{fu}	8, 10, 10.1, 11, 12, 13, 13.2, 58	58		
E^f	8, 10.1			
σ^{cu}	13		13, 13.3	
E^c	13	13, 81	13, 13.3	
σ^{si}	8, 9, 10, 10.1, 10.2, 12, 13, 13.2, 47, 58	13, 22, 47, 58, 81	13, 13.3	59, 60
η^t	45	20		
σ^{by}			13, 13.3	
σ^{I*}	9, 10.2	81		
λ	13, 17, 18, 38	13, 38, 63, 81		
$\Delta L/L$	10, 13, 13.2, 17, 18, 36, 51, 52, 84, 88	13	13, 13.3	59, 60
c_p	13	13	13, 13.3	

* includes fracture toughness

Miscellaneous properties

Notch tensile strength Glass-Epoxy (3—3.2, 3.4, 3.5, 43, 46)

Vapour permeability Glass-Epoxy (28)

Modulus of rigidity Glass-Epoxy (53), Glass-Teflon (80), Boron-Epoxy (53)

Poissons ratio Glass-Epoxy (53), Boron-Epoxy (53)

Proportional limit in tension Glass-Epoxy (55, 56), Glass-Polyester (1—1.3, 55, 56)

Static fatigue Glass-Epoxy (66, 99), PRD 49-Epoxy (44)

Environmental effects Glass-Epoxy (4—4.4), Graphite-Epoxy (13, 13.2, 17, 58) Boron-Epoxy (13, 58), Boron-Aluminium (13, 36), PRD 49-Epoxy (44)

Electrical resistivity Graphite-Epoxy (13), Boron-Epoxy (13)

Thermo-optical effects Graphite-Epoxy (13, 84), Boron-Epoxy (13)

Density Glass-Epoxy, Polyester, Phenolic, Silicone, Phenyl Silane (14, 57), Glass-Teflon (14), Glass-Polybenzimidazole (16), Graphite-Epoxy (9, 13), Graphite-Phenolic (14), Graphite-Polyimide (12.1)

Radiation effects (13.2, 33, 37, 40, 51, 52, 64, 65, 75, 94, 112, 113)

Cryogen competability (33)

Miscellaneous composites

Glass-Polyimide σ^{tu} (24, 67, 68), σ^{fu} (89), σ^{si} (12.1, 89) $\Delta L/L$ (67)

Glass-Melamine σ^{tu} (65), ϵ^l (65), λ (90)

Glass-Viton σ^{tu} (68)

Glass-Phenyl formaldenhyde σ^l (110), λ (72), c_p (72)

SiO_2-Epoxy σ^{tu} (31), $\Delta L/L$ (28)

Graphite-Aluminium σ^{tu} (thermal cycling effects 6—6.2)

Graphite-Polyimide σ (14, 16—16.3) $\Delta L/L$ (14, 16—16.3)

Steel-Aluminium σ^{tu} (7, 7.1), ϵ^t (7.1), σ^t (7, 7.1)

Steel-Epoxy σ^{tu} (2, 30), E^t (2, 30), σ^{fu} (2), σ^{cu} (2), E^c (2), n^t (2)

Boron/Steel-Aluminium, *Boron/Titanium-Aluminininium* } σ^{tu}, E^t, σ^{cu}, E^c, σ^{by}, $\Delta L/L$, C_p (13, 13.3), σ^{si}, ϵ^t, n^t (13)

Potassium titanate-epoxy λ (16), C_p (16)

Pressure vessel applications

Glass-filament (19, 20, 39, 42, 46—48, 53, 67, 69, 76, 77, 91, 92, 95, 96, 98—100, 104—108, 113)

Graphite-filament (8, 10, 10.1, 45, 47, 100)

Boron-filament (20, 47, 53, 78)

PRD 40-filament (59, 60)

SEMI-ANNUAL REPORT ON MATERIALS RESEARCH
IN SUPPORT OF SUPERCONDUCTING MACHINERY

ELASTIC PROPERTIES OF ENGINEERING MATERIALS AT CRYOGENIC TEMPERATURES

H. M. Ledbetter and D. T. Read

Cryogenics Division
Institute for Basic Standards
National Bureau of Standards
Boulder, Colorado 80302

April 1976

Summary: Elastic Properties

During the six months preceding March 1976, the following studies were completed:

(1) 2000-series aluminum alloys. Two alloys -- 2014 (Al-Cu-Si-Mg) and 2219 (Al-Cu) were studied in their precipitation-hardened conditions by a pulse-echo method between room temperature and liquid-helium temperature. These alloys exhibit similar elastic properties and regular behavior with respect to temperature. They are slightly stiffer elastically than some of the other aluminum alloys that were reported on previously in these reports. Results of the study are given in an accompanying manuscript "Low-temperature elastic properties of aluminum alloys 2014 and 2019" by D. T. Read and H. M. Ledbetter.

(2) Face-centered-cubic, iron-nickel, high-permeability alloy. Iron-47.5 nickel was studied between room temperature and liquid-helium temperature by a pulse-echo method. Besides invar, iron-36 nickel, this is the only material of this type for which low-temperature elastic constants have been determined. Contrary to some previous reports, the room-temperature thermo-elastic coefficients are normal for this material. Results of the study are given in an accompanying manuscript "Low-temperature elastic properties of iron-47.5 nickel" by H. M. Ledbetter and D. T. Read.

(3) Nickel-chromium-iron-molybdenum alloy. There is an accompanying reprint of our previously described results on Inconel 718: W. F. Weston and H. M. Ledbetter, "Low-temperature elastic properties of a nickel-chromium-iron-molybdenum alloy," Mater. Sci. Engg. 20 (1975) 287-90.

(4) Aluminum alloys 1100, 5083, 7005, 7075. There is an accompanying reprint of our previously described results on four aluminum alloys: E. R. Naimon, H. M. Ledbetter, and W. F. Weston, "Low-temperature elastic properties of four wrought and annealed aluminium alloys," J. Mater. Sci. 10 (1975) 1309-16.

(5) Copper-nickel alloys. Our study on copper, copper-10 nickel, and copper-30 nickel was published: H. M. Ledbetter and W. F. Weston, "Low-temperature elastic properties of some copper-nickel alloys," 1975 Ultrasonics Symp. Proc., IEEE Cat. No. 75 CHO 994-45U, 623-7. A reprint is not included here because it is indentical to the preprint version given previously.

(6) Superconducting-coil composite. There is an accompanying reprint of our previously described results on a niobium-titanium, copper-stabilized, epoxy-impregnated, superconducting-coil composite: W. F. Weston, "Low-temperature elastic constants of a superconducting coil composite," J. Appl. Phys. 46 (1975) 4458-65.

LOW-TEMPERATURE ELASTIC CONSTANTS OF PRECIPITATION-HARDENED ALUMINUM ALLOYS 2014 and 2219+

D. T. Read* and H. M. Ledbetter

Cryogenics Division
Institute for Basic Standards
National Bureau of Standards
Boulder, Colorado 80302

+ Contribution of NBS, not subject to copyright. This work was partially supported by the Advanced Research Projects Agency of the U. S. Dept. of Defense.

* NRC-NBS Postdoctoral Research Associate, 1975-76.

Abstract

Elastic properties of aluminum alloys 2014 and 2219 were studied in their precipitation-hardened conditions between 4 and 300 K using an ultrasonic pulse-echo superposition technique. Results are given for longitudinal sound velocity, transverse sound velocity, Young's modulus, shear modulus, bulk modulus, and Poisson's ratio. The Young's moduli increase about eleven percent on cooling. The shear moduli are about ten percent higher than for unalloyed aluminum. All the elastic constants show regular temperature behavior.

Key words: Aluminum alloys; bulk modulus; compressibility; Debye temperature; Poisson's ratio; precipitation-hardening alloys; shear modulus; sound velocity; Young's modulus.

Introduction

The combination of a high ratio of strength to weight and high toughness at low temperatures makes many aluminum alloys attractive for cryogenic structural applications. In this report, the cryogenic elastic properties of two aluminum alloys, 2014 and 2219, used frequently at low temperatures, are described. All 2000-series alloys are precipitation hardenable, containing copper as the principal alloying element.

Alloy 2014 has better mechanical properties, but alloy 2219 has superior weldability. This is believed to be the first report of a complete set of low-temperature polycrystalline elastic constants for a series of 2000-type aluminum alloys.

Elastic constants are necessary parameters in the design of critical load-bearing members; they relate the stress applied to an object to its change in dimensions produced by the stress. Elastic constants are also used in analyzing the fracture properties of a material. The factor $E/(1 - \nu^2)$, where E is Young's modulus and ν is Poisson's ratio, occurs frequently when the strength properties of materials are considered.

Some elastic-property data on these alloys were reported previously[1]. However, the inaccuracies of those data were high, and the shear modulus was not reported. Thus, neither the bulk modulus nor Poisson's ratio, which are frequently of interest in engineering design, can be computed.

In the present study, an ultrasonic (10 MHz) pulse-superposition method[2] was used for determining the velocity v of an ultrasonic pulse propagated through the specimen. Appropriate moduli C were calculated using equations of the type $C = pv^2$, where p is the mass density. This indirect technique is more accurate than the more familiar direct

measurement of the change in length of a specimen under load where large errors can arise from mechanical misalignments. Ultrasonic methods have many advantages: small specimens are sufficient, so that ancillary equipment such as probes and dewars can also be small, and refrigeration costs are low; specimens can have a simple geometry and can be easily prepared; measurements can be made as nearly continuously as desired; relative imprecision is low, about one part in 10^5 for the velocities; laboratory-to-laboratory variations of the elastic constants are typically a few percent or less; and the relevant properties of the quartz transducer used to generate and detect ultrasonic pulses are affected only slightly by temperature.

Materials

Aluminum alloys 2014 and 2219 are precipitation-hardenable alloys containing copper and other alloy elements. Their chemical compositions are given in Table 1. The 2014 alloy was tested in the T652 condition: solution heat-treated, artificially aged, and stress relieved by rolling. The 2219 alloy was tested in the T87 condition: solution heat treated, cold worked, and artificially aged. The 2014-T652 and 2219-T87 alloys had Rockwell hardnesses of B 80.6 and B 81.1 and mass densities of 2.810 and 2.835 g/cm^3, respectively. Metallographic examination of these alloys revealed severely elongated grains. Surfaces perpendicular to the rolling direction showed nearly equi-axed grains with diameters of about 0.02 cm in the 2014 alloy and 0.03 cm in the 2219 alloy. Surfaces parallel to the rolling direction showed grains so severely elongated that their dimensions could not be determined accurately.

Procedures

The specimen materials were obtained from commercial sources; the

2014 alloy was obtained as a 7.6-cm thick forging, and the 2219 alloy was received in the form of a 3.8-cm thick plate. The hardnesses were determined by a standard technique; the mass densities were determined by the method of Archimedes using distilled water as a standard.

Quartz transducers were bonded to the specimens with phenyl salicylate (salol) for room temperature measurements and with stopcock grease for the initial part of the low-temperature measurements. These bonds failed around 70 K, so that a silicone fluid (viscosity = 20 kPa·s at 25^{o} C) was used for bonding at very low temperatures. The low-temperature apparatus was described previously[3].

Elastic constants were determined from sound-velocity measurements between room temperature and liquid-helium temperature. The inaccuracy of the velocities is estimated to be less than $\pm$ 1%.

Transducer and bond effects were minimized by measuring the transit times for both the one-transducer (usual) case and the two-transducer case, using "identical" transducers and bonds. The corrections were about one percent.

Low-temperature data were obtained by a pulse-echo-superposition method[2], which gives the ratio of the low-temperature velocity to the room-temperature velocity with an imprecision of about 0.001%.

The main limitation on the usefulness of the present results is the batch-to-batch variation of commercial materials. Due to this factor, variations in the elastic constants as large as one percent could be expected, but temperature coefficients should be unaffected. Thus, measurements on similar alloys at room temperature should establish their elastic constants over the entire 0-300 K region.

Results and Discussion

The measured longitudinal moduli $C = \rho v_\ell^2$ for both alloys are shown in Fig. 1. The small steps between adjacent data points for the 2219 alloy at 80 K and 140 K are not representative of the material's elastic behavior, but are artifacts of the measurement process. They are due to the use of two different bonding agents to seal the quartz transducer to the specimen for the low temperature measurements. The temperature dependences of the longitudinal moduli of both the 2014 and the 2219 alloys are quite regular.

The measured transverse moduli are shown in Fig. 2. Again, the small step at 120 K in the modulus of the 2219 alloy is a measurement artifact. The temperature dependences of the transverse moduli of both alloys are also quite regular. The data shown in Figs. 1 and 2 were fitted to a function of temperature suggested by Varshni[4]:

$$C = C^0 - \frac{s}{\exp(t/T)-1}, \qquad (1)$$

where C is any elastic stiffness constant (C_l and C_t in this case), C^0, s, and t are the fitting parameters, and T is the temperature. The fitted curves are shown along with the data in Figs. 1 and 2. Values of the fitting parameters are given in Table 2. Average differences between the measured moduli and the fitted curves were about 0.05%.

The elastic Debye temperatures for these alloys were calculated from their elastic constants at T = 0 K, and they are given in Table 2.

As expected from their higher shear moduli (discussed below), the alloys have higher Debye temperatures than "pure" aluminum where Θ = 431 K.

Values of the longitudinal and transverse moduli calculated using the fitted Varshni parameters were used to calculate other elastic constants. The additional elastic constants reported here: the shear modulus G, the Young's modulus E, the bulk modulus B, and the Poisson's ratio ν, are given by the following formulas[5]:

$$G = C_t = \rho v^2_t , \tag{2}$$

$$E = 3G(C_l - 4/3\ C_t)/(C_l - C_t), \tag{3}$$

$$B = C_l - 4/3\ C_t, \tag{4}$$

and

$$\nu = 1/2(C_l - 2\ C_t)/(C_l - C_t). \tag{5}$$

The four elastic constants obtained using these relations are shown as functions of temperature in Figs. 2-5. Values of these elastic constants at selected temperatures are given in Table 3, along with some previous results.

As shown by the data in Table 3, changes in the elastic constants of aluminum alloys 2014 and 2219 between 300 and 0 K are about 12% for E and G, and about 4% for B and ν. These changes are much larger than those

observed in alloys based on iron[6] and copper[7], two other common base metals. Most of the changes in the elastic constants of these aluminum alloys with temperature occur above liquid-nitrogen temperature, 77 K.

The outstanding feature of the data shown in Figs. 1-5 is the regular temperature dependence of all the elastic constants. These two aluminum alloys are good examples of materials with simple, ordinary elastic behavior with respect to temperature. This regular behavior was not evident from some previous reports on these alloys.

The bulk moduli of the 2014 and 2219 alloys differ by 0.3% and 3.9% from that of pure aluminum, while the shear moduli of these alloys differ by 8.5% and 11.9% from that of pure aluminum[8]. Thus, the alloying elements increase not only the yield strength but also the shear modulus of the base material. Alloying effects in these materials are complicated by the large number of alloying elements, but it is clear that the alloying raises the shear moduli much more than is expected from a simple rule of mixtures, while the bulk modulus is affected only slightly.

These alloys were not examined for anisotropic elastic behavior because aluminum single crystals are only slightly anisotropic[8]. Even strongly textured polycrystalline aggregates of aluminum should exhibit nearly isotropic elastic properties.

Compared to other aluminum alloys that were studied previously[9], 2000-series alloys have higher longitudinal and transverse moduli, resulting in higher Young's moduli and higher bulk moduli than the other alloys; but they have the same Poisson's ratio. The higher elastic moduli of the 2000-series alloys may be useful in critical design situations.

Conclusions

(1) With respect to unalloyed aluminum, alloys 2014 and 2019 have

higher Young's moduli ($\sim$ 9%), higher shear moduli ($\sim$ 10%), higher bulk moduli ($\sim$ 2%), and lower Poisson ratios ($\sim$ 3%).

(2) These elastic moduli are also higher than those reported previously for 5000-series and 7000-series aluminum alloys.

(3) Alloy 2219 has a slightly higher shear modulus, but a slightly lower bulk modulus, than alloy 2014.

(5) The temperature behaviors of the two alloys are very similar. Between 300 and 0 K, B increases about 4%, E increases about 11%, G increases about 12%, and ν decreases about 3 %.

References

1. Christian, J. L. and Watson, J. F., "Mechanical Properties of Several 2000 and 6000 Series Aluminum Alloys," Advan. Cryo. Eng., Vol. 10, 1965, pp. 63-76.

2. McSkimin, H. J., "Pulse Superposition Method for Measuring Ultrasonic Wave Velocities in Solids," J. Acoust. Soc. Amer., Vol. 33, 1961, pp. 12-16.

3. Naimon, E. R., Weston, W. F., and Ledbetter, H. M., "Elastic Properties of Two Titanium Alloys at Low Temperatures," Cryogenics, Vol. 14, 1974, pp. 246-249.

4. Varshni, Y. P., "Temperature Dependence of the Elastic Constants," Phys. Rev. B, Vol. 2, pp. 3952-3958.

5. Landau, L. D. and Lifshitz, E. M., "Theory of Elasticity," Pergamon, London, 1959, pp. 13, 99.

6. Ledbetter, H. M. and Reed, R. P., "Elastic Properties of Metals and Alloys. I. Iron, Nickel, and Iron-Nickel Alloys," J. Phys. Chem. Ref. Data, Vol. 2, 1973, pp. 531-618.

7. Ledbetter, H. M. and Naimon, E. R., "Elastic Properties of Metals and Alloys. II. Copper," J. Phys. Chem. Ref. Data, Vol. 3, 1974, pp. 897-935.

8. Kamm, G. N. and Alers, G. A., "Low-Temperature Elastic Moduli of Aluminum," J. Appl. Phys., Vol. 35, 1964, pp. 327-330. Polycrystalline averages were calculated from the single-crystal data in this reference using the Voigt-Reuss-Hill-arithmetic method.

9. Naimon, E. R., Ledbetter, H. M., and Weston, W. F., "Low-Temperature Elastic Properties of Four Wrought and Annealed Aluminium Alloys," J. Mat. Sci., Vol. 10, 1975, pp. 1309-1316.

Table 1 Chemical compositions of studied aluminum alloys, wt. %[a]

Alloy	Cu	Fe	Mg	Mn	Sn	Ti	V	Zn	Zr	Al
2014	4.4		0.05	0.8	0.8					Bal
2219	6.4	0.20	0.01	0.26	0.15	0.16	0.12	0.09	0.16	Bal

[a] For 2014, nominal composition. For 2219, plasma arc analysis.

Table 2 Varshni-function parameters determined from a least-squares fit of the data (see equation 1) and elastic Debye temperature, Θ

Alloy	Mode	$C^o(10^{11}\ Nm^{-2})$	$s(10^{11}\ Nm^{-2})$	t(K)	Θ(K)
2014	l	1.241	0.0781	217	439
	t	0.3152	0.0339	212	
2219	l	1.220	0.0859	230	443
	t	0.3250	0.0345	209	

Table 3 Values of the elastic constants of two aluminum alloys at selected temperatures in units of 10^{11} Nm^{-2}, except ν, which is dimensionless

Alloy	Temperature(K)	Present Results B	E	G	ν	Previous results[a] E
2014	300	.791	.757	.282	.341	.73
	200	.805	.794	.297	.336	.74
	100	.817	.827	.311	.331	.76
	0	.821	.838	.315	.330	---
2219	300	.758	.774	.291	.330	.72
	200	.772	.812	.306	.325	.72
	100	.784	.845	.320	.320	.74
	0	.787	.857	.325	.318	---

[a] 2014 alloy in the T-6 condition, average of longitudinal and transverse, interpolated data; 2219 alloy in the T-81 condition, average of longitudinal and transverse, interpolated data.

List of Figures

Fig. 1. Longitudinal modulus $C_l = \rho v_l^2$ for two 2000-series aluminum alloys in precipitation-hardened condition as a function of temperature.

Fig. 2. Shear modulus $G = C_t = \rho v_t^2$ for two aluminum alloys.

Fig. 3. Young's modulus for two aluminum alloys.

Fig. 4. Bulk modulus for two aluminum alloys.

Fig. 5. Poisson's ratio for two aluminum alloys.

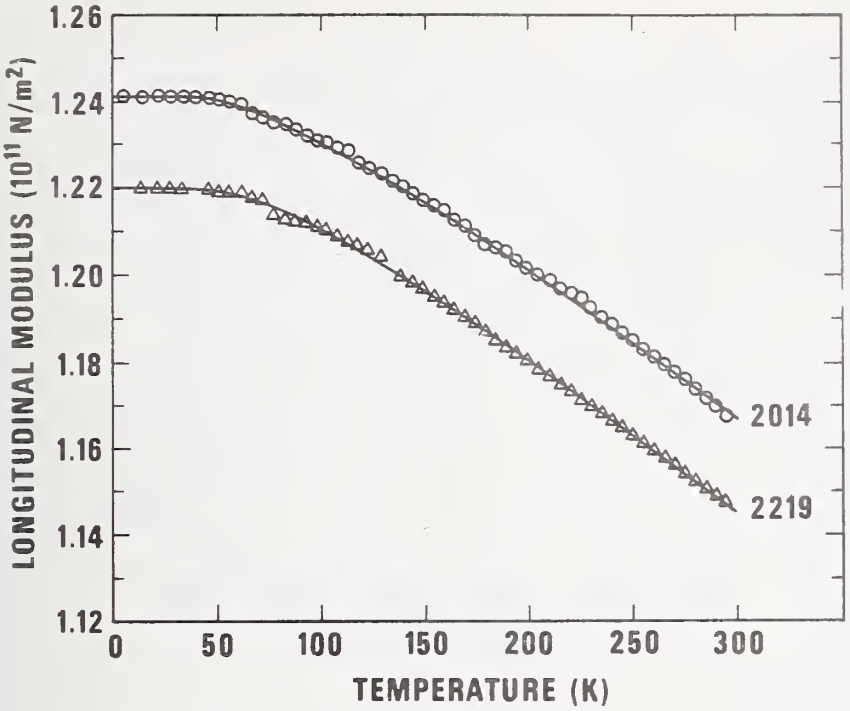

Fig. 1. Longitudinal modulus $C_l = \rho v_l^2$ for two 2000-series aluminum alloys in precipitation-hardened condition as a function of temperature.

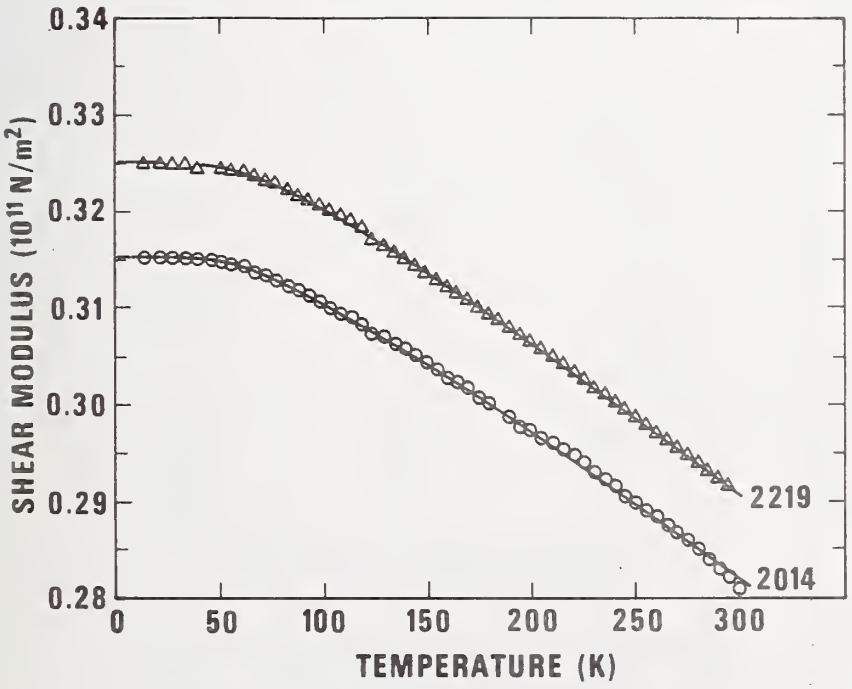

Fig. 2. Shear modulus $G = C_t = \rho v_t^2$ for two aluminum alloys.

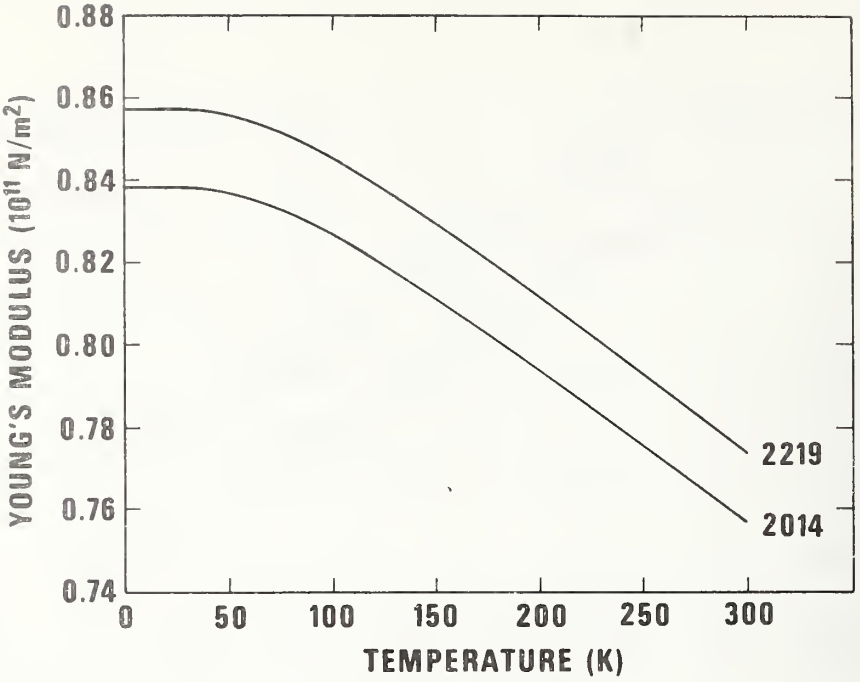

Fig. 3. Young's modulus for two aluminum alloys.

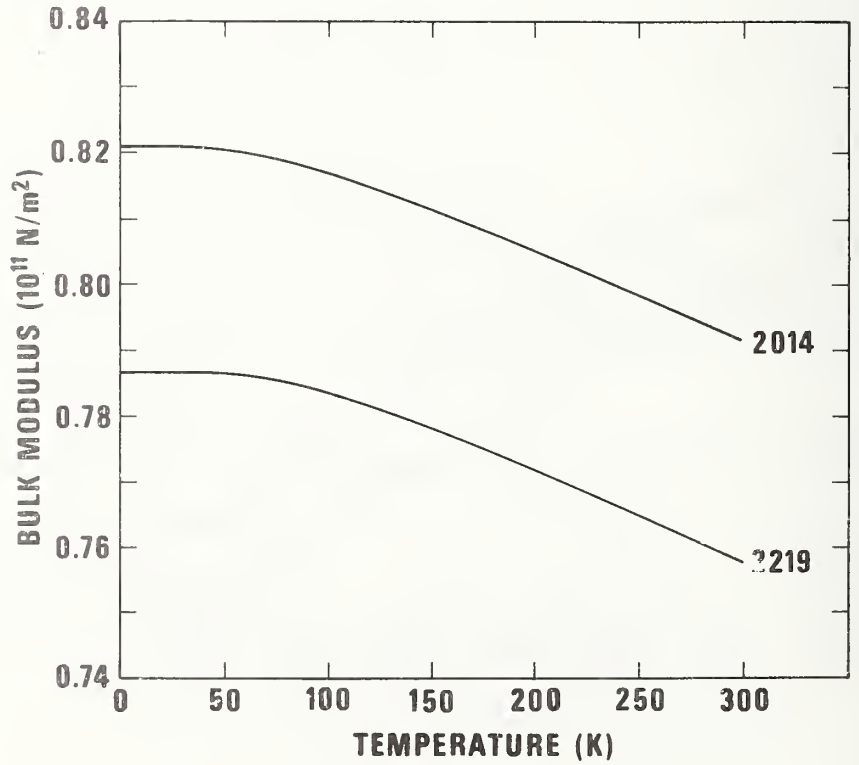

Fig. 4. Bulk modulus for two aluminum alloys.

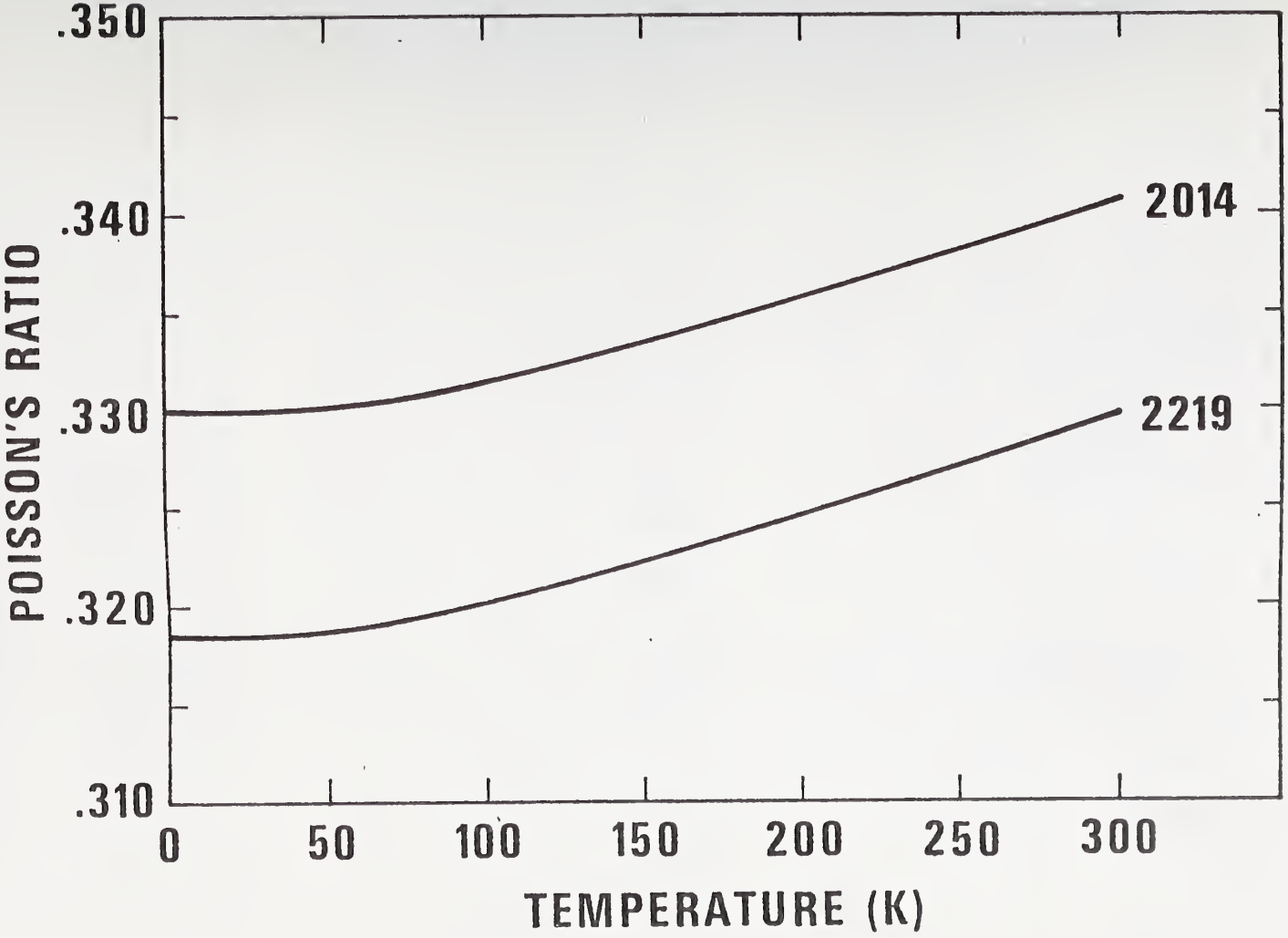

Fig. 5. Poisson's ratio for two aluminum alloys.

Low-Temperature Elastic Properties of an Iron-47.5 Nickel Alloy[+]

H. M. Ledbetter and D. T. Read*

Cryogenics Division
Institute for Basic Standards
National Bureau of Standards
Boulder, Colorado 80302

ABSTRACT

Elastic properties of a polycrystalline iron-47.5 wt. pct. nickel alloy were studied between room temperature and liquid-helium temperature. Room-temperature longitudinal and transverse ultrasonic velocities were determined by a pulse-echo technique. Low-temperature velocities were determined by a pulse-echo-superposition technique. The reported elastic constants are: longitudinal modulus, shear modulus, Young's modulus, bulk modulus, Poisson ratio, and elastic Debye temperature. Low-temperature elastic constants of face-centered cubic iron-nickel alloys are reviewed. Contrary to some previous reports, the elastic constants behave regularly in the temperature range studied.

Key words: Bulk modulus; compressibility; Debye temperature; iron alloy; nickel alloy; Poisson ratio; shear modulus; sound velocity; Young's modulus.

[+] Contribution of NBS, not subject to copyright.

* NRC-NBS Postdoctoral Research Associate, 1975-6.

INTRODUCTION

Elastic properties of an iron-47.5 nickel alloy were studied between room temperature and liquid-helium temperature. Elastic constants were determined by measuring the velocities of both longitudinal and transverse ultrasonic waves in a polycrystalline aggregate. The following constants are reported here: C_ℓ = longitudinal modulus, G = shear modulus, B = bulk modulus, E = Young's modulus, ν = Poisson's ratio, and Θ = elastic Debye temperature.

Iron alloys containing 30-100 percent nickel have a face-centered cubic crystal structure, and they are magnetic at room temperature. These alloys have many interesting properties that are exploited technologically.[1-3] Many of these properties involve magnetostriction, the coupling between magnetization and elastic strain. Recently, some of the alloys, developed originally for high-temperature applications, have been used cryogenically. The alloy reported on here--Fe-47.5Ni--is a candidate material for shaping magnetic fields in superconducting machinery. Desirable properties for such an application include: (a) ferromagnetism with high permeability, (b) absence of phase transitions, (c) at least moderate yield strength, and (d) adequate low-temperature mechanical properties, including both fatigue and fracture.

Elastic constants are interesting for two principal reasons. First, elastic constants are related directly to interatomic forces; thus, they are connected with a variety of solid-state phenomena, including maximum attainable strengths, phase stabilities, and lattice specific heats. Second, elastic constants are essential design parameters; to compute deflections due to applied loads or stresses due to temperature changes of constrained components, the elastic constants must be known.

While the elastic constants of iron-nickel alloys have been studied extensively,[4] no low-temperature elastic data exist for any of the face-centered cubic alloys except invar,[5] iron-36 nickel. Because of the many elastic anomalies exhibited by iron-nickel alloys,[6] characteristic of magnetic materials, all predictive schemes for elastic constants are unreliable for Fe-47.5Ni. Therefore, detailed experimental studies are required in this case.

EXPERIMENTAL

Material

The studied material was obtained from a commercial source in the form of a 10 X 23 X 108 cm ingot. The chemical (mill) analysis of the material by weight was: 0.012C, 0.33Mn, 0.25Si, 0.002P, 0.004S, and 47.47Ni. On an atomic basis, the alloy contained 46.2 Ni. The grain size was 0.12 mm determined by an intercept method. The diamond-pyramid hardness number was 123 for a 1 kg load. The mass density was 8.19 g/cm^3, as determined by Archimedes's method using distilled water as a standard.

Room-Temperature Sound Velocities

Room-temperature sound velocities were measured by a pulse-echo technique.[7] Briefly, a quartz piezoelectric transducer with a fundamental resonance frequency of 10 MHz was cemented with phenyl salycilate (salol) to one end of a specimen having flat and parallel faces. The specimen in this case was a 1.25 X 1.25 X 1.6 cm parallepiped with opposite faces ground flat and parallel within 2.5 μm. Ultrasonic pulses about one μs in duration were sent into the specimen by electrically exciting the transducer. The pulses propagated through the specimen, reflected from the end, and propagated

back. The echoes were detected by the transducer and displayed on an oscilloscope. The sound velocity was computed by

$$v = 2\ell/t \tag{1}$$

where ℓ is the specimen length and t is the transit (round-trip) time. On the oscilloscope, t was the time between subsequent echoes. The oscilloscope was calibrated against a precision time-mark generator. An x-cut quartz transducer was used for longitudinal waves, and an ac-cut quartz transducer was used for transverse waves.

Low-Temperature Sound Velocities

Low-temperature measurements of the sound velocities were made by a pulse-echo-superposition technique.[8] Briefly, the repetition rate of the pulse was increased so that each pulse coincided with the second echo of the preceding pulse. Since the excitation voltage was large compared with the echo voltages, the oscilloscope display consisted of alternating pulses of excitation voltages and "echo" voltages where the "echo" voltage represented the sum of all odd-numbered echoes of the non-superimposed case. Because of interference effects, the envelope of the summed odd-numbered echoes is highly sensitive to small changes, cuased in this case by cooling, in the ultrasonic velocity.

The transducer-specimen bonding material was a stopcock grease. Temperatures were monitored with a chromel-constantan thermocouple placed near the specimen. Cooling rates were about 2 K/min. The specimen holder was described previously.[9] Cooling was achieved by lowering the specimen-holder assembly stepwise into the ullage of a helium dewar. No thermal contraction corrections were made. For this alloy, the maximum thermal contraction correction to the elastic constant, which applied at T = 0 K, is 0.3 percent. No correction was made for the transducer-cement-coupling phase shift; the McSkimin[10] analysis gives a correction of less than 0.5 percent in the velocity, assuming a maximum phase shift of π. The transit time was corrected to allow for the thickness of the transducer; this correction is approximately one cycle at 10 MHz; thus, the observed longitudinal and transverse wave transit times were reduced about 1.0 and 0.5 percents, respectively.

RESULTS

Room-temperature sound velocities and elastic constants are given in Table 1. Both velocities were measured in three orthogonal directions and averaged to allow for texture. For each direction, shear velocities were measured for two orthogonal polarizations.

Longitudinal and shear elastic constants were computed from the velocities according to

$$C_\ell = \rho v_\ell^2 \tag{2}$$

and

$$G = C_t = \rho v_t^2 \tag{3}$$

where ρ is the mass density.

The temperature variation of these is shown in Figs. 1 and 2. Curves in those figures are least-squares fits of the data to the Varshni[11] relationship:

$$C = C^{o} - \frac{s}{\exp(t/T)-1} \tag{4}$$

where C is C_{ℓ} or C_{t}, C^{o}, s, and t are adjustable parameters, and T is temperature. The value of C at T = 0 K is C^{o}, and -s/t is the high-temperature limit of the temperature derivative dC/dT. By invoking and Einstein oscillator model, it can be shown that t is the Einstein temperature. Parameters C^{o}, s, and t are given in Table 2. Average differences between measured and curve values are 0.04 and 0.05 percent for the longitudinal and transverse cases, respectively.

Temperature variations of Young's modulus, the bulk modulus, and Poisson's ratio are shown in Figs. 3-5. These elastic constants were computed from Eq.(4) and the parameters in Table 2 using the relationships:

$$B = C_{\ell} - 4/3G, \tag{5}$$

$$E = 9GB/(G + 3B), \tag{6}$$

and

$$\nu = (E/2G)-1. \tag{7}$$

The elastic Debye temperature was computed according to

$$\Theta = \frac{h}{k}\left(\frac{3N\rho}{4\pi A}\right)^{\frac{1}{3}} v_{avg} \tag{8}$$

where h is Planck's constant, k is Boltzmann's constant, A is the effective atomic weight (57.00), and the average sound velocity is given by

$$v_{avg} = \left(\frac{v_{\ell}^{-3} + 2v_{t}^{-3}}{3}\right)^{-1/3} \tag{9}$$

The result was found to be Θ = 432 K, using the elastic data extrapolated to T = 0 K.

DISCUSSION

A. Temperature Dependence of the Elastic Constants

In the temperature region studied, T = 0 - 300 K, all the polycrystalline elastic constants behave regularly with respect to temperature changes. The longitudinal, Young's, shear, and bulk moduli all increase monotonically with decreasing temperature, show linear behavior at higher temperatures, show a continuously decreasing slope with decreasing temperature, approach relative flatness at low temperatures, and approach zero slope at T = 0 K, in accordance with the third law of thermodynamics. The Poisson ratio (which can be considered to be a function of the ratio of any combination of C_{ℓ}, B, E, or G) shows the same behavior, except that it decreases with decreasing temperature, which is usual for Poisson's ratio.

The temperature dependences of Young's modulus and the shear modulus are very similar. This can be understood simply as follows. Differentiation of Eq.(8) with the approximation that $\nu \simeq 1/3$ gives:

$$\frac{1}{E} \cdot \frac{dE}{dT} \simeq \frac{8}{9} \cdot \frac{1}{G} \cdot \frac{dG}{dT} + \frac{1}{9} \cdot \frac{1}{B} \cdot \frac{dB}{dT}$$

Thus, for usual values of the Poisson ratio, changes in Young's modulus depend almost entirely in changes in the shear modulus and only slightly on changes in the bulk modulus.

At higher temperatures, as the Curie temperature of the alloy ($T_C \simeq 730$ K) is approached, the temperature behavior of the elastic constants may become irregular.

B. Other Topics

In a final manuscript, several additional topics will be discussed. These include: (i) a comparison of the present temperature coefficients with those reported previously by other researchers; (ii) a review of the low-temperature elastic-constant data for face-centered-cubic iron-nickel alloys; (iii) a brief discussion of the elastic Debye temperature of fcc iron-nickel alloys; (iv) the relationship between single-crystal and polycrystal elastic constants for the case of magnetic materials; and (v) the effect of magnetism and magnetic fields on the elastic constants per se.

CONCLUSION

Contrary to some previous reports, all of the polycrystalline elastic constants of iron-47.5 nickel exhibit regular behavior with respect to temperature in the region T = 0 - 300 K.

ACKNOWLEDGMENT

This work was supported in part by the Advanced Research Projects Agency of the U.S. Department of Defense.

REFERENCES

1. S. J. Rosenberg: Nickel and Its Alloys, National Bureau of Standards Monograph 106, May 1968.

2. R. M. Bozorth: Ferromagnetism, pp. 102-28, Van Nostrand, New York, 1951.

3. S. Chickazumi: Physics of Magnetism, pp. 495-97, Wiley, New York, 1964.

4. H. M. Ledbetter and R. P. Reed: J. Phys. Chem. Ref. Data, 1974, Vol. 2, pp. 531-618.

5. H. M. Ledbetter, E. R. Naimon, and W. F. Weston: Proc. ICMC-CEC (Kingston, Ontario, July 1975), forthcoming.

6. G. Hausch and H. Warlimont: Acta Metall., 1973, Vol. 21, pp. 401-14.

7. R. T. Beyer and S. V. Letcher: Physical Ultrasonics, pp. 79-87, Academic, New York, 1969.

8. H. J. McSkimin: J. Acoust. Soc. Amer., 1961, Vol. 33, pp. 12-16.

9. E. R. Naimon, W. F. Weston, and H. M. Ledbetter: Cryogenics, 1974, Vol. 14, pp. 246-49.

Table I. Room-temperature Acoustic-wave Velocities in Fe-47.5 Ni, 10^6 cm/s

Propagation Direction	v_l	v_{t_1}	v_{t_2}
x	0.5673	0.2882	0.2879
y	0.5648	0.2881	0.2865
z	0.5589	0.2848	0.2841

Table II. Parameters Determined from the Varshni Equation

	Longitudinal	Transverse
C^o, 10" N/m^2	2.654	0.7047
S, 10" N/m^2	0.1036	0.05959
t, K	221.9	264.4

LIST OF FIGURES

Fig. 1. Longitudinal modulus $C_l = \rho v_l^2$ for iron-47.5 nickel as a function of temperature.

Fig. 2. Shear modulus $G = C_t = \rho v_t^2$ for iron 47.5 nickel.

Fig. 3. Young's modulus for iron-47.5 nickel.

Fig. 4. Bulk modulus for iron-47.5 nickel.

Fig. 5. Poisson's ratio for iron-47.5 nickel.

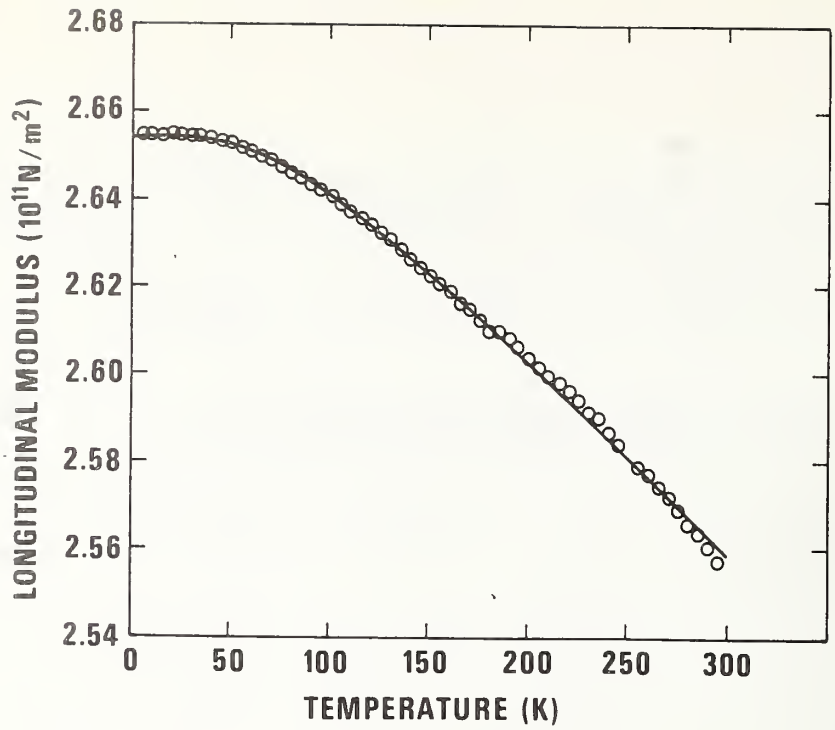

Fig. 1. Longitudinal modulus $C_l = \rho v_l^2$ for iron-47.5 nickel as a function of temperature.

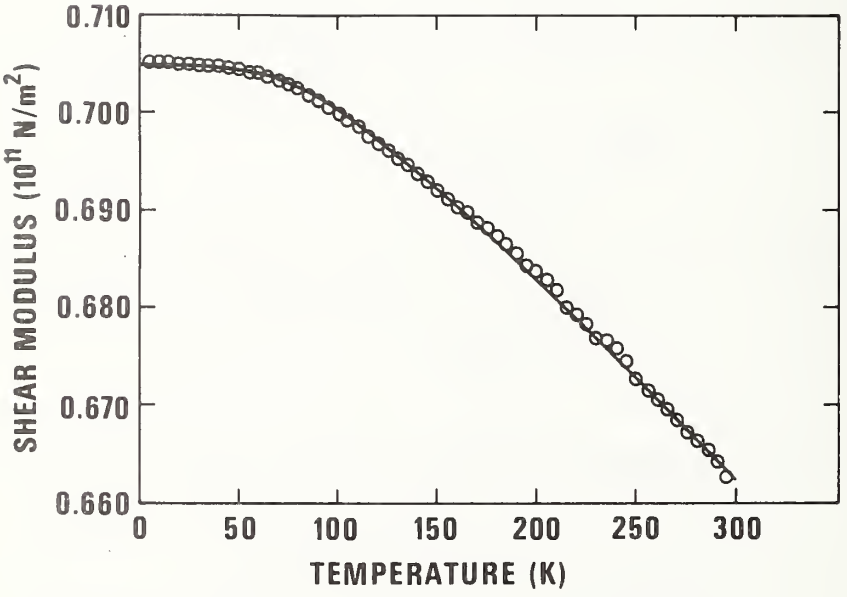

Fig. 2. Shear modulus $G = C_t = \rho v_t^2$ for iron-47.5 nickel.

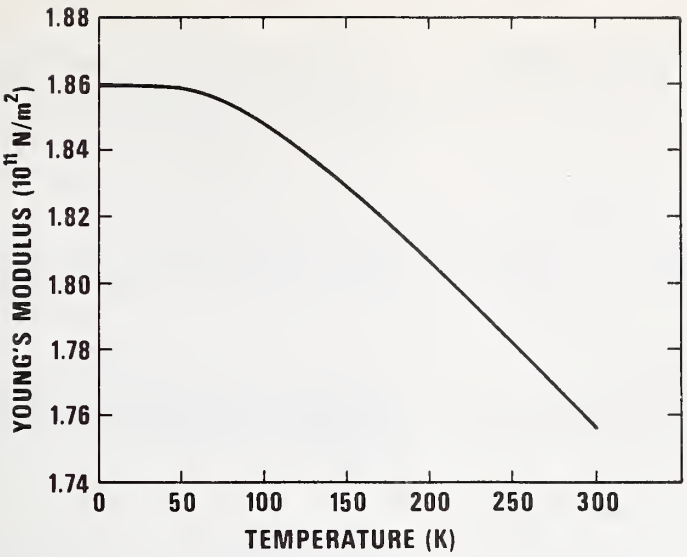

Fig. 3. Young's modulus for iron-47.5 nickel.

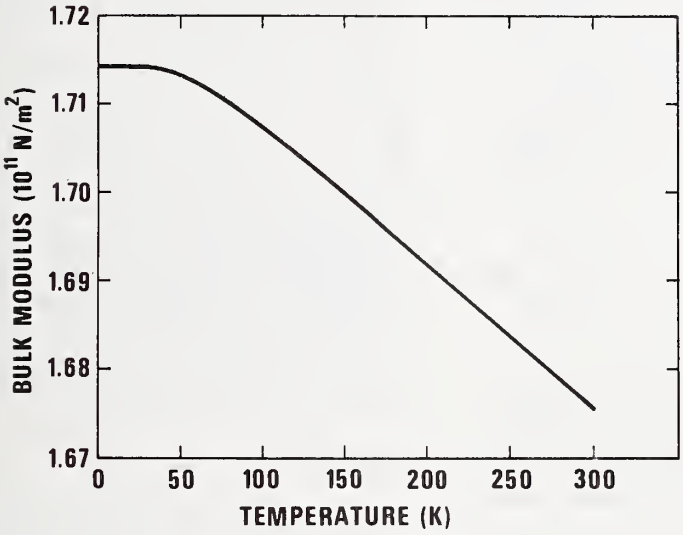

Fig. 4. Bulk modulus for iron-47.5 nickel.

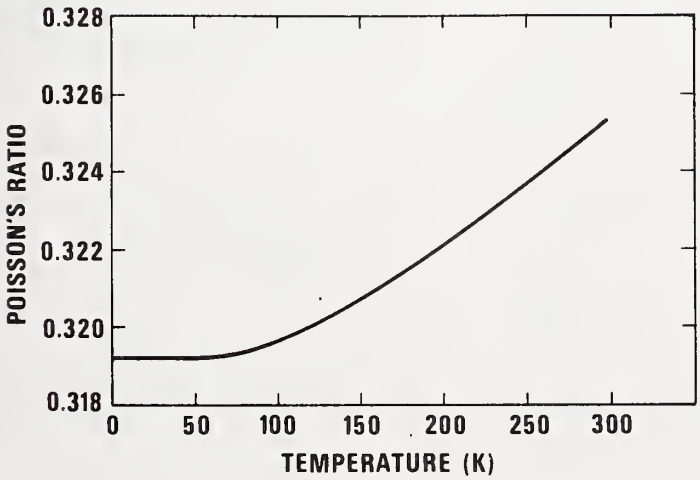

Fig. 5. Poisson's ratio for iron-47.5 nickel.

Materials Science and Engineering, 20 (1975) 287—290
© Elsevier Sequoia S.A., Lausanne — Printed in The Netherlands

Short Communication

Low-temperature Elastic Properties of a Nickel—Chromium—Iron—Molybdenum Alloy*

W.F. WESTON+ and H.M. LEDBETTER

Cryogenics Division, Institute for Basic Standards, National Bureau of Standards, Boulder, Colorado 80302 (U.S.A.)

(Received in revised form May 12, 1975)

The low-temperature elastic properties of two nickel - chromium - iron alloys, Inconel 600** and Inconel X-750, were reported recently [1]. The same properties — the longitudinal modulus, Young's modulus, the shear modulus, the bulk modulus (reciprocal compressibility) and Poisson's ratio — are reported here for a nickel - chromium - iron - molybdenum alloy, Inconel 718. Except for being slightly softer elastically, it resembles Inconel X-750.

The low-temperature elastic properties of Inconel 718 are of interest mainly because it is a candidate material for cryogenic structural applications [2]. The elastic properties are important both for the design of structural components and for understanding the basic physical properties of a material. From the temperature-dependent elastic constants, deflections can be predicted for any combination of stress and temperature. Also, the Debye characteristic temperature can be calculated from the elastic constants. The Debye temperature relates in turn to a wide variety of solid-state phenomena [3].

Inconel 718 is made precipitation hardenable by its niobium-plus-tantalum content. (Inconel X-750 is made precipitation hardenable by its aluminum-plus-titanium content.) It differs from the nickel - chromium - iron alloys in having superior mechanical properties such as yield, creep, rupture and fatigue strengths [2]. Its sluggish response to precipitation hardening permits annealing and welding without significant property changes.

EXPERIMENTAL METHODS

Ultrasonic (10 MHz) longitudinal and transverse sound-wave velocities were measured between room temperature and liquid-helium temperature (4 K) using a pulse-echo-superposition method [4]. Experimental procedures were identical with those reported previously [1] except that the material was obtained from

* Contribution of NBS, not subject to copyright.
+ NRC-NBS Postdoctoral Research Associate, 1973 - 74.
** Tradenames are used to identify the materials tested; they are not NBS endorsements of particular products.

TABLE 1

Composition and properties of the alloy

Chemical composition, mill analysis (wt.%)						Hardness (DPH No., 1 kg load)	Mass density at 294 K (g/cm^3)
Ni	Cr	Fe	Nb + Ta	Mo	Ti	425	8.229
53.73	18.49	17.62	5.17	2.98	1.01		
Al	C	Mn	Si	S	Cu	Condition: As-received; hot-rolled	
0.58	0.05	0.08	0.17	0.007	0.04		

a commercial source in the form of 3/4-inch (1.9 -cm) rods. Chemical and physical data on the material are given in Table 1.

RESULTS

The longitudinal modulus

$$C_l = \rho v_l^2 \tag{1}$$

is shown *versus* temperature in Fig. 1, where ρ is the mass density and v_l is the longitudinal sound-wave velocity. The transverse modulus

$$C_t = \rho v_t^2 = G \tag{2}$$

is shown *versus* temperature in Fig. 2, where v_t is the transverse sound-wave velocity and G is the shear modulus. Young's modulus E, the bulk modulus B and Poisson's ratio ν were calculated from the formulas [5]:

$$E = 3C_t(C_l - \tfrac{4}{3}C_t)/(C_l - C_t), \tag{3}$$

$$B = C_l - \tfrac{4}{3}C_t, \tag{4}$$

$$\nu = (1/2)(C_l - 2C_t)/(C_l - C_t); \tag{5}$$

and these elastic constants are shown *versus* temperature in Figs. 3 - 5. For comparison, Figs. 1 - 5 also show as dashed lines the elastic constants of Inconel X-750, which were reported previously [1].

The temperature dependences of both C_l and C_t were fitted to a theoretical relationship suggested by Varshni [6]:

$$C = C^0 - s/(e^{t/T} - 1) \tag{6}$$

where C^0, s, and t are adjustable parameters

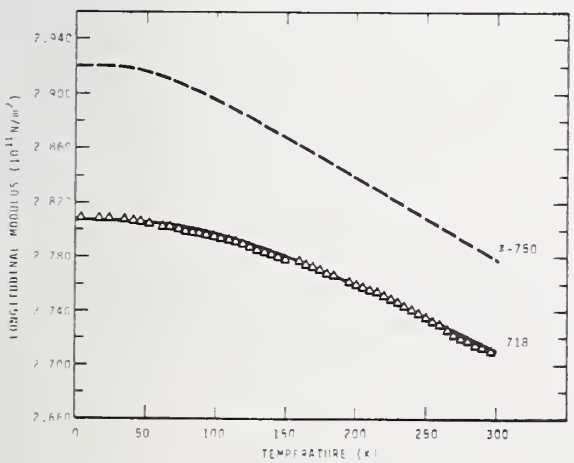

Fig. 1. Longitudinal modulus *vs.* temperature for two Inconel alloys.

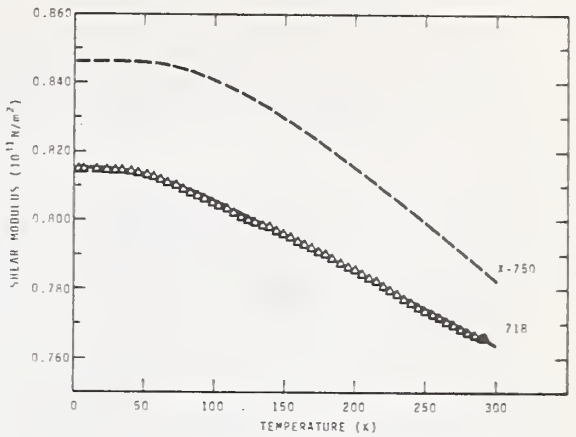

Fig. 2. Transverse (= shear) modulus *vs.* temperature for two Inconel alloys.

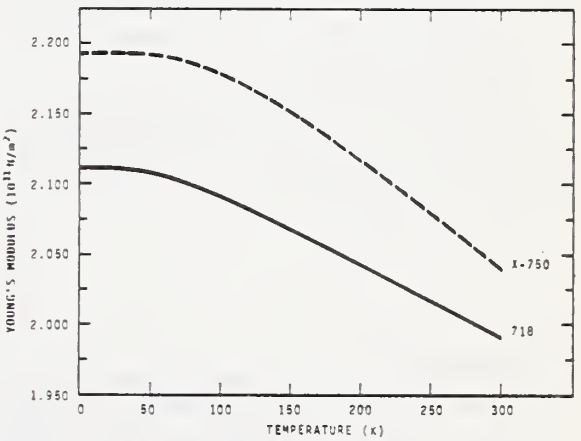

Fig. 3. Young's modulus *vs.* temperature for two Inconel alloys.

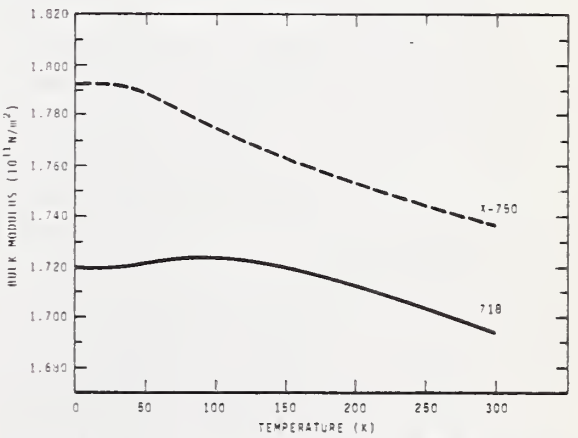

Fig. 4. Bulk modulus (reciprocal compressibility) *vs.* temperature for two Inconel alloys.

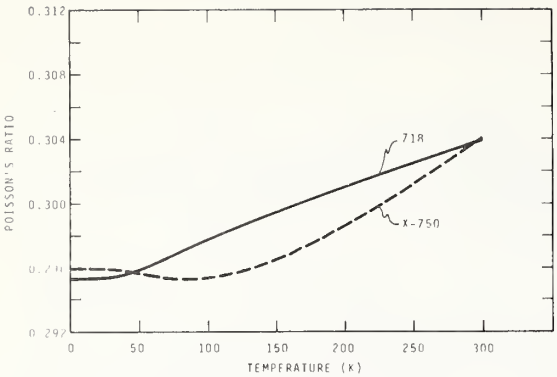

Fig. 5. Poisson's ratio *vs.* temperature for two Inconel alloys.

and T is temperature. The average difference between curve values and measured values was 0.06 and 0.05% for the transverse and the longitudinal modes, respectively.

The elastic Debye temperature was calculated from C_l and C_t using standard formulas [1] and was found to be θ = 446 K at absolute zero. For comparison, θ (nickel) = 476 K and θ (Inconel X-750) = 474 K.

DISCUSSION

Basically, the low-temperature elastic properties of Inconel 718 are very similar to those of Inconel X-750. The higher-iron, lower-nickel content of Inconel 718 accounts for its slightly lower elastic Debye temperature. Inconel 718 is also similar to Inconel X-750 in the temperature dependences of its elastic constants for the cases of E, G, and C_l, which show regular behavior. By regular behavior is meant: continuously decreasing with increasing temperature, linear behavior at higher temperatures, relative flatness at low temperatures, and zero slope at T = 0 K. Both materials show slight anomalies in the temperature dependence of the bulk modulus. While Inconel X-750 shows a concavity upwards in the $B(T)$ curve, Inconel 718, as shown in Fig. 4, shows a maximum near 100 K in its $B(T)$ curve. Based on the previous experience of this laboratory, it is believed in this case that the imprecisions in both C_l and C_t are a few parts in 10^4. Thus, this anomaly (though small) is believed to be real and not a measurement-computational artifact.

The interpretation of the maximum in the $B(T)$ curve of Inconel 718 can only be speculative. Unlike Inconel X-750, it was verified during the present study that Inconel 718 is non-magnetic between room temperature and liquid-nitrogen temperature (77 K). In some respects, the low-temperature behavior of the bulk modulus of Inconel 718 resembles that of stainless steels AISI 304, 310 and 316 reported previously [7]. In those cases, the anomalous behavior was interpreted in terms of the Döring effect that results from a large volume magnetostriction accompanying a paramagnetic-to-antiferromagnetic transition. However, no evidence of a low-temperature magnetic transition in Inconel 718 seems to exist; and neither the longitudinal modulus nor Young's modulus shows any evidence of a dilatational anomaly. Thus, the nature of this anomaly, its magnitude and perhaps even the question of its existence deserve further study.

Comparisons with some previous results [8] show reasonable agreement for both the room-temperature elastic constants and the temperature derivatives of E and G. It is easy to verify that the temperature derivative of ν reported here is more reasonable than that obtained from data in ref. 8. Differentiation of the standard relationship

$$\nu = \frac{E}{2G} - 1 \tag{7}$$

gives

$$\frac{1}{\nu}\frac{d\nu}{dT} = \frac{E}{E-2G}\left(\frac{1}{E}\frac{dE}{dT} - \frac{1}{G}\frac{dG}{dT}\right). \tag{8}$$

The present data satisfy eqn. (8) exactly, while the data from ref. 8 give a L.H.S./R.H.S. ratio of 2.6. Temperature derivatives of B have apparently not been reported previously. The only previously reported elastic constant at 4 K is Young's modulus [2]; this value, 2.11 $\times$ 10^{11}N/m^2, is identical with the present value.

This work was supported in part by the Advanced Research Projects Agency of the U.S. Department of Defense. Dr. E.R. Naimon of Dow Chemical (Rocky Flats Division) commented on the manuscript.

REFERENCES

1 W.F. Weston, H.M. Ledbetter and E.R. Naimon, Mater. Sci. Eng., to be published.

2 Handbook on Materials for Superconducting Machinery, Battelle Metals and Ceramics Information Center, Columbus, Ohio, 1974.
3 F.H. Herbstein, Adv. Phys., 10 (1961) 313.
4 H.J. McSkimin, J. Acoust. Soc. Am., 33 (1961) 12.
5 H.M. Ledbetter and R.P. Reed, J. Phys. Chem. Ref. Data, 2 (1974) 531.
6 Y.P. Varshni, Phys. Rev., B2 (1970) 3952.
7 H.M. Ledbetter, W.F. Weston and E.R. Naimon, J. Appl. Phys., to be published.
8 Huntington Alloys: Inconel Alloy 718, Intern. Nickel Co., Huntington, West Virginia.

JOURNAL OF MATERIALS SCIENCE 10 (1975) 1309–1316

Low-temperature elastic properties of four wrought and annealed aluminium alloys

E. R. NAIMON*, H. M. LEDBETTER, W. F. WESTON
Cryogenics Division, Institute for Basic Standards, National Bureau of Standards, Boulder, Colorado, USA

The elastic properties of four annealed polycrystalline commercial aluminium alloys were studied between 4 and 300 K using a pulse-superposition method. Results are given for longitudinal sound velocity, transverse sound velocity, Young's modulus, shear modulus, bulk modulus (reciprocal compressibility), Poisson's ratio, and elastic Debye temperature. The elastic stiffnesses of the alloys increase 4 to 13% on cooling from room temperature to liquid helium temperature. The elastic constant–temperature curves exhibit regular behaviour.

1. Introduction

Aluminium alloys are used extensively at cryogenic temperatures because of their favourable mechanical properties. These properties include increased strength without loss of ductility at lower temperatures, absence of a ductile–brittle fracture transition, and, for some alloys, high strength-to-weight ratios.

Knowledge of a material's elastic constants is essential for understanding its mechanical behaviour. Most mechanical behaviour is best described by a dislocation model, and the elastic constants (usually the shear modulus and Poisson's ratio) occur in most equations describing the stress–strain state of a dislocated solid.

In this paper, the elastic properties of four wrought aluminium alloys (commonly designated 1100, 5083, 7005, and 7075) are reported over the temperature range 300 to 4 K. These properties include the longitudinal modulus, Young's modulus, the shear modulus, the bulk modulus (reciprocal compressibility), and Poisson's ratio. While the changes of the elastic constants in this temperature range are only moderate (4 to 13%), exact values of the elastic constants are very useful design parameters, permitting accurate calculations of deflections for any combination of stress and temperature. Low-temperature elastic constants are also quite valuable theoretically; they permit the calculation of the Debye characteristic temperature, which is related in turn to a wide variety of solid-state phenomena that depends on the vibrational properties of solids.

An ultrasonic (10 MHz) pulse-superposition method was used for determining the velocity, v, of a sound pulse propagated through the specimen. The elastic modulus, C, is then given by $C = \rho v^2$, where ρ is the mass density. Different elastic constants were determined from different modes of ultrasonic excitation. This method has many advantages: small specimens are sufficient, thus ancillary equipment such as probes and dewars can also be small, and refrigeration costs are low; specimens can have a simple geometry and can be easily prepared; measurements can be made as nearly continuously as desired; relative precision is high, about one part in 10^5 for the velocities; laboratory-to-laboratory variations of the elastic constants are typically a few percent or less; and tests are completely non-destructive.

Low-temperature elastic data for aluminium alloys have two-fold interest. First, the elastic constants provide basic information about interatomic forces. Second, the same numbers are essential design parameters for stress-bearing members. Data given here permit the load-deflection behaviour of the alloys to be accurately predicted between room temperature and liquid helium temperature. Accurate elastic data

*Present address: Dow Chemical USA, Rocky Flats Division, Golden, Colorado, 80401

© *1975 Chapman and Hall Ltd.*

become especially important in applications involving high stresses, large structural parts, or precision parts.

2. Materials

Aluminium alloy 1100 is commercial quality aluminium. It has good corrosion resistance, high electrical and thermal conductivities, high ductility, but low strength properties. Strength can be improved somewhat by strain-hardening without significantly decreasing other properties. The main impurities in this alloy are usually iron and silicon.

Aluminium alloy 5083 is characterized by good welding properties and by good corrosion resistance in marine environment. Magnesium is the major alloying element and, along with manganese, produces a moderately strong, yet ductile alloy, which does not respond to heat-treatment. The strength properties of 5083 improve with lower temperatures. The main advantage of 5083 seems to be its weldability: welds as strong as the base metal can be obtained. Currently this alloy is being used in a number of applications involving the manufacture, transfer, and storage of liquefied natural gas; these applications require many millions of kilograms of material.

Aluminium alloy 7005 is a heat-treatable alloy containing zinc and magnesium, which are balanced to obtain a natural-ageing alloy. Chromium is added to reduce corrosion of the heat-affected weld zones, and zirconium is added to reduce weld cracking and to improve mechanical properties.

Aluminium alloy 7075 contains zinc as the major alloying element, together with a small percentage of magnesium. This alloy can be precipitation-hardened to produce high strength. (However, the studies reported here were made on annealed alloys.)

Details of compositions, heat-treatments, mass densities, and hardnesses of the alloys are given in Tables I and II.

3. Experimental

Alloys were obtained from commercial sources; 1100 and 7075 in the form of 1.9 cm rods, 5083 and 7005 in the form of 1.9 cm thick plate. Cylindrical specimens 1.6 cm diameter and 1.6 cm long were prepared by grinding. Opposite faces were flat and parallel within 2.5 μm. Specimens were annealed at a pressure of 5×10^{-6} Torr, or less, and cooled in the furnace. Hardnesses were determined by standard metallurgical methods, and mass densities were determined by Archimedes's method using distilled water as a standard.

Quartz transducers (10 MHz) were bonded to the specimens with phenyl salicylate for room-temperature measurements and with a stopcock grease for lower temperatures. In a few cases, failure of these bonds at very low temperatures required using a silicone fluid (viscosity = 2×10^3 P at 25 C) for bonding. The low-temperature apparatus was described previously [1].

A pulse-superposition method was used to determine the sound-wave velocities over the temperature range 300 to 4 K. Details concerning this method were given elsewhere [2].

4. Results

Quantities that were measured directly are the longitudinal and the transverse sound-wave

TABLE I Compositions of the alloys, mill analyses, wt %

Alloy	Al	Cr	Cu	Fe	Mg	Mn	Ni	Si	Ti	V	Zn	Zr
1100	Bal		0.2	0.6				0.1				
5083	Bal	0.13	0.04	0.19	4.75	0.63	0.003	0.08	0.01	0.007	0.04	
7005	Bal	0.25	< 0.1	< 0.4	1.2	< 0.2		< 0.3	< 0.1		4.6	0.3
7075	Bal	0.3	1.6	0.7	2.5	0.3		0.5	0.2		5.6	

TABLE II Properties of the alloys

Alloy	Hardness (DPH no., 1 kg load)	Mass density at 294 K (g cm^{-3})	Condition
1100	28	2.818	Annealed 345 C; furnace cooled
5083	78	2.666	Annealed 413 C, ½ h; furnace cooled
7005	77	2.779	Annealed 400 C, 3 h; furnace cooled
7075	67	2.721	Annealed 413 C, 3 h; furnace cooled

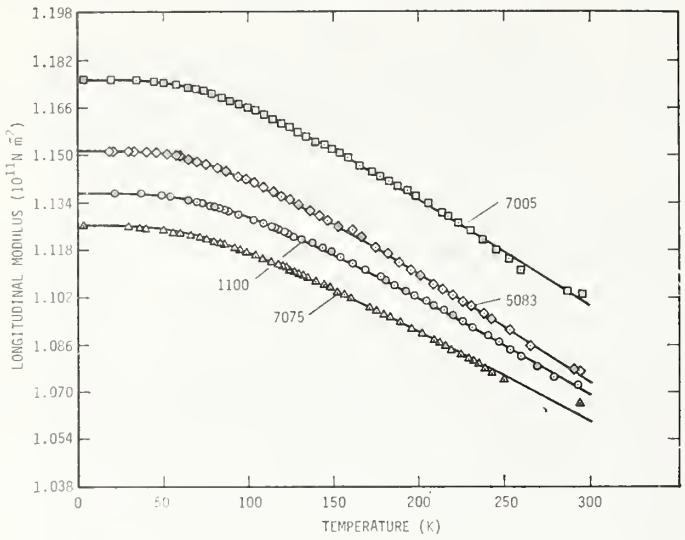

Figure 1 Temperature variation of the longitudinal modulus.

velocities v_l and v_t. From these, the longitudinal modulus, C_l, and the transverse modulus, C_t, were calculated according to

$$C_l = \rho v_l^2 \qquad (1)$$

and

$$C_t = \rho v_t^2 \,. \qquad (2)$$

These moduli are shown in Figs. 1 and 2 for the temperature range studied. No corrections were made for the change of mass density with temperature; for aluminium this introduces a maximum error, over 300 K, of 0.4%. Errors in the absolute velocities are believed to be about $\frac{1}{2}$% or less. All the other elastic constants that are used to describe polycrystalline aggregates are simply related to these two moduli. The moduli considered here – the shear modulus G, Young's modulus E, the bulk modulus B, and Poisson's ratio ν – are given by:

$$G = C_t \,, \qquad (3)$$

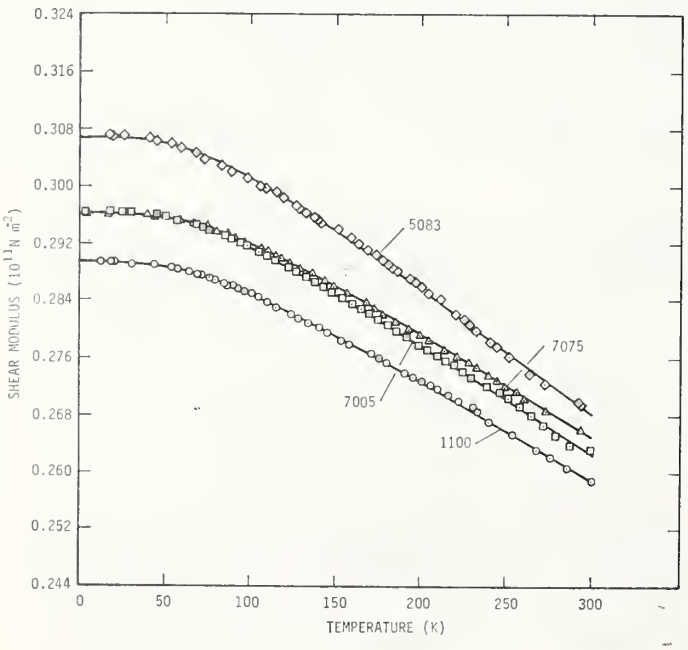

Figure 2 Temperature variation of the transverse or shear modulus.

1311

$$E = 3G(C_l - \tfrac{4}{3}C_t)/(C_l - C_t)\,, \quad (4)$$

$$B = C_l - \tfrac{4}{3}C_t\,, \quad (5)$$

and

$$\nu = \tfrac{1}{2}(C_l - 2C_t)/(C_l - C_t)\,. \quad (6)$$

The elastic constants obtained from these relationships are shown as functions of temperature in Figs. 3 to 5. Values of the elastic constants at selected temperatures are given in Table III.

The temperature variations of the elastic constants can be described mathematically in various ways. In this case, the temperature dependences of both C_l and C_t were fitted to a theoretical relationship suggested by Varshni [3]:

$$C = C^\circ - \frac{s}{e^{t/T} - 1}\,, \quad (7)$$

where C is any elastic constant (C_l and C_t in this case), C°, s, and t are adjustable parameters and T is temperature. The value of C at $T = 0$ K is C°, and $-s/t$ is the high-temperature limit of the temperature derivative dC/dT. By invoking an Einstein oscillator model of solids, it can be shown (in the absence of electronic effects) that t is the Einstein characteristic temperature.

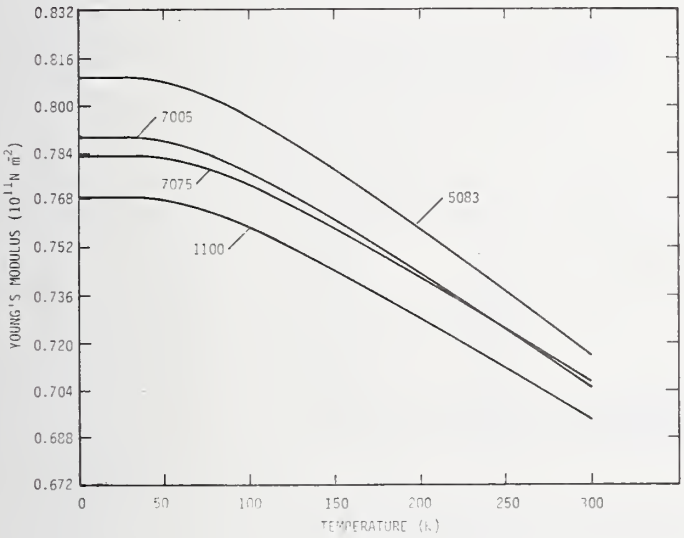

Figure 3 Temperature variation of Young's modulus.

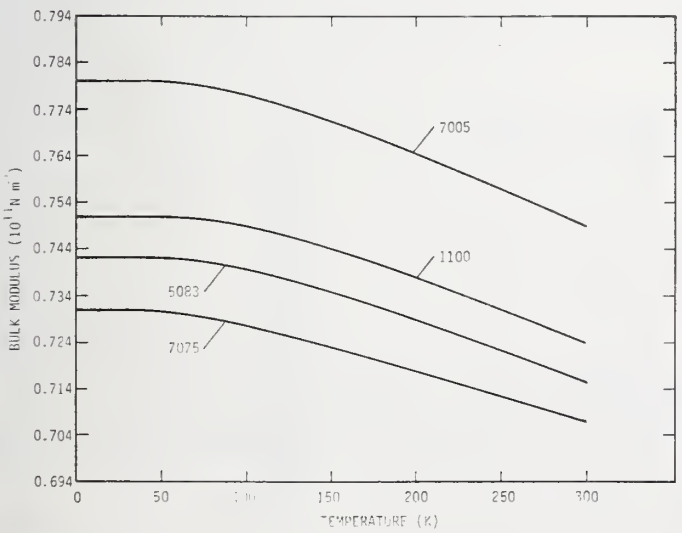

Figure 4 Temperature variation of the bulk modulus (reciprocal compressibility).

TABLE III Values of the elastic constants of aluminium alloys at selected temperatures in units of 10^{11} N m^{-2} except ν, which is dimensionless

	Present results					Previous results†					
Alloy	Temperature (K)	B	E	G	ν	Temperature (K)	B	E	G	ν	Reference
1100	300	0.724	0.694	0.259	0.340	300	(0.697)	0.689	0.258	0.33	[7]
	200	0.738	0.728	0.273	0.336						
	100	0.749	0.758	0.285	0.331						
	0	0.751	0.769	0.289	0.329						
5083	300	0.716	0.715	0.268	0.333	300	(0.762)	0.710	0.264	0.33	[7]
	200	0.729	0.758	0.286	0.327						
	100	0.739	0.796	0.301	0.321						
	0	0.742	0.809	0.307	0.318						
7005	300	0.749	0.705	0.262	0.343	300	(0.635)	0.711	0.271	(0.313)	[8]
	200	0.765	0.743	0.278	0.338	77	(0.735)	0.779	0.294	(0.323)	
	100	0.777	0.777	0.291	0.333	20	(0.671)	0.792	0.304	(0.303)	
	0	0.780	0.789	0.296	0.331						
7075	300	0.707	0.707	0.265	0.333	298		0.731			[9]
	200	0.718	0.742	0.279	0.328	200		0.786			
	100	0.728	0.773	0.292	0.323	20		0.786			
	0	0.731	0.783	0.296	0.321						
Alumin-	300	0.761	0.701	0.260	0.347						
ium*	200	0.777	0.738	0.275	0.342						
	100	0.790	0.771	0.288	0.337						
	0	0.794	0.784	0.293	0.336						

*Calculated from single-crystal data in [4].
†Entries in parentheses were derived using standard formulae.

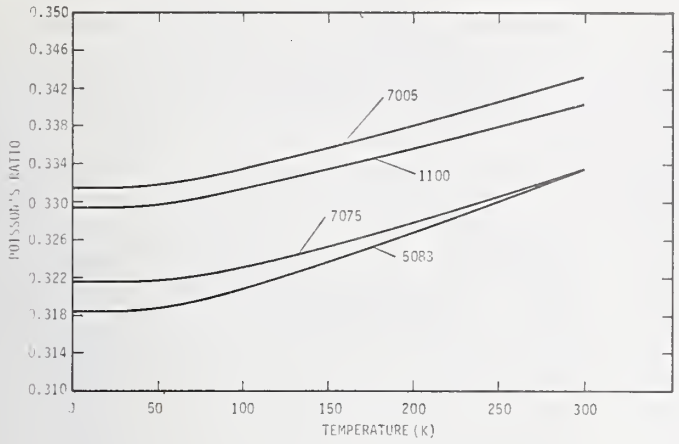

Figure 5 Temperature variation of Poisson's ratio.

Parameters C^0, s, and t (determined by a least-squares fit of Equation 7 to the data) are given in Table IV. Average differences between

TABLE IV Parameters in Equation 7

Alloy	Mode	C^0 (10^{11} N m^{-2})	s (10^{11} N m^{-2})	t (K)
1100	l	1.136	0.0903	255.9
	t	0.2892	0.0301	206.9
5083	l	1.151	0.0926	235.3
	t	0.3067	0.0381	206.7
7005	l	1.175	0.0928	240.0
	t	0.2963	0.0327	203.4
7075	l	1.126	0.0707	219.6
	t	0.2961	0.0344	223.3

measured and curve values are 0.03% and 0.06% for the longitudinal and transverse moduli, respectively. Room-temperature values of the temperature coefficients of the elastic moduli are given in Table V; these values occur in the linear high-temperature region.

TABLE V Temperature coefficients of the elastic constants at room temperature (10^{-4} K^{-1})

Alloy	$\frac{1}{B}\frac{dB}{dT}$	$\frac{1}{E}\frac{dE}{dT}$	$\frac{1}{G}\frac{dG}{dT}$	$\frac{1}{\nu}\frac{d\nu}{dT}$
1100	−2.01	−5.01	−5.37	1.41
5083	−1.92	−6.06	−6.58	2.08
7005	−2.13	−5.48	−5.88	1.54
7075	−1.58	−5.08	−5.52	1.75
Aluminium*	−1.97	−5.53	−5.77	1.80

*Derived from single-crystal data in [4].

The elastic Debye temperature, θ, can be calculated from the elastic wave velocities by [5]:

$$\theta = K\langle v \rangle , \tag{8}$$

where

$$K = \frac{h}{k}\left(\frac{3N\rho}{4\pi A}\right)^{1/3} . \tag{9}$$

Here h is Planck's constant, k is Boltzmann's constant, N is Avogadro's constant, ρ is the mass density, and A is the effective atomic weight. The average velocity is given by

$$\langle v \rangle = \left(\frac{v_l^{-3} + 2v_t^{-3}}{3}\right)^{-1/3} . \tag{10}$$

The elastic Debye temperatures for the four alloys at $T = 0$ K, and also for unalloyed aluminium are given in Table VI.

TABLE VI Elastic Debye temperatures at $T = 0$ K

Alloy	θ (K)
1100	426.2
5083	440.4
7005	425.9
7075	422.2
Aluminium	430.6*

*Calculated from single-crystal data in [4].

5. Discussion

As shown by the data in Table III, changes in the elastic constants of aluminium and its alloys between 300 and 4 K are about 4% for B and ν, and 12% for E and G. These changes are somewhat larger than those observed in alloys based on copper or iron, for example. Most of the changes occur above about 100 K. Below this temperature the elastic constants change only slightly with temperature. Thus, any changes in the mechanical behaviour of these

alloys in this temperature region probably cannot be ascribed to an elastic origin.

The temperature behaviour of the elastic constants of the aluminium alloys reported on here is quite regular. The moduli decrease regularly with increasing temperature and the modulus–temperature curves are relatively flat at low temperatures. Also, in accord with the third law of thermodynamics, the slopes dC/dT approach zero at zero temperature. A linear temperature dependence is exhibited above about 150 K, which is roughly one-third of the Debye temperature. Besides indicating the absence of magnetic or structural transitions, this ideal temperature behaviour suggests that the anharmonic properties of these alloys can probably be explained by a relatively simple model.

These alloys were not examined for texture. However, texture would have little effect on their elastic properties. Aluminium single crystals are only slightly anisotropic; the Zener anisotropy ratio for aluminium is 1.2; it is 1.0 for the isotropic case. Aluminium's isotropy is purely accidental since aluminium, because of its three valence electrons, has a large band-structure contribution to the elastic constants [10]. This contribution is usually anisotropic; the anisotropy is cancelled in the case of aluminium by other energy terms. Thus, since aluminium single crystals are only slightly anisotropic, even a strongly textured polycrystalline aggregate of aluminium would have nearly isotropic elastic behaviour.

It should be emphasized that the data reported here are dynamic (adiabatic) rather than static (isothermal); they apply strictly to rapid rather than slow loading. However, the differences between adiabatic and isothermal elastic constants are small. They become smaller at lower temperatures because of the diminishing thermal-expansion coefficient, and they vanish at zero temperature. Using formulae given by Landau and Lifshitz [6] it can be shown for aluminium at room temperature:

$$\frac{E_S - E_T}{E_T} = 0.005\,, \quad \frac{B_S - B_T}{B_T} = 0.045 \quad (11)$$

$$\frac{\nu_S - \nu_T}{\nu_T} = 0.020\,, \text{ and } \frac{G_S - G_T}{G_S} = 0\,,$$

where subscripts S and T denote the adiabatic and the isothermal cases, respectively. For E, B, ν and G, these corrections are typically in the ratio 1:9:4:0 if ν has a value near $\frac{1}{3}$.

Effects of alloying on the elastic properties of aluminium cannot be accurately determined from the present study because of the large number of alloying elements and their interactions. Such effects have been considered elsewhere [11]. However, some general observations can be made concerning alloying. Disregarding alloy 1100, with respect to "pure" aluminium, the shear modulus and Young's modulus increased in all cases while the bulk modulus decreased, and by a larger percentage. Poisson's ratio decreased in all four alloys. The 1100 alloy, which contains only 1% of impurities, presents an interesting case. The data indicate that while the shear modulus of this alloy is identical to that of unalloyed aluminium, the bulk modulus is higher by about 5%. Since the bulk modulus is not measured directly, but is calculated from the difference of two velocities according to Equation 5, a compounding of errors may account for this discrepancy. If the effect is real, then it has important consequences for the problem of averaging single-crystal elastic coefficients to obtain the bulk modulus of a polycrystalline aggregate.

Finally, approximate relationships among the elastic constants are indicated. For all the alloys and for all temperatures, as a first approximation,

$$\nu \approx \tfrac{1}{3} \quad (12)$$

and

$$B \approx E \approx (8/3)G\,. \quad (13)$$

These should be useful for many engineering purposes where only rough numbers are needed and only one of the elastic constants is known.

6. Conclusions

From the results of this study the following conclusions are drawn:

(1) all the elastic properties of aluminium alloys 1100, 5083, 7005, and 7075 behave regularly with respect to temperature;

(2) for all alloys studied, the temperature behaviour of both C_l and C_t can be described accurately by a theoretical relationship suggested by Varshni;

(3) in this series of alloys, in the annealed condition, alloy 5083 has the highest Young's modulus, the highest shear (rigidity) modulus, and the lowest Poisson's ratio. Alloy 7005 has the highest bulk modulus.

Acknowledgement

This work was supported in part by the Advanced Research Projects Agency of the U.S. Department of Defense.

References

1. E. R. NAIMON, W. F. WESTON and H. M. LEDBETTER, *Cryogenics* **14** (1974) 246.
2. H. J. MCSKIMIN, *J. Accoust. Soc. Amer.* **33** (1961) 12.
3. Y. P. VARSHNI, *Phys. Rev.* **B2** (1970) 3952.
4. G. N. KAMM and G. A. ALERS, *J. Appl. Phys.* **35** (1964) 327.
5. P. DEBYE, *Ann. Phys.* (*Leipz.*) **39** (1912) 789.
6. L. D. LANDAU and E. M. LIFSHITZ, "Theory of Elasticity" (Pergamon, London, 1959) p. 17.
7. T. LYMAN, Ed., "Metals Handbook" (ASM, Metals Park, Ohio, 1961).
8. R. DEVELAY, A. FAURE, S. LEHONGRE, D. MUGNIER and D. SCHROETER, in "Advances in Cryogenic Engineering", Vol. 12, edited by K. Timmerhaus (Plenum, New York, 1967) p. 484.
9. J. L. CHRISTIAN and J. F. WATSON, *ibid*, Vol. 6, (1961) p. 604.
10. T. SUZUKI, *Phys. Rev.* **B3** (1971) 4007.
11. W. KÖSTER, *Z. Metallk.* **32** (1940) 282.

Received 11 December 1974 and accepted 28 January 1975.

Low-temperature elastic constants of a superconducting coil composite

W. F. Weston*

Cryogenics Division, Institute for Basic Standards, National Bureau of Standards, Boulder, Colorado 80302
(Received 27 February 1975; in final form 17 June 1975)

A resonant piezoelectric oscillator method for measuring elastic moduli was applied to composite materials. The complete set of elastic compliances of a superconducting coil composite was determined semicontinuously between 4 and 300 K. Also, two moduli of a layered fiber-glass–epoxy composite were determined; this composite is essentially the matrix material of the coil composite. The Young's moduli, shear moduli, Poisson ratios, and elastic stiffness coefficients are also reported. Results agree closely with elastic data obtained by conventional testing methods.

PACS numbers: 62.20.D, 74.50.

I. INTRODUCTION

The elastic properties of composite materials are currently of considerable interest. Many composites, because they have high mechanical strength and a high modulus-to-density ratio, are useful as strong lightweight structural materials. Some composites have been designed for use at low temperatures, for example, as superconducting coils for high-field magnets. However, few elastic data are available for composite materials, particularly at low temperatures. To the author's knowledge, no complete sets of elastic data are available for composite materials at 4 K. Some data are useful as design parameters, and elastic constants are among the most accurately known fundamental physical properties of solids.

Because composite materials are usually highly anisotropic, the determination of their elastic constants is much more difficult than for the more usual quasi-isotropic engineering materials. Conventional methods of measuring the elastic properties of solids have been applied to composites with only limited success. These methods usually require relatively large specimens and considerable time and effort, especially if a complete set of elastic constants is required.[1] These methods, as applied to composites, include vibrating[2,3] or resonant-beam[4–6] tests, tensile or compressive tests,[1,7,8] torsion tests,[1,9] bending tests,[1,10] and pressure tests.[11–13] Generally, the elastic constants measured by these methods are less accurate than those acquires by ultrasonic tests.

Ultrasonic pulse techniques are limited by the necessity of using wavelengths that are large compared with fiber diameters and at the same time sufficiently small compared with the dimensions of the specimen so that true plane-wave conditions can exist. Since ultrasonic pulse methods are typically performed at megahertz frequencies, this condition cannot be met for many composites. If the wavelength is not larger than the fiber diameter, the wave is attenuated and scattered. Ultrasonic pulse-echo methods have been applied to some metal-matrix composites with extremely small fibers.[14–16] Even in these cases the pulse-echo trains are poor because of high attenuation and dispersion.[15] In fact, Achenbach and Herrman[17] predicted large dispersive effects for shear waves propagated in the fiber direction, even when the wavelength is much larger than fiber diameters. Zimmer and Cost[18] verified this prediction by measuring sound velocities in a unidirectional glass-reinforced epoxy-fiber composite. For wavelength-to-fiber diameter ratios of roughly 50, dispersion increased some phase velocities by a factor of 2. Elastic constants of some carbon-fiber-reinforced plastics have also been measured by ultrasonic pulse-echo techniques.[19–21]

Attempts to use 10-MHz pulse-echo techniques on the composite studied herein were unsuccessful. Both longitudinal and shear waves were propagated along all orientations and produced no detectable echoes. This is understandable since the filament sizes for this composite, as described in the text, are larger than the sound wavelength. Larger specimens than are currently available would be needed for 1—5-MHz pulses, although it is doubtful that even these frequencies would produce useable echo patterns for this material.

The ultrasonic immersion technique, as described by Markham,[22] is fast and accurate and offers the possibility of measuring all the elastic properties on one specimen. However, this technique is also limited by fiber size and by sample dimensions.[23,24] The choice of ultrasonic modes that can be propagated in a given direction in a specimen is also limited, and the technique is inapplicable to low-temperature measurements.

Zecca and Hay[25] avoided the problems encountered with megahertz frequencies by using electrostatic transducers to generate and to detect resonant kilohertz frequencies of a metal-matrix composite. Electrostatic transducers, however, cannot be used with nonmetallic materials.

The most widely used ultrasonic technique, using kilohertz frequencies, is the resonant piezoelectric oscillator. This method is due principally to Quimby and associates.[26] Quimby thoroughly analyzed the vibrations of solid rods driven by a piezoelectric crystal, and Balamuth[27] first employed drivers and specimens of matching fundamental frequencies. Rose[28] extended this method to torsional oscillators. Basically, the piezoelectric properties of quartz are used to generate and to detect resonant frequencies of an oscillator consisting of one or two quartz crystals, a specimen, and perhaps a dummy rod, all cemented together. This method has been used to measure elastic moduli at both high[29,30] and

 Copyright © 1975 American Institute of Physics

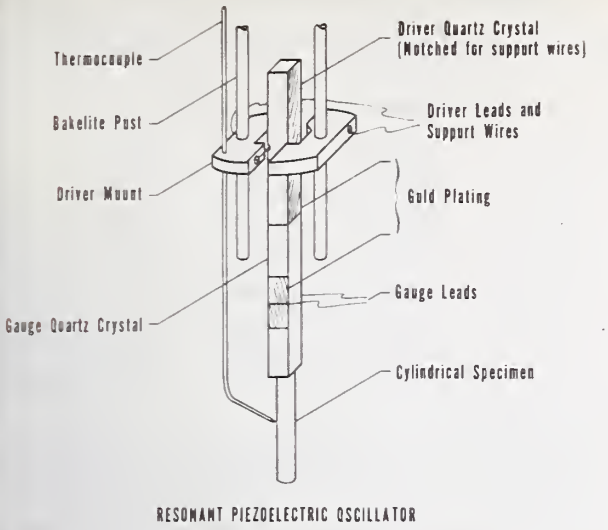

FIG. 1. Resonant piezoelectric oscillator apparatus.

low[27,28,30,31] temperatures, and has worked well with both metals[32,33] and nonmetals.[27–31] Thus, this technique is well understood both theoretically and practically, and it would seem to be well suited for testing composites. The long wavelengths used (typically on the order of centimeters in the kilohertz region) are much larger than fiber diameters, and, since the technique employs standing waves rather than traveling waves, specimen sizes can still be kept small.

In the present paper it is described how this resonance technique was used to measure the complete set of elastic compliances of a superconducting coil composite, which was essentially composed of an epoxy matrix and unidirectional copper-niobium-titanium fibers. The compliances were measured semicontinuously from 300 to 4 K. Results are given also for an epoxy—fiber-glass layered composite. The results generally agreed closely with the few existing static measurements on the same composite.

II. EXPERIMENTAL PROCEDURE

A. Resonant piezoelectric oscillator

The three-component resonant piezoelectric oscillator technique was originally described by Marx,[34] and was discussed in detail by Fine.[35] The technique consists of bonding quartz-driver and quartz-gauge piezoelectric crystals to a specimen to produce and to detect a standing longitudinal (or torsional) resonant wave. Each component's length is adjusted so that its resonant frequency is closely matched to that of the other components. The system is then driven by the driver transducer at its resonant frequency, which is monitored by the gauge crystal.

Longitudinal waves are excited by α-quartz bars of square cross section, excited into longitudinal vibration by an ac signal applied to full-length adherent electrodes (see Fig. 1). The driver quartz was fully gold plated on two parallel sides (z faces) with a shallow notch cut in the center of each electrode. Fine gold-plated tungsten wires, seated in these notches, served to suspend the resonator assembly at displacement nodes and provided the necessary electrical contact. The gauge quartz was gold plated only over the center third of the two parallel faces and electrical contact was made through fine wires adhered into the notches with silver conducting paint. The electric axes of the driver and the gauge crystals were perpendicular to reduce electrical pickup.

The longitudinal oscillator apparatus is illustrated in Fig. 1. The driver-quartz crystal was suspended by 0.003 in gold-plated tungsten wires. The driver mounts, which were aluminum, were removed during the torsional measurements, since the torsional driver crystal was suspended between the Bakelite posts by nylon threads. The specimens were cylindrical for all measurements. The chromel-constantan thermocouple was placed near, but not touching, the specimen. The entire apparatus was sealed in a thin-walled stainless-steel can. The can was partially evacuated, placed in the ullage of a helium Dewar, and lowered stepwise to achieve cooling.

The torsional quartz crystals were circular with their length in the x direction and with four gold-plated electrodes running the length of the crystal.[36] Opposite pairs of electrodes were electrically connected. The driver quartz was suspended vertically by means of fine nylon treads attached with varnish to opposite sides of the quartz near a displacement node of vibration.

The quartz crystals were bonded together with a semipermanent adhesive, Eastman 910.[37] The specimens were right-circular cylinders and were also bonded to the gauge quartz with the same adhesive. For some torsional experiments, this cement occasionally failed at low temperatures; such experiments were repeated until successful. Other materials such as vacuum grease and epoxy resin have been used as low-temperature bonding agents.[38]

The quartz crystals used had resonant frequencies of 60 and 100 kHz. Most of the measurements were done with the 60-kHz quartz crystals ($\frac{3}{16}$-in. square cross for longitudinal, and $\frac{3}{16}$ in. in diameter for torsional), but some were done with the 100-kHz crystals ($\frac{1}{8}$ in. in diameter). The mass of each driver-gauge combination was noted and the resonant frequencies were monitored from 300 to 4 K. The length of each specimen was determined such that its resonant frequency for the entire temperature range was within approximately 5% of the oscillator assembly although in some cases the specimen frequency differed by as much as 10%. The mass, length, and diameter of each specimen were noted and its mass density was determined by Archimedes's method using distilled water as a standard. The specimen was then cemented to the quartz crystals and the resonant frequency of the oscillator was monitored from 300 to 4 K. No thermal contraction corrections were made; for the coil composite described below this introduces a maximum error (over a 300 K range) of about 0.5%.[39] Maximum uncertainties in the frequency measurements are estimated to be about one part in 10^5.

B. Electronics

Most workers who have used the piezoelectric oscillator technique have employed electronics similar to those described by Marx.[34] This system requires manual adjustment of the input frequency to the driver crystal to keep the oscillator at resonance. A less time-consuming and more accurate system is the regenerative system designed by Gerk[40] and slightly modified by Johnson.[41]

Gerk's system consists primarily of a closed loop containing an amplifier and the driver-gauge combination of piezoelectric crystals, which act as a resonant element, with a feedback circuit to control the gain of the amplifier. This system is based on the principles of an oscillator; that is, the output of an amplifier is fed into the input through a frequency-selective network (the quartz crystals). The phase shifts are corrected with a variable phase shifter. A more complete description of the system was given by Gerk.[40] This system locks onto the resonant frequency and automatically stays at the resonant frequency if this frequency changes, due to a change of the specimen's environment, for example.

C. Specimens

The superconducting coil composite is fully described elsewhere.[39] Basically, the coil is composed of a copper-stabilized niobium-titanium wire (0.56 ×0.72 mm cross section) coil impregnated with epoxy. The wire layers are separated by layers of dry fiber-glass cloth (0.1 mm thick). The copper-to-superconductor volume ratio of the wire is 1.8–1. The wire-to-epoxy cross-sectional area fraction is about 3 to 1. The coil dimensions were approximately 19 cm i.d., 24 cm o.d., and 10 cm long.

Coordinate axes were chosen to coincide with the specimen axes. The longitudinal axis (3 axis) coincides with the axis of the wire, which was assumed to have zero helix angle. The 1 and 2 axes lie along the radius and coil axes, respectively, and form an orthogonal set with the 3 axis. The symmetry of the coil (orthorhombic) requires nine elastic constants to characterize the material. By assuming the material to be transversely isotropic and by neglecting the effects of curvature, the number of independent elastic constants is reduced to five. An orthotropic body with transverse isotropy has the same symmetry as close-packed hexagonal crystals such as magnesium and zinc. Justification for equating the 1 and 2 axes is given elsewhere,[39] and additional experimental data show that the effect of curvature on the moduli is minor.[42]

The masses, lengths, and angles between the specimen axis and the 3 axis are given in Table I. The density of the coil composite was found to be 6.000 g/cm^3.

Besides the superconducting coil, some specimens composed only of the fiber-glass cloth and epoxy were available. The fiber-glass—to—epoxy volume ratio in these samples was approximately the same as in the coil composite. Measurements were made on two specimens of this material. Dimensions and orientations of these specimens are also reported in Table I, with the angle θ corresponding to the angle between the specimen axis and the direction parallel to the layers of fiber-glass cloth. The density of this material was found to be 1.931 g/cm^3. This material can also be considered transversely isotropic, if the fiber-glass is considered transversely isotropic. Thus, five constants are again needed to completely characterize the material elastically. Cylindrical specimens of only one orientation were available; thus, only two elastic constants of the fiber-glass—epoxy matrix material were determined.

TABLE I. Dimensions and orientations of specimens.

Specimen No.	Diameter (in.)	Mass (g)	Length (cm)	θ (deg)
Superconducting coil composite specimens				
1	0.1250	0.540	1.1128	90
2	0.1250	0.925	1.9439	0
3	0.1863	1.081	1.0818	0
4	0.1890	1.248	1.1481	90
5	0.1875	1.874	1.7600	60
6	0.1851	1.327	1.2555	60
Epoxy-fiber-glass composite specimens				
1	0.1875	0.885	2.5387	0
2	0.1878	0.520	1.4862	0

III. RESULTS

The directly measured quantity in these measurements is f_0, the frequency of the three-component piezoelectric resonator. For longitudinal resonance the frequency of the specimen (f_s) can be found from f_0, the frequency of the driver-gauge quartz assembly (f_q), the mass of the specimen (m_s), and the mass of the quartz (m_q) [43]:

$$f_s^2 = f_0^2 + (f_0^2 - f_q^2) m_q / m_s . \tag{1}$$

This formula is more exact than the approximation

$$f_s = f_0 + (f_0 - f_q) m_q / m_s , \tag{2}$$

which is usually quoted and used for resonant oscillators.[34]

The formula for the torsional oscillator is somewhat more complicated since the moments of inertia (rather than the masses) of the components are involved[36]:

$$f_s^2 = f_0^2 + (f_0^2 - f_q^2) m_q r_q^2 / m_s r_s^2 . \tag{3}$$

Here, r_q is the radius of the quartz and r_s is the radius of the specimen.

The Young's modulus E or shear modulus G for the particular orientation of the specimen is given by

$$E \text{ or } G = 4L^2 f_s^2 \rho . \tag{4}$$

E is found from the longitudinal-mode fundamental frequency and G is found from the torsional-mode fundamental frequency. In Eq. (4), L is the specimen length and ρ is the mass density.

Thus, the measured quantities are the Young's and shear moduli, which are directly related to the elastic compliances S_{ij}. However, if the wavelength is not much larger than the sample dimensions, a correction for the Poisson contraction (or lateral motion) must be

TABLE II. Experiments performed on superconducting coil composite.

Exp. No.	Spec. No.	Mode	θ	Measured quantity
1	1	L	90	$E_{11}=\frac{1}{S_{11}}$
2	2	L	0	$E_{33}=\frac{1}{S_{33}}$
3	3	T	0	$G_{13}=\frac{1}{S_{44}}$
4	4	T	90	$G'=\frac{2}{S_{44}+S_{66}}$
5	5	L	60	$E_{\theta=60°}=\frac{16}{9S_{11}+S_{33}+6S_{13}+3S_{44}}$
6	6	T	60	$G_{\theta=60°}=\frac{8}{3S_{11}+3S_{33}-6S_{13}+2S_{44}+3S_{66}}$

applied to Young's modulus.[35] When the length-to-diameter ratio is 10 to 1, this correction amounts to about one part in 10^3.

The value of Young's modulus for an arbitrary direction in a specimen with transverse isotropy is given in terms of the elastic compliances by[44]

$$1/E=S_{11}\sin^4\theta+S_{33}\cos^4\theta+(2S_{13}+S_{44})\sin^2\theta\cos^2\theta, \quad (5)$$

where θ is the angle between the specimen axis and the unique axis. Similarly, the shear modulus is

$$1/G=S_{44}+(S_{11}-S_{12}-\tfrac{1}{2}S_{44})\sin^2\theta+2(S_{11}+S_{33}-2S_{13}-S_{44})\sin^2\theta\cos^2\theta. \quad (6)$$

Most measurements were made during cooling. All experiments were performed at least twice, and any unusual behavior was examined on heating as well as cooling, for reversibility.

A. Superconducting coil composite

Measurements made on the coil composite are listed in Table II. Again, θ is the angle between the specimen axis and the 3 axis (longitudinal axis). The mode specifies either longitudinal or torsional oscillations. The subscripts on E and G designate the direction of the force and the plane on which the force is applied, respectively. The compliances S_{11}, S_{33}, and S_{44} are found directly from experiments 1, 2, and 3, respectively. From experiment 4, S_{12} is found using the relation $2(S_{11}-S_{12})=S_{66}$ and the value of S_{44} from experiment 3. Either specimen 5 or 6 can be used to determine S_{13}. This compliance must be determined from a measurement on a specimen with its axis at an angle to the longitudinal direction. As can be seen from Table II, however, the Young's or shear modulus measured on specimens with $0°<\theta<90°$ is only partly dependent on S_{13}. Thus, S_{13} will be the least accurately determined compliance. The measurement of this compliance corresponds to the measurement of the elastic stiffness C_{13} by megahertz ultrasonic techniques. Zimmer and Cost[17] encountered difficulty in measuring C_{13} for a composite material and their estimated uncertainty in this elastic constant (100%) was ascribed to dispersion as well as to the relatively high inaccuracy.

The experimental data are presented in Figs. 2–7. The smooth curves represent regular temperature be-

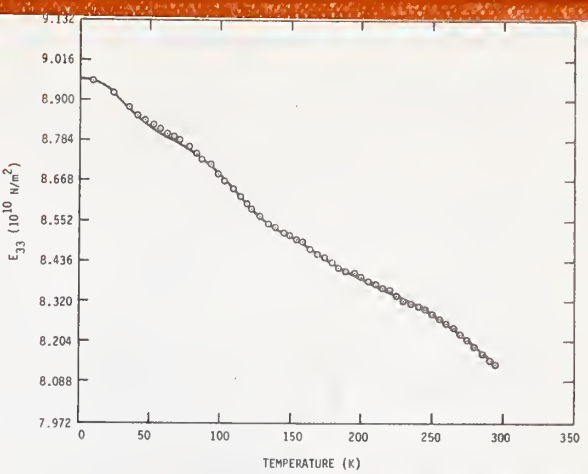

FIG. 3. Young's modulus of the superconducting coil composite, $\theta=0°$.

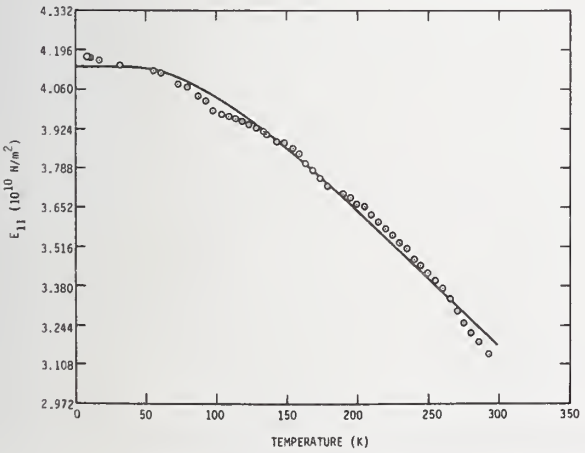

FIG. 2. Young's modulus of the superconducting coil composite, $\theta=90°$.

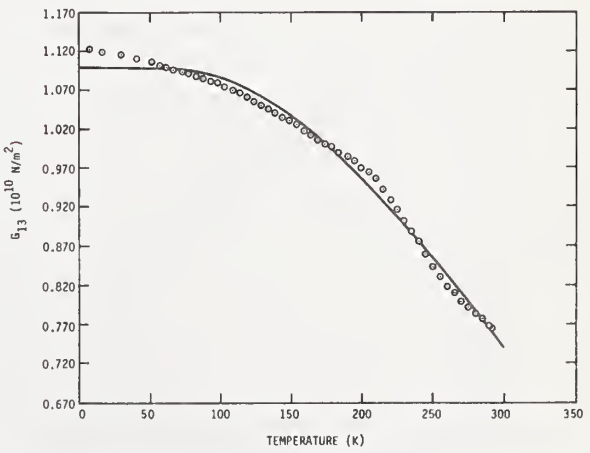

FIG. 4. Shear modulus of the superconducting coil composite, $\theta=0°$.

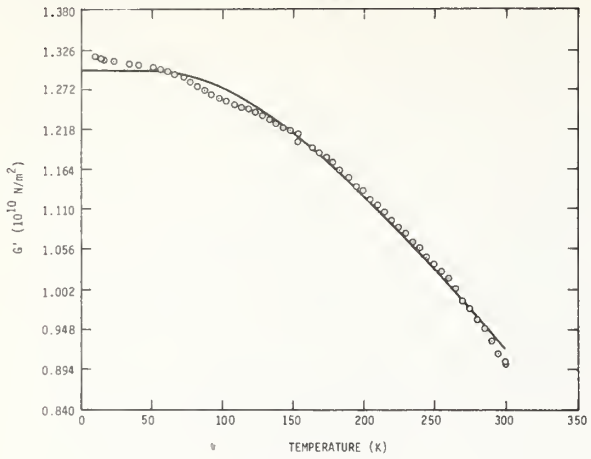

FIG. 5. Shear modulus of the superconducting coil composite, $\theta = 90°$.

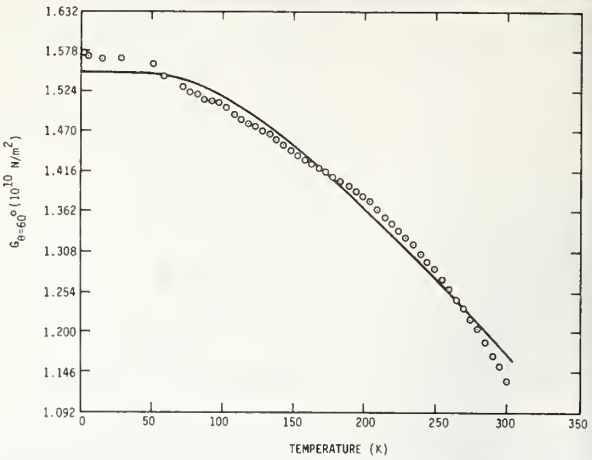

FIG. 7. Shear modulus of the superconducting coil composite, $\theta = 60°$.

havior as given by a theoretical relationship suggested by Varshni[45] that has been used successfully to represent the temperature dependences of metals,[45] ionic solids,[45] and several alloys.[46] The over-all fit of this function to these data is not nearly as good as for other materials, and the data for E_{33} could not be fitted to the Varshni function because of its concave-upward curvature. A smooth curve was drawn through the data points and the actual point values were used in calculations. This modulus was measured several times to check its behavior, and data from different measurements agreed closely. These data had completely reversible temperature response.

The shear modulus corresponding to shearing the axial planes in the radial direction G_{12}, or vice versa, is shown in Fig. 8. This modulus was calculated from the curve values of G_{13} and G', since $G_{12} = 1/S_{66}$.

Because of the difficulty in machining the specimens to small radii, the ratios of lengths to diameters were in some cases on the order of 4 or 5 to 1. The estimated correction to the Young's moduli in these cases is still only about 1%.

The elastic compliances as functions of temperature are given in Table III. The compliances S_{11}, S_{33}, and S_{44} are just reciprocals of E_{11}, E_{33}, and G_{13}, as mentioned previously. The error in the directly measured moduli is estimated to be about 1%; thus these compliances should be accurate to 1% also. The compliance S_{12} is found from combining the results of three measurements. Thus, S_{12} may be less accurately known. It was found that in solving for S_{13} from either Eq. (5) or (6), a 1% error in the measured modulus led to a 10—20% error in S_{13}. Thus, the error associated with S_{13} is considerable, perhaps as much as 100%. The values reported for S_{13} are the average of the values found from experiments 5 and 6, which are -0.110 and -0.058, respectively. From the material available, it was not possible to machine specimens with $\theta < 60°$ for other determinations of S_{13}. As expected, the material was found to be highly anisotropic with $s_{11} \approx 2s_{33}$.

It is emphasized that the data reported here are dynamic (adiabatic) rather than static (isothermal) and apply to rapid, rather than slow, loading. Conversion formulas are given in Landau and Litschitz,[47] for ex-

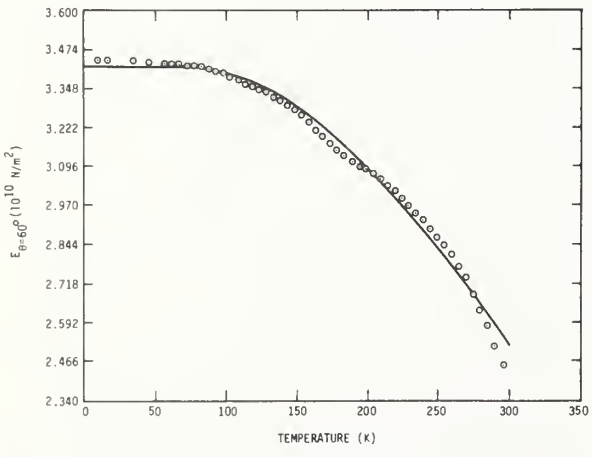

FIG. 6. Young's modulus of the superconducting coil composite, $\theta = 60°$.

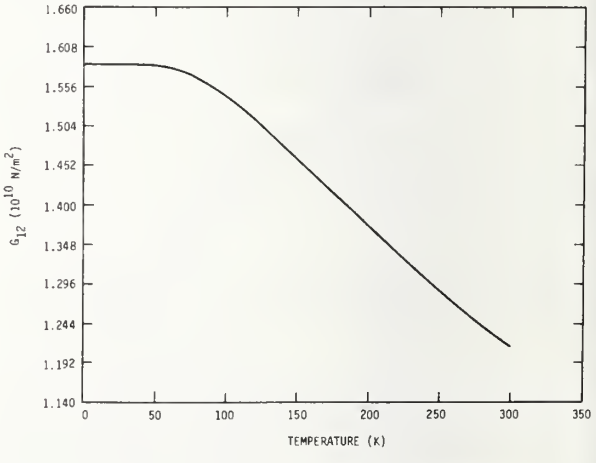

FIG. 8. Shear modulus G_{12} of the superconducting coil composite.

TABLE III. Elastic compliances of the superconducting coil composite at selected temperatures (10^{-10} m^2/N) as determined by resonance oscillator techniques.

T (K)	S_{11}	S_{12}	S_{13}	S_{33}	S_{44}	S_{66}
0	0.242	−0.074	−0.061	0.112	0.910	0.631
50	0.242	−0.074	−0.061	0.113	0.910	0.632
100	0.248	−0.076	−0.066	0.115	0.920	0.648
150	0.260	−0.083	−0.073	0.118	0.964	0.684
200	0.275	−0.089	−0.079	0.119	1.046	0.728
250	0.294	−0.094	−0.082	0.121	1.170	0.776
300	0.316	−0.096	−0.084	0.123	1.350	0.823

ample; in most cases the differences between adiabatic and isothermal elastic constants are small. These formulas involve the thermal-expansion coefficients and the specific heat. The thermal-expansion coefficients are known for this composite,[39] but the specific heat has not yet been determined. If an estimate of the specific heats of the components, the difference between the adiabatic and isothermal Young's moduli is at most 0.5%. The adiabatic and isothermal shear moduli are, of course, equal.

B. Epoxy-fiber-glass composite

Measurements were also made on the epoxy—fiber-glass specimens listed in Table I. These specimens were oriented with the layers of fiber-glass cloth running the length of the specimen; these were the only orientations available. The Young's and shear moduli are shown in Figs. 9 and 10. The shear modulus is well represented by the Varshni function, and is seen to have normal temperature behavior. A smooth curve was drawn through the Young's modulus data, which could not be fitted to the Varshni function because of the low-temperature maximum.

IV. DISCUSSION

Some elastic data, taken by conventional static methods, were available for the superconducting coil composite and the epoxy—fiber-glass composite.[39] These data generally compared very favorably with the resonance data. For example, resonance values of E_{11} at room temperature and 4 K are 12 and 1% larger than the static data taken at these temperatures. The inaccuracy of the static values is given as about 10%. Also, resonance values of E_{33} agree with the static data within 5—7%, and resonance values of G_{13} agree with the static values within 6—11%.

Other elastic constants of interest include the Poisson ratios:

$$\nu_{12} = -S_{12}/S_{11} \tag{7}$$

and

$$\nu_{13} = -S_{13}/S_{33}, \tag{8}$$

where ν_{ij} represents the negative ratio of strain in the j direction to strain in the i direction.

The value of ν_{12} at room temperature is 0.304. The reported[39] static value is 0.335, with the inaccuracy again believed to be about 10%. Thus, this result gives added confidence to the resonance value of S_{12}. However, the Poisson ratio ν_{13}, involves the compliance S_{13}, which has already been noted to be much more inaccurate than the other four compliances. In fact, if the room-temperature values of S_{13} and S_{33} are used, $\nu_{13} = 0.683$, whereas the static value is 0.333.[39] Since the other elastic constants are all in relatively good agreement with the static values, it is reasonable to expect that ν_{13} should be also. Thus, the value of S_{13} is highly suspect, especially since a value near $\frac{1}{3}$ seems more realistic for Poisson's ratio.

It is also of interest to consider the compressibilities. For a material with transverse isotropy, the linear compressibilities are

$$k_1 = S_{11} + S_{12} + S_{13}$$

and (9)

$$k_3 = 2S_{13} + S_{33},$$

where the subscripts designate the axis. Also, the volume compressibility is

$$K = 2k_1 + k_3. \tag{10}$$

If the room-temperature values of the compliances, as given in Table III, are used, then $k_1 = 0.136 \times 10^{-10}$

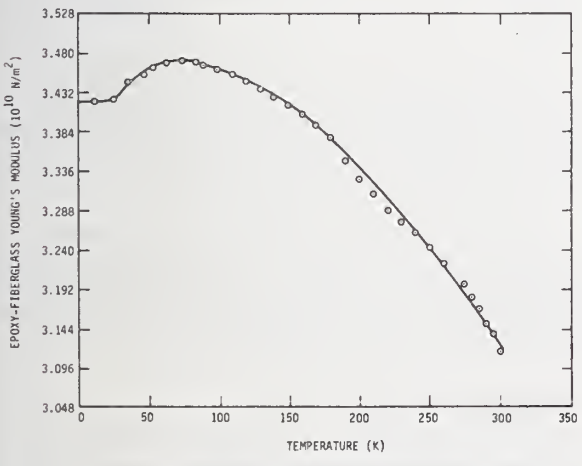

FIG. 9. Young's modulus of epoxy—fiber-glass, $\theta = 0°$.

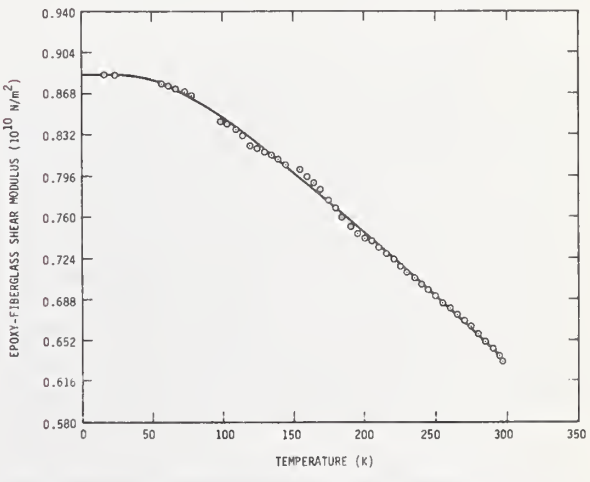

FIG. 10. Shear modulus of epoxy—fiber-glass, $\theta = 0°$.

TABLE IV. Elastic stiffnesses of the superconducting coil composite at selected temperatures (10^{10} N/m^2).

T (K)	C_{11}[a]	C_{12}[a]	C_{13}[a]	C_{33}[a]	C_{44}	C_{66}
0	5.10	1.94	2.39	10.59	1.10	1.58
50	5.10	1.93	2.39	10.46	1.10	1.58
100	4.99	1.90	2.34	10.27	1.09	1.54
150	4.80	1.87	2.27	10.05	1.04	1.46
200	4.54	1.79	2.15	9.86	0.96	1.37
250	4.21	1.63	1.99	9.64	0.85	1.29
300	3.82	1.39	1.77	9.35	0.74	1.22

[a]These constants are dependent on ν_{13}, and were calculated using the static value of ν_{13}, which was taken as independent of temperature.

m^2/N, $k_3 = -0.045\times10^{-10}$ m^2/N, and $K = 0.027\times10^{-10}$ m^2/N. However, if the Poisson ratio ν_{13} is taken as $\frac{1}{3}$, then $S_{13} = -0.041\times10^{-10}$ m^2/N at room temperature, and $k_1 = 0.179\times10^{-10}$ m^2/N $k_3 = 0.041\times10^{-10}$ m^2/N, and the volume compressibility $K = 0.399\times10^{-10}$ m^2/N. The relatively large value for ν_{13} and the negative k_3 that result from the resonance S_{13} may not be unreasonable, considering the multicomponent material. The elastic stiffness coefficients, however, can be calculated from the compliances and indicate that the resonance value of S_{13} is in error.

The elastic stiffnesses (C_{ij}) can be directly calculated by inverting the S_{ij} matrix if all the compliances are known. The explicit relationships are[48]

$$
\begin{aligned}
C_{11} &= \frac{S_{11}S_{33} - S_{13}^2}{(S_{11} - S_{12})\tilde{S}}, \\
C_{12} &= \frac{S_{13}^2 - S_{12}S_{33}}{(S_{11} - S_{12})\tilde{S}}, \\
C_{13} &= \frac{-S_{13}}{\tilde{S}}, \\
C_{33} &= \frac{S_{11} + S_{12}}{\tilde{S}}, \\
C_{44} &= \frac{1}{S_{44}},
\end{aligned}
\tag{11}
$$

and

$$
C_{66} = \frac{1}{S_{66}},
$$

where $\tilde{S} = S_{33}(S_{11} + S_{12}) - 2S_{13}^2$. Except for C_{44} and C_{66}, these relationships depend strongly on S_{13}. Using the resonance value of S_{13}, the elastic stiffnesses that depend on S_{13} are found to increase with increasing temperature, which is contrary to normal behavior. Since the Young's and shear moduli all behave fairly regularly with temperature, the resonance value of S_{13} seems unreasonable. In calculating the elastic stiffnesses, then, a value of $\frac{1}{3}$ for ν_{13} was used, and this Poisson's ratio was taken as constant with temperature.[39] It is believed that the elastic stiffnesses obtained this way are more accurate than those obtained using the resonance value of S_{13}. The elastic stiffnesses are given in Table IV.

As expected, the elastic properties of this composite are highly anisotropic. The anisotropy is best described by considering the percent elastic anisotropy as discussed by Chung and Buessem.[49] For transversely isotropic symmetry, this scheme involves using the conventional anisotropy ratios (the linear compressibility ratio $A_c = k_3/k_1$, and the shear anisotropy $A_s = C_{44}/C_{66}$) to calculate anisotropy parameters A_c^* and A_s^* with the following properties: A^* is zero for materials that are elastically isotropic, i.e., $A = 1$; A^* is always positive and a single-valued measure of the elastic anisotropy of a material regardless of whether $A < 1$ or $A > 1$; and A^* gives the relative magnitude of the elastic anisotropy present in the material. For this composite $A_c \approx 0.23$, $A_c^* \approx 8.4\%$, $A_s \approx 0.61$, and $A_s^* \approx 12.3\%$. For comparison, $A_c^* \approx 9.9\%$ and $A_s^* \approx 13.7\%$ for zinc,[49] which is one of the most anisotropic hexagonal metals.

The static value of Young's modulus of the fiberglass—epoxy is also available.[40] This Young's modulus was measured on a specimen oriented like the one used for the resonance measurements. The resonance and static values differ by 4—10%. There was no evidence of a maximum in the static data, but it is believed that the maximum is real. This maximum was observed during several measurements and was completely reversible. No explanation for this behavior can be given at this time.

V. CONCLUSIONS

The resonant piezoelectric oscillator method used in this work is generally suitable for measuring the elastic properties of composite materials. This method is accurate, fast, and requires only small specimens. It is suitable for measurements at all temperatures from 0 K to greater than 1000 °C.[29,30] The general techniques and theory of this method are well understood. This method does not appear to have the limitations of static and other ultrasonic techniques.

The elastic compliance data presented in this work generally agree well with existing data taken by conventional static methods, with the exception of S_{13}. It is believed, however, that if specimens with different orientations were available, a more accurate determination of S_{13} could be made. These data can be used to calculate other elastic properties, such as the elastic stiffness coefficients and compressibilities. However, many of these elastic properties depend on S_{13}, and their accuracies would also benefit from a better determination of S_{13}.

The superconducting coil composite was highly anisotropic, with elastic anisotropies similar to those of zinc. This high anisotropy, characteristic of many composite materials, necessitates careful measurements of elastic properties of these materials.

The measured elastic moduli of the composite are not as well represented by the Varshni function as they are for most metals and alloys; i.e., the elastic moduli of the superconducting coil composite are less regularly behaved with respect to temperature.

ACKNOWLEDGMENTS

The author would like to express his graditude to D. L. Johnson for his considerable assistance with the piezoelectric oscillator techniques. He would also like to

data on the coil composite, and H. Dickinson, who aided in the experiments. The author is also indebted to H.M. Ledbetter for many helpful discussions on elastic properties in general and for a critical reading of the manuscript. This work was supported in part by the Annapolis Laboratory of the Naval Ship Research and Development Center and in part by the Advanced Research Projects Agency of the U.S. Department of Defense.

*NRC-NBS Postdoctoral Research Associate, 1974—5.
[1]P.R. Goggin, J. Mater. Sci. 8, 233 (1973).
[2]T.J. Dudek, J. Compos. Mater. 4, 232 (1970).
[3]T. Hirai and D.E. Kline, J. Compos. Mater. 7, 160 (1973).
[4]Albert B. Schultz and Stephen W. Tsai, J. Compos. Mater. 2, 368 (1968).
[5]R.C. Rossi, J.R. Cost, and K.R. Janowski, J. Am. Ceram. Soc. 55, 234 (1972).
[6]G.C. Wright, J. Sound Vib. 21, 205 (1972).
R.E. Allred and W.R. Hoover, J. Compos. Mater. 8, 15 (1974).
[8]L.J. Cohen and O. Ishai, J. Compos. Mater. 1, 1030 (1967).
[9]N.L. Hancox, J. Mater. Sci. 7, 1030 (1972).
[10]T.R. Tauchert, J. Compos. Mater. 5, 456 (1971).
[11]A. Smith, J. Phys. E 5, 274 (1972).
[12]A. Smith, W.N. Reynolds, and N.L. Hancox, J. Compos. Mater. 7, 138 (1973).
[13]A. Smith, S.J. Wilkinson, and W.N. Reynolds, J. Mater. Sci. 9, 547 (1974).
[14]J.V. Grabel and J.R. Cost, Met. Trans. 3, 1973 (1972).
[15]A.E. Lord and D. Robert Hay, J. Compos. Mater. 6, 278 (1972).
[16]W. Sachse, J. Compos. Mater. 8, 378 (1974).
[17]J.O. Achenbach and G. Hermann, AIAA J. 6, 1832 (1968).
[18]J.E. Zimmer and J.R. Cost, J. Acoust. Soc. Am. 47, 795 (1970).
[19]W.N. Reynolds and S.J. Wilkinson, Ultrasonics 12, 109 (1974).
[20]S.J. Wilkinson and W.N. Reynolds, J. Phys. D 7, 50 (1974).
[21]T.R. Tauchert and A.N. Guzelsu, Trans. ASME 39, 93 (1972).
[24]Robert S. Smith, J. Appl. Phys. 43, 2555 (1972).
[25]A.R. Zecca and D.R. Hay, J. Compos. Mater. 4, 556 (1970).
[26]S.L. Quimby, Phys. Rev. 25, 558 (1925).
[27]L. Balamuth, Phys. Rev. 45, 715 (1934).
[28]F.C. Rose, Phys. Rev. 49, 50 (1936).
[29]L. Hunter and S. Siegel, Phys. Rev. 61, 84 (1942).
[30]J.W. Marx and J.M. Silvertsen, J. Appl. Phys. 24, 81 (1953).
[31]M.E. Fine, Rev. Sci. Instrum. 25, 1188 (1954).
[32]S. Siegel and S.L. Quimby, Phys. Rev. 49, 663 (1936).
[33]J. Zacarias, Phys. Rev. 44, 116 (1933).
[34]J. Marx, Rev. Sci. Instrum. 22, 503 (1951).
[35]M.E. Fine, ASTM Special Technical Publication No. 129, 1952, p. 48 (unpublished).
[36]W.H. Robinson, S.H. Carpenter, and J.L. Tallon, J. Appl. Phys. 45, 1975 (1974).
[37]The use in this paper of trade names of specific products is essential to a proper understanding of the work presented. Their use in no way implies any approval, endorsement, on recommendation by NBS.
[38]A.J. Matheson, J. Phys. E 4, 796 (1971).
[39]C.W. Fowlkes, P.E. Angerhofer, R.N. Newton, and A.F. Clark, National Bureau of Standards Report No. NBSIR 73-349, 1973 (unpublished).
[40]A.P. Gerk, Rev. Sci. Instrum. 43, 1786 (1972).
[41]D.L. Johnson (private communication).
[42]A.F. Clark, V.D. Arp, W.F. Weston, and J.G. Hust, National Bureau of Standards Report No. NBSIR 74-399, 1974 (unpublished).
[43]W.N. Robinson and A. Edgar, IEEE Trans. Sonics Ultrason. 21, 98 (1974).
[44]W. Voigt, *Lehrbuch der Kristallphysik* (Teubner, Berlin, 1928), pp. 746—7.
[45]Y.P. Varshni, Phys. Rev. B 2, 3952 (1970).
[46]E.R. Naimon, W.F. Weston, and H.M. Ledbetter, Cryogenics 14, 721 (1973).
[47]L.D. Landau and E.M. Lifshitz, *Theory of Elasticity* (Pergamon, London, 1959), p. 17.
[48]R.F.S. Hearmon, Rev. Mod. Phys. 18, 409 (1946).
[49]D.H. Chung and W.R. Buessem, *Anisotropy in Single-Crystal Compounds*, edited by F.W. Vahldiek and S.A. Mersol (Plenum, New York, 1968), Vol. 2, p. 217.

SEMI-ANNUAL REPORT ON MATERIALS RESEARCH
IN SUPPORT OF SUPERCONDUCTING MACHINERY

FRACTURE MECHANICS PARAMETERS OF ENGINEERING MATERIALS AT CRYOGENIC TEMPERATURES

R. L. Tobler, D. T. Read, and R. P. Reed

Cryogenics Division
Institute for Basic Standards
National Bureau of Standards
Boulder, Colorado 80302

April 1976

Summary: Fracture Mechanics Parameters of Engineering Materials at Cryogenic Temperatures

This section of the report contains two manuscripts. Fracture mechanics design data are presented for a nickel base superalloy, Inconel 718, and an aluminum base alloy, 2219-T6. The plane strain fracture toughness parameters (K_{Ic} and J_{Ic}), tensile, and fatigue crack growth rates (da/dN) were measured using state-of-the-art test procedures. The results are summarized as follows:

(1) The tensile, fatigue, and fracture properties of Inconel 718 alloy are nearly constant or slightly improved at decreasing temperatures between 295 and 4 K. The fracture toughness (K_{Ic}) at 4 K is 16% higher than the room temperature value of 96.3 MPa·$m^{1/2}$. This alloy is useful for cryogenic structural applications requiring an exceptional yield strength (1.172 GPa at 295 K) and moderate fracture toughness.

(2) J-integral resistance curves for three specimen thicknesses and valid (according to ASTM Method E 399) K_{Ic} values at 76 K are reported for aluminum alloy 2219. The J-integral values were independent of thickness at small crack extensions, but at substantial crack extensions the values for the thin specimens were larger than those for the thick specimens. The measured J_{Ic} values were less than those calculated from the measured K_{Ic} values. The reason for this discrepancy was that crack extension occurred before the K_{Ic} measurement point was reached.

LOW TEMPERATURE EFFECTS ON THE FRACTURE BEHAVIOR OF INCONEL 718[†]

R. L. Tobler

Cryogenics Division
Institute for Basic Standards
Boulder, Colorado 80302

ABSTRACT

The mechanical properties of a solution treated and double aged Inconel 718 forging were studied to assess its utility at temperatures in the ambient-to-cryogenic range. Uniaxial tensile property measurements using unnotched specimens at decreasing temperatures between 295 and 4 K show that yield and ultimate strengths increase by 20% and 29%, respectively, while ductility remains virtually constant. Fracture mechanics tests using 2.54 cm-thick compact specimens revealed that the fatigue crack growth resistance of this alloy improves slightly at extreme cryogenic temperatures, and its plane strain fracture toughness, K_{Ic}, increases from 96.3 MPa$\cdot$m$^{1/2}$ at 295 K to 112.3 MPa$\cdot$m$^{1/2}$ at 4 K. These results are compared with similar data for Inconel 750 alloys.

Key words: Fatigue; fracture; low temperature tests; mechanical properties; nickel alloys; superalloys.

[†] Contribution of NBS, not subject to copyright.

INTRODUCTION

A precipitation hardenable nickel base superalloy known as Inconel 718* was first developed for elevated temperature service. Then, by virtue of its austenitic structure, high strength, and weldability, the alloy found applications in the ambient-to-cryogenic temperature region as well. Current applications at temperatures as low as 20 K include liquid oxygen and liquid hydrogen pressure vessels for spacecraft. Emerging applications related to superconducting machinery (torque tubes, damper shields) will probably further extend the utility of Inconel 718 to temperatures approaching absolute zero.

A need for reliable mechanical property data accompanies the expanded use of this alloy. Conventional tensile properties for the temperature range 295 to 4 K [1-14] are insufficient to characterize the load-carrying capability of large structures subject to fatigue. As demonstrated by this study, relatively brittle fractures may occur when fatigue cracks are located in thick sections of Inconel 718, despite the fact that this material exhibits appreciable ductility in the unnotched condition.

The existing fatigue crack growth and fracture toughness data [12-17] relate predominantly to thin sections and non-standard specimen geometries, or concentrate only on room temperature properties. The present study describes the mechanical behavior of Inconel 718 at several temperatures including 295, 195, 76, and 4 K. In addition to conventional tensile property determinations, fatigue crack growth resistance was evaluated, and the ASTM standard method of test for plane strain fracture toughness of metallic materials (ASTM E-399-74) [18] was applied to generate valid K_{Ic} data for this alloy.

MATERIAL

The Inconel 718 alloy was purchased in the form of a forged 7.7 cm x 7.7 cm square bar that had been annealed at 1200 K for 1h. As quoted from the mill sheet, the chemical composition in weight percent is: 53.4 Ni, 18.5 Fe, 18.1 Cr, 5.24 Nb + Ta, 2.95 Mo, 0.90 Ti, 0.49 Al, 0.17 Co, 0.10 Mn, 0.10 Cu, 0.10 Si, 0.05 C, 0.01 P, 0.003 B, 0.002 S. All test specimens were machined prior to precipitation hardening, which followed the standard heat treatment:

1) Solution treatment (1256 K for 3/4h, air cool);

and 2) Double age (992 K for 8h, furnace cool to 894 K, hold 10h, and air cool).

PROCEDURES

Tensile

Tensile tests were conducted at room, liquid nitrogen, and liquid helium temperatures at a crosshead velocity of 0.008 mm per second. Reed [19] described the 44.5 kN screw-driven machine, cryostat, and low temperature techniques used here. The tensile specimens had a

---

* Tradenames are used in this report for clarity and in no way imply endorsement or recommendation by NBS.

reduced section 3.8 cm long and 0.51 cm in diameter. The tensile axis was transverse to the forging axis, such that the fracture plane orientation matched that of the compact specimens described below. The outputs of a commercial load cell and clip-on strain gage extensometer were recorded and analyzed as outlined in ASTM Method E8-72 [20].

Fracture

The compact specimens used for fatigue and fracture tests had a thickness, B, of 2.54 cm and a width, W, of 5.08 cm. These specimens were machined in the TS orientation [18], with their loading axis and crack propagation directions transverse to the original forging axis. Other specimen features were in accordance with the E-399-74 method, except that a modified notch was incorporated. As shown in Figure 1, the modified notch permits clip gage attachment at knife edges in the loadline.

Room temperature tests were conducted using a 100 kN servo-hydraulic test machine and cryostat in ambient air. Low temperature environments were achieved by immersing the load frame, specimen, and clip gage in alcohol and dry ice (195 K), liquid nitrogen (76 K) or liquid helium (4 K). The clip gage satisfied E-399-74 linearity requirements at each temperature. A detailed description of the low temperature apparatus and techniques was given by Fowlkes and Tobler [21].

Fracture toughness specimens were precracked at their K_{Ic} test temperatures and loaded to fracture at 1 $MPa \cdot m^{1/2}$ per second. Following the E-399-74 method, K_{Ic} was calculated from the solution for compact specimens:

$$K_{Ic} = P_Q B^{-1} W^{-1/2} [f(a/W)] \quad (1)$$

where

$$f(a/W) = 29.6 (a/W)^{1/2} - 185.5 (a/W)^{3/2} + 655.7 (a/W)^{5/2} - 1017.0 (a/W)^{7/2} + 638.9 (a/W)^{9/2} \quad (2)$$

In these equations, P_Q is the load defined by the secant offset procedure [18], and a is the average of three crack length measurements at 25, 50, and 75% of specimen thickness.

Fatigue

Fatigue crack growth rates were measured during the precracking of K_{Ic} specimens where the maximum stress intensity factor never exceeded 0.6 K_{Ic}. Additional specimens were tested to obtain growth rates at higher stress intensities. Although most specimens were 2.54 cm thick (W/B = 2), four tests of a 0.508 cm thickness (W/B = 10) were also included. The fatigue operations were conducted using controlled load, a sinusoidal load cycle, and a cycle frequency of 20 Hz; the ratio, R, of minimum/maximum load was 0.1.

Crack growth was monitored indirectly by compliance measurements, as previously described [21]. Briefly, a correlation between crack length and specimen deflection per unit load (δ/P) was determined by measurements on fractured specimens. The fatigue tests were

interrupted periodically to record δ/P, from which crack lengths could be inferred and plotted as a function of fatigue cycles, N. A computer program was used to fit the a-versus-N curves with a third order polynomial, to differentiate the curves to obtain da/dN values, and to calculate the associated stress intensity factor ranges, ΔK, from the peak fatigue loads:

$$\Delta K = (P_{max} - P_{min}) B^{-1} W^{-1/2} [f(a/W)] \quad (3)$$

RESULTS

Tensile

Table 1 lists the yield and ultimate strengths, elongation, and reduction in area measurements for Inconel 718 at 295, 76, and 4 K. These data are plotted in Figures 2-4, along with data for other Inconel 718 forgings in the 1256 K solution treated and double aged condition. The temperature dependences of these tensile parameters illustrate what are considered to be classical trends for face centered cubic metals and alloys [22-24]: ductility remains nearly constant, there is a moderate increase of yield strength, and a larger increase of ultimate strength. The yield strength of the present alloy ranges from 1.172 to 1.408 GPa over the temperature interval investigated, showing good agreement with other results [9-13].

On the other hand, the heat-to-heat variations of ductility appear to be sizable. With reference to Figure 4, reduction in area measurements at room temperature range from 14 to 30%, but the values for our alloy are intermediate at 19%.

Handbooks [1-3] contain other low temperature tensile data for thin sheet and other Inconel 718 stock having thermal or mechanical treatments differing from the 1256 K solutioning and double aging treatment studied here. The comparisons above are sufficient to demonstrate that the present is representative of commercially available forgings.

Fracture

The load-deflection behavior and fracture surface of a compact specimen tested at 4 K are shown in Figure 5. "Type I" test records [18] with slight nonlinearity prior to maximum load were observed at each temperature. The fracture surfaces displayed no shear portions but were flat and granular in appearance, and uninfluenced by test temperature.

The K_{Ic} calculations are itemized in Table 2. The 2.54 cm-thick specimens tested here amply satisfy the E-399-74 criterion for thickness, $B \geq 2.5 \left(\frac{K_{Ic}}{\sigma_y}\right)^2$, which requires a minimum thickness of 1.9 cm for this alloy at room temperature. Other information pertinent to assessing the validity of K_{Ic} measurements are included in Table 2. In three tests, a/W exceeded the 0.45 to 0.55 range. However, these three deviations are minor, and any effects on K_{Ic} results are considered negligible compared to the degree of scatter among specimens.

The average K_{Ic} value at each temperature is plotted in Figure 6. The data are mildly temperature dependent, showing a 16% increase from 96.3 to 112.3 $MPa \cdot m^{1/2}$ as temperature is lowered from 295 to 4 K. Logsdon, et al. [12] reported a 14% increase for compact specimens of an Inconel 718 alloy tested at 295 and 4 K. Note that their K_{Ic} values are lower (70 to

80 $MPa \cdot m^{1/2}$) compared to the present results; They also reported lower tensile ductility, as shown in Figures 3 and 4. Note also that the temperature dependence of fracture toughness for Inconel 718 is opposite to that for Inconel 750 alloys: as temperature is lowered, Inconel 750 shows moderate decreases in K_{Ic} amounting to 8% between 295 and 76 K [26], and 11% between 295 and 4 K [25].

The literature [13-16] contains other fracture toughness data for Inconel 718 which were not obtained by the E-399-74 method. Those measurements were derived from tests of center-notched, single-edge-notched, or surface-flawed specimens. To their advantage, surface-flawed specimens simulate a flaw type that commonly occurs in pressure vessels, but the fracture toughness results are directly applicable only when the service conditions match the specifics of specimen flaw shape and thickness. Hall's experimental results indicate that surface flawed specimens produce high apparent fracture toughness values as compared with the true K_{Ic} values from standard compact or bend specimens [27]. Further difficulty arises from the fact that the Inconel 718 specimens tested by Witzell [13], Pettit, Feddersen, and Mindin [14] and Taylor [16], are too thin (1.6 to 3.5 mm) to avoid size effects according to the E-399-74 criterion. For these reasons, such data are of limited value to designers. On the other hand, the K_{Ic} data of Figure 6 are independent of specimen geometry and represent true material constants which are generally applicable in design.

Fatigue Crack Growth Rates

As demonstrated by Paris and Erdogan [28], fatigue crack growth rates can usually be described as power-law functions of the stress intensity factor range, ΔK:

$$\frac{da}{dN} = C(\Delta K)^n \qquad (4)$$

where C and n are material constants that depend on environment and test variables. Logarithmic plots of da/dN-versus-ΔK measurements that are in agreement with Eq. (4) reveal linear trends from which n and C can be determined as the slope and ordinate intercept at $\Delta K = 1$, respectively.

The fatigue crack growth rates of Inconel 718 at 295, 195, 76, and 4 K are plotted on logarithmic coordinates in Figure 7. The data define a scatterband approximately 7 to 12 $MPa \cdot m^{1/2}$ wide. At equivalent ΔK values, the rates at cryogenic temperatures are slightly lower than at room temperature. However, the improvement in fatigue crack propagation resistance is modest, and barely distinguishable beyond the scatter of replicate tests unless the temperature differential exceeds 150 to 200 kelvins.

Linear segments representing two Paris equations were chosen to approximate the upper (295 K) and lower (4 K) extremes of data in Figure 7. Thus, at 295 K:

$$\frac{da}{dN} = 8 \times 10^{-11} (\Delta K)^4 \qquad (5)$$

and at 4 K:

$$\frac{da}{dN} = 4.8 \times 10^{-11} (\Delta K)^4 \qquad (6)$$

where ΔK is in $MPa \cdot m^{1/2}$ and da/dN is in mm/cycle. The exponent, n = 4, which some theories predict [29], provides a good approximation for these experimental results.

Figures 8 and 9 compare the fatigue crack propagation resistance of Inconel 718 with the available results for other nickel base alloys and stainless steels which could be considered material competitors for various applications. Note that the room temperature crack growth rates reported by Shahinian, Watson, and Smith [17] are in close agreement with the present data for Inconel 718. As shown in Figures 8 and 9, the fatigue crack propagation resistance of Inconel 718 is intermediate compared with other austenitic alloys.

DISCUSSION

The low temperature tensile properties of this Inconel 718 alloy were equivalent or superior to its properties at room temperature. Other studies of Inconel 718 alloys have shown that, as the temperature decreases to 4 K, Young's modulus increases by 6% [31], fatigue strength at 10^6 cycles increases by approximately 75% [8], and Charpy impact values show little change [11]. Since none of these parameters are deleteriously affected, the reliability of Inconel 718 structures will not be decreased at extreme cryogenic temperatures.

The attractive feature of a high yield strength which increases at cryogenic temperatures without sacrifice of tensile ductility justifies Inconel 718's selection for numerous applications. Nevertheless, this alloy is susceptible to brittle fracture in thick sections containing flaws. The fracture toughness at ambient and cryogenic temperatures is useful but moderate; therefore, accurate fracture mechanics evaluations seem necessary to assure structural safety and efficient design.

In the fracture mechanics approach, K is proportional to the magnitude of elastic stresses at the crack tip. Upon reaching a critical value, K_{Ic}, the material fractures catastrophically, without significant plastic deformation. Using handbook [32] equations for various component geometries of known dimensions and loadings, the maximum flaw size that a structure will tolerate can be calculated based on the material's K_{Ic} value. Fatigue crack growth rates enable a prediction of the total number of load cycles required to propagate an initial crack to critical proportions. Thus, the da/dN and K_{Ic} data of this report can be used to assess the safe operating lifetimes of Inconel 718 structures.

The significant finding that Inconel 718's da/dN and K_{Ic} parameters are nearly invariant at temperatures below 295 K should facilitate fracture mechanics analyses. For example, the performance of a component of this material at cryogenic temperatures could be conservatively predicted using room temperature data obtained from quality control tests of production material. Similarly, for convenience and economy, cryogenic structures might be proof-tested at room temperature.

An important question regarding alloy selection is whether Inconel 718 might supersede Inconel 750 as a construction material for some applications in superconducting generators.

Inconel 750 and 718 alloys possess a high resistance to fatigue crack propagation which seems to be a characteristic of austenitic alloys in general [30]. Figures 8-9 compared the fatigue crack growth rates of Inconel 750 and 718 with those reported for several austenitic stainless steels. Dismissing minor differences in the rates for Inconel 750 and 718, attention centers on yield strength and fracture toughness comparisons. At 4 K, the yield strengths of solution treated and double aged Inconel 750 alloys range from 0.736 to 1.194 GPa, depending on manufacturing process and heat treatment variations [25]; K_{Ic} values for the same heats range from 102 to 239 $MPa \cdot m^{1/2}$. Based on the present study, Inconel 718 offers a higher yield strength, 1.408 GPa, but its K_{Ic} value of 112 $MPa \cdot m^{1/2}$ is on the low side of the range for Inconel 750 alloys. This trade-off between yield strength and fracture toughness will determine alloy selection relative to the specific requirements of each application.

CONCLUSIONS

Uniaxial tensile properties and fracture mechanics data were obtained for a precipitation hardened Inconel 718 forging at temperatures in the ambient-to-cryogenic range. The temperature dependences of the mechanical properties of this alloy may be considered typical, qualitatively, of austenitic alloys in general. At 4 K, the yield strength of this Inconel 718 alloy was 20% greater than the room temperature value of 1.172 GPa. The K_{Ic} values showed that fracture toughness varies from 96.3 to 112.3 $MPa \cdot m^{1/2}$ between 295 and 4 K, whereas tensile ductility and fatigue crack growth resistance remain nearly constant. Based on these data trends, the load-carrying capability of flawed or unflawed Inconel 718 structures is not expected to decrease at cryogenic temperatures.

ACKNOWLEDGEMENTS

This program was sponsored by the Advanced Research Projects Agency of the U.S. Department of Defense. The contributions of Dr. R. P. Mikesell and R. L. Durcholz in conducting the tensile tests are gratefully acknowledged.

REFERENCES

1. Handbook on Materials for Superconducting Machinery, MCIC-HB-04 (Battelle Columbus Laboratories, 1974).
2. Cryogenic Materials Data Handbook, AFML-TDR-64-280 (Martin Marietta Co., 1964).
3. Materials Data Handbook: Inconel Alloy 718, NASA-CR-123774 (Western Res. and Dev. Inc., 1972).
4. Inconel Alloy 718, Bulletin T-39 (Huntington Alloy Products Division, International Nickel Co., 1973).
5. Wagner, H. J., Hall, A. M., Physical Metallurgy of Alloy 718, Defense Metals Information Center Report 217 (Battelle Memorial Institute, 1968).
6. Christian, J. L., in Advances in Cryogenic Engineering 12 (1962) 520.
7. Nachtigall, A. J., in Properties of Materials for Liquefied Natural Gas Tankage, ASTM STP 579 (Amer. Soc. Test. Mater., Philadelphia, 1975) 378.
8. Nachtigall, A. J., Klima, S. J., Freche, J. C., J. Materials, JMLSA 3 (1968) 425.
9. Inouye, F. T., Hunt, V., Janser, G. R., Frick, V., NASA Tech. Rept. CR-788 (Aerojet General Corp., 1967).
10. Morgan, W. R., NASA Internal Note IN-P and VE-M-66-2 (George C. Marshall Space Flight Center, 1966).
11. Malin, C. O., NASA Tech. Brief MFS-18244 (George C. Marshall Space Flight Center, 1965).
12. Logsdon, W. A., Kossowsky, R., Daniel, M. R., Wells, J. M., in Materials Research for Superconducting Machinery IV, Reed, R. P., Clark, A. F., and van Reuth, E. C., Eds., Semi-Annual Tech. Rept., October 1975 (Advanced Research Projects Agency, 1975).
13. Witzell, W. E., Tech. Rept. AFML-TR-67-257 (General Dynamics-Convair, 1967).
14. Pettit, D. E., Feddersen, C. E., Mindin, H., NASA CR 101942 (Battelle Memorial Institute, 1969).
15. Forman, R. G., NASA Tech. Note TN D-7665 (National Aeronautics and Space Administration, 1974).
16. Taylor, J. L., in Proceedings of the Seventh Symposium on Nondestructive Evaluation of Components and Materials in Aerospace (Amer. Soc. Nondestructive Testing, San Antonio, 1969) 420.
17. Shahinian, P., Watson, H. E., Smith, H. H., J. Materials, JMLSA 7 (1972) 527.
18. Annual Book of ASTM Standards, Part 10 (Amer. Soc. Test. Mater. Philadelphia, 1974) 432.
19. Reed, R. P., in Advances in Cryogenic Engineering 7 (1962) 448.
20. Annual Book of ASTM Standards, Part 31 (Amer. Soc. Test. Mater., Philadelphia, 1973) 220.
21. Fowlkes, C. W., Tobler, R. L., Eng. Fract. Mechs., to be published.
22. McLean, D., Mechanical Properties of Metals (Wiley, New York, 1962).
23. Conrad, H., in High Strength Materials (Wiley, New York, 1964).
24. Wigley, D. A., Mechanical Properties of Materials at Low Temperatures (Plenum, New York, 1971).
25. Logsdon, W. A., in International Cryogenic Materials Conference Proceedings (Plenum, New York, 1976) to be published.

26. Tobler, R. L., Mikesell, R. P., Durcholz, R. L., Reed, R. P., in Materials Research for Superconducting Machinery II, Clark, A. F., Reed, R. P., and van Reuth, E. C., Eds., Semi-Annual Tech. Rept., October 1974 (Advanced Research Projects Agency, 1974).
27. Hall, L. R., in Fracture Toughness Testing at Cryogenic Temperatures, ASTM STP 496 (Amer. Soc. Test. Mater., Philadelphia, 1970) 40.
28. Paris, P. C., Erdogan, F., J. Basic Engrg., Trans. ASME Series D, 85 (1963) 528.
29. Johnson, H. H., Paris, P. C., Eng. Fract. Mech. 1 (1968) 3.
30. Tobler, R. L., Reed, R. P., in International Cryogenic Materials Conference Proceedings (Plenum, New York, 1976) to be published.
31. Weston, W. F., Ledbetter, H. M., Mater. Sci. Eng. 20 (1975) 287.
32. Tada, H., Paris, P. C., Irwin, G. R., The Stress Analysis of Cracks Handbook (Del Research Corp., Hellertown, PA, 1973).

Table 1. Tensile property results for Inconel 718.

Temperature K		0.2% Yield Strength GPa	(ksi)	Ultimate Strength GPa	(ksi)	Elongation %	Reduction in Area %
295		1.165		1.391		16.1	19.5
		---		1.396		14.3	18.4
		1.178		1.425		15.8	16.8
	Avg	1.172	(170.0)	1.404	(203.6)	15.4	18.2
76		1.326		1.649		20.2	20.6
		1.359		1.649		20.9	18.9
	Avg	1.342	(197.4)	1.649	(239.2)	20.6	19.8
4		1.371		1.802		21.7	24.0
		1.445		1.830		19.5	16.3
		1.408	(204.2)	1.816	(263.4)	20.6	20.2

Table 2. Fracture toughness results for Inconel 718.

Temperature K	Specimen Number	a/W	K_f (a) $MPa \cdot m^{1/2}$	$\frac{a_{edge}}{a}$ (b)	P_m/P_Q (c)		K_{Ic} $MPa \cdot m^{1/2}$	($ksi \cdot in^{1/2}$)
295	3	0.461	30	0.92	1.02		104	
	4	0.499	37.5	0.95	1.01		91.5	
	9	0.575	54	0.93	1.01		93.5	
						Avg	96.3	(87.8)
195	2	0.565	51	0.93	1.08		100	
	5	0.465	38	0.95	1.06		112	
						Avg	106	(96.5)
76	1	0.536	43.5	0.95	1.02		110	
	14	0.561	55	0.92	1.03		96.5	
	16	0.480	45	0.92	1.03		103	
						Avg	103.2	(94)
4	8	0.555	55	0.93	1.05		104	
	13	0.512	48	0.95	1.09		119	
	15	0.470	50	0.92	1.05		114	
						Avg	112.3	(102.3)

[a] $K_f \leq 0.6\ K_{Ic}$ is required by the E-399-74 method.

[b] an edge-crack-to-average-crack-length ratio, $a_{edge}/a \geq .90$ is required.

[c] $P_m/P_Q < 1.10$ is required.

LIST OF FIGURES

Figure 1. Compact specimen used for fatigue and fracture tests.

Figure 2. Yield and ultimate tensile strengths of Inconel 718 forgings in the solution treated (1225 to 1256 K) and double aged condition.

Figure 3. Tensile elongation of Inconel 718 forgings in the solution treated and double aged condition.

Figure 4. Reduction in area of Inconel 718 forgings in the solution treated and double aged condition.

Figure 5. Fracture toughness test record for Inconel 718, showing fracture surface appearance.

Figure 6. Temperature dependence of fracture toughness for two Inconel 718 alloys.

Figure 7. Fatigue crack propagation rates for Inconel 718.

Figure 8. Comparison of fatigue crack propagation rates of Inconel alloys 718 and 750.

Figure 9. Comparison of fatigue crack propagation rates of Inconel 718, Inconel 750, and austenitic stainless steels at 4 K.

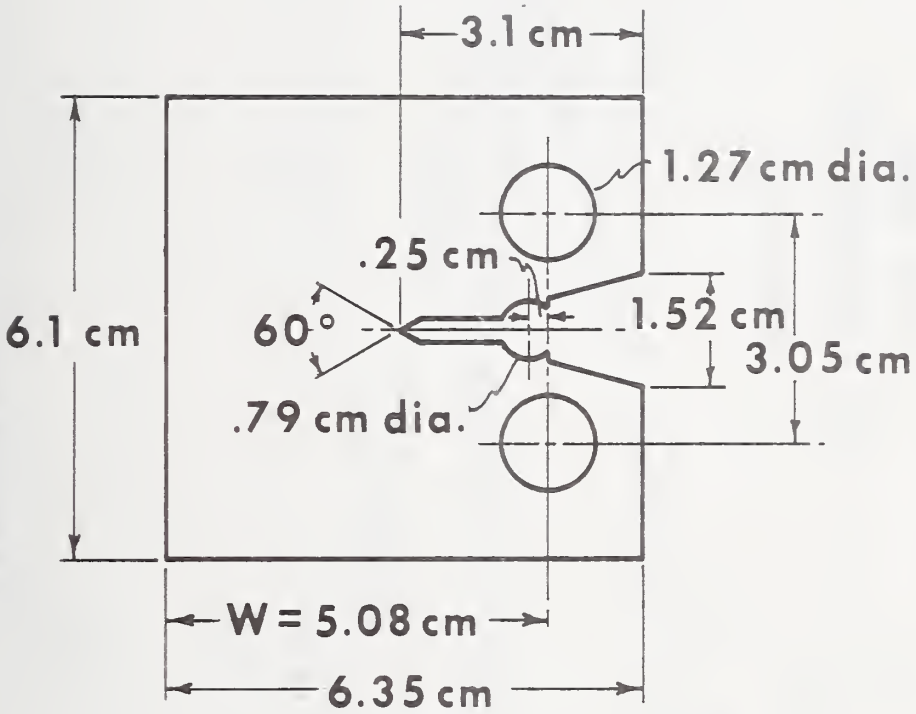

THICKNESS, B = 2.54 cm; W/B = 2

Figure 1. Compact specimen used for fatigue and fracture tests.

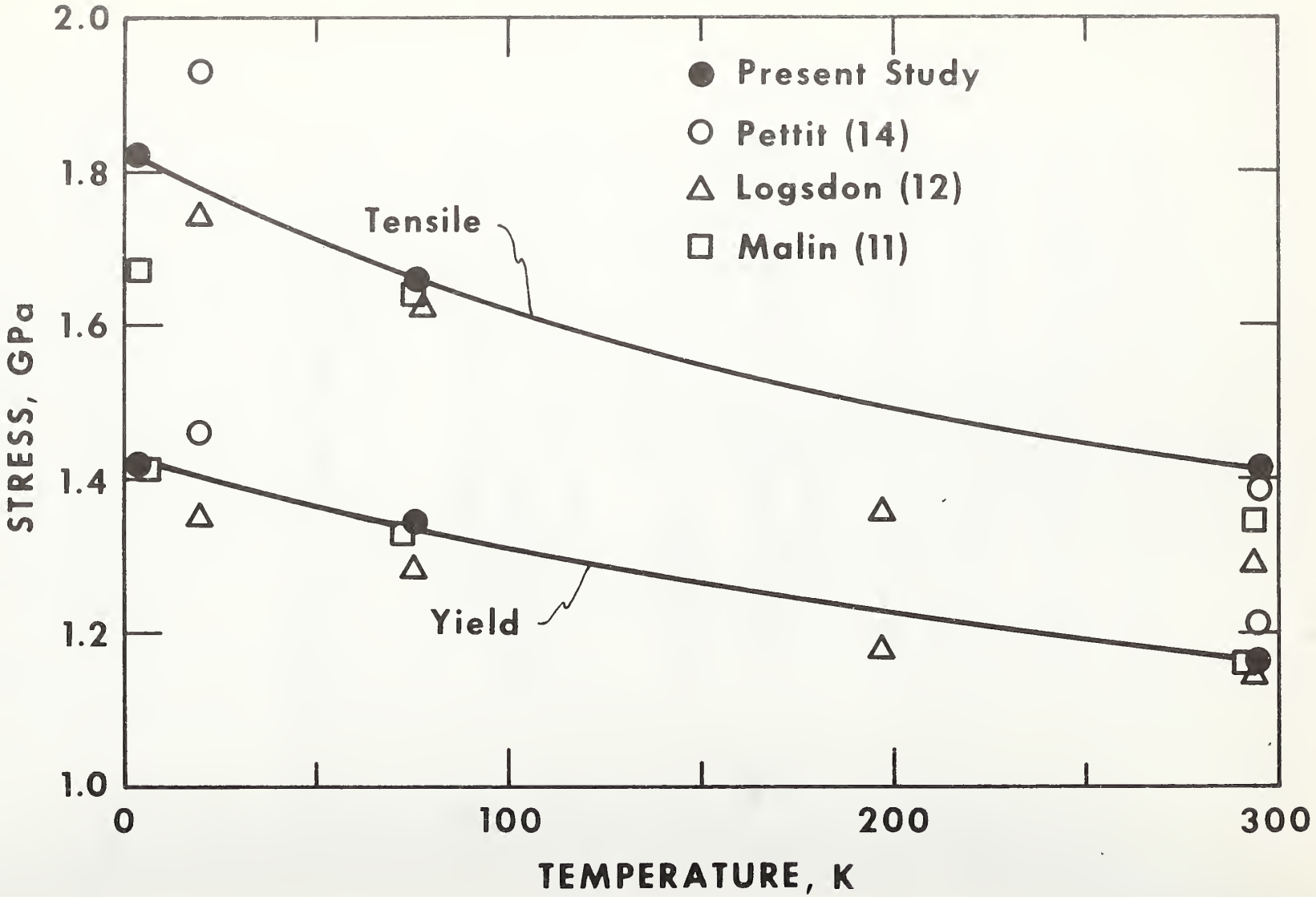

Figure 2. Yield and ultimate tensile strengths of Inconel 718 forgings in the solution treated (1225 to 1256 K) and double aged condition.

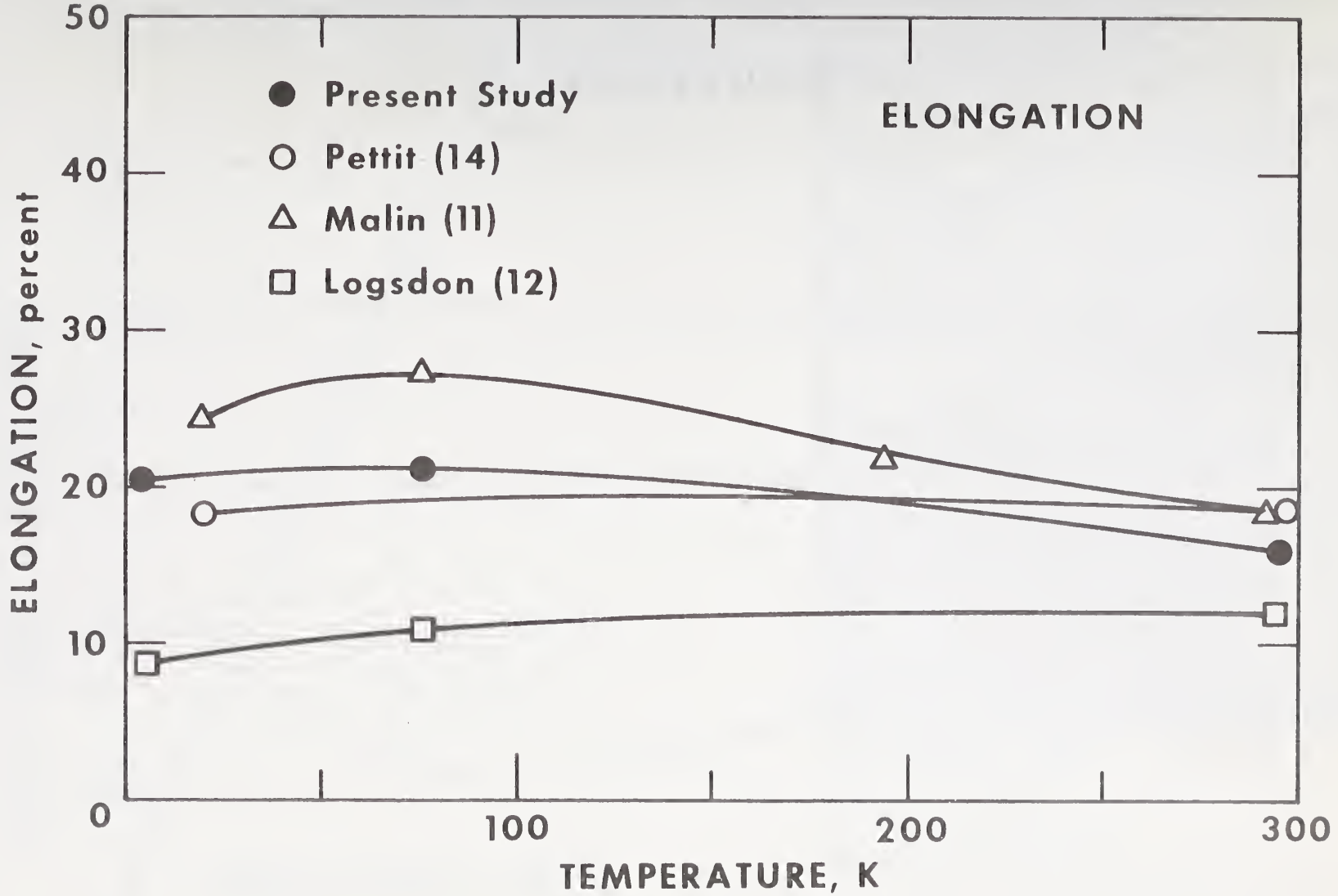

Figure 3. Tensile elongation of Inconel 718 forgings in the solution treated and double aged condition.

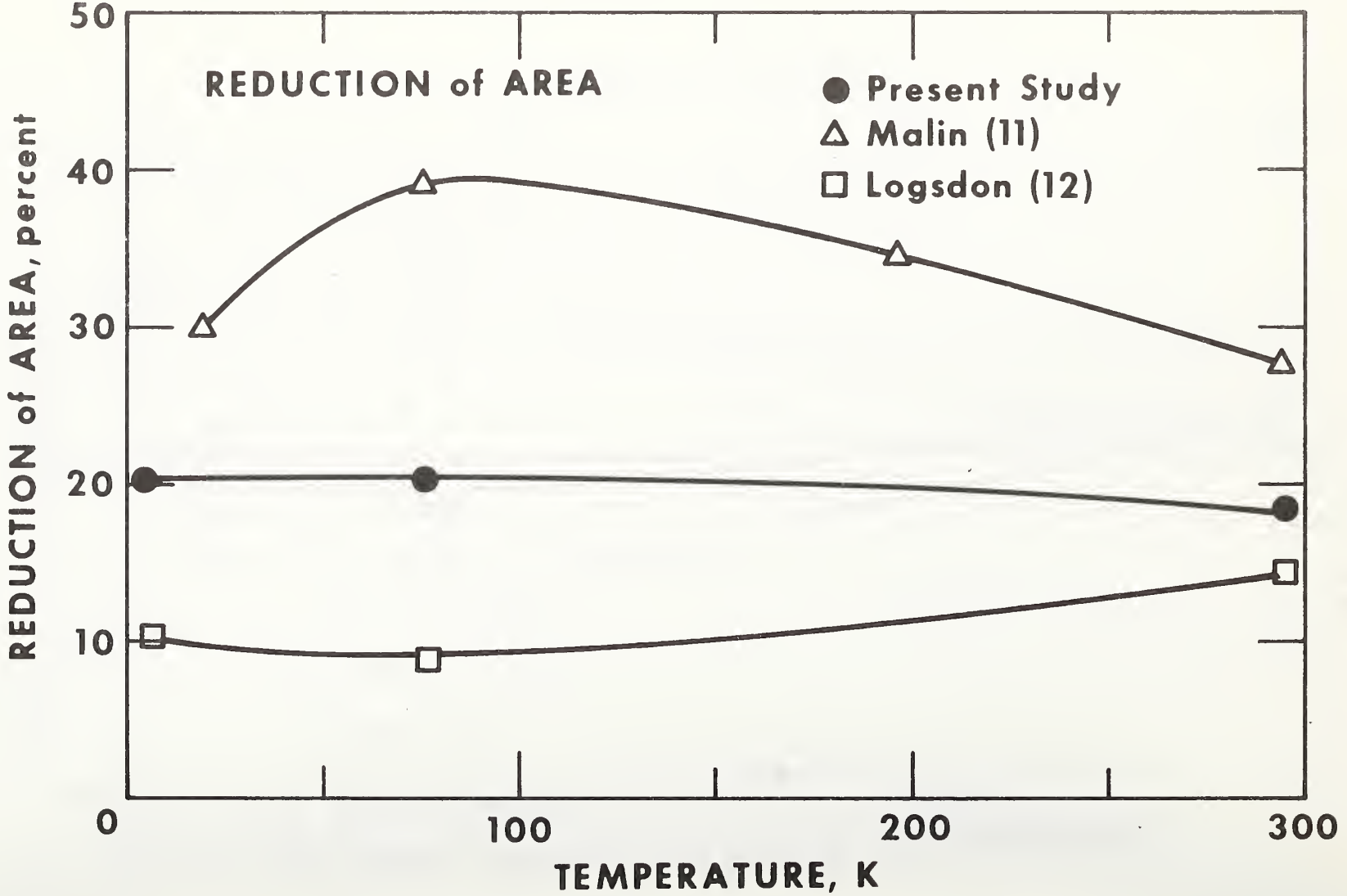

Figure 4. Reduction in area of Inconel 718 forgings in the solution treated and double aged condition.

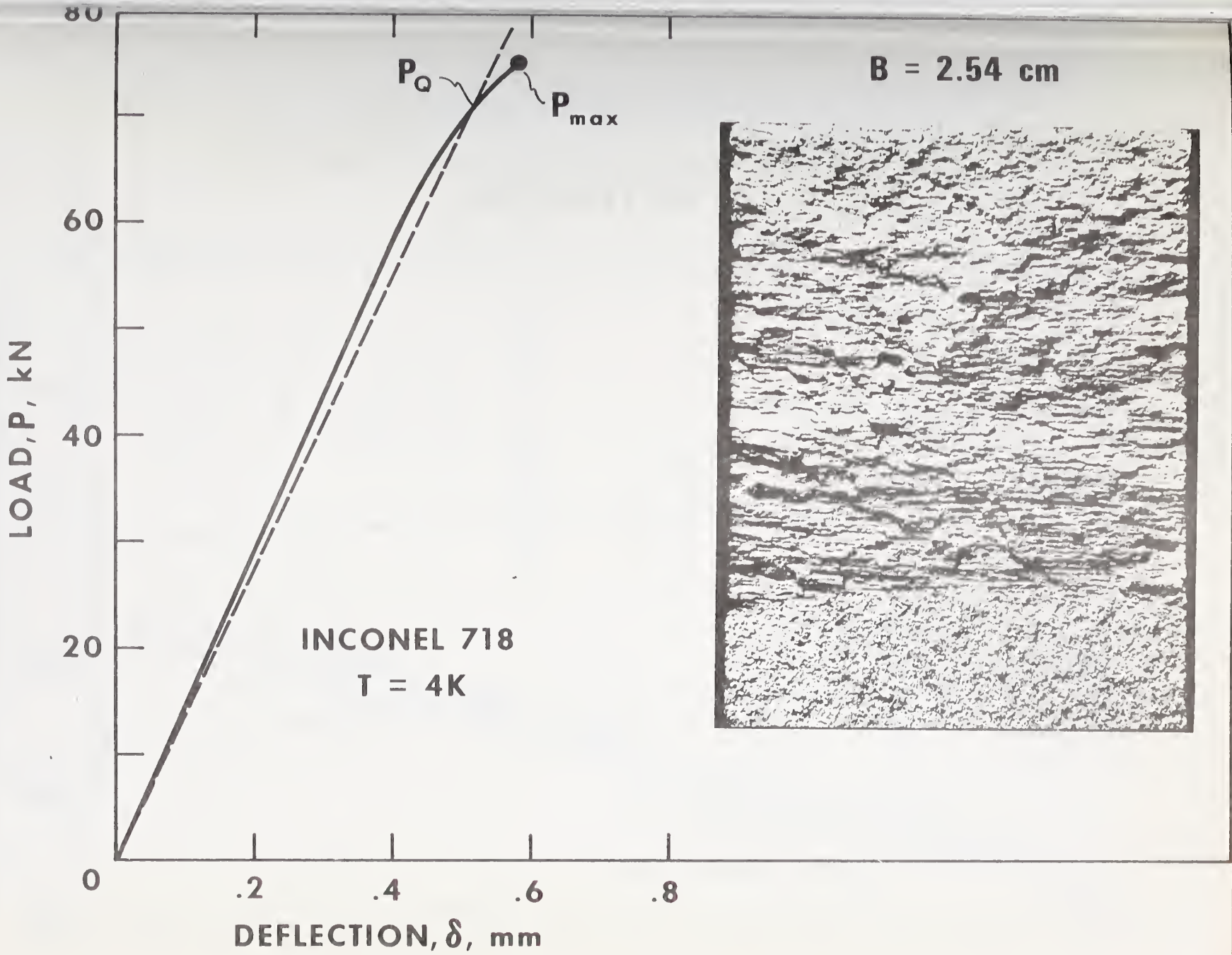

Figure 5. Fracture toughness test record for Inconel 718,

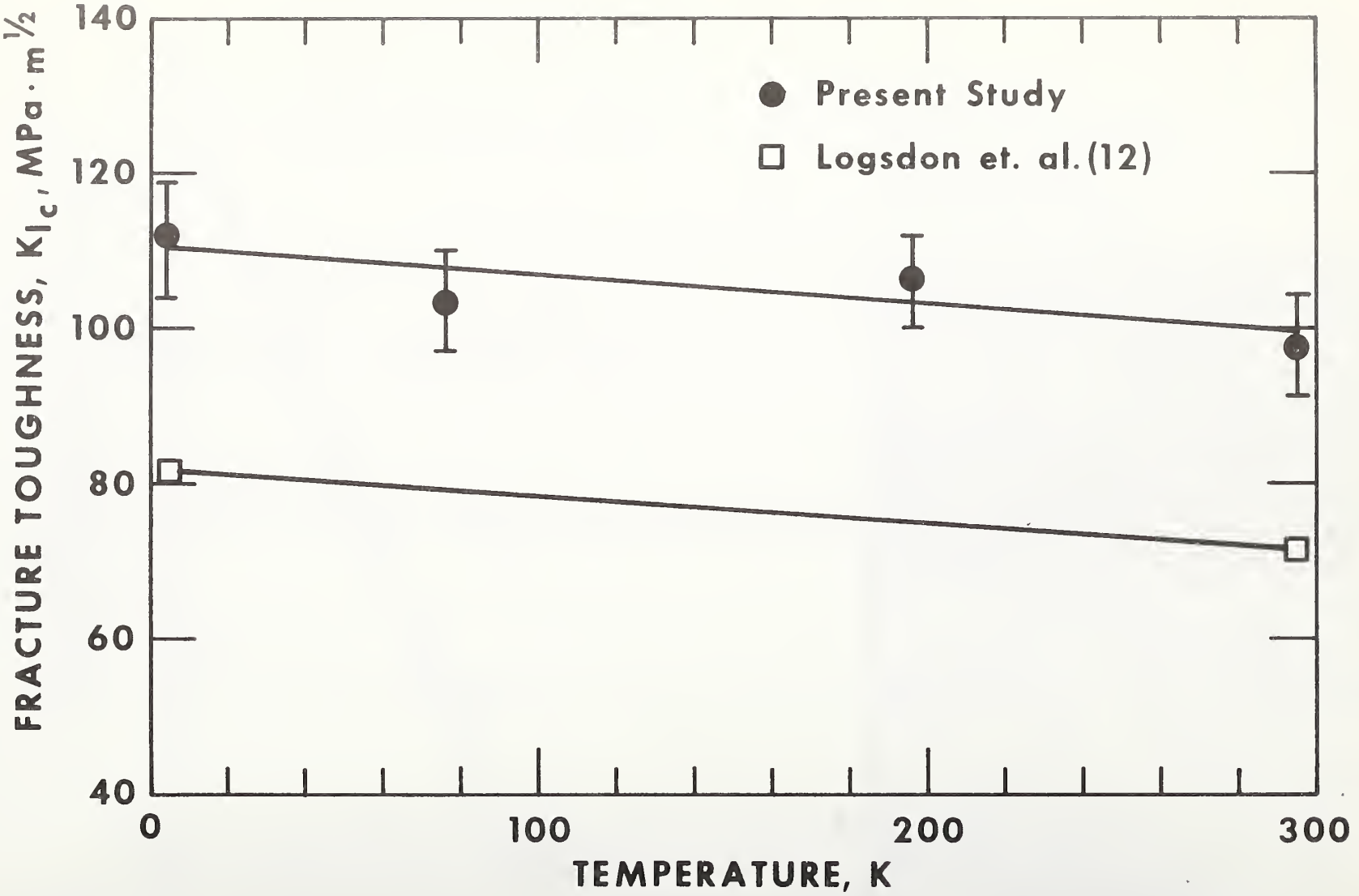

Figure 6. Temperature dependence of fracture toughness for two Inconel 718 alloys.

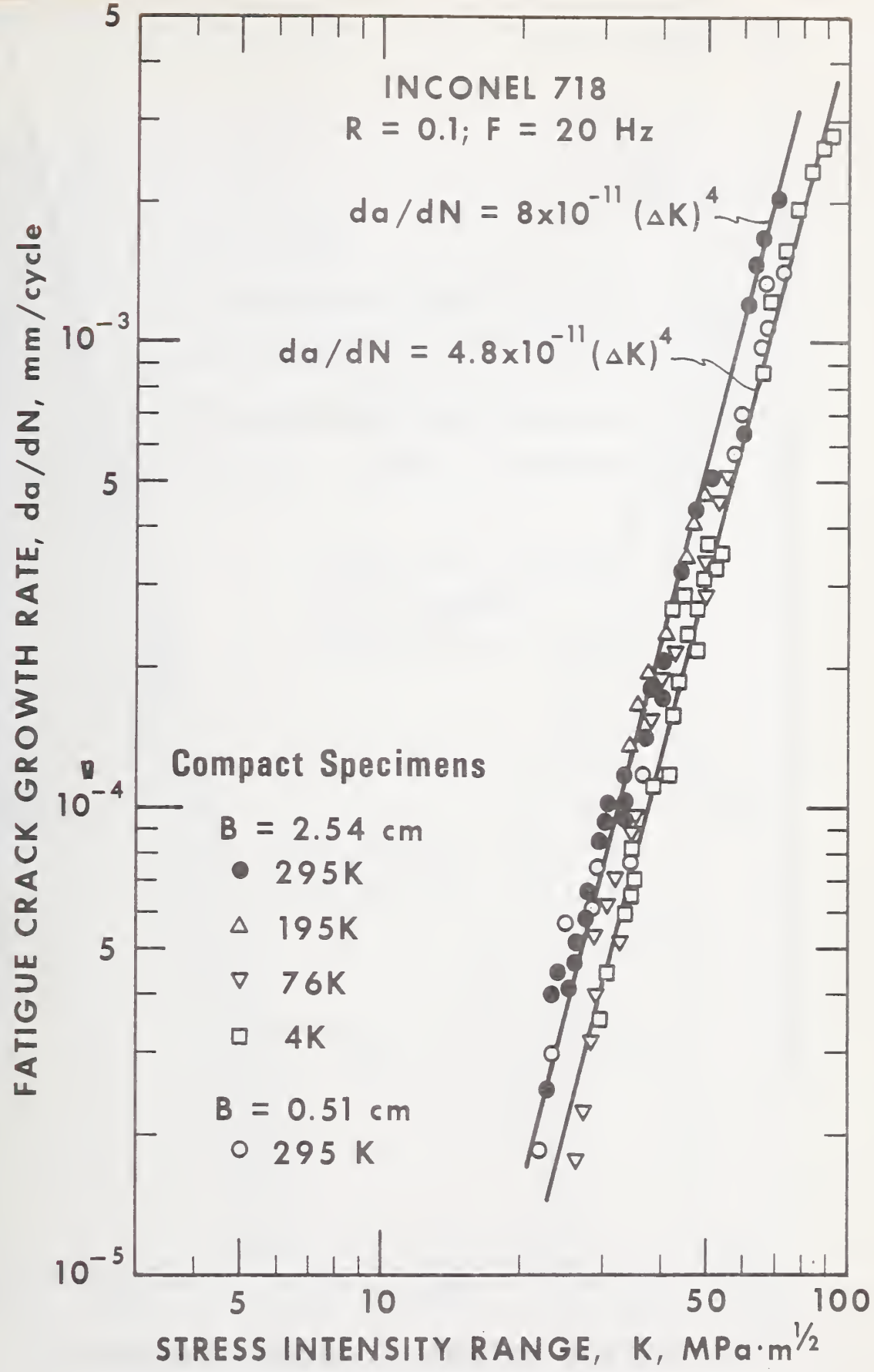

Figure 7. Fatigue crack propagation rates for Inconel 718.

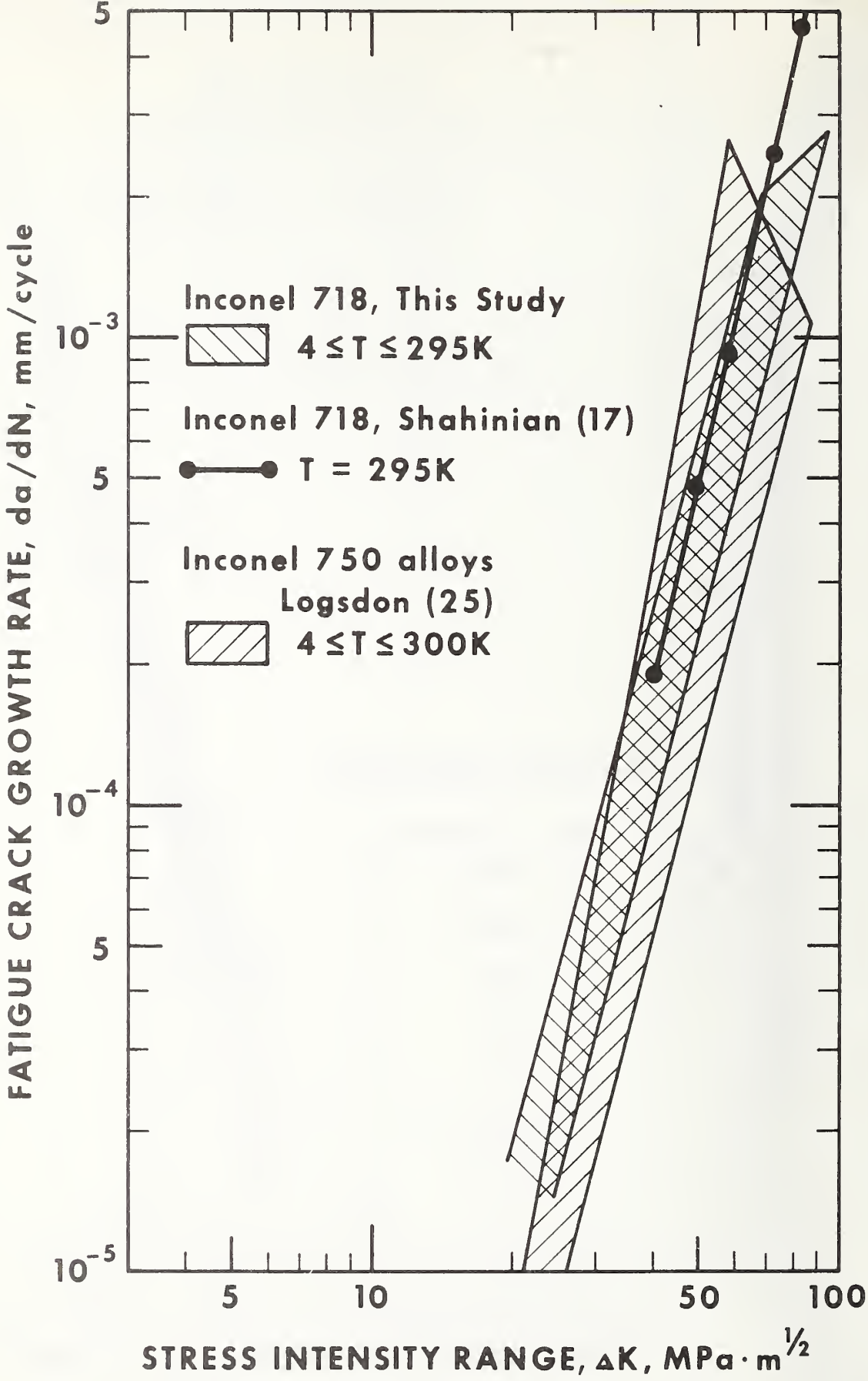

Figure 8. Comparison of fatigue crack propagation rates of Inconel alloys 718 and 750.

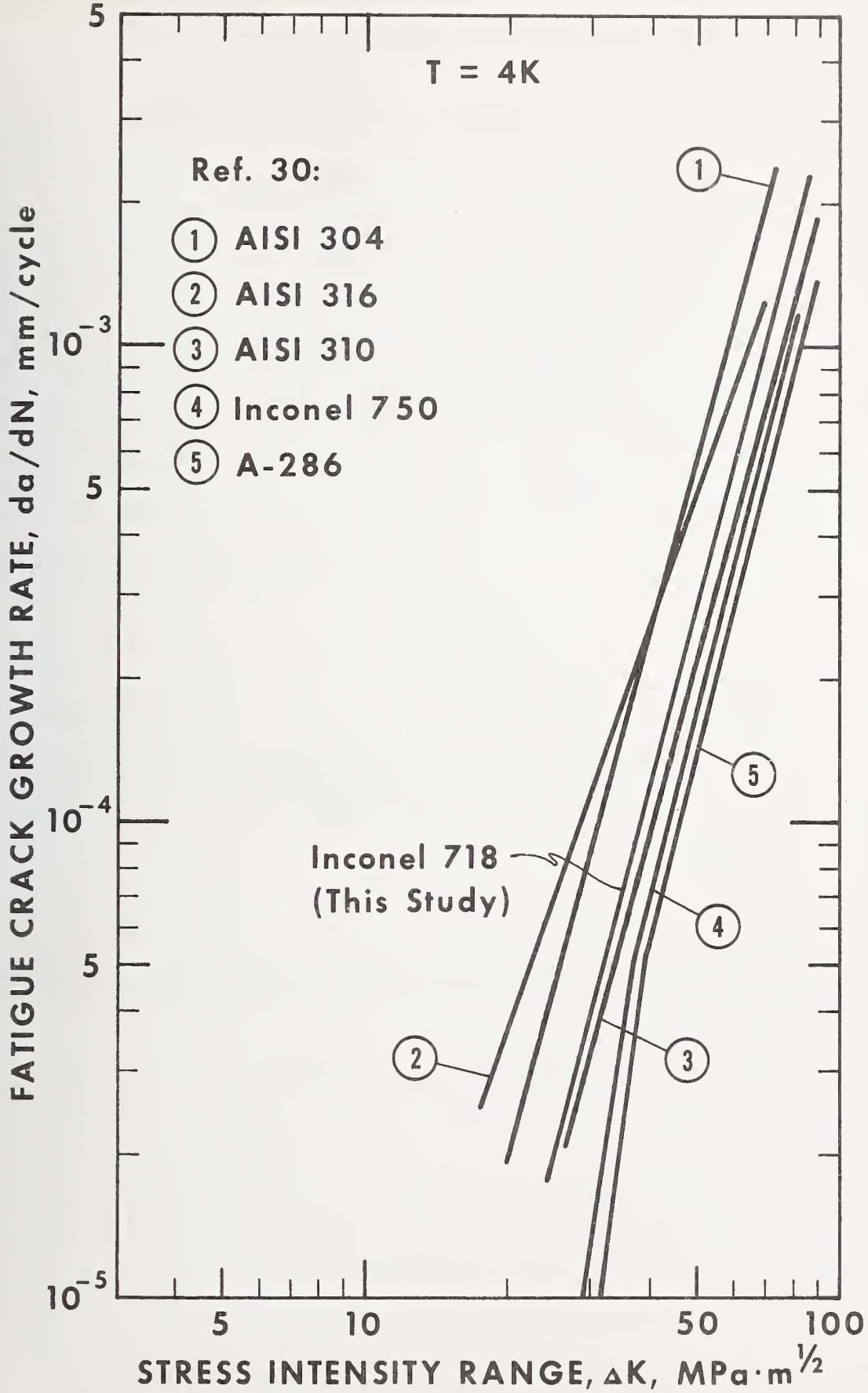

Figure 9. Comparison of fatigue crack propagation rates of Inconel 718, Inconel 750, and austenitic stainless steels at 4 K.

EFFECTS OF SPECIMEN THICKNESS ON FRACTURE TOUGHNESS OF SOME ALUMINUM ALLOYS*

D. T. Read[+] and R. P. Reed

Cryogenics Division
Institute for Basic Standards
National Bureau of Standards
Boulder, CO 80302

*This research was partically supported by the Advanced Research Projects Agency of the U. S. Department of Defense; it is a contribution of NBS, not subject to copyright.

[+]NRC-NBS Postdoctoral Research Associate, 1974-1975.

EFFECTS OF SPECIMEN THICKNESS ON FRACTURE TOUGHNESS OF SOME ALUMINUM ALLOYS

J-integral resistance curves for three specimen thicknesses and valid (according to ASTM Method E 399) K_{Ic} values at 76 K are reported for aluminum alloy 2219. The J-integral values were independent of thickness at small crack extensions, but at substantial crack extensions the values for the thin specimens were larger than those for the thick specimens. The measured J_{Ic} values were less than those calculated from the measured K_{Ic} values. The reason for this discrepancy was that crack extension occurred before the K_{Ic} measurement point was reached.

Key words: Aluminum alloys; critical stress intensity, cryogenic temperature; fracture toughness; J-integral; sub-critical crack extension.

1. Introduction

The generally accepted measure of the fracture toughness of a metal is the plane strain fracture toughness, K_{Ic}, as measured by ASTM Method E 399-74 (Ref. 1). However, the specimen size required for a valid measurement of K_{Ic} may be so great that tests to obtain K_{Ic} may be too difficult or too expensive to perform (Ref. 2). An alternative method of measuring plane strain fracture toughness known as the J-integral method (Refs. 3, 4) is being widely considered because of its less stringent requirements on specimen size. The results described in this report are of use in evaluating the J-integral method of fracture toughness testing.

The parameter characteristic of fracture toughness which is measured in a J-integral test is J_{Ic}, the value of the J-integral at the onset of crack extension. In the linear elastic case, K_{Ic} and J_{Ic} are related as (Ref. 3):

$$J_{Ic} = \frac{K^2_{Ic}}{E} (1 - \nu^2) \qquad (1)$$

where E is Young's modulus and ν is Poisson's ratio of the material.

The J-integral test can be traced back to the Griffith criterion (Refs. 5, 6) for crack extension and to the analytical work of Eshelby (Ref. 7). However, Rice (Ref. 8) and Begley and Landes (Refs. 3, 4) have been mainly responsible for the formulation of the current concept of the J-integral and its uses in fracture toughness testing. Landes and Begley (Ref. 4) have recently proposed a standard test method for determining J_{Ic}.

There are two major obstacles to the successful implementation of the J-integral test method. The proposed test method is an attempt to resolve the first of these, namely, the choice of a measurement point. The basic procedure in a J-integral test is to determine experimentally a resistance curve consisting of a set of measured J-integral versus crack extension (J versus Δa) data points, and then to determine J_{Ic} from this curve according to a rule which specifies the measurement point. In the proposed J-integral test method, the measurement point is chosen at a knee in the J-Δa curve, and thus the shape of this curve is critical to the measurement. It is asserted that if J_{Ic} is chosen properly, Eq.(1) holds, and a measurement of J_{Ic} is equivalent to a measurement of K_{Ic}. The second major problem with the J-integral method is that the validity of Eq.(1) for useful structural materials has not been demonstrated theoretically (Ref. 9). The attempted extension of the equivalence of J_{Ic} and K_{Ic} from the linear elastic to the elastic plastic case has been supported by appeal to experimental results. There is evidence that for some materials J_{Ic} and K_{Ic} are equivalent (Ref. 4). However, J_{Ic} and K_{Ic} have been found not to be related by Eq. (1) in some other materials (Ref. 10).

The objectives of the present study were to determine experimentally:

(1) J_{Ic} as a function of specimen thickness for an aluminum alloy;

(2) the relationship between J_{Ic} and K_{Ic}, when K_{Ic} is determined according to ASTM Method E 399;

(3) the effect of specimen thickness on the shape of the J-Δa curve. Information of this kind is quite scarce, and is necessary before the J-integral method can be standardized as a reliable test method.

2. Materials

Two aluminum alloys, 2014-T652 and 2219-T87, were used as specimen materials. The chemical compositions of these alloys are given in Table 1. The 2014-T652 designation indicates that this material has been heat-treated, artificially aged, and stress relieved by compressing. The 2219-T87 designation indicates that this material has been solution heat-treated, cold-worked, and then artificially aged. After polishing and etching, the grains in both alloys were seen to be severely elongated. A section cut perpendicular to the rolling direction shows some grains about .02 cm (.008 inch) in diameter and some larger grains of various sizes in the 2014 alloy, while the same treatment reveals grains about .03 cm (.012 inch) in diameter in the 2219 alloy. On sections cut parallel to the rolling direction, only grain boundaries approximately parallel to the rolling direction, spaced .02 cm were seen in the 2014 alloy. The 2014-T652 and 2219-T87 alloys had Rockwell hardness of B 80.6 and B 81.1, respectively.

The yield strength σ_y, ultimate tensile strength σ_{uts}, Young's modulus E, Poisson's ratio ν, and plane strain fracture toughness K_{Ic} values obtained for the two alloys tested are listed in Tables 2 and 3 (Ref. 11). For measurements of K_{Ic} and J, the 2014 alloy specimens were machined in the L-T orientation, and the 2219 specimens were machined in the T-L orientation. For comparison, handbook (Ref. 12) values of K_{Ic} are also shown. The unusually high K_{Ic} of the 2014 alloy specimens is probably due to nonuniformities in the specimen material produced during forging. Metallographic evidence for such nonuniformities is discussed below. Originally, the 2014 alloy was chosen for its availability and the convenience of machining and testing the specimens. The 2014 alloy specimens were cut

from a 7.6 cm (3 inch) thick forged plate.

The J-Δa data for the 2014 alloy summarized in Table 4 exhibited an uneven dependence of J upon Δa. This scatter was attributed to variation of properties among the specimens. The specimens used in the tests were examined metallographically. On sections cut perpendicular to the rolling direction, some relatively large grains several millimeters in diameter were observed along with the small grains .02 cm in diameter. The fraction of the surface which was made up of small grains was recorded in Table 4 for the 2014 alloy specimens. Both the raw J-Δa data and the data classified by grain size for the 2014 alloy exhibited so much scatter that they were useless for the purposes of the present study. For this reason, a plate 3.8 cm (1.5 inch) thick of aluminum alloy 2219-T87 was obtained and tested. The remainder of this report is concerned with the results of measurements made on the 2219 alloy.

3. Procedures

The specimen geometry used was a modified compact specimen, as shown in Fig. 1. The normal dimensions of all the specimens tested are listed in Table 5. Tests were conducted in an electrohydraulic testing apparatus equipped with a stand-off and dewar for cryogenic service which has been described previously (Ref. 13). The specimens were mounted in the loading fixtures and cooled to 76 K by immersion in liquid nitrogen. Each specimen was precracked by loading in tension-tension fatigue at 20 Hz at a load which in most cases was 60% or less of the quasistatic load used in the J test. The precracking was continued to a nominal crack length of a/W = .60. Typically the precrack reached the desired length of about .5 cm (.2 inch) after approximately 60,000 fatigue cycles. After precracking, each specimen was loaded quasistatically to a stress

equal to or less than the maximum load used in the precracking procedure, and the load-displacement line was recorded. This line was extended to high loads, and a secant line deviating from this anticipated load line by a preselected amount was also drawn. After these preliminary steps, the quasistatic crack extension was accomplished by loading the specimen until the actual load-displacement curve intersected the pre-drawn secant line, and immediately unloaded. Then the specimen was refatigued, beginning with a load of about half the maximum load reached during the measurement of the load-displacement curve. After the refatigue crack had grown to several millimeters in length, the specimen was pulled apart so that the fracture surfaces were accessible for examination. The crack growth produced during the static load cycle was visible as a dark, rough band between the two bright, relatively smooth, fatigue surfaces.

Each value of the J-integral was computed from the load-displacement record obtained during the static load cycle, using the procedure recommended by Merkle and Corten (Ref 14). This procedure results in a value of the J-integral of

$$J = \frac{\lambda A}{Bb}, \qquad (2)$$

where A is the area under the load displacement curve, B is the specimen thickness, b is the specimen ligament remaining after precracking, and λ is a function of the crack length and the nonlinearity of the load-displacement record. The value of λ was approximately 2.4 in all the tests performed in this study.

In the proposed standard method for determining J_{Ic} (Ref. 4) the crack extension Δa is defined to include both the stretch zone and the zone of material separation, if any. If the crack extension consists

only of a stretch zone, the J-Δa graph is expected to fall along the line given by

$$J = 2\,\sigma_{flow}\,\Delta a \qquad (3)$$

where σ_{flow} is the arithmetic mean of the yield strength and the ultimate tensile strength. J_{Ic} is defined as the value of J at the intersection of the line given by Eq.(3) with the back-extrapolation of the J-Δa curve from the region where material separation does take place. According to the proposed method, the back-extrapolated J-Δ curve is expected to have a slope different from that of the line given by Eq.(3), so that the measured J-Δa curve ought to have a relatively sharp knee in it.

Because of the relatively high value of the yield and ultimate tensile stresses of the 2219-T87 alloy, J_{Ic} as defined by this proposed standard occurs at a crack extension of less than .002 cm. Due to the difficulty of measuring extremely small values of crack extensions, and the apparent unreliability of extrapolating to zero crack extension, the initiation of crack extension was taken as the point of .005 cm crack extension for purposes of the present study. This point was determined by interpolation or extrapolation on graphs of J-Δa. The J_{Ic} values obtained in this way were higher than those which could have been obtained by extrapolation according to the proposed standard, but they were less uncertain.

4. Results and Discussion

The J-Δa data for aluminum alloy 2219 are listed in Table 6 and plotted in Fig. 2. The J_{Ic} values obtained from the J-Δa curves are listed in Table 7. The values of J_{Ic} range from 9.5 to 10.3 kJ · m^{-2}

over a tenfold variation in specimen thickness. Thus, J_{Ic} is indeed a thickness-independent measure of the fracture resistance of the material.

Using the measured value of K_{Ic} and Eq. (1), one would expect a J_{Ic} of 13.6 kJ · m^{-2}, 38% larger than the values actually found. Thus, for aluminum alloy 2219, K_{Ic} and J_{Ic} are <u>not</u> related by Eq. (1). This finding was attributed to the difference in the measurement point for the two test methods; subsequent experimental measurements showed this to be the correct explanation for the observed discrepancy. The measurement point for determining J_{Ic} was chosen as the initiation of crack extension, whereas the measurement point for determining K_{Ic} was chosen as set forth in ASTM Method E 399, that is, at 2% apparent crack extension. The apparent crack extension includes the plastic zone, but the possibility exists that significant actual crack extension may occur before the K_{Ic} measurement point is reached. If this is the case, the values of K_{Ic} obtained may be characteristic of a somewhat extended crack, and not of crack initiation. This possibility is widely suspected (Ref. 15) as a cause of discrepancy between observed values of K_{Ic} and J_{Ic} as related by Eq. (1), and was used by Logsdon (Ref. 10) to explain some of his data. But it appears that this explanation has never been tested experimentally.

To determine the extent of crack extension in a valid K_{Ic} test, three 3.8 cm (1.5 inch) thick compact tensile specimens, more than twice as thick as necessary to obtain valid K_{Ic} data, were tested according to the J-procedure described in Section 3. In two tests, the specimen was unloaded prior to the intersection of the load line with the 5% offset secant, and in the other test the specimen was unloaded just after this intersection. The records of these tests were analyzed as follows. A

line was drawn through the origin of the test record and the point on the record at which unloading was begun. The percent difference between the slope of this secant line and the tangent to the initial linear portion of the load record, referred to as the percent secant deviation, was recorded. This procedure allowed a correlation of secant deviation with crack extension to be made. The data are listed in Table 8 and plotted in Fig. 3. These data clearly show that the critical point in the K_{Ic} test of 2219 aluminum alloy, that is, the point of 5% secant deviation, occurs at a crack extension of about .064 cm (.025 inch) in specimens which satisfy the thickness requirements by a wide margin. As a double check, a similar plot for the 1.42 cm (.56 inch) thick specimens, which are almost exactly in the minimum thickness required in a K_{Ic} test, shows the same characteristic; i.e., crack extension of about .064 cm (.025 inch) before the 5% secant offset is reached. If the J_{Ic} evaluation point were chosen not at crack initiation but at .064 cm (.025 inch) crack extension in these specimens, good agreement could be found between K_{Ic} and J_{Ic}. Thus, the discrepancy between the measured values of K_{Ic} and J_{Ic} related by Eq. (1) is explained. However, because of the observed dependence of the J integral value at significant crack extensions on specimen thickness, the critical state for J_{Ic} measurement cannot be chosen as a point of significant crack extension such as .064 cm (.025 inch) because this would defeat the purpose of J-integral testing, which is to obtain a parameter characteristic of the material tested independent of specimen thickness. Thus, in this alloy it is impossible to obtain agreement between K_{Ic} and J_{Ic} in Eq.(1) that is independent of thickness.

An obvious feature of the J-resistance curves of Fig. 2 is that the curves for the three different material thicknesses separate for

the larger values of crack extension but converge near zero crack extension. It can be seen for this material that the effect of increasing specimen thickness is to decrease the J values at sizable values of Δa while leaving them unchanged, within experimental uncertainties, near zero crack extension. A similar divergence in thickness was observed by Griffis and Yoder (Ref. 16) for 2024-T351 aluminum tested at room temperature using a three-point-bend specimen and thus may be a normal feature of J-integral behavior of many aluminum alloys. Thickness effects are discussed further in the Appendix below.

5. Conclusions

The following conclusions have been drawn from the present study:

(1) In specimens cut from a plate of 2219 aluminum alloy, crack extension was initiated at a constant value of the J-integral over a ten-fold range of specimen thickness, extending from well above to well below the minimum specimen thickness given in ASTM Method E 399 for valid K_{Ic} measurement. This result supports the hypothesis that J_{Ic} is a useable measure of material toughness.

(2) J_{Ic} and K_{Ic} (K_{Ic} determined according to ASTM Method E 399) are not equivalent measurements of fracture toughness for 2219 aluminum because of subcritical crack growth in K_{Ic} tests; the J_{Ic} value anticipated from measurements of K_{Ic} was 38% larger than the measured J_{Ic} value.

(3) As crack extension increased, the J-integral value was significantly larger for thin specimens than for thick ones.

Appendix. Observations on Plane Stress Toughening

The specimen thickness B may be expressed in dimensionless form:

$$\gamma = \frac{B}{(K_{Ic}/\sigma_y)^2} \qquad (A1)$$

The parameter γ can be used as an index of the operative fracture mode. The possible modes are plane strain, mixed, and plane stress. According to Eq.(A1) and the measured values of the parameters K_{Ic} and σ_y, the samples used in the present study fall at γ = .72, 1.34, 2.68, and 7.19. Values of γ equal to or greater than 2.5 correspond to the criteria of ASTM Method E-399 for plane strain testing. Thus, for values of γ below 2.5, we may expect plane stress toughening effects, whereas for γ above 2.5 plane strain should dominate. A strong increase in apparent sample toughness is to be expected as the thickness is decreased (Ref. 17).

An experimental search for such a dependence of apparent toughness on specimen thickness may be made by observing the maximum stress intensity sustained by the samples as a function of thickness. Such stress intensities may be calculated using the maximum load sustained by the sample and the crack length present at the initiation of loading. Values of the maximum stress intensity measured in this manner are denoted K_M. K_M may be corrected for the plastic zone size as follows. First, the plastic zone radius is calculated from the uncorrected stress intensity according to (Ref. 18):

$$r_y = \frac{1}{2\pi} \left(\frac{K_{Ic}}{\sigma_y}\right)^2 \qquad \text{(A2)}$$

Then the effective crack length $a_{eff} = a + r_y$ is used to find the first corrected stress intensity factor according to:

$$K_{Ic} = \frac{P\, f(a_{eff}/W)}{B\, W^{1/2}} \qquad \text{(A3)}$$

where $f(\frac{a_{eff}}{W})$ is given by Newman (Ref. 19). This corrected stress intensity is used to calculate a new value of r_y, which is then used to calculate a new stress intensity, and the iteration continues in this manner. If this process converges, the final value of r_y is not too large and the plastic zone correction has been made successfully. An asterisk indicates a stress intensity value which includes the plastic zone correction. For instance, K_{M*} is the stress intensity at maximum load corrected for the plastic zone.

Measured values of K_M and K_{M*} are listed in Table A-1 and plotted versus thickness in Fig. A-1. The classic decrease of this measure of material toughness with increasing specimen thickness is emphasized by the plastic zone correction. The curve shown in this figure is given by

$$K_{M*} = K_{Ic}\sqrt{1.4\ \gamma^{-2}} \qquad (A4)$$

where γ was defined in Eq.(A1). This equation was used by Irwin et al. (Ref. 19) to curve-fit some fracture toughness data on aluminum. The qualitative agreement between this curve and the measured values of K_{M*} indicates that the anticipated strong increase in apparent sample toughness with decreasing thickness was indeed found in the present study. The increase of K_{M*} indicates that plane stress toughening occurs as the specimen thickness decreases. From these data, we may conclude that the border between plane strain and mixed modes occurs at about $\gamma = 2.5$; thus, the requirements of ASTM Method E-399 are adequate to insure plane strain conditions, but are not excessive. Due to limitations on the specimen size, the pure plane stress region was not attained in these tests. Nevertheless, the data are sufficient to show tendencies of the difference between plane strain and plane stress modes of fracture.

References

1. Standard Method of Test for Plane Strain Fracture Toughness of Metallic Materials (Designation E 399-74), 1974 Annual Book of ASTM Standards, Part 10, 1974, pp. 432-451.
2. Kaufman, J. G. and Kelsey, R. A., in: Properties of Materials for Liquefied Natural Gas Tankage, ASTM STP 579, American Society for Testing and Materials, Philadelphia, PA (1975), pp. 138-158.
3. Begley, J. A. and Landes, J. D., in: Fracture Toughness, Proceedings of the 1971 National Symposium on Fracture Mechanics, Part II, ASTM STP 514, American Society for Testing and Materials, Philadelphia, PA (1972), pp. 1-20.
4. Landes, J. D. and Begley, J. A., in: Fracture Analysis, ASTM STP 560, American Society for Testing and Materials, Philadelphia, PA (1974), pp. 170-186.
5. Griffith, A. A., Phil. Trans. Royal Soc. 221A, 163 (1920-21); Reprinted with corrections in Trans. Quart. ASM 61, 861 (1968).
6. Griffith, A. A., Proc. First International Congress on Applied Mechanics, Delft (1924), p. 55.
7. Eshelby, J. D., "The Force on an Elastic Singularity," Trans. Roy. Soc. Lond. A244, 87 (1951).
8. Rice, J. R., in: Fracture, Vol. II, H. Liebowitz, ed., Academic Press, New York (1968), p. 191.
9. Eftis, J. and Liebowitz, H., Engr. Fracture Mechanics 7, 101 (1975).
10. Logsdon, A. W., "Elastic Plastic (J_{Ic}) Fracture Toughness Values: Their Experimental Determination and Comparison with Conventional Linear Elastic (K_{Ic}) Fracture Toughness Values for Five Materials," Westinghouse Research Laboratories, Pittsburgh, PA, Scientific Paper 74-1E7-FMPWR-P1 (1974).

11. The yield strengths, ultimate tensile strengths, and fracture toughnesses were measured using standard techniques; Young's modulus and Poisson's ratio for the specimen materials were measured by an ultrasonic technique as described by D. T. Read and H. M. Ledbetter, to be published.

12. Matthews, W. T., "Plain Strain Fracture Toughness (K_{Ic}) Data Handbook for Metals," Army Materials and Mechanics Research Center, AMMRC MS 73-6, Watertown, MA (1973).

13. Fowlkes, C. W. and Tobler, R. L., "Fracture Testing and Results for a Ti-6Al-4V Alloy at Liquid Helium Temperature," to be published in Engineering Fracture Mechanics.

14. Merkle, J. G. and Corten, H. T., "A J-Integral Analysis for the Compact Specimen, Considering Axial Force as Well as Bending Effects," presented at the Pressure Vessels and Piping Conference with Nuclear Engineering and Mechanical Divisions, American Society Mechanical Engineers, Paper No. 74-PVP-33 (1974).

15. Tobler, R., Sha, G. and Begley, J., personal communication.

16. Griffis, C. A. and Yoder, G. R., "Application of the J-Integral to Crack Initiation in a 2024-T351 Aluminum Alloy," Naval Research Report 7676, (1974), p. 21.

17. Srawley, J. E. and Brown, W. F., in: Fracture Toughness Testing and Its Applications, ASTM STP 381, American Society for Testing and Materials, Philadelphia, PA (1965), pp. 133-196.

18. Weiss, V. and Yukawa, S., in: Fracture Toughness Testing and Its Applications, ASTM STP 381, American Society for Testing and Materials, Philadelphia, PA (1965), pp. 1-22.

19. Newman, J. C., Jr., in: Fracture Analysis, ASTM STP 560, American Society for Testing and Materials, Philadelphia, PA (1974), pp. 105-121.

20. Irwin, G. R., Krafft, J. M., Paris, P. C., Wells, A. A., "Basic Aspects of Crack Growth and Fracture," Naval Research Laboratory Report No. 6598, 1967, p. 50.

LIST OF TABLES

Table 1. Chemical compositions of the alloys, wt. %.

Table 2. Tensile and fracture data for aluminum alloy 2014-T652 in the L-T orientation.

Table 3. Tensile and fracture data for aluminum alloy 2219-T87 in the T-L orientation.

Table 4. J-integral data for aluminum alloy 2014-T652 in the T-L orientation at 76 K.

Table 5. Dimensions of specimens used in the present study.

Table 6. J-integral data for aluminum alloy 2219-T87 in the L-T orientation at 76 K.

Table 7. Measured and predicted (from K_{Ic}) values of J_{Ic} for four specimen thicknesses of aluminum alloy 2219-T87 at 76 K.

Table 8. Measured values of crack extension and secant deviation for two specimen thicknesses of aluminum alloy 2219-T87 at 76 K.

Table A1. Maximum stress intensity and maximum stress intensity corrected for the plastic zone for four specimen thicknesses of aluminum alloy 2219-T87 at 76K.

Table 1. Chemical compositions of the alloys, wt. %.[a]

	Cu	Fe	Mg	Mn	Si	Ti	V	Zn	Zr
2014	4.4		0.5	0.8	0.8				
2219	6.4	0.20	<.01	0.26	0.15	0.16	0.12	0.09	0.16

[a] For 2014, nominal composition. For 2219, plasma arc analysis.

Table 2. Tensile and fracture data for aluminum alloy 2014-T652 in the L-T orientation.

T(K)	300	76	4
σ_y (MPa)	405	442	561
	402	436	534
	Avg = 403.5	Avg = 439.	Avg = 547.
σ_y (ksi)	58.8	64.1	81.3
	58.4	63.3	77.4
	Avg = 58.6	Avg = 63.7	Avg = 79.4
σ_{uts} (MPa)	476	524	700
	475	536	663
	Avg = 475.5	Avg = 530.	Avg = 681.5
σ_{uts} (ksi)	69.1	76.0	101.5
	68.9	77.7	96.2
	Avg = 69.0	Avg = 76.8	Avg = 98.8
E(GPa)	75.6	83.3	83.8
E(Msi)	11.0	12.1	12.1
ν	.341	.331	.330
K_{Ic} (MPa $\cdot$ $m^{1/2}$)	53.4	49.9	53.4
	46.7	53.4	
	Avg = 50.1	51.3	
		Avg = 51.5	
K_{Ic} (ksi $\cdot$ $in^{1/2}$)	48.6	45.4	48.6
	42.5	48.6	
	Avg = 45.6	46.7	
		Avg = 46.9	
K_{Ic} (MPa $\cdot$ $m^{1/2}$) (handbook value)	26.4	33.0	---
K_{Ic} (ksi $\cdot$ $in^{1/2}$) (handbook value)	24	30	---

Table 3. Tensile and fracture data for aluminum alloy 2219-T87 in the T-L orientation.

T(K)	300	76	4
σ_y (MPa)	411	490	547
	412	496	514
	Avg = 411.5	Avg = 493.	Avg = 531.
σ_y (ksi)	59.6	71.1	79.4
	59.7	72.0	74.6
	Avg = 59.65	Avg = 71.6	Avg = 77.0
σ_{uts} (MPa)	509	630	734
	503	630	706
	Avg = 506.	Avg = 630.	Avg = 720.
σ_{uts} (ksi)	73.8	91.4	106.5
	73.0	91.3	102.4
	Avg = 73.4	Avg = 91.35	Avg = 104.4
E(GPa)	77.4	85.2	85.7
E(Msi)	11.2	12.4	12.4
ν	.330	.319	.318
K_{Ic} (MPa $\cdot$ $m^{1/2}$)	31.0	37.2	---
	30.6	33.5	---
	Avg = 30.8	Avg = 35.9	
K_{Ic} (ksi $\cdot$ $in^{1/2}$)	28.2	33.9	---
	27.9	30.5	---
	Avg = 28.1	Avg = 32.7	
K_{Ic} (MPa $\cdot$ $m^{1/2}$) (handbook value)[14]	33.0	---	---
K_{Ic} (ksi $\cdot$ $in^{1/2}$) (handbook value)[14]	30.0	---	---

Table 4. J-integral data for aluminum alloy 2014-T651 in the T-L orientation at 76 K.

Sample #	B(cm)	B(in)	b(cm)	b(in)	Δa(cm)	Δa(10^{-3} in)	J($\frac{kJ}{m^2}$)	J($\frac{in\text{-}lb}{in^2}$)	% small grains
A-6	.508	0.2	3.71	1.46	.011	4.3	33.6	191.9	10%
A-15	.508	0.2	3.56	1.40	.027	10.5	54.0	308.2	30%
A-1	.508	0.2	3.58	1.41	.036	14.2	29.6	169.2	100%
A-2	.508	0.2	3.62	1.42	.071	27.8	56.0	320.0	50%
A-3	.508	0.2	3.66	1.44	.116	45.2	100.5	573.7	50%
B-8	1.27	0.5	3.61	1.42	.009	3.4	13.4	76.8	100%
B-3	1.27	0.5	3.35	1.32	.009	3.5	26.7	152.3	20%
B-7	1.27	0.5	3.56	1.40	.010	4.0	17.1	97.8	60%
B-2	1.27	0.5	3.43	1.35	.033	13.0	27.3	156.0	100%
B-6	1.27	0.5	3.48	1.37	.045	17.9	24.9	142.0	100%
B-1	1.27	0.5	3.43	1.35	.054	21.2	34.7	197.9	40%
B-5	1.27	0.5	3.45	1.36	.057	22.5	46.2	264.1	0%
B-4	1.27	0.5	3.53	1.39	.141	55.5	37.5	214.2	50%
C-6	2.54	1.0	3.63	1.43	.008	3.1	13.2	75.1	50%
C-1	2.54	1.0	3.45	1.36	.017	6.6	21.1	120.5	100%
C-5	2.54	1.0	3.51	1.38	.018	7.0	30.2	172.7	20%
C-8	2.54	1.0	3.63	1.43	.036	14.1	28.6	162.9	60%
C-3	2.54	1.0	3.68	1.45	.056	22.0	33.0	188.7	25%
C-7	2.54	1.0	3.51	1.38	.067	26.5	40.3	230.3	50%
C-4	2.54	1.0	3.38	1.33	.129	50.9	37.6	215.0	50%
C-2	2.54	1.0	3.30	1.30	.218	86.0	59.2	338.3	100%

Table 5a. Dimensions of aluminum 2014 specimens used in the present study. B and W have the meanings indicated in Fig. 1.

B	W	a	Number of specimens tested
0.51 cm (0.2 in)	7.62 cm (3 in)	4.57 cm (1.8 in)	5
1.27 cm (0.5 in)	7.62 cm (3 in)	4.57 cm (1.8 in)	7
2.54 cm (1.0 in)	7.62 cm (3 in)	4.57 cm (1.8 in)	7
3.81 cm (1.5 in)	7.62 cm (3 in)	4.01 cm (1.58 in)	6

Table 5b. Dimensions of aluminum 2219 specimens used in the present study. B and W have the meanings indicated in Fig. 1.

B	W	a	Number of specimens tested
0.38 cm (.15 in)	5.08 cm (2 in)	3.05 cm (1.2 in)	5
0.72 cm (.28 in)	5.08 cm (2 in)	3.05 cm (1.2 in)	5
1.44 cm (.56 in)	5.08 cm (2 in)	3.05 cm (1.2 in)	5
3.81 cm (1.5 in)	7.62 cm (3 in)	4.19 cm (1.65 in)	7

Table 6. J-integral data for aluminum alloy 2219-T87 in the L-T orientation at 76 K.

Sample #	B(cm)	B(in)	b(cm)	b(in)	Δa(cm)	$\Delta a(10^{-3}$ in)	$J(\frac{kJ}{m^2})$	$J(\frac{in\text{-}lb}{in^2})$
A-4	.38	.15	2.03	.80	0	0	10.0	57.2
A-5	.38	.15	2.04	.80	.013	5.1	12.6	72.1
A-3	.38	.15	2.03	.80	.033	12.8	16.7	95.4
A-1	.38	.15	2.04	.80	.074	29.0	21.8	124.6
A-2	.38	.15	2.02	.80	.130	51.0	33.7	192.3
B-4	.71	.28	2.03	.80	.001	0.4	9.6	54.7
B-5	.71	.28	2.09	.82	.008	3.4	10.9	62.2
B-3	.71	.28	2.06	.81	.024	9.3	13.1	74.8
B-1	.71	.28	2.11	.83	.097	38.1	12.5	105.5
B-2	.71	.28	2.06	.81	.183	71.9	27.3	155.8
C-3	1.42	.56	2.08	.82	.002	0.7	9.0	51.5
C-5	1.42	.56	2.02	.80	.013	5.1	11.7	66.8
C-1	1.42	.56	2.09	.82	.020	8.0	13.0	74.1
C-2	1.42	.56	1.99	.78	.076	30.0	16.6	94.6
C-7	1.42	.56	2.01	.79	.157	62.0	20.2	115.3
D-7	3.81	1.5	3.65	1.44	.009	3.8	10.0	56.9
D-6	3.81	1.5	3.47	1.37	.067	26.2	13.4	76.4
D-5	3.81	1.5	3.51	1.38	.072	28.5	14.8	84.8

Table 7. Measured and predicted (from K_{Ic}) values of J_{Ic} for four specimen thicknesses of aluminum alloy 2219-T87 at 76 K.

		MEASURED		PREDICTED	
B(cm)	B(in)	$J_{Ic}(kJ/m^2)$	$J_{Ic}(\frac{in\text{-}lb}{in^2})$	$J_{Ic}(kJ/m^2)$	$J_{Ic}(\frac{in\text{-}lb}{in^2})$
.38	.15	10.3	59	13.6	77.5
.71	.28	10.0	57	13.6	77.5
1.42	.56	9.6	55	13.6	77.5
3.81	1.50	9.5	54	13.6	77.5

Table 8. Measured values of crack extension and secant deviation for two specimen thicknesses of aluminum alloy 2219-T87 at 76 K.

Sample #	B(cm)	B(in)	Δa(cm)	$\Delta a(10^{-3}$ in)	secant deviation (per cent)
C-3	1.42	.56	.002	.7	0
C-5	1.42	.56	.013	5.1	0
C-1	1.42	.56	.020	8.0	2.1
C-2	1.42	.56	.076	30.0	7.1
C-7	1.42	.56	.157	62	14.0
D-7	3.81	1.5	.010	3.8	3.0
D-6	3.81	1.5	.067	26.2	4.0
D-5	3.81	1.5	.072	28.5	5.7

Table A1. Maximum stress intensity and maximum stress intensity corrected for the plastic zone for four specimen thicknesses of aluminum alloy 2219-T87 at 76 K.

Sample #	B(cm)	B(in)	K_M(MPa·m$^{1/2}$)	K_M(ksi·in$^{1/2}$)	K_M*(MPa·m$^{1/2}$)	K_M*(ksi·in$^{1/2}$)
A-4	.38	.15	46.2	42.0	57.6	52.4
B-4	.71	.28	38.1	34.7	42.3	30.5
C-3	1.42	.56	34.8	31.7	37.9	34.5
D-7	3.81	1.5	34.1	31.0	35.6	32.4
O-1	3.81	1.5	37.6	34.2	39.3	35.8
O-2	3.81	1.5	37.8	34.4	39.6	36.0

List of Figures

Figure 1. Specimen configuration used in the present study.

Figure 2. J-Δa data for aluminum alloy 2219.

Figure 3. Secant deviation versus crack extension for aluminum alloy 2219.

Figure A1. Observed maximum stress intensity versus specimen thickness.

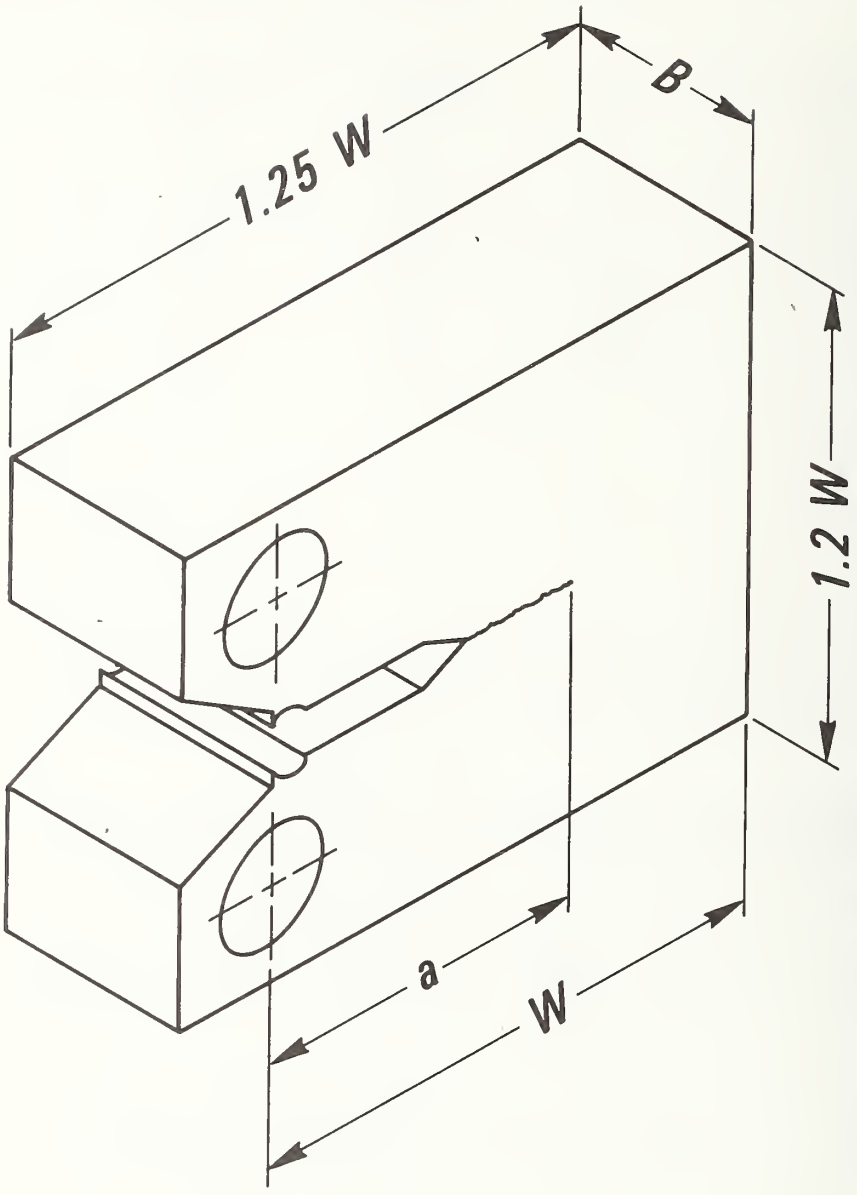

Figure 1. Specimen configuration used in the present study.

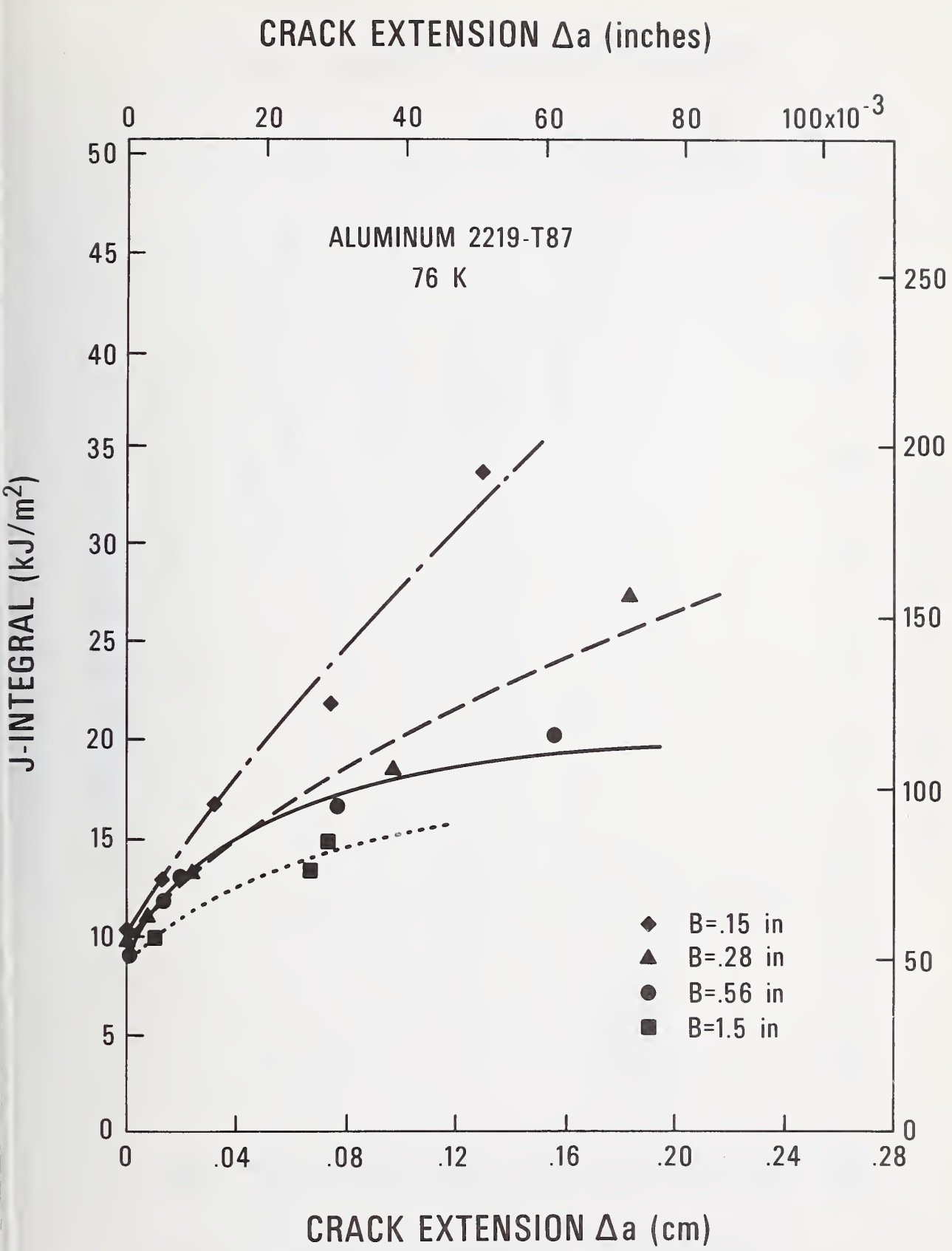

Figure 2. J-Δa data for aluminum alloy 2219.

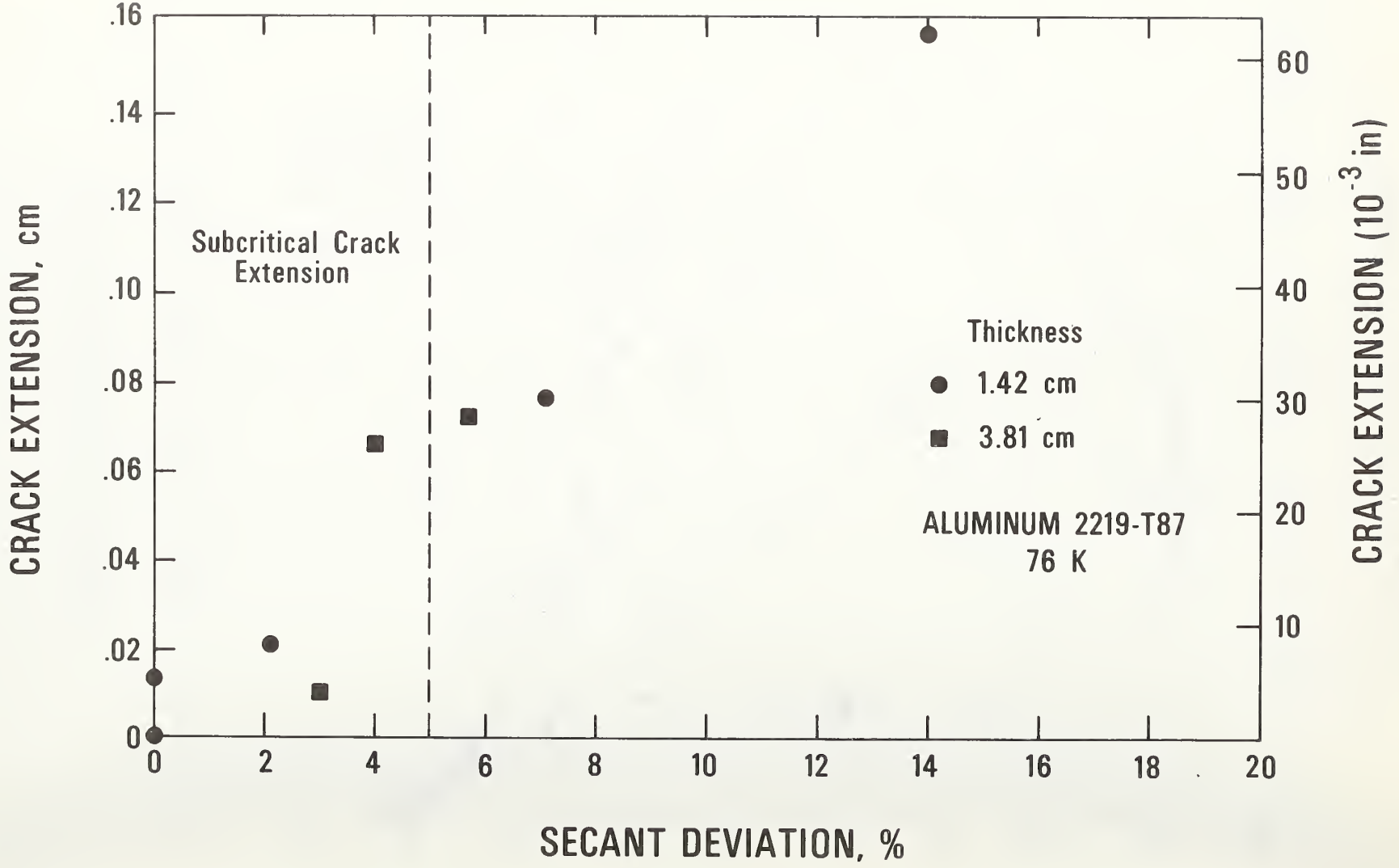

Figure 3. Secant deviation versus crack extension for aluminum alloy 2219.

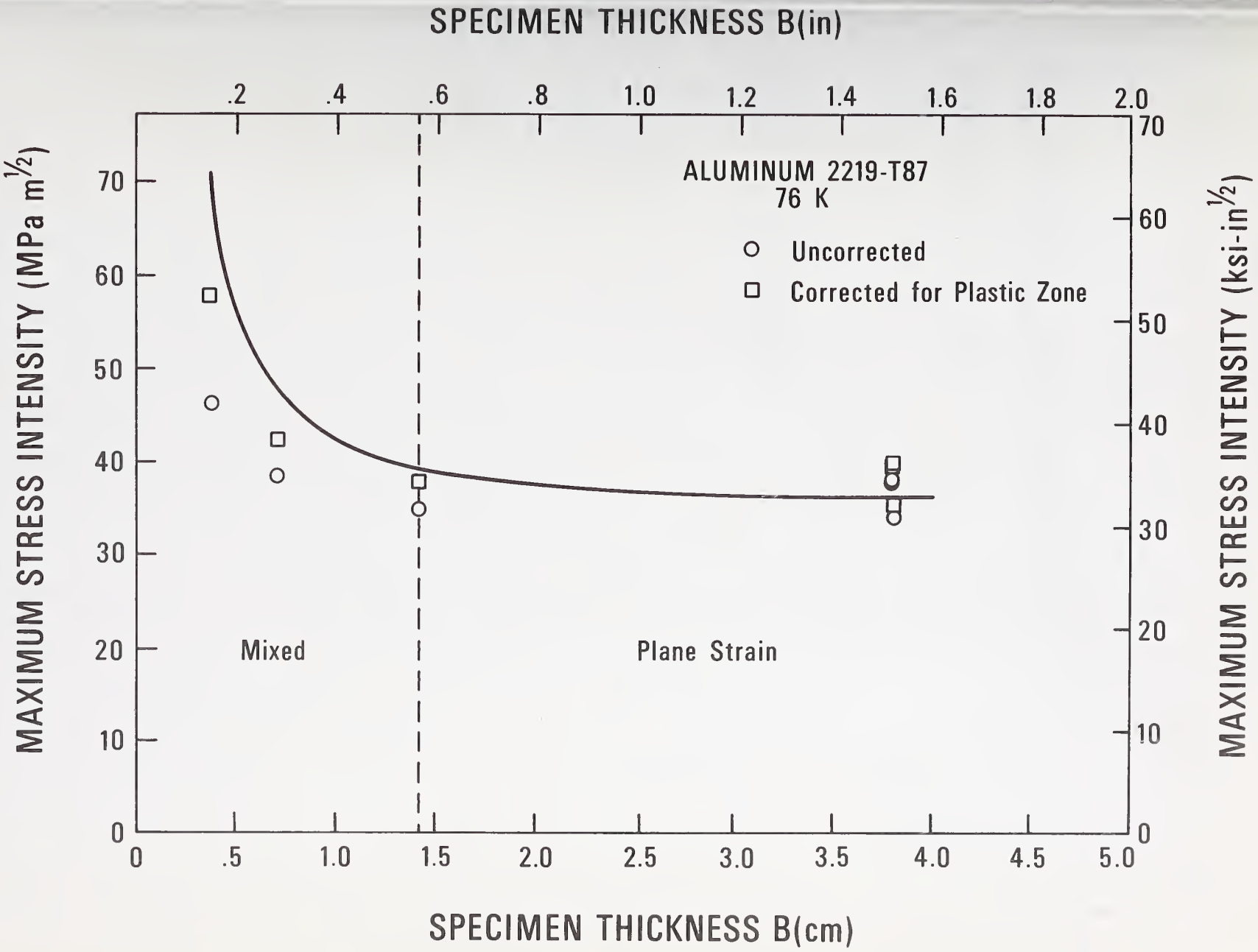

Figure A1. Observed maximum stress intensity versus specimen thickness.

SEMI-ANNUAL REPORT ON MATERIALS RESEARCH IN
SUPPORT OF SUPERCONDUCTING MACHINERY

MAGNETOTHERMAL CONDUCTIVITY

L. L. Sparks

Cryogenics Division
Institute for Basic Standards
National Bureau of Standards
Boulder, Colorado 80302

April 1976

Summary: Magnetothermal Conductivity

The thermal conductivity and effect of a magnetic field on the thermal conductivity of UNS-A91100 in the "0" anneal condition (aluminum 1100 annealed at 350° C for 1 hour) have been determined in the temperature range 5 K to 20 K. A magnetic field typically increases the electronic thermal resistance and thus lowers the total observed thermal conductivity of a metal. For the present aluminum specimen (RRR = 32.6) the data indicate that a 6366 kA/m (80 kOe) magnetic field reduces the thermal conductivity by 29% at 5.5 K and by 50% at 20 K. Electrical resistivity data have also been determined and show an increase in resistivity with increasing magnetic field.

Contents: Magnetothermal Conductivity

		Page
1.	Introduction	141
2.	Procedures	141
	2.1 Apparatus	141
	2.2 Material	142
3.	Results	142
4.	Discussion	142
5.	References	143
	List of Figures	144

MAGNETOTHERMAL CONDUCTIVITY

L. L. Sparks

Cryogenics Division
Institute for Basic Standards
National Bureau of Standards
Boulder, Colorado 80302

1. Introduction

The objective is to determine the effect of magnetic fields on the thermal conductivity of technically important metals. The need for this information arises from the development of rotating machinery operating at cryogenic temperatures. The existing world's literature on magnetothermal conductivity, $\lambda(H)$, is concerned almost exclusively with scientific materials, e.g., very pure materials and single crystals. A complete bibliography of the subject was given by Sparks and Fickett [1].

The materials studied in this program are being used or are candidates for use in superconducting motors and generators. Optimum design of these machines, which must operate at low temperatures while in magnetic fields, requires a detailed knowledge of how the thermal properties of the constituent materials are affected by a magnetic field. The broad material categories of interest include superconductor stabilizing materials such as copper and aluminum, and structural materials such as nickel alloys, stainless steels, and metallic composites.

2. Procedures

2.1 Apparatus

The principal components of the $\lambda(H)$ system are shown schematically in Figure 1. Since the detailed operation of the system has been described in previous reports [1,2] and the details of several system modifications were discussed in [3], only a very brief reiteration of the system and its operation is included here. The specimen chamber, as shown in Figure 1, is evacuated (operating pressure is less than 10^{-4} Pa) and immersed in liquid helium. The liquid helium provides refrigeration to the specimen via the THERMAL LINKS (capitalized terms refer to Figure 1). The specimen is shown mounted with its axis parallel to the axis of the superconducting solenoid which allows the longitudinal field effect to be determined.

The basic operation of the system involves balancing electrical power supplied to three heaters with the heat leak to the liquid helium bath via the THERMAL LINKS. The electrical heaters were wound, one each, on the TEMPERATURE CONTROLLED HEAT SINK (TCHS), the SPECIMEN, and the TEMPERING POST. The power supplied to the TCHS determines the approximate temperature of the specimen; the SPECIMEN HEATER is used to establish a temperature gradient along the specimen; and the TEMPERING POST HEATER is used to reduce the temperature difference between the specimen and the tempering post to less than $\pm$ 5 mK. The TEMPERING POST and TCHS heaters are automatically controlled during all tests while a constant current is supplied to the SPECIMEN HEATER. The temperature difference existing along the sample due to the specimen heater current is determined at the two THERMOMETER BLOCKS. The thermal conductivity of the specimen is then computed from a knowledge of the specimen geometry (area/length), the specimen heater power ($\dot{Q}$), and the measured temperature difference along the specimen (ΔT). The

relationship of λ to these parameters is given by

$$\lambda = \frac{\dot{Q}}{\frac{A}{\ell}\Delta T}. \qquad (1)$$

A series of measurements of ΔT and $\dot{Q}$ at various fields ($0 \leq H \leq 6366$ kA/m)* and temperatures ($4 < T < 20$ K) result in the data presented in this report.

2.2 Materials

One material, UNS-A91100 (aluminum 1100), was tested during this reporting period. The mill analysis in weight percent of the stock used for the $\lambda(H)$ specimen is as follows: Cu = 0.2, Fe = 0.6, Si = 0.1, and the balance is Al. The test specimen is in the "0" condition after being annealed for 1 hour at 350° C in a vacuum of 1.33×10^{-7} Pa and then furnace cooled. The DP hardness of the annealed specimen is 28 (1 kg load) and its density is 2.818×10^{3} kg/m^3 at 294 K. The residual resistance ratio, R_{273K}/R_{4K}, is 32.6, and the ratio of area to length is 4.84×10^{-4} m.

The THERMOMETER BLOCKS and the SPECIMEN HEATER are attached to the specimen by soldering as detailed in [3]. In order to avoid the difficulties involved in soldering to aluminum, thin copper strips were electroplated to the specimen as needed after the specimen was annealed.

3. Results

The thermal conductivity of the present specimen is shown in Figure 2 as a function of temperature with magnetic field as a parameter. The reduction in conductivity from the zero field values caused by a 6366 kA/m (80 kOe) field is 29% at 5 K and 50% at 20 K. The estimated uncertainty of the thermal conductivity data points is $\pm$ 6% at T = 4 K and $\pm$ 8% at T = 20 K. Figure 3 presents the relative change in the thermal resistance, $\Delta W/W_{H=0} \equiv (W_H - W_{H=0})/W_{H=0}$, as a function of magnetic field with temperature as a parameter. The electrical resistivity is shown in Figure 4. The estimated uncertainty of the electrical resistivity data points is $\pm$ 8%.

4. Discussion

Attempts to find corroborating data have, to a large extent, been unsuccessful both for the case where $H = 0$ and $H \neq 0$. The literature contains many references to papers dealing with the thermal conductivity of aluminum at zero-magnetic field [4], and several references given in [1] deal with thermal conductivity of aluminum in magnetic fields. With two exceptions, however, the low temperature thermal conductivity of aluminum data pertain to very high purity polycrystalline or single crystal specimens. This, coupled with the fact that thermal and electrical conductivities of most good conductors are extremely dependent on trace impurities and thermal history, makes direct comparison to the present data difficult.

Powell, et al. [5] measured the thermal and electrical conductivity of two UNS-A91100 specimens; one was used in the "F" condition (as fabricated)

* The International System of Units (SI) designation for magnetic field strength is ampere per meter, and this unit is used throughout this paper. The more conventional unit of magnetic field strength, the oersted, is also given. Conversion of oersteds to amperes/meter is accomplished by multiplying oersteds by $1000/4\pi$.

and the other in the "0" condition (fully annealed). His results for the "0" specimen were anomalous in that the observed thermal conductivity was even lower than that of the "F" specimen. The RRR for his "0" specimen was around 15 when the expected value for this grade of aluminum is ∿ 32. The behavior of the "0" specimen was attributed to high impurity levels in the stock material. Present results can also be compared with those of de Nobel [6]. In this case the data extend down to only 15 K (a 5 K overlap with the present data) and the material is not well characterized. de Nobel's material was intended to be used in construction of laboratory apparatus (therefore, not of extremely high purity); its conductivity is approximately 5% lower than the present data.

The temperature dependence of the relative change in thermal resistivity, $\Delta W/W_{H=0}$, as shown in Figure 3 is opposite that of the copper specimens tested earlier [7]. This temperature dependence has been observed before [8] for single crystal specimens at lower temperatures. Further study of the present data will be necessary to examine the possible scattering mechanisms responsible for this behavior.

The uncertainty in the electrical resistivity data shown in Figure 4 is high due to the short specimen length and low allowable specimen current (due to small wires). The scatter in the zero field data was considerably higher than the $H \neq 0$ data. These data sets ($H = 0$ and $H \neq 0$) were taken on different days but were otherwise the same. The $H = 0$ curve shown in this figure is from Clark, et al. [9]; their specimen had the same RRR as the present specimen within experimental uncertainty. An analysis of these $\Delta\rho/\rho_{H=0}$ data indicate that the magnetic field effect on the resistivity is only a very weak function of temperature.

In conclusion, the thermal conductivity of aluminum UNS-A91100 in the "0" annealed condition is reduced when a magnetic field is applied. The magnitude of the reduction caused by a 6366 kA/m field is 29% at 5 K and 50% at 20 K. The temperature dependence of $\Delta W/W_{H=0}$ is the inverse of that found for the copper specimens measured previously.

5. References

1. L. L. Sparks and F. R. Fickett; in Materials Research in Support of Superconducting Machinery - I; R. P. Reed, A. F. Clark, E. C. van Reuth (Eds.); Nat. Bur. Stds., Boulder, CO; March 1974; AD780596.

2. L. L. Sparks and F. R. Fickett; in Materials Research in Support of Superconducting Machinery - II; R. P. Reed, A. F. Clark, E. C. van Reuth (Eds.); Nat. Bur. Stds., Boulder, CO; October 1974; ADA004586.

3. L. L. Sparks; in Materials Research in Support of Superconducting Machinery - IV; R. P. Reed, A. F. Clark, E. C. van Reuth (Eds.); Nat. Bur. Stds., Boulder, CO; October 1975; ADA019230.

4. Childs, G. E., Ericks, L. W. and Powell, R. L., Thermal conductivity of solids at room temperature and below, National Bureau of Standards (U.S.), Monogr. 131, 608 pages (September 1973).

5. Powell, R. L., Hall, W. J. and Roder, R. H., Low-temperature transport properties of commercial metals and alloys. II. Aluminums, J. Appl. Phys. 31, No. 3, p. 496 (March 1960).

6. de Nobel, J., Heat conductivity of steels and a few other metals at low temperatures, Physica 17, No. 5, p. 551 (May 1951).

7. L. L. Sparks; in Materials Research in Support of Superconducting Machinery - III; R. P. Reed, A. F. Clark, E. C. van Reuth (Eds.); Nat. Bur. Stds., Boulder, CO; April 1975; ADA012365.

8. Amundsen, T. and Sovik, R. P., Measurements of the thermal magnetoresistance of aluminum, J. Low Temp. Phys. 2, No. 1, 1970.

9. Clark, A. F., Childs, G. E. and Wallace, G. H., Electrical resistivity of some engineering alloys at low temperatures, Cryogenics 10, No. 4, p. 295 (August 1970).

List of Figures

Figure 1. Magnetothermal conductivity probe and magnet.

Figure 2. Thermal conductivity of UNS-A91100 "0" as a function of temperature with magnetic field as a parameter.

Figure 3. Relative change in thermal resistance as a function of magnetic field with temperature as a parameter.

Figure 4. Electrical resistivity as a function of temperature with magnetic field as a parameter. The dashed line represents H = 0 data from Clark, et al.[9].

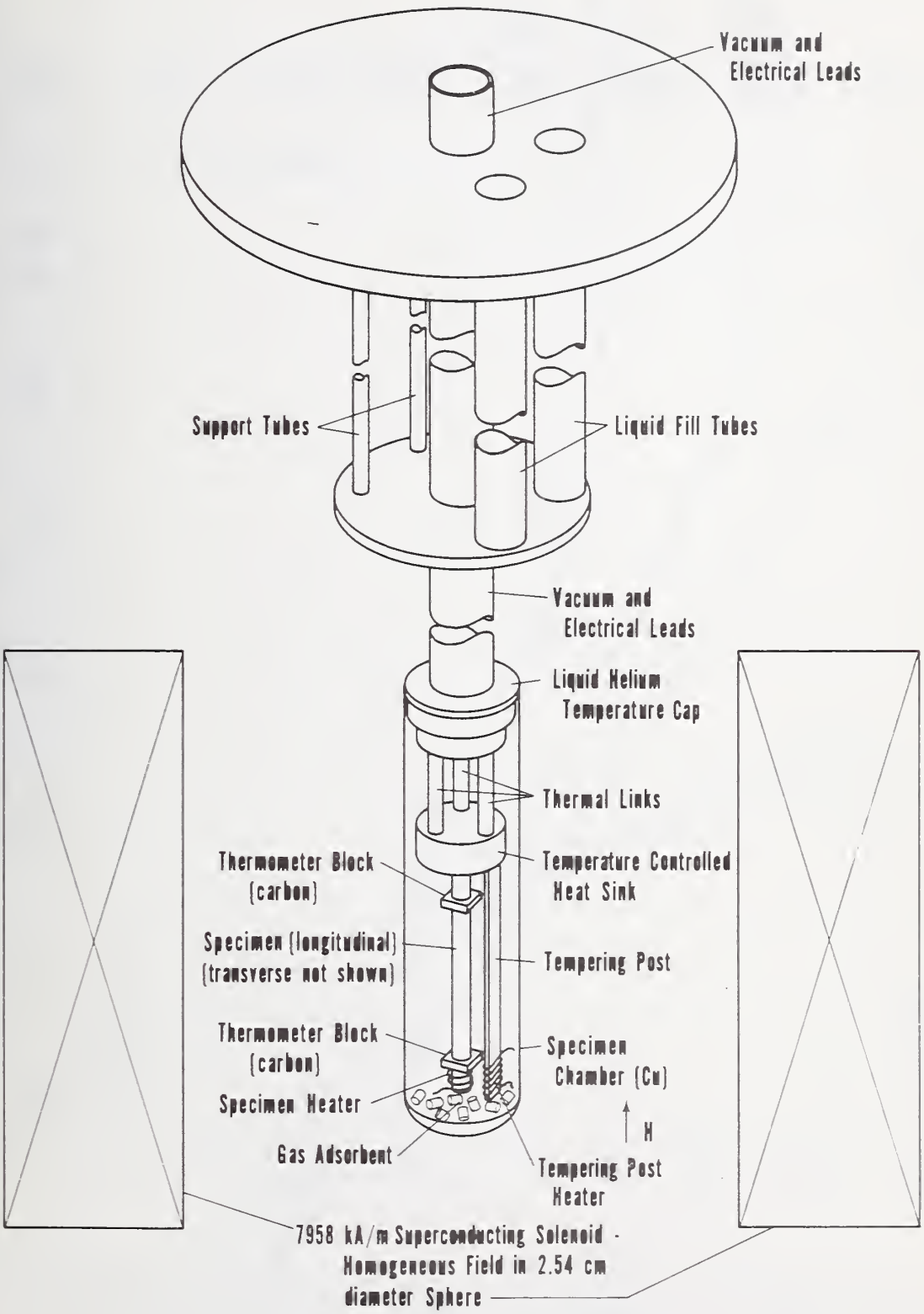

Figure 1. Magnetothermal conductivity probe and magnet.

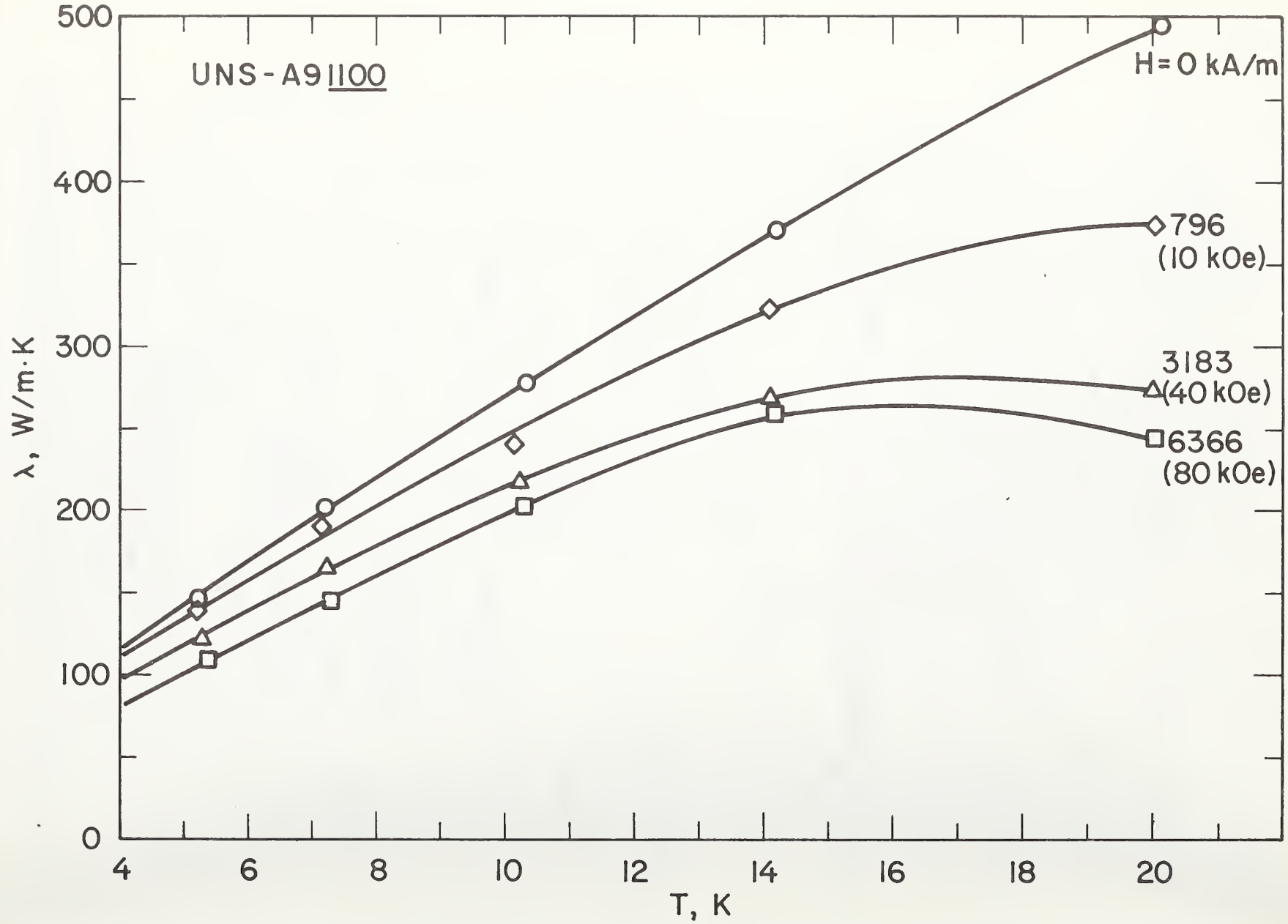

Figure 2. Thermal conductivity of UNS-A91100 "0" as a function of temperature with magnetic field as a parameter.

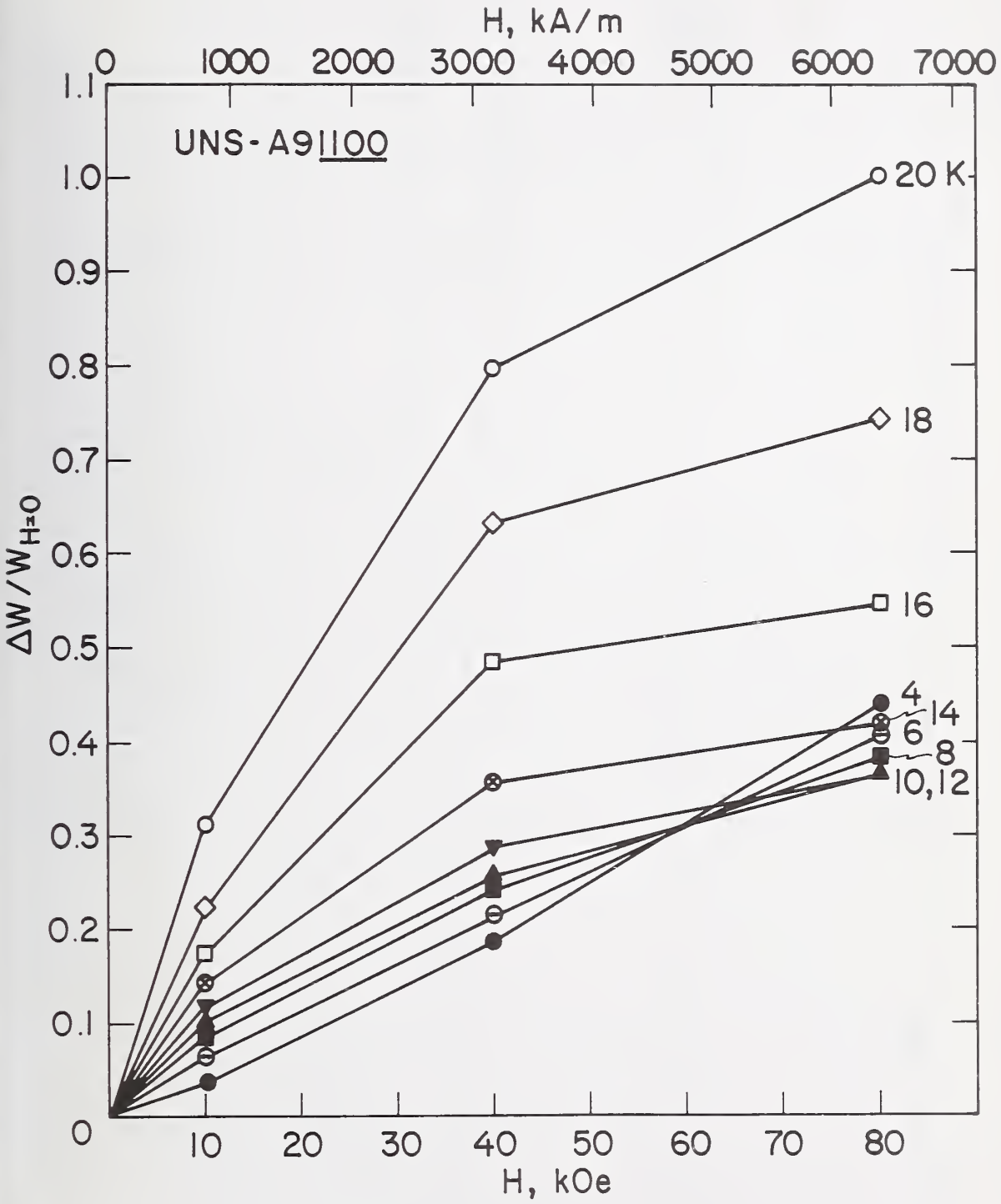

Figure 3. Relative change in thermal resistance as a function of magnetic field with temperature as a parameter.

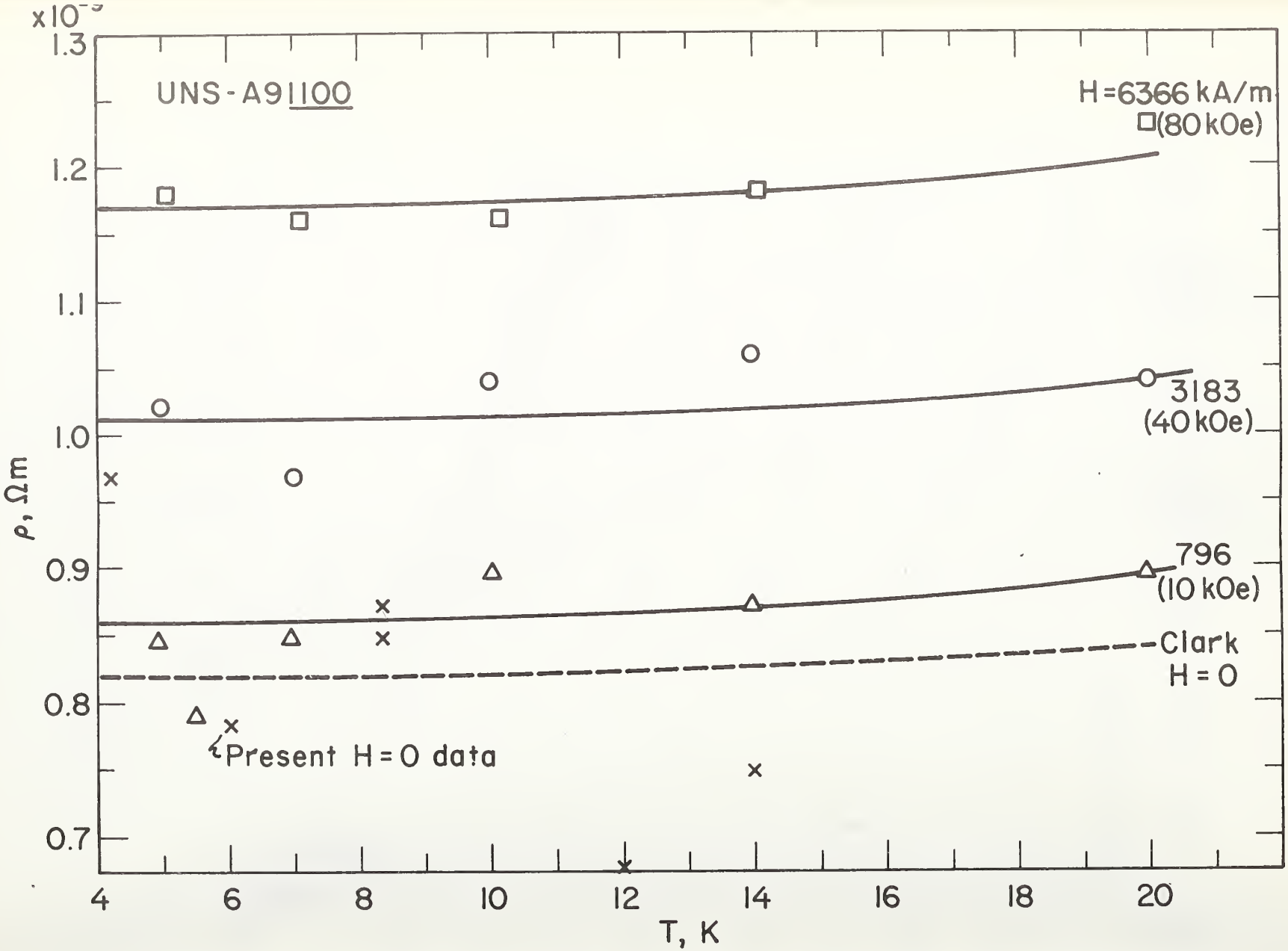

Figure 4. Electrical resistivity as a function of temperature with magnetic field as a parameter. The dashed line represents H = 0 data from Clark, et al.[9].

SEMI-ANNUAL REPORT ON MATERIALS RESEARCH
IN SUPPORT OF SUPERCONDUCTING MACHINERY

THERMAL CONDUCTIVITY

J. G. Hust

Cryogenics Division
Institute for Basic Standards
National Bureau of Standards
Boulder, Colorado 80302

April 1976

Summary: Thermal Conductivity

During the current reporting period no thermal conductivity measurements were performed. The final measurements for this program will be performed during the next, and final, reporting period. Measurements are scheduled for the following materials:

Maraging steel 300 (Fe-18Ni-9Co-5Mo)
Carpenter 49 steel (Fe-49Ni)
Boron-Aluminum Composite (longitudinal)
Graphite-Epoxy Composite (longitudinal, transverse)

The final report will contain the results of these measurements and a summary of the thermal conductivities of materials pertinent to this program.

NBS-114A (REV. 7-73)

U.S. DEPT. OF COMM. BIBLIOGRAPHIC DATA SHEET	1. PUBLICATION OR REPORT NO. NBSIR 76-839	2. Gov't Accession No.	3. Recipient's Accession No.

4. TITLE AND SUBTITLE
Semi-Annual Report on Materials Research in Support of Superconducting Machinery

5. Publication Date
April 1976

6. Performing Organization Code
275.03

7. AUTHOR(S) R. P. Reed, J. G. Hust, M. B. Kasen, H. M. Ledbetter, D. T. Read, R. E. Schramm, L. L. Sparks, and R. L. Tobler

8. Performing Organ. Report No.

9. PERFORMING ORGANIZATION NAME AND ADDRESS

NATIONAL BUREAU OF STANDARDS
DEPARTMENT OF COMMERCE
WASHINGTON, D.C. 20234

10. Project/Task/Work Unit No.
2756530

11. Contract/Grant No.
ARPA Order 2569

12. Sponsoring Organization Name and Complete Address (*Street, City, State, ZIP*)
Advanced Research Projects Agency
1400 Wilson Boulevard
Arlington, VA 22209

13. Type of Report & Period Covered

14. Sponsoring Agency Code
4D10

15. SUPPLEMENTARY NOTES

16. ABSTRACT (*A 200-word or less factual summary of most significant information. If document includes a significant bibliography or literature survey, mention it here.*)

Results are reported of a six-month study, ending March 1976, on candidate materials for superconducting machinery. The results cover five areas--advanced composites, elastic properties, fatigue resistance and fracture toughness, magnetothermal conductivity, and thermal conductivity. Material properties were studied over the temperature range 4 to 300 K. Materials studied include: aluminum alloys 1100, 2014, 2219; a nickel-chromium-iron alloy; iron-47.5 nickel; and the composite materials boron/aluminum, boron/epoxy, S-glass/epoxy; graphite epoxy. Some notable results of the study are: first reports of compressive mechanical testing on composite materials at 4 K; regular temperature behavior of the elastic constants of aluminum 2014 and 2219 and of iron-47.5 nickel, which is magnetic; none of the mechanical properties of the nickel-chromium-iron alloy tested were affected deleteriously by cryogenic temperatures; in aluminum alloy 2219, J_{Ic} and K_{Ic} are not equivalent because of sub-critical crack extension; both electrical and thermal conductivities of aluminum alloy 1100 are reduced by magnetic fields.

17. KEY WORDS (*six to twelve entries; alphabetical order; capitalize only the first letter of the first key word unless a proper name; separated by semicolons*)
Aluminum alloys; composites; elastic properties; engineering materials; fatigue; fracture; iron alloys; cryogenic temperatures; mechanical properties; nickel alloys; superconducting machinery; thermal conductivity.

18. AVAILABILITY
[X] UnLimited
[ ] For Official Distribution. Do Not Release to NTIS
[ ] Order From Sup. of Doc., U.S. Government Printing Office Washington, D.C. 20402, SD Cat. No. C13
[X] Order From National Technical Information Service (NTIS) Springfield, Virginia 22151

19. SECURITY CLASS (THIS REPORT)	21. NO. OF PAGES
UNCLASSIFIED	155
20. SECURITY CLASS (THIS PAGE)	22. Price
UNCLASSIFIED	$6.25

USCOMM - ERL USCOMM-DC 29042-P74